Supersonic Constricted Plasma Flows

Teck Seng Ho

A thesis submitted for the degree of
Doctor of Philosophy
of The Australian National University

June 2018

Declaration

This thesis is an account of research undertaken between February 2014 and June 2018 at the Research School of Physics and Engineering, College of Science, The Australian National University, Canberra, Australia. Except where acknowledged in the customary manner, the material presented in this thesis is, to the best of my knowledge, original and has not been submitted in whole or part for a degree in any university.

Teck Seng Ho

6 June 2018

Dedicated to my 倬懿,
and every single moment with you
since that first double take.

Acknowledgements

Foremost, I am forever indebted to my supervisors Christine Charles and Rod Boswell at the Space Plasma, Power and Propulsion Laboratory. I joined SP^3 with little more than just my enthusiasm for plasma physics, and left with more skills and knowledge than what could be condensed in this thesis alone. Christine, thank you for believing in me. You are an inspiring leader and deserve more recognition for being part of the modern vanguard for women in science. Rod, like the long lineage of students who ran the gauntlet before me, I have thoroughly enjoyed your mentorship in both physics and life. You truly are a fount of wisdom. I must also convey my admiration of your sharp wit; I am in awe of its effects on different people!

I am beholden to my seniors who trained me in the lab: Samuel Dixon, Yunchao Zhang, and especially Amelia Greig, from whom I inherited the *Pocket Rocket* experiment. To my juniors: Alex Bennet, Thomas Charoy, Ashley Pascale, Alex Stuchbery, and Dimitrios Tsifakis, it has been an honour to share the lab with you. I couldn't have asked for a better team, and I will hold fond memories of the days abound with vivid discussions and fruitful exchange of ideas. My gratitude also goes to Andrew Bish, Peter Alexander, Stephen Holgate, and Rhys Hawkins for your expertise in hardware and code. Each of you have left your own unique mark not just on *Pocket Rocket* but also on my experience at SP^3.

This research was enabled by the generous support of the scholarships offered by the Australian Government, The Australian National University, and the Research School of Physics and Engineering. I would also like to acknowledge the support of the Centre for Plasmas and Fluids as well as the technical and administrative staff at RSPE, especially Karen Nulty and Uyen Nguyen, who are always happy to help. To my thesis examiners, I am grateful for your insightful comments and most flattered by your wonderful reviews. Your magnanimous recognition has made all the long hours well worth the effort.

I have had the privilege of collaborating with an international spread of researchers: Scott Doyle, James Dedrick, Endre Szili, Jun-Seok Oh, Juan Rivas-Davila, and Luke Raymond;

I am both enlightened and humbled by the experience. To Meliza Clancy and your rapt audience of young science students in our annual livestream laboratory tours, the pleasure is all ours. Your dazzling thank-you cards are displayed proudly in our corridor.

My fascination with the sciences began at a young age under the tutelage of my grandfather, and has continuously escalated ever since. My deepest respect goes to my father for your tireless support of the family which has made everything possible. Much of what my brother and I have accomplished must also be credited to my mother for raising us with your unconditional love and encouragement to pursue whatever interested us the most. Despite being the older sibling, I am constantly being kept on my toes by my brother's impressive academic achievements, so good job to you. To Elynor Liu, Daniel Jacobs, and Alan Lim, I am fortunate to have had your friendship for the last decade and more, and thankful for the multiple ways our paths have crossed while on the journey towards our respective Ph.D. termini.

Finally, I must express my heartfelt appreciation for my one and only Zhuoyi He. You have been the most enduring source of motivation during these four and a half years. I cannot bear to imagine what my life would be like without the alignment of all the serendipitous moments that conspired to bring us together. This is for you.

23 October 2018

Abstract

The *Pocket Rocket* electrothermal microthruster is a miniaturised electric propulsion system designed for nanosatellites operating in space. A weakly ionised capacitively coupled plasma is ignited in the flowing Ar gas propellant within a constricted discharge chamber at $\gtrsim 1\,\mathrm{Torr}$ using $\lesssim 10\,\mathrm{W}$ of radiofrequency power. The discharge can operate either continuously or in rapid pulsed mode since plasma breakdown initiates almost instantaneously on a $\sim$ µs time scale. The propellant is heated to temperatures approaching $\sim 1000\,\mathrm{K}$ and is expanded through a converging-diverging nozzle into vacuum at supersonic velocities. Thrust on the order of $\sim 1\,\mathrm{mN}$ is generated as a reactionary force to the linear momentum of the expelled neutral gas propellant.

This thesis presents a comprehensive model of *Pocket Rocket* developed with computational fluid dynamics and plasma simulations.

Boundary layer effects are significant in the rarefied flow within the constricted discharge chamber. A slip boundary condition with the appropriate tangential momentum and thermal accommodation coefficients must be used to produce results that precisely match experimental measurements. The problem of including vacuum regions within a fluid simulation domain is unconventionally circumvented by taking advantage of the flow velocity choking. The computed sonic surface, thrust force, and specific impulse are in good agreement with theoretical predictions.

Volumetric plasma-induced heating of the background neutral gas is primarily due to ion-neutral charge exchange collisions, with very little contribution from electron-neutral elastic collisions. The propellant temperature is described by two local models based on the different ion transport behaviour in the plasma bulk and plasma sheath. The most dominant process is surface bombardment by ions accelerated through the plasma sheath, which heats the discharge chamber wall and is responsible for the creation of secondary electrons that sustain the gamma mode discharge.

The geometrical area asymmetry of the grounded and powered electrodes results in a self-bias that manifests as a spatially nonuniform negative charging within the dielectric discharge chamber wall. In the thin sheath regime, the self-biased waveform has a diminished trailing edge at each positive peak, and asymmetrically displaced negative peaks due to the extraneous impedance of the dielectric wall. This leads to a redefinition of the self-bias voltage that uses the maxima envelope of the self-biased waveform instead of the mean, which maintains consistency with different extraneous impedances.

The performance of *Pocket Rocket* is improved by optimising the physical and electrical geometry for thrust and boundary layer effects, and plasma confinement is achieved through the formation of a conical plasma sheath at the nozzle throat. Enhanced recombination in the supersonic expanding plume creates a neutral exhaust, thereby avoiding contamination of externally mounted solar panels and interference with sensitive instruments. Most importantly, the combination of flow velocity choking and plasma confinement results in a convergent plasma simulation that accurately models plasma expansion into vacuum.

The computational fluid dynamics and plasma modelling technique and analysis presented in this thesis are not restricted to the *Pocket Rocket* discharge and may be adapted for other discharges at different pressure regimes and physical scales.

Publications

The work presented in this thesis has resulted in the following publications in peer reviewed journals and conference proceedings:

- S. J. Doyle, A. R. Gibson, J. Flatt, **T. S. Ho**, R. W. Boswell, C. Charles, P. Tian, M. J. Kushner, and J. Dedrick. 'Spatio-temporal plasma heating mechanisms in a radio-frequency electro-thermal microthruster'. *Plasma Sources Science and Technology* 27.8 (Aug. 2018), p. 085011. DOI: 10.1088/1361-6595/aad79a.

- **T. S. Ho**, C. Charles, and R. W. Boswell. 'Redefinition of the self-bias voltage in a dielectrically shielded thin sheath RF discharge'. *Journal of Applied Physics* 123.19 (May 2018), p. 193301. DOI: 10.1063/1.5023076.

- **T. S. Ho**, C. Charles, and R. W. Boswell. 'Performance modelling of plasma microthruster nozzles in vacuum'. *Journal of Applied Physics* 123.17 (May 2018), p. 173301. DOI: 10.1063/1.5012765.

- C. Charles, **T. S. Ho**, A. Pascale, T. Charoy, A. Bennet, A. Stuchbery, R. W. Boswell, W. Liang, L. Raymond, and J. Rivas-Davila. 'The *Pocket Rocket* electro-thermal plasma thruster for 'CubeSat' nano-satellites'. *International Astronautical Congress*. Adelaide, Sept. 2017.

- **T. S. Ho**, C. Charles, and R. W. Boswell. 'Neutral gas heating and ion transport in a constricted plasma flow'. *Physics of Plasmas* 24.8 (July 2017), p. 084501. DOI: 10.1063/1.4996014.

- **T. S. Ho**, C. Charles, and R. W. Boswell. 'A comprehensive cold gas performance study of the *Pocket Rocket* radiofrequency electrothermal microthruster'. *Frontiers in Physics* 4 (Jan. 2017), p. 55. DOI: 10.3389/fphy.2016.00055.

- C. Charles, A. Bish, R. W. Boswell, J. Dedrick, A. Greig, R. Hawkins, and **T. S. Ho**. 'A short review of experimental and computational diagnostics for radiofrequency plasma microthrusters'. *Plasma Chemistry and Plasma Processing* 36.1 (Sept. 2015), pp. 29–44. DOI: 10.1007/s11090-015-9654-5.

Contents

List of Figures

List of Tables

Symbols and abbreviations

Symbol	Description
PR	*Pocket Rocket* (asterisks * denote identical original PR geometry)
* PR-A	Al_2O_3 discharge chamber wall, 2.1 mm internal radius
PR-Z	ZrO_2 discharge chamber wall, 1.833 mm internal radius
PR-05	0.5 mm discharge chamber wall thickness
* PR-10	1.0 mm discharge chamber wall thickness
PR-15	1.5 mm discharge chamber wall thickness
* PR-O	straight cylinder, 2.1 mm internal radius
PR-C	constricted nozzle, 1.05 mm throat internal radius
PR-N	converging-diverging nozzle, 0.75 mm throat internal radius
MiniPR	*Mini Pocket Rocket*
P	Plenum
C	Discharge chamber
D, D1 to D6	Downstream
CW	Discharge chamber wall
E	Powered electrode
I	Insulation
S	Structure
A_{ex}	discharge chamber exit area
A_{gnd}	grounded electrode surface area
A_{pwr}	powered electrode surface area
A_{tt}	nozzle throat area
c_p	specific heat at constant pressure
c_{s}	sound speed
$c_{\mathrm{s,i}}$	ion sound speed
C_{block}	blocking capacitor capacitance
$C^{+}_{\mathtt{PR}}$	PR discharge series capacitance
$C^{\parallel}_{\mathtt{PR}}$	PR discharge parallel capacitance
C_{s}	plasma sheath capacitance
C_{wall}	discharge chamber wall capacitance
D	mass diffusivity
e	Euler's number, 2.718281828459046
exp	exponential function

E_r	radial electric field
f_x	pointwise transformation function for parameter x
F_t, $\boldsymbol{F}_\mathrm{t}$	thrust force
F_bl	boundary layer friction force
F_p	internal pressure force
g_0	standard gravity, $9.80665\,\mathrm{m\,s^{-2}}$
h, h_i	enthalpy; excitation or ionisation energy
GCF	gas correction factor
	Ar, 1.441
i_f	fluid iteration for CFD-plasma simulations
i_p	plasma iteration for CFD-plasma simulations
i_s	steady state iteration for CFD simulations
$i_{\mathrm{s}:n}$	n^{th} steady state iteration for CFD simulations
I_e	electron current at discharge chamber wall
$I_{\mathrm{e}'}$	secondary electron current at discharge chamber wall
I_i	ion current at discharge chamber wall
I_sp	specific impulse
$\bar{I}_\mathrm{RF}$	RMS plasma RF current
$\bar{I}_\mathrm{wall}$	RMS plasma RF current at discharge chamber wall
$\hat{I}_\mathrm{sp}$	theoretical maximum specific impulse
	Ar at $T_\mathrm{st} = 300\,\mathrm{K}$, 57.0 s
	N_2 at $T_\mathrm{st} = 300\,\mathrm{K}$, 80.5 s
	Xe at $T_\mathrm{st} = 300\,\mathrm{K}$, 31.4 s
k	thermal conductivity
k_B	Boltzmann constant, $1.38064852 \times 10^{-23}\,\mathrm{J\,K^{-1}}$
Kn	Knudsen number
	continuum regime, $\mathrm{Kn} \lesssim 0.01$
	slip regime, $0.01 \lesssim \mathrm{Kn} \lesssim 0.1$
	transitional regime, $0.1 \lesssim \mathrm{Kn} \lesssim 10$
	free molecular regime, $\mathrm{Kn} \gtrsim 10$
L	characteristic length
$L_\mathtt{C}$	discharge chamber characteristic length
$L_\mathtt{D}$	downstream region characteristic length
$L_\mathtt{P}$	plenum characteristic length
m	molecular mass
	Ar, 39.9481 u
	N_2, 28.01348 u
	Xe, 131.29 u
m_e	electron mass
m_i	ion molecular mass
$\dot{m}$	propellant mass flow rate
M	spacecraft mass
Ma	Mach number
n_e	electron number density
n_i	ion number density
p	static pressure
p_0	background pressure or outlet boundary static pressure

p_e	electron partial pressure
p_ex	thruster exit static pressure
p_st	stagnation pressure or macroscopic plenum pressure
$\boldsymbol{p}$	momentum
P	power
P_f	forward power
P_gen	RF power generator output power
$P_\mathtt{PR}$	PR power draw
P_r	reflected power
P_RF	RF electrical power
P_S	power deposited in surface processes
P_sub	RF power subsystem output power
P_V	power deposited in volumetric processes
Pr	Prandtl number
q_e	elementary charge, $1.6021766208 \times 10^{-19}\,\mathrm{C}$
Q_bias	self-bias charge
Q_e	collected electron charge
Q_i	collected ion charge
R_exp	PR experimental setup total resistance
$R_\mathtt{PR}$, $R^{+}_\mathtt{PR}$	PR discharge series resistance
$R^{\parallel}_\mathtt{PR}$	PR discharge parallel resistance
R_α	alpha mode direct ionisation rate by bulk electrons
R_α	gamma mode ionisation rate by secondary electrons
Sc	Schmidt number
SWR	standing wave ratio
t_n	n^th CFD-plasma simulation time-step
T	temperature
T_0	outlet boundary backflow temperature
T_e	electron temperature $k_\mathrm{B}T_\mathrm{e}$, electron energy $3/2 \cdot T_\mathrm{e}$, Maxwellian electron temperature
T_ext	external wall boundary temperature
$T_\mathtt{R}$	reactant species temperature in Arrhenius equation
T_slip	temperature jump
T_st	stagnation temperature
u	velocity magnitude
$\boldsymbol{u}_\mathrm{ex}$	propellant exit flow velocity
u_r	radial flow velocity
$u_{r,\mathrm{i}}$	radial ion drift velocity
u_slip	slip velocity
u_T	thermal velocity
$u_{T,\mathrm{i}}$	ion thermal velocity
$u_{z,\mathrm{i}}$	axial ion drift velocity
u_z	axial flow velocity
v_i	ion velocity
V_b	breakdown voltage
V_bias	self-bias voltage

V_{block}	blocking capacitor DC bias voltage
V_{gen}	RF power generator RF voltage amplitude
V_{pwr}	powered electrode RF voltage amplitude
$\bar{V}_{\text{p}}$	RMS RF voltage across plasma / both plasma sheaths
$\bar{V}_{\texttt{PR}}$	RMS RF voltage across `PR` discharge
$\bar{V}_{\text{pwr}}$	powered electrode RMS RF voltage
$\bar{V}_{\text{s}}$	RMS RF voltage across plasma sheath
$\bar{V}_{\text{wall}}$	RMS RF voltage across discharge chamber wall
X_{exp}	`PR` experimental setup total reactance
$X_{\texttt{PR}}$	`PR` discharge reactance
Z_{exp}	`PR` experimental setup total impedance
Z_{gen}	RF power generator impedance
Z_{IMN}	impedance matching network impedance
$Z_{\texttt{PR}}$	`PR` discharge impedance
Z_{s}	plasma sheath impedance
Z_{wall}	discharge chamber wall impedance

α	accommodation coefficient
α_u	tangential momentum accommodation coefficient Ar, 0.9 N_2, 0.9 Xe, 1.0
α_T	thermal accommodation coefficient Ar, 0.9 N_2, 0.8 Xe, 0.8
α'_T	modified thermal accommodation coefficient Ar, 0.9 N_2, 0.9 Xe, 0.8
α_{el}	temperature coefficient for electrical resistivity
α'	polarisability volume Ar, 1.664 Å^3 N_2, 1.710 Å^3 Xe, 4.0 Å^3
γ	gas adiabatic index monatomic gas, 5/3 diatomic gas, 7/5
$\gamma_{\text{e}'}$	secondary electron emission coefficient
ϵ_{c}	chemical energy per surface recombination or deexcitation reaction
ϵ_{e}	thermal energy per electron-neutral elastic collision
ϵ_{i}	thermal energy per ion-neutral charge exchange collision
ϵ_{k}	kinetic energy per ion bombardment
ϵ_{S}	surface energy ($\epsilon_{\text{k}} + \epsilon_{\text{c}}$)
ϵ_{V}	volumetric energy ($\epsilon_{\text{e}} + \epsilon_{\text{i}}$)
ϵ_σ	Lennard-Jones characteristic energy

	Ar, 93.3 K
	N_2, 71.4 K
	Xe, 206.9 K
ε_0	vacuum permittivity, $8.854187817 \times 10^{-12}\,\mathrm{F\,m^{-1}}$
ε_r	relative permittivity or dielectric constant
	Al_2O_3, 9.6
	Macor, 6.0
	electrically conductive solid materials, 1.0
	fluid species, 1.0
η_IMN	impedance matching network power transfer efficiency
η_sub	RF power subsystem power transfer efficiency
λ, λ_LJ	kinematic mean free path
λ_i	ionisation mean free path
λ_μ	fluid mean free path
μ	dynamic viscosity
μ_i	ion mobility
μ_q	electrical mobility
ρ	mass density
ρ_el	electrical resistivity
σ	Lennard-Jones collision diameter
	Ar, 3.542 Å
	N_2, 3.798 Å
	Xe, 4.047 Å
σ_q	charge exchange cross section
	Ar, 49.0 $\mathrm{Å}^2$
	N_2, 40.0 $\mathrm{Å}^2$
	Xe, 88.4 $\mathrm{Å}^2$
$\sigma_\mathtt{R}$	reactant collision cross section
$\Delta\tau_\mathrm{f}$	fluid dynamics solver time-step
$\Delta\tau_\mathrm{p}$	plasma dynamics solver time-step
τ_RF	13.56 MHz RF period, 73.75 ns
	τ_+, positive period
	τ_-, negative period
τ_i	ion transit time
Φ	electric potential
Φ_gnd	grounded electrode electric potential
Φ_p	plasma potential
	Φ_p^+, maxima
	Φ_p^-, minima
Φ_pwr	powered electrode electric potential
Φ_wall	discharge chamber wall electric potential
	Φ_wall^+, maxima
	Φ_wall^-, minima
φ	particle flux
φ_i	ion flux
ω	angular frequency

Chapter 1

Introduction

1.1 Microspacecraft

In recent years, there has been a steady impetus in the satellite industry towards miniaturised microspacecraft, primarily driven by the desire to reduce spacecraft mass in order to reduce launch costs. This has led to the development of micro- ($\lesssim 100\,\mathrm{kg}$), nano- ($\lesssim 10\,\mathrm{kg}$), and picosatellites ($\lesssim 1\,\mathrm{kg}$), where the dramatic reduction in cost increases the accessibility to space, and brings with it the possibility of funding more missions and more frequent launches.

The CubeSat – a type of nanosatellite which is made up of one or multiple $\sim 1\,\mathrm{kg}$, $1\,\mathrm{dm}^3$ units – has become ever more prevalent in the recent years. One example of an international scientific endeavour enabled by the affordability of CubeSats is the QB50 mission [1] launched into orbit in 2017. The mission employs a network of 50 CubeSats, built by university teams all over the world, tasked with studying the lower thermosphere and reentry research. It also demonstrates the possibility of using a large fleet of low-cost microspacecraft to reduce mission risks by distributing functionality and incorporating redundancy, where the loss of one or even multiple microspacecraft does not jeopardise the entire mission.

Microspacecraft are typically launched into low Earth orbit where they experience atmospheric drag which inevitably slows them down, shortening their operational lifetime before reentry. Options to mitigate this include designing a minimum drag spacecraft [2], or the implementation of an onboard micropropulsion system. An ideal micropropulsion system must be designed around stringent volume, mass, and power budgets of the microspacecraft, while meeting the unique propulsion needs of each specific mission which may include attitude control, orbital station-keeping, drag compensation to slow orbital decay, de-orbit manoeuvres, or constellation formation and maintenance.

1.2 Propulsion technologies

Two main classes of propulsion technologies have been envisioned and flown for spacecraft. The first is gas and chemical propulsion which ranges from the traditional or microelectromechanical systems-based (MEMS) cold gas thrusters [3], to warm gas and chemical propellant systems. The second is electric propulsion which has emerged as a more viable and attractive alternative to chemical propulsion due to continuous improvements in electric thruster technologies and restrictions on hazardous and volatile propellants.

Electric propulsion can be grouped into three distinct categories: electrothermal, electrostatic, and electromagnetic. Electrothermal propulsion includes devices like resistojets [4, 5], arcjets [6–8], hollow cathode thrusters [9–12], and the *Pocket Rocket* microthruster [13–16]. Electrostatic propulsion has been dominated by a large variety of gridded ion thrusters. These include NASA's annular-geometry ion engine (AGI-Engine) [17, 18] and the NASA evolutionary xenon thruster (NEXT) [19, 20], and experimental technologies like the field emission electric propulsion (FEEP) concept [21] and its precedent colloid thrusters. Finally, electromagnetic propulsion includes the mature Hall effect thruster [22] and its variants [23–31], the helicon double layer thruster (HDLT) [32], as well as newer technologies like magnetoplasmadynamic (MPD) thrusters [33, 34] and ablative pulsed plasma thrusters (PPTs) [35] that use the Lorentz force to accelerate the plasma plume.

In electrothermal propulsion systems, thrust is derived from heated neutral gas propellant; whereas in electrostatic and electromagnetic propulsion systems, thrust is derived from highly accelerated ions generated from the propellant. The components and electronics of electrothermal propulsion systems are considerably less complex than electrostatic or electromagnetic propulsion systems, and thus may be more easily miniaturised for use on microspacecraft. Electrostatic and electromagnetic propulsion systems on the other hand are typically large, massive, and require high amounts of power, and are therefore more suited for use on small ($\lesssim 500\,\mathrm{kg}$) or medium ($\lesssim 1000\,\mathrm{kg}$) sized spacecraft.

This thesis only focuses on electrothermal micropropulsion devices and operational parameters that are admissible under the stringent volume, mass, and power design requirements for microspacecraft. For wider coverage on the topic, a comprehensive review of electric propulsion is available in [36, 37], while [38, 39] compiles a review of both classes of propulsion technologies with a specific focus on micropropulsion for microspacecraft.

1.3 Micropropulsion

1.3.1 Cold gas thruster

The cold gas thruster is the simplest form of propulsion. An inert propellant gas is stored in a pressurised vessel aboard a spacecraft. When required, a valve releases the propellant, which flows through a nozzle and exits into space.

Momentum is being carried off by the escaping propellant. The rate of change of momentum $\dot{\boldsymbol{p}}$ is given by:

$$\dot{\boldsymbol{p}} = \frac{\mathrm{d}}{\mathrm{d}t}\left(m\boldsymbol{u}_{\mathrm{ex}}\right) = \dot{m}\boldsymbol{u}_{\mathrm{ex}} \tag{1.1}$$

where $\dot{m}$ is the mass flow rate of the propellant and $\boldsymbol{u}_{\mathrm{ex}}$ is the velocity at which the propellant exits the thruster, with the assumption of an ideal case where $\boldsymbol{u}_{\mathrm{ex}}$ is uniform across the thruster exit. By Newton's second law of motion, a nonzero $\dot{\boldsymbol{p}}$ is equivalent to a nonzero force acting on the propellant. If that is the case, then Newton's third law of motion necessitates a force equal in magnitude but opposite in direction that acts on the thruster. Assuming ideal nozzle expansion, then the instantaneous thrust force $\boldsymbol{F}_{\mathrm{t}}$ acting on a spacecraft of total mass M including its onboard propellant is:

$$\boldsymbol{F}_{\mathrm{t}} = -\dot{m}\boldsymbol{u}_{\mathrm{ex}} = M\dot{\boldsymbol{v}} \tag{1.2}$$

which accelerates the spacecraft at $\dot{\boldsymbol{v}}$ in the direction opposite to $\boldsymbol{u}_{\mathrm{ex}}$.

On a spacecraft, M and $\dot{m}$ are limited by mission specifications and propellant budget. The only other way to obtain higher $F_{\mathrm{t}} = |\boldsymbol{F}_{\mathrm{t}}|$ is by increasing $u_{\mathrm{ex}} = |\boldsymbol{u}_{\mathrm{ex}}|$ which is primarily dependent on temperature and the nature by which the propellant is accelerated. In a cold gas thruster the only means of accelerating propellant is by using a converging-diverging nozzle. The convergent section accelerates subsonic flow up to the local sound speed c_{s} at the nozzle throat. For an ideal gas:

$$c_{\mathrm{s}} = \sqrt{\frac{\gamma k_{\mathrm{B}} T}{m}} \tag{1.3}$$

where γ is the gas adiabatic index, k_{B} is the Boltzmann constant, m is the molecular mass of the gas, and T is the temperature of the propellant. Since the propellant is not heated, c_{s} is low. The divergent section then accelerates the sonic flow to supersonic velocities, but the increase in velocity is fixed by the geometry of the nozzle and also dependent on other factors such as temperature, pressure, and boundary layer frictional losses. Consequently, u_{ex} is ultimately limited by c_{s}. As such, F_{t} produced by cold gas thrusters is typically in the $\sim$ µN to $\sim$ mN range, scaling roughly linearly with $\dot{m}$.

The specific impulse I_{sp} is a convenient measure of thruster effectiveness, defined as the change in momentum delivered per unit mass of propellant. From an experimental perspective using measurable parameters:

$$I_{\mathrm{sp}} = \frac{u_{\mathrm{ex}}}{g_0} \tag{1.4}$$

where g_0 is the standard gravity. The relation is independent of $\dot{m}$, and solely dependent on u_{ex}. From a theoretical perspective, the maximum specific impulse $\hat{I}_{\mathrm{sp}}$ a gas can achieve is given by the thermodynamic relation:

$$\hat{I}_{\mathrm{sp}} = \frac{1}{g_0}\sqrt{\frac{k_{\mathrm{B}}T_{\mathrm{st}}}{m}\frac{2\gamma}{\gamma-1}\left[1-\left(\frac{p_{\mathrm{ex}}}{p_{\mathrm{st}}}\right)^{\frac{\gamma-1}{\gamma}}\right]} \tag{1.5}$$

The whole term after the $1/g_0$ prefix represents the theoretical maximum velocity $\hat{u}_{\mathrm{ex}}$ of the propellant exiting from the thruster [40], where T_{st} and p_{st} are the stagnation temperature and pressure respectively taken upstream of the nozzle, and p_{ex} is the pressure at the thruster exit. Assuming $p_{\mathrm{ex}} = 0\,\mathrm{Torr}$ for ideal vacuum expansion, $\hat{I}_{\mathrm{sp}}$ becomes dependent only on T_{st} and m. For a cold gas thruster operating with inert gas propellants such as argon, xenon, or nitrogen at a fixed $T_{\mathrm{st}} = 300\,\mathrm{K}$, the respective values are $\hat{I}_{\mathrm{sp}}(\mathrm{Ar}) = 57.0\,\mathrm{s}$, $\hat{I}_{\mathrm{sp}}(\mathrm{Xe}) = 31.4\,\mathrm{s}$, and $\hat{I}_{\mathrm{sp}}(\mathrm{N_2}) = 80.5\,\mathrm{s}$. In practice however, the actual I_{sp} achieved can be significantly less than $\hat{I}_{\mathrm{sp}}$ due to boundary layer frictional losses and nonideal expansion.

1.3.2 Chemical propellant thruster

A straightforward way to increase I_{sp} is by raising the temperature of the propellant. Warm gas and chemical propellant thrusters commonly use monopropellants such as hydrazine ($\mathrm{N_2H_4}$) and hydrogen peroxide ($\mathrm{H_2O_2}$). The propellant is catalytically decomposed in an exothermic reaction, whereby the release of chemical energy heats the propellant to temperatures up to $\sim 1000\,\mathrm{K}$. Bi- or tripropellant systems also exist but have increased system complexity and cost. Chemical propellant thrusters are able to produce F_{t} from $\sim$ mN up to $\sim$ N, with $\hat{I}_{\mathrm{sp}}$ on the order of $\sim 100\,\mathrm{s}$. However, it is difficult to finely manipulate thrust from chemical propellant thrusters for precision manoeuvres and attitude control, which limits their applications to ballistic trajectories.

While better performing than a cold gas thruster, the flammability and toxicity of chemical propellants result in higher costs in ground handling and propellant loading procedures, and may require a significant portion of a microspacecraft mission financial budget. Additionally, the operational lifetime of a chemical propellant thruster is limited by the lifetime of the catalyst which is prone to degradation and failure over time.

1.3.3 Resistojet

If hazardous chemical propellants are not desirable, then an inert propellant may heated electrically using a resistive heating element. In a resistojet, propellant flowing past the surface of the heating element is heated via conduction and convection, and then thermally expanded through a nozzle. Propellant options include water (H_2O) and nitrous oxide (N_2O) but chemical propellants like butane (C_4H_{10}) and N_2H_4 are also compatible.

The main drawback of a resistojet is the long warm up time of the heating element which means that thrust production is suboptimal before thermal equilibrium is attained. Furthermore, thermal conductance to a gas propellant is inefficient, and a significant amount of the thermal energy is sunk into the thermally insulating walls of the thruster. A resistojet has similar performance as a chemical propellant thruster, with F_t production on the $\sim$ mN to $\sim$ N scale, and $\hat{I}_{sp}$ on the order of $\sim$ 100 s, scaling with power. Resistojets typically operate with $\sim$ kW of electrical power. Their use on microspacecraft missions with limited power budgets requires the development of miniaturised low power versions of the current resistojet technologies [5].

1.3.4 Arcjet

An arcjet is an electrothermal thruster whereby propellant is heated using a direct current (DC) arc discharge. The design of an arcjet typically consists of a nozzle-shaped anode wall and a cathode spike located slightly upstream of the nozzle throat, around which propellant is flowed in a swirl pattern. High voltage $\gtrsim$ kV pulses are sent to the cathode spike until breakdown is initiated in the surrounding propellant, after which a low voltage at high current sustains the arc discharge. Outside of the arc, the degree of ionisation is small, and plasma effects may be neglected when considering the flow behaviour of the propellant at the nozzle exit.

Arcjets typically use inert propellants, but extra energy may be extracted from chemically reactive propellants like N_2H_4. Propellant flowing through the arc volume is heated to temperatures exceeding $\sim$ 1000 K. The volumetric heating process is more effective than surface heating, and less thermal energy is lost to the thruster walls. However, plasma ignition and the transition to steady state must be carefully and reliably controlled to minimise damage and wear to the exposed thruster walls. Most arcjets operate at powers above $\sim$ 1 kW but there is interest in the development of $\lesssim$ 100 W arcjets for use on microspacecraft [6, 7]. Low power arcjets can attain $\hat{I}_{sp}$ on the order of $\sim$ 100 s but the value can be a few times higher at $\sim$ kW levels, and likewise achieve F_t on the scale of $\sim$ mN up to $\sim$ N.

1.3.5 Hollow cathode thruster

There are four main components in a hollow cathode thruster. A heating element surrounds a hollow refractory cathode tube which contains an insert made from a low work function material. These three components are enclosed by a keeper electrode. An inert propellant like Ar or Xe is flowed through the cathode tube. The insert is heated to temperatures required for thermionic emission, producing electrons which ionise the propellant. Initial breakdown is facilitated by the keeper electrode which is biased positively relative to the cathode. A restrictive orifice plate or nozzle at the end of the cathode tube contains the plasma at a high pressure. The plasma volumetrically heats the propellant which exits through the orifice or nozzle to produce thrust. During plasma operation, the insert is also heated by the hot propellant, high energy electrons, and ion bombardment. If there is sufficient thermal energy deposited to maintain the thermionic emission temperature of the insert, a hollow cathode thruster can function in a 'self-heating' mode, whereby the heating element is no longer required and can be turned off to conserve power. Heater-less hollow cathode thrusters also exist, but require an ignition phase to achieve plasma breakdown, followed by a plasma-induced heating phase prior to regular operation [11, 12].

The lifetime of a hollow cathode thruster is severely limited by the susceptibility of the insert to contamination, as well as the eventual erosion of the insert and keeper electrode due to sputtering and bombardment of high energy ions. Presence of energetic ions in the exhaust plume may also result in sputtering and contamination of solar panels and other surfaces on the exterior of the spacecraft [22]. Like the resistojet, a hollow cathode thruster is also subjected to long warm up times, but it is able to divert the thermal energy loss from the hot propellant to heating the insert for more efficient operation. A hollow cathode thruster has similar advantages as the arcjet in terms of volumetric heating of the propellant, and is able to achieve similar performance with F_t on the $\sim$ mN scale and $\hat{I}_\mathrm{sp}$ on the order of $\sim 100\,\mathrm{s}$ with $\lesssim 100\,\mathrm{W}$ of power [9, 10].

1.3.6 *Pocket Rocket*

Pocket Rocket (henceforth abbreviated as `PR`) is a radiofrequency plasma electrothermal microthruster currently under active development by the Space Plasma, Power and Propulsion (SP^3) Laboratory at The Australian National University, Canberra [15, 16, 41, 42]. `PR`, along with the propellant [43–45] and RF power [46, 47] subsystems, are being designed and tested for deployment on the CubeSat platform [16].

At the core of PR is an annular electrode fitted coaxially around the outside of a hollow refractory tube discharge chamber [13]. PR can operate with a wide range of gas propellants but performs best with monatomic inert gas propellants such as Ar and Xe. A weakly ionised plasma is ignited in the propellant flowing through the discharge chamber with $\lesssim 10\,\mathrm{W}$ of radiofrequency (RF) power supplied to the electrode [14, 48]. The propellant is heated volumetrically via ion-neutral charge exchange collisions [14, 49, 50]. At low power and on short time scales, heating in the plasma bulk dominates, and the temperature of the propellant peaks in the middle of the discharge [50]. At high power and on long time scales, heating in the plasma sheath dominates, and the temperature of the propellant peaks near the discharge chamber wall instead [51, 52]. Operating at low power minimises the conductive losses to the discharge chamber wall; thermal energy is retained in the propellant, which is beneficial for thrust. PR is able to achieve F_t on the order of $\sim 1\,\mathrm{mN}$ [48, 53], scaling with $\dot{m}$ and RF power. Like the other electrothermal thrusters, $\hat{I}_\mathrm{sp}$ is on the order of $\sim 100\,\mathrm{s}$, and scales with RF power.

An advantage of the PR RF discharge over DC discharges like arcjets and hollow cathode thrusters is its ability to initiate plasma breakdown in a smaller volume and at lower voltages. In the presence of an electric field set up by an applied voltage, electrons are accelerated and subsequently undergo ionising collisions with the background neutral gas medium. Each ionising collision creates an ion-electron pair, resulting in an 'electron avalanche' characterised by an exponential growth of the electron number density n_e:

$$n_\mathrm{e} = n_{\mathrm{e},0} \exp\left(\frac{d}{\lambda_\mathrm{i}}\right) \tag{1.6}$$

where $n_{\mathrm{e},0}$ is the initial electron population, λ_i is the ionisation mean free path, and d is the path length travelled by the electron avalanche [54]. Breakdown occurs when n_e surpasses a sufficiently high threshold for the medium to become electrically conductive, and a stable plasma is sustained when the creation and loss of charged plasma species are at equilibrium. During breakdown, n_e is limited by d, which in the case of a DC discharge is the distance between the cathode and the anode along the unidirectional DC electric field. In a RF discharge on the other hand, the alternating electric field causes electrons to oscillate within the medium, thereby extending the path length of the electron avalanche before it terminates at an electrode or wall. The increase in d effectively magnifies the electric field, thus allowing breakdown to initiate at a lower applied voltage, and the breakdown threshold is also surpassed more quickly given the exponential growth of n_e.

Plasma breakdown in PR can be initiated at RF voltages as low as $\sim 100\,\mathrm{V}$ [42], and occurs almost instantaneously on a $\sim$ µs time scale [55]. Unlike hollow cathode thrusters

and arcjets, there is no warm up time and high voltage arcs are not required for plasma ignition. The propellant reaches target temperatures of up to $\sim$ 1000 K on a time scale of $\sim$ 100 ms [50, 55], which allows PR to operate with rapid pulsing of both the propellant flow and RF power. The discharge chamber wall in PR is heated by ion bombardment, and thermal equilibrium with the propellant is attained on a time scale of $\sim$ 10 s [50, 51, 55]. Higher performance can be achieved during continuous operation on this time scale as the discharge chamber wall acts as a source of thermal energy for the propellant in addition to the volumetric plasma-induced heating [52].

Another compelling design feature of PR is the shielding of the RF powered electrode from the plasma by discharge chamber wall. As such, ion bombardment onto the refractory discharge chamber wall is not a concern, unlike the exposed metallic anode in an arcjet or the unprotected insert and keeper electrode in a hollow cathode thruster. On the contrary, because PR is a 'gamma mode' discharge [56] sustained mainly by secondary electrons (as opposed to an 'alpha mode' discharge sustained mainly by primary electrons in the plasma bulk [57]), ion bombardment is in fact favourable since it facilitates the emission of high energy secondary electrons from the discharge chamber wall.

Further improvements are made to the design of PR to confine the plasma within the discharge chamber, thereby releasing an essentially neutral exhaust plume with a very low electric potential. This prevents the contamination of externally mounted solar panels by a return ion current, as well as electrical interference with sensitive instruments [48].

1.4 Thesis scope

The primary aim of the work presented in this thesis is to study, optimise, and enhance the discharge characteristics and performance of the *Pocket Rocket* microthruster. This is achieved by means of computational fluid dynamics (CFD) and plasma modelling and iterative design explorations, building upon and verified against previous experimental and simulation works. The scope of the thesis is as follows.

Chapter 1. Introduction introduces PR in the context of electric micropropulsion, comparing it with other electrothermal propulsion systems that have been used in space. Basic thrust concepts and the advantages of using a RF discharge are outlined.

Chapter 2. Apparatus describes each component of the PR experimental apparatus, and details the CFD-plasma modelling technique used to produce the CFD and CFD-plasma

simulations that are discussed in the subsequent chapters. The fluid and plasma numerical methods are outlined, and the steady state and periodic convergence of the respective fluid and plasma parameters are demonstrated. Temperature dependent data used for the CFD-plasma simulations are listed.

Chapter 3. Slip flow develops a cold gas benchmark model of `PR` that precisely matches experimental measurements. Rarefied gas dynamics in the slip regime is explained from both macroscopic and microscopic perspectives. CFD simulations with different gas species and `PR` geometries demonstrate that using the correct slip boundary conditions with the appropriate tangential momentum and thermal accommodation coefficients is essential for producing accurate results.

Chapter 4. Plasma-induced heating develops a plasma benchmark model of `PR` by incorporating the described plasma model into the cold gas benchmark model. The considered plasma chemistry and plasma dynamics are detailed. Heat transfer mechanisms (volumetric heating via electron-neutral elastic collisions and ion-neutral charge exchange collisions, and surface heating via ion bombardment) and ion transport in the discharge are investigated. Fluid and plasma parameters from the CFD-plasma simulation are compared against experimental measurements to validate the accuracy of the model, and corresponds to conditions at $\sim 1\,\mathrm{s}$ after plasma ignition.

Chapter 5. Self-bias develops a RF circuit model of the `PR` discharge using electrical and plasma parameters obtained from the CFD-plasma simulation. The spatially nonuniform self-bias that manifests in the dielectric discharge chamber wall, arising from the geometrical area asymmetry of the grounded and powered electrodes, is examined along with secondary electron emission from the surface of the wall. The plasma is in the thin sheath regime, whereby the ion transit time through the powered sheath is on the order of the RF period. An extensive examination of RF circuit model leads to a redefinition of the self-bias voltage.

Chapter 6. Vacuum expansion develops a cold gas vacuum expansion model of `PR`. The CFD modelling technique takes advantage of the flow velocity choking phenomenon to unconventionally circumvent the problem of including vacuum regions within a CFD simulation. The conditions required for flow velocity choking are explained, and its effects are demonstrated by the behaviour of the fluid parameters and the sonic surface. The general thrust equation is introduced, along with the concept of the boundary layer friction force which is dominant in slip regime flow. The thrust force during cold gas operation is calculated from the CFD simulation results, and compared with experimental measurements and theoretical predictions.

Chapter 7. Discharge geometry develops an extrapolated plasma vacuum expansion model of PR by incorporating the cold gas benchmark and vacuum expansion models with the plasma benchmark model. A sculpted nozzle is designed to shape the physical and electrical geometry of the PR discharge. Thrust performance is improved while also achieving plasma confinement due to the formation of a conical plasma sheath and a virtual cathode at the nozzle throat. The ion density, ionisation profiles, and propellant behaviour are examined in detail, and comparisons are made between different geometrical variations of PR. The calculated thrust force demonstrates the transient performance at $\sim 1\,\mathrm{s}$ after plasma ignition, showing a marked increase from cold gas operation. The thrust to power ratio of PR fares well in comparison to other electrothermal and Hall effect thrusters.

Finally, **Chapter 8. Conclusion** consolidates the findings presented in this thesis with a summary of the important results, and closes with a brief overview of the future work that has been enabled by the CFD-plasma modelling technique developed for PR in this thesis.

Chapter 2

Apparatus

2.1 *Pocket Rocket* experimental apparatus

The following sections provide an overview of the PR microthruster, covering its conception from a precursor plasma processing device to the present prototype. Its key features are identified, along with a detailed description of the whole experimental setup.

2.1.1 DASH precursor

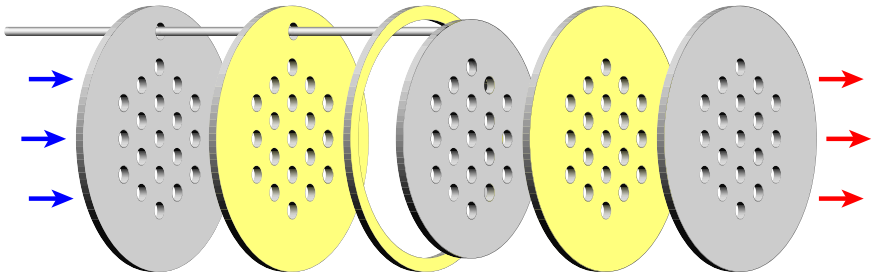

Figure 2.1: Exploded view of DASH, precursor to PR.

The design of PR is derived from the Distributed Array Shower Head (DASH) hollow cathode system [58] envisioned for plasma etching and deposition. DASH (Figure 2.1) comprises of five adjacently stacked plates alternating between aluminium (Al, grey) electrodes and alumina (Al_2O_3, yellow) separators. A rod (electrically insulated within a Macor housing, omitted for clarity) extending from the middle electrode connects it to a RF power supply. The powered electrode is surrounded by an Al_2O_3 guard ring and sandwiched between the separators, thus insulating it from the two grounded electrodes on either end. The whole

DASH plasma source is placed in a vacuum chamber held at $\sim$ mTorr pressures. A process gas such as Ar, sulphur hexafluoride (SF_6), or hydrogen (H_2) is introduced into DASH at pressures around $\sim$ 1 Torr. The process gas flowing along the pressure gradient through each hollow cathode cavity in the plate stack is ignited into individual plasmas, delivering ions and radical neutral species towards the target wafer located at a remote distance downstream.

PR is geometrically analogous to a single hollow cathode in DASH. Instead of plasma processing, PR uses the plasma to heat propellant for the production of thrust on a spacecraft. The following sections gives a description of the PR device and the purpose of each of its constituent components.

2.1.2 PR device

Figure 2.2 displays a cutaway illustration of main components inside the PR device. PR has an Al structure containing a plenum of dimensions 12 mm length and internal diameter 40 mm. A 3 mm internal diameter hole through the structure allows the flow of propellant gas into the plenum. Another identical hole on the opposite side is used for static pressure diagnostics. The front end of the structure has a KF-25 vacuum flange that allows either physical access to the PR interior with experimental instruments, or optical access via a glass viewport. Adjacent to the plenum, a bored passage accommodates the discharge chamber and RF powered electrode.

At the core of PR is a hollow Al_2O_3 dielectric refractory tube discharge chamber of dimensions 18 mm in length, 4.2 mm internal diameter, and 1.0 mm wall thickness. A copper (Cu) annular RF powered electrode is fitted coaxially around the outside middle section of the discharge chamber of dimensions 5 mm in length, 6.2 mm internal diameter, and 16 mm external diameter. A Cu feedthrough pin connects the RF powered electrode to a vacuum sealed coaxial RF feedthrough connector on the external face of the PR structure, which receives a voltage waveform from a RF power supply via an impedance matching network. The powered electrode is electrically and thermally insulated from the grounded Al structure by machined Macor discs, while the feedthrough pin is insulated with a small Al_2O_3 tube. The internal surface of the PR structure acts as the grounded electrode. By virtue of its modular design, the individual components in PR may be conveniently substituted or replaced, for the purposes of testing different materials or geometries.

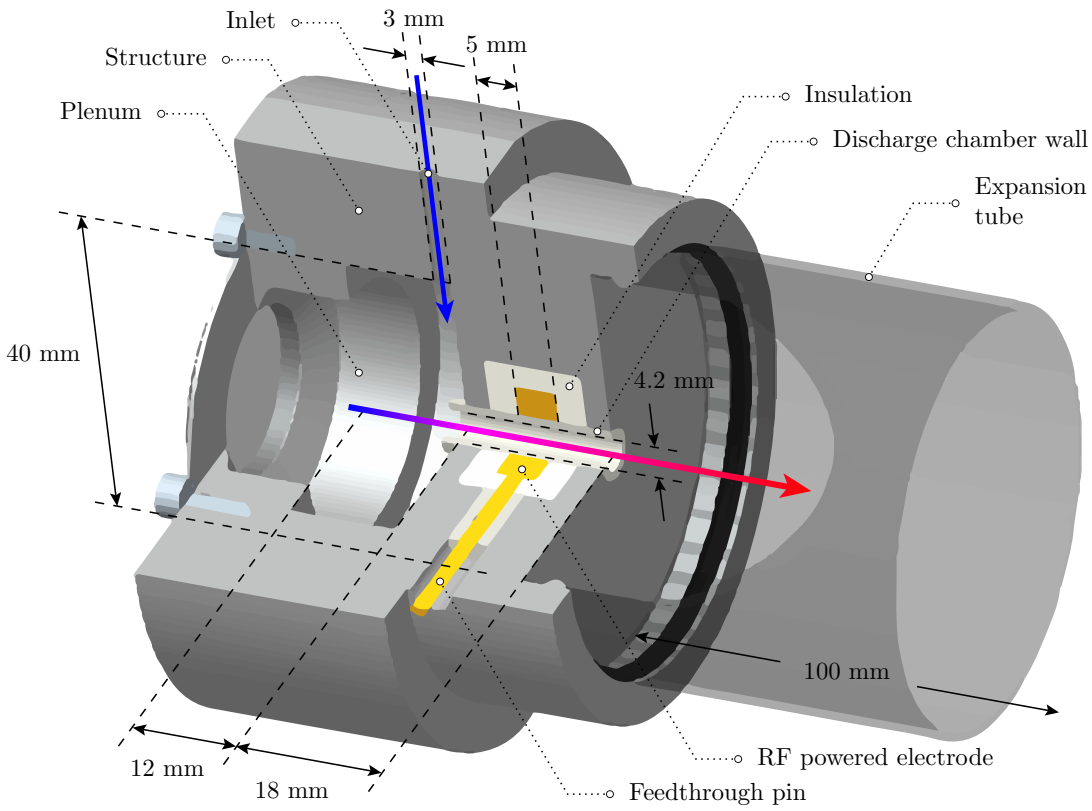

Figure 2.2: PR cutaway illustration.

2.1.3 Propellant flow circuit

Figure 2.3 shows a flowchart of the propellant flow circuit in the PR experimental setup. PR (highlighted in blue) is connected to a vacuum system downstream. Upstream of PR, there is a choice to operate with either the laboratory gas supply or the propellant subsystem (highlighted in red) [43–45]. Different instruments (dashed blocks) are used to monitor the static pressure at various points in the flow circuit.

Laboratory gas supply

In the laboratory, Ar propellant is sourced from a high pressure industrial gas storage tank. A regulator sets the gas pressure to levels manageable for the mass flow controller (MFC). The experimental setup has a thermal-based MFC (MKS 2179A) calibrated for N_2 at 100 SCCM (standard cubic centimetres per minute) full scale, linked with a multi-channel power supply, readout, and set-point source (MKS 247D) for monitoring and controlling the MFC.

When using Ar, which has different thermal properties to the MFC calibration gas, the

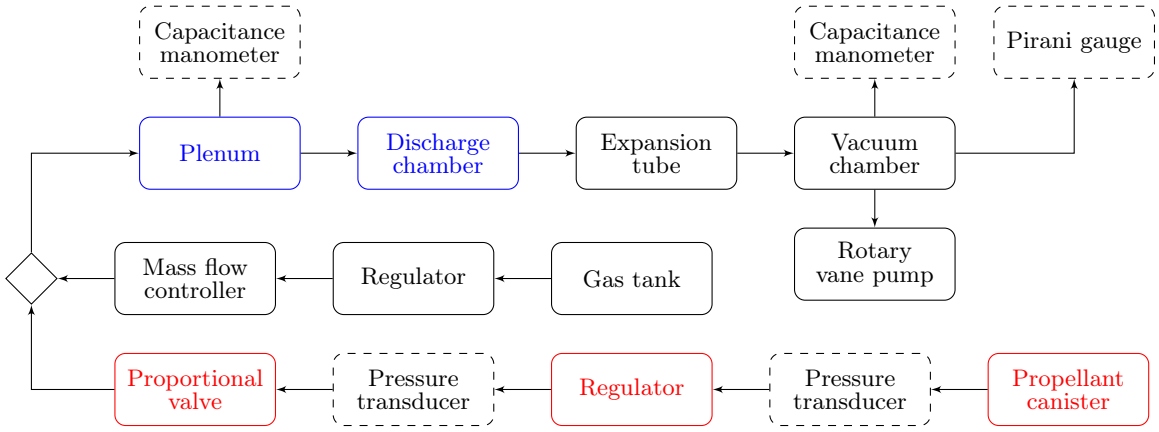

Figure 2.3: Propellant flow circuit. PR (blue), propellant subsystem (red).

calibration of the MFC must be adjusted according to the gas correction factor GCF:

$$\mathrm{GCF(Ar)} = 1.030 \cdot \frac{\rho(\mathrm{N_2})\, c_p(\mathrm{N_2})}{\rho(\mathrm{Ar})\, c_p(\mathrm{Ar})} = 1.441 \tag{2.1}$$

where ρ is the mass density and c_p is the specific heat at constant pressure of the respective gas species at $T = 273.15\,\mathrm{K}$ and $p = 1\,\mathrm{atm}$. The nondimensional multiplicative constant is the molecular structure correction factor, which is 1.030 for monatomic, 1.000 for diatomic, 0.941 for triatomic, and 0.880 for polyatomic gases [59]. Hence, a 100 SCCM full scale MFC calibrated for N_2 dispenses 144.1 SCCM of Ar at full scale, with linear calibration. If $\dot{m} = 100\,\mathrm{SCCM}$ of Ar is desired, the MFC must therefore be set to 69.4 % of the full scale. A feedback loop in the MFC ensures smooth dispensation of the gas at the set $\dot{m}$.

Propellant subsystem

For operation on a spacecraft, the onboard propellant subsystem must be small and lightweight, with minimal power requirements. Ar or carbon dioxide (CO_2) propellant is stored in a pressurised 21 mL canister at 2600 psig or 800 psig respectively. A miniature proportional solenoid valve replaces the MFC for controlling the $\dot{m}$ into PR. It has a fixed electrical resistance of 100 Ω, and can be controlled electronically with 120 mA of electrical current required to hold the valve fully opened. A miniature regulator is used to reduce the pressure of the incoming propellant to below the leakage rating of the proportional valve. The regulator has an adjustable range of 5 psig to 30 psig relative to the ambient pressure, and has been experimentally verified for operation in vacuum. The design and development of the PR propellant subsystem is extensively documented in the following theses [43–45].

Vacuum system & pressure diagnostics

For normal laboratory experiments, both the laboratory gas supply and the propellant subsystem are connected to PR by a three way ball valve, used for selecting the propellant source. Propellant flows into PR via an inlet on the side of the structure at a nominal rate of $\dot{m} = 100\,\text{SCCM}$, and fills the plenum to $p \sim 1\,\text{Torr}$ static pressure. The plenum pressure varies with the species of gas used, as well as the geometry of the discharge chamber which dictates the flow behaviour in PR. Since the flow in the plenum is mostly stationary, the static pressure p in the plenum is equivalent to the stagnation pressure p_{st}, which has the definition:

$$p_{\text{st}} = \frac{1}{2}\rho u^2 + p \tag{2.2}$$

where ρ is the mass density and u is the flow velocity. Henceforth, p_{st} is used to represent the macroscopic plenum pressure, as distinct from the static pressure p at a particular point in the flow.

PR is attached to a glass expansion tube 100 mm in length and 45 mm internal diameter, and mounted to a KF-40 flange on the face of a 20 L six-way cross vacuum chamber. When no propellant is flowing, PR and the rest of the vacuum system achieves a base pressure of $\leq 1\,\text{mTorr}$ with a rotary vane pump (Edwards XDS10) connected to the vacuum chamber. Due to the small volume of the vacuum chamber and the limited pumping speed, the static pressure in the vacuum chamber rises to $p_0 = 0.349\,\text{Torr}$ when $\dot{m} = 100\,\text{SCCM} = 2.97\,\text{mg}\,\text{s}^{-1}$ of Ar is flowing, or $p_0 = 0.321\,\text{Torr}$ with $\dot{m} = 100\,\text{SCCM} = 2.083\,\text{mg}\,\text{s}^{-1}$ of N_2.

Different instruments are used to monitor the static pressure at various points in the vacuum system. A 10 Torr full scale capacitance manometer (MKS 626B) mounted to the PR structure on the opposite side of the inlet measures the static pressure in the plenum. It functions by measuring the capacitance between a metal-on-ceramic electrode disc and a radially tensioned metal diaphragm which is displaced with variations in static pressure. The static pressure in the vacuum chamber is measured using a 20 Torr full scale capacitance manometer (MKS 626B), as less precision is required. A Pirani gauge (Granville-Phillips 275) is also used on the vacuum chamber to monitor the static pressure above the range of the capacitance manometer up to 760 Torr during evacuation or return to atmospheric pressure. Unlike a capacitance manometer which measures true physical pressure, a Pirani gauge indirectly infers static gas pressure by measuring the rate of heat loss from a filament controlled at constant temperature in the gas medium. As such, it is sensitive to the species or chemical composition of the gas, and separate calibration is required if not operating with the default N_2 calibration gas. The capacitance manometers are run from a multi-channel

power supply and readout unit (`MKS PR4000B`), while a separate power supply and readout unit (`Granville-Phillips 307`) serves the Pirani gauge.

The propellant subsystem is equipped with pressure transducers placed in series between the propellant canister, regulator, and proportional valve. The propellant subsystem components are calibrated with these transducers to supply the nominal $\dot{m}$ of propellant to `PR`. For experiments conducted with `PR` and the propellant subsystem wholly within a vacuum chamber, no pressure measurement instruments are used on board as the present instruments are not designed to operate in vacuum. However, there has been investigation into miniature transducers that can be placed inside of the plenum or be integrated with the propellant subsystem [43–45].

2.1.4 RF electrical circuit

Figure 2.4 shows the RF electrical circuit of the `PR` experimental setup. The main components are the RF power supply, the impedance matching network, and the `PR` discharge. Different instruments are used for monitoring the RF system at various points in the circuit.

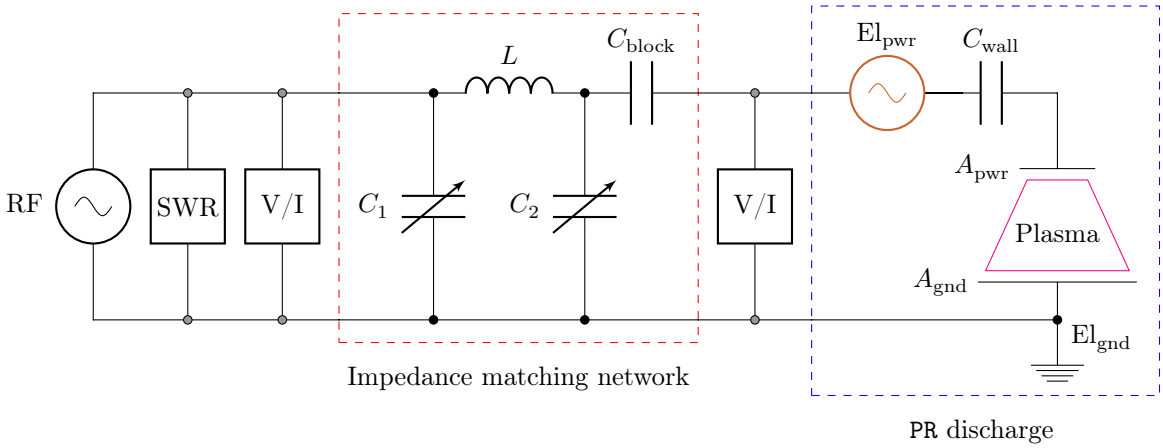

Figure 2.4: RF electrical circuit of the `PR` experimental setup.

`PR` discharge

The standard operating conditions for `PR` is with $\dot{m} = 100\,\text{SCCM}$ of Ar cold gas propellant and a $V_{\text{pwr}} = 300\,\text{V}$ amplitude sinusoidal waveform at 13.56 MHz on the powered electrode. This puts the `PR` discharge close to the Paschen minimum pressure of $\sim 1.5\,\text{Torr}$ [42], and the power target of $\sim 5\,\text{W}$. Each physical component in the `PR` discharge may be represented as an electrical component (Figure 2.4, blue -- box). The powered electrode may be designated

as a RF voltage 'source' ($\mathrm{El}_{\mathrm{pwr}}$, brown) with the aforementioned voltage amplitude and frequency. A capacitor (C_{wall}) in series represents the dielectric discharge chamber wall in front of the powered electrode, while the `PR` structure acts as the grounded electrode ($\mathrm{El}_{\mathrm{gnd}}$).

A capacitively coupled plasma (CCP) (magenta — trapezium) is ignited and sustained in the discharge chamber between the shielded powered electrode and the grounded electrode. The surface area of the grounded electrode A_{gnd} which includes the walls facing the plenum and downstream:

$$A_{\mathrm{gnd}} \approx 3 \times \pi \left(20\,\mathrm{mm}\right)^2 - 2 \times \pi \left(3.1\,\mathrm{mm}\right)^2 + 2\pi \left(20\,\mathrm{mm}\right)\left(12\,\mathrm{mm}\right) \approx 5200\,\mathrm{mm}^2 \tag{2.3}$$

is much larger than that of the powered electrode A_{pwr} which is the interior surface of the discharge chamber wall:

$$A_{\mathrm{pwr}} \approx 2\pi \left(2.1\,\mathrm{mm}\right)\left(5\,\mathrm{mm}\right) \approx 66\,\mathrm{mm}^2 \tag{2.4}$$

This makes the `PR` discharge a highly asymmetric system with an area ratio of $A_{\mathrm{gnd}}/A_{\mathrm{pwr}} \lesssim 80$. The approximate inequality sign is used here since the effective A_{gnd} is likely to be slightly smaller than the calculated value since the grounding of the plasma is preferential to the structure surfaces closer to the discharge chamber.

Unlike most other asymmetric discharges, the self-bias in `PR` manifests at C_{wall} as a spatially nonuniform negative charging of the dielectric discharge chamber wall rather than at the blocking capacitor (C_{block}). Consequently, the electric potential that the plasma is exposed to is different to the supplied RF waveform, and unknown. RF electrical circuit models become inadequate for describing the discharge, and a comprehensive fluid, electrical, and plasma numerical model must be employed to accurately quantify the behaviour of the plasma [56].

Laboratory RF power supply

A RF power generator (`ENI OEM-25`) supplies a fixed 13.56 MHz frequency RF voltage waveform with a source impedance of $Z_{\mathrm{gen}} = 50\,\Omega$. During continuous wave operation, the output power P_{gen} is manually selected using an analogue dial on the RF generator with reference to a standing wave ratio (SWR) meter (`Daiwa CN-801`) for coarse control. Fine control is achieved with reference to an inline digital voltage/current (V/I) probe (`Impedans Octiv`) which is capable of measuring RF waveform parameters such as forward and reflected power, voltage, current, phase angle, impedance, as well as DC voltage. Pulsed operation is also possible by triggering with a signal generator or a computer controlled interface at a set voltage amplitude, pulse period, and duty cycle. Although the RF power generator has a

maximum output power of 2600 W, it is typically run at only $P_{\text{gen}} \sim 10\,\text{W}$, and occasionally up to $P_{\text{gen}} \sim 100\,\text{W}$, as PR is intended for use on small or microspacecraft with a limited power budget.

The experimental setup uses coaxial cables with a combination of Type N, BNC, and SMA connectors, and the cable lengths are kept to a minimum. The RF power supply, impedance matching network, PR device, vacuum chamber, and all instruments are connected to a common grounding point in the laboratory.

Impedance matching network

The IMN (Figure 2.4, red -- box) is a Π-match consisting of two variable capacitors (C_1 and C_2) and an inductor (L). C_1 and C_2 have ranges of $1050\,\text{pF} \leq C_1 \leq 2000\,\text{pF}$ (Meiden SCV-510M in parallel with a 1000 pF fixed ceramic capacitor) and $50\,\text{pF} \leq C_2 \leq 500\,\text{pF}$ (Meiden SCV-115M), and the vacuum variable capacitors are tuned manually by turning a drive shaft. The inductor is 4.5 turns of $10\,\text{mm}^2$ copper wire shaped into a coil 70 mm in diameter with 10 mm spacing between each loop. A $C_{\text{block}} = 100\,\text{pF}$ blocking capacitor is connected after the IMN in series. The IMN circuit is enclosed in an electrically grounded copper box $\sim 10\,\text{dm}^3$ in volume. A second V/I probe is used after the IMN to monitor V_{pwr} on the PR powered electrode, and V_{gen} is manually adjusted at the RF power generator in the event of V_{pwr} drifting away from the set value. At standard operating conditions, the post-match V/I probe measures a negative DC bias voltage of $V_{\text{block}} = -1.10\,\text{V}$, which is a negligible magnitude relative to V_{pwr}. This is verified separately using an analogue oscilloscope, thus confirming that the self-bias indeed does not manifest at the blocking capacitor, and therefore must be at the dielectric discharge chamber wall instead.

The present experimental setup requires an IMN as the PR CCP discharge has a highly reactive load impedance that is significantly different from $Z_{\text{gen}} = 50\,\Omega$. At standard operating conditions, $Z_{\text{PR}} = R_{\text{PR}} + iX_{\text{PR}} \approx (15.2 - i373.3)\,\Omega$, which gives an almost purely capacitive phase angle of $-87.7°$. In order to maximise forward power P_{f} transfer and minimise reflected power P_{r}, the IMN is tuned such that the total load impedance of the experimental setup $Z_{\text{exp}} = Z_{\text{IMN}} + Z_{\text{PR}}$ is equal to Z_{gen}. At standard operating conditions, this requires an equivalent series impedance of $Z_{\text{IMN}} = (34.8 + i373.3)\,\Omega$, thus giving $Z_{\text{exp}} = 50\,\Omega$ and zero reactance. Note that the quoted Z_{PR} and Z_{IMN} values are accurate for the standard operating conditions with $\dot{m} = 100\,\text{SCCM}$ of Ar and $V_{\text{pwr}} = 300\,\text{V}$. Z_{PR} varies with different propellant species, $\dot{m}$, and V_{pwr}, and may drift as the plasma increases in temperature after operating for long durations.

To obtain the match, Z_{exp} is monitored at the pre-match V/I probe. First, the resistive component is tuned to $R_{\text{exp}} = 50\,\Omega$. If the reactive component iX_{exp} is positive, then C_2 is slightly decreased (↺ anticlockwise) while increasing C_1 (↻ clockwise) to compensate. The opposite action is performed if the reactive component is negative. As tuning C_1 and C_2 alters the resistive and reactive components by different magnitudes, the procedure usually requires a few iterations before the match is obtained. When matched, P_{f} measured at the pre-match V/I probe is maximum and $P_{\text{r}} = 0\,\text{W}$. The quality of the match may be quantified by the standing wave ratio SWR, defined as:

$$\text{SWR} = \frac{1 + \sqrt{P_{\text{r}}/P_{\text{f}}}}{1 - \sqrt{P_{\text{r}}/P_{\text{f}}}} \tag{2.5}$$

An unmatched system has a SWR greater than unity, while a matched system has SWR = 1. In all PR experiments, matching is achieved to $Z_{\text{exp}} = Z_{\text{gen}} = 50\,\Omega$, within $\Delta R_{\text{exp}} + \Delta iX_{\text{exp}} = (\pm 0.1 \pm i0.2)\,\Omega$, and with the SWR at or close to unity. The instruments, cables, and connectors used are kept constant in all experiments, as removing any component changes Z_{exp} and thus alters the match. All the PR experiments and data points presented in this thesis are precisely matched with $Z_{\text{exp}} = Z_{\text{gen}}$ for their respective operating conditions.

Figure 2.5 plots V_{pwr} at every 100 V against the required V_{gen}, measured using the post- and pre-match V/I probes over a duration of 60 s while operating with $\dot{m} = 100\,\text{SCCM}$ of Ar (blue ○ markers) and $\dot{m} = 50\,\text{SCCM}$ of Ar (red △ markers). In the latter case, the lower $\dot{m}$ results in a lower p_{st}, and $V_{\text{pwr}} = 100\,\text{V}$ becomes insufficient for plasma breakdown. Since the IMN is a resonant circuit that yields voltage amplification, its quality factor is given by the ratio of its output voltage to the input voltage. The general trend is independent of $\dot{m}$, with a constant $Q = V_{\text{pwr}}/V_{\text{gen}} \approx 9.7$, obtained by a linear fit (black — line) from the origin through all the data points.

Figure 2.6 plots P_{PR} the power drawn by PR against P_{gen} the power provided by the RF power generator, measured under the aforementioned conditions. Again, the general trend is independent of $\dot{m}$, giving a constant and approximately stable power transfer efficiency of $\eta_{\text{IMS}} \approx 58.5\,\%$, obtained by a linear fit (black — line) from the origin through all the data points. The present IMN is an improvement over the older model which has a significant drop in efficiency under $\lesssim 10\,\text{W}$ [60], and ensures consistent experimental conditions at low power through better construction and selection of circuit components.

Figure 2.7 shows the relation between P_{PR} and the root mean square (RMS) voltage $\bar{V}_{\text{pwr}} = V_{\text{pwr}}/\sqrt{2}$ on the powered electrode, relative to a second degree polynomial $P_{\text{PR}} = \bar{V}_{\text{pwr}}^2/7.85\,\text{k}\Omega$ (black — line) fitted from the origin through all the data points. Again, $\dot{m} = 100\,\text{SCCM}$ of Ar (blue ○ markers) and $\dot{m} = 50\,\text{SCCM}$ of Ar (red △ markers) give

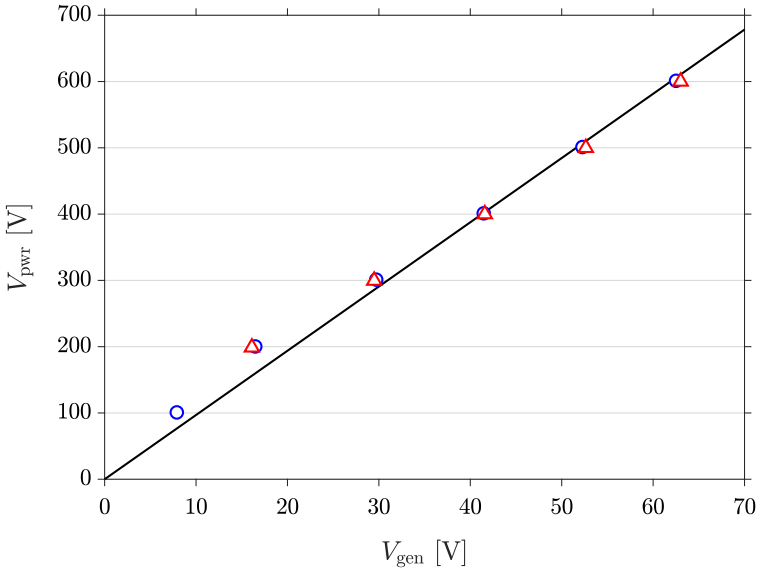

Figure 2.5: Impedance matching network input (V_{gen} from the RF power generator) and output (V_{pwr} on the PR powered electrode) voltages, operating with $\dot{m} = 100\,\text{SCCM}$ of Ar (blue ○ markers) and $\dot{m} = 50\,\text{SCCM}$ of Ar (red △ markers). The quality factor Q is represented by the black — line.

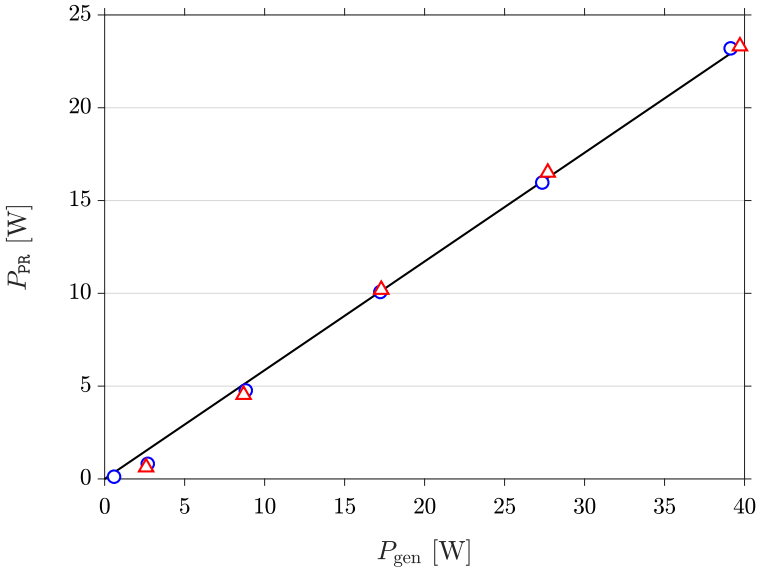

Figure 2.6: Impedance matching network power transfer efficiency η_{IMS} (black — line) while operating with $\dot{m} = 100\,\text{SCCM}$ of Ar (blue ○ markers) and $\dot{m} = 50\,\text{SCCM}$ of Ar (red △ markers).

similar results. However, the data points deviate from the fitted curve below $\bar{V}_{\text{pwr}} = 212.1\,\text{V}$ ($V_{\text{pwr}} = 300\,\text{V}$), indicating that the magnitude of the impedance of the PR discharge $|Z_{\text{PR}}| = \sqrt{R_{\text{PR}}^2 + X_{\text{PR}}^2}$ tends to be larger at lower V_{pwr}. In fact, this is registered at the post-match V/I probe, where Z_{PR} tends to become slightly less resistive but significantly more reactive at lower $\bar{V}_{\text{pwr}}$.

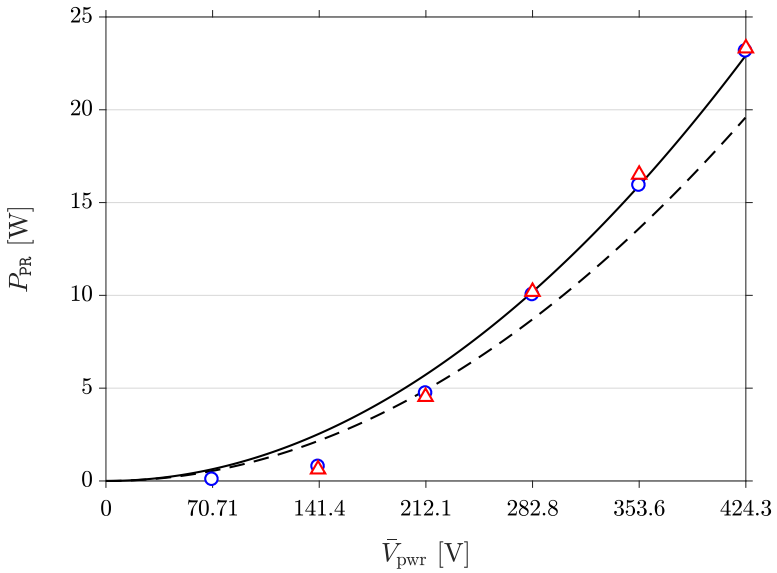

Figure 2.7: PR power draw P_{PR} at different RMS voltages $\bar{V}_{\text{pwr}}$ while operating with $\dot{m} = 100\,\text{SCCM}$ of Ar (blue ○ markers) and $\dot{m} = 50\,\text{SCCM}$ of Ar (red △ markers). The black — line is the best fit line through all the data points, while the black -- line is plotted using the calculated parallel equivalent circuit resistance $R_{\text{PR}}^{\parallel}$ at the standard operating conditions.

At standard operating conditions, the measured impedance of $Z_{\text{PR}} \approx (15.2 - i373.3)\,\Omega$ is equivalent to having a resistor and a capacitor in series, with resistance $R_{\text{PR}}^{+} \approx 15.2\,\Omega$ and capacitance $C_{\text{PR}}^{+} \approx 31.44\,\text{pF}$ at 13.56 MHz. However, PR is more appropriately modelled as a equivalent circuit consisting of a resistor and a capacitor in parallel between El_{pwr} and El_{gnd}, as P_{PR} is mostly dissipated resistively (through plasma-induced heating of the propellant and the discharge chamber wall) and capacitive loss is minor. Thus, the parallel equivalent circuit has resistance $R_{\text{PR}}^{\parallel} \approx 9.18\,\text{k}\Omega$ and capacitance $C_{\text{PR}}^{\parallel} \approx 31.39\,\text{pF}$ at 13.56 MHz. The curve of $P_{\text{PR}} = \bar{V}_{\text{pwr}}^2/9.18\,\text{k}\Omega$ (black -- line) is plotted in Figure 2.7 and intersects the data point at $\bar{V}_{\text{pwr}} = 212.1\,\text{V}$ (blue ○ marker), demonstrating that the parallel equivalent circuit is a useful and accurate model of PR at standard operating conditions. Similar calculations may be performed for the other operating conditions with their respective measured impedances.

RF power subsystem

The laboratory RF power generator and IMN can only be used in a terrestrial setting due to their mass and physical size, and their components are not designed to operate in a vacuum. These limitations led to the development of a lightweight ($\sim 90\,\mathrm{g}$) small form factor IMN, consisting of a tightly wound wire loop inductor and three banks of miniature ceramic capacitors soldered onto a printed circuit board (PCB) [46]. This PCB IMN is designed to operate with a $Z_{\mathrm{gen}} = 50\,\Omega$ source impedance variable frequency RF power generator, and up to $V_{\mathrm{pwr}} = 1000\,\mathrm{V}$ before reaching the thermal design power.

More recently, a miniaturised RF power subsystem has been developed [16, 47] for the CubeSat form factor, with dimensions of $10\,\mathrm{cm} \times 10\,\mathrm{cm} \times 0.7\,\mathrm{cm}$ and weighing at $\sim 150\,\mathrm{g}$. The RF power subsystem consists of a switch mode power amplifier, which converts DC to RF by switching the gate signal of a metal-oxide-semiconductor field-effect transistor (MOSFET), and an integrated solid state IMN. The RF power subsystem is capable of a power output of $P_{\mathrm{sub}} = 20\,\mathrm{W}$ in continuous wave mode with variation in power achieved by operating in pulsed mode, and has a high efficiency of $\eta_{\mathrm{sub}} \approx 80\,\%$. It is designed to output $V_{\mathtt{pwr}} = 300\,\mathrm{V}$ optimally at the resonant frequency of $\sim 13.17\,\mathrm{MHz}$. The RF power subsystem has been experimentally tested within a vacuum chamber on a smaller version of the `PR` device called `MiniPR`.

2.2 CFD-plasma modelling

Computational fluid dynamics (CFD) and plasma simulation modelling of `PR` is employed as a complement to experimentation. The main advantage of CFD-plasma modelling is its ability to provide data that are otherwise difficult, expensive, or impossible to obtain by experimental techniques, and at high spatial and temporal resolution. This is especially valuable in the field of micropropulsion, as the small dimensions of most microthruster devices prevent or limit physical access of conventional experimental instruments. Additionally, accurate measurement of the $F_{\mathrm{t}} \sim \mu\mathrm{N}$ to mN thrust forces require exceptionally sensitive equipment and must be carried out in vacuum, and ideally in a weightless environment.

From a research and development perspective, CFD-plasma modelling saves on manufacturing time and cost. During the iterative design stage of the device prototyping cycle, multiple geometrical variations of the device may be tested simultaneously by running simulations in parallel. Minimal intervention is required while the simulation is running, provided that the modelling technique used is robust and mature. Manufacturing can then proceed

after a viable design has been finalised, thus reducing risk and increasing the baseline performance of the device.

However, certain tasks remain better suited for experimentation due to the higher starting inertia involved in conducting simulations. While PR plasma experiments can be set up within minutes, and completed within a few hours, running high quality CFD-plasma simulations can take up to many weeks. Moreover, the steep learning curve of the simulation program and the complex pre- and post-processing procedures make simulations unsuitable for performing certain minor or one-off tasks. Hence, the best way forward is to use both experimentation and simulation optimally in accordance with their respective strengths, and progress in a leapfrogging manner between the two techniques: experimentation is used to verify simulation results, while simulation is used to supplement otherwise unattainable measurements and provide recommendations to improve the device design and performance.

2.2.1 CFD-ACE+ multiphysics

The CFD-plasma simulations presented in this thesis are performed using the commercial Computational Fluid Dynamics Advanced Computational Environment (CFD-ACE+) multiphysics package. Other tools available in this space include COMSOL Multiphysics and the Hybrid Plasma Equipment Model (HPEM).

While COMSOL offers more flexibility in terms of allowing the user access to the underlying solver equations, it is limited to using a single automatically selected time-step for solving the entire system of equations for both electron and heavy particle dynamics. CFD-ACE+ on the other hand allows individual control of two distinct time-steps for dealing with the vastly disparate time scales for fluid and plasma dynamics, which results in more accurate and convergent solutions [61, 62].

HPEM is a hybrid solver used in the semiconductor manufacturing industry, tailored to modelling low pressure plasmas typically in the ~ 1 mTorr to ~ 1 Torr range for plasma etching and deposition [63–65]. CFD-ACE+ as a fluid solver is able to handle plasma modelling from ~ 0.1 Torr up to 1 atm and beyond, and is therefore more suitable for modelling PR with pressures up to ~ 10 Torr as well as atmospheric pressure discharges. Most importantly, CFD-ACE+ is validated for supersonic flow which is essential for modelling nozzle expansion. While it lacks hybrid methods appropriate for high vacuum conditions, compressible flow effects inherent in PR extricate the need for accurate modelling of the external vacuum environment.

2.2.2 PR simulation mesh

A 2D axisymmetric mesh (Figure 2.8) reproduces the interior of the PR device at actual scale in the CFD-ACE+ simulation domain. Dimensions are given in [mm] on the z- and r-axes. The solid regions in the simulation domain include the Al structure (S, grey), Macor insulation (I, dark green), Cu powered electrode (E, brown), and Al_2O_3 discharge chamber wall (CW, yellow). The fluid regions (aqua) are contiguous, consisting of the plenum (P), discharge chamber (C), and downstream (D, or D1 to D6). Rotating the mesh about the horizontal axis of symmetry renders the cylindrical geometry of PR and a hemispherical downstream region representing the vacuum chamber or space environment.

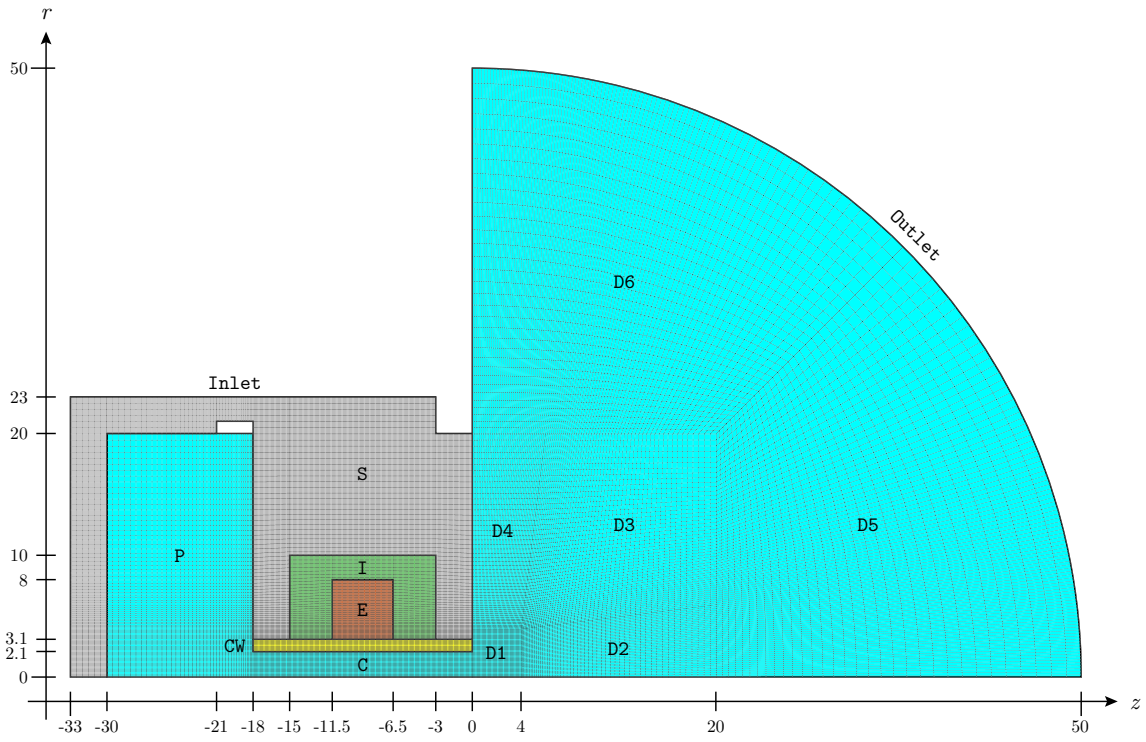

Figure 2.8: PR simulation mesh (36,288 cells). Fluid regions (aqua): plenum (P), discharge chamber (C), and downstream (D). Solid regions: Al structure (S, grey), Macor insulation (I, dark green), Cu powered electrode (E, brown), and Al_2O_3 discharge chamber wall (CW, yellow).

C is the region of primary interest for resolving fluid, electrostatic, and plasma dynamics, and features a uniform orthogonal square grid consisting of 0.1 mm × 0.1 mm cells in a structured mesh. The same mesh density is used for the neighbouring CW and D1. In P, the cells smoothly increase in size with increasing distance from C, up to 0.5 mm × 0.5 mm at the top left corner. The size of the cells scales by a hyperbolic tangent function with set initial

and final dimensions. By using larger cells in regions of less importance, the total number of cells in the simulation mesh can be reduced, thus reducing computation time. Orthogonality and zero skew are maintained in the P, C, and D1 regions for compatibility with the plasma numerical method employed by CFD-ACE+.

The PR simulation domain has three notable differences from the PR device (Figure 2.2). First, as the external dimensions of S are inconsequential to the flow or plasma behaviour in PR, they have been reduced to decrease the number of cells in the simulation mesh. The reduced thermal mass is not a concern since the structure does not heat up during the $\sim$ ms time scale that the CFD-plasma simulations are modelling. Second, the inlet boundary in the PR simulation domain is a 3 mm section at the top right edge of P. When the simulation mesh is rotated about the axis of symmetry, the inlet boundary traces out a cylinder instead of a single hole like in the PR device. This difference is also inconsequential as the flow in P is mostly stationary. and the inlet boundary is sufficiently far away from C. As the flow velocity of the propellant entering through the inlet boundary is axisymmetric and orthogonal to the flow direction in C, it does not carry any axial momentum and therefore does not affect the thrust force.

Finally, D has a hemispherical shape instead of reproducing the exact geometry of the glass expansion tube. At high pressures, the flow behaviour is insensitive to the shape of the downstream region, and the CFD simulation can be directly compared with experiment. At low pressures, the outlet boundary of the downstream region has to be placed sufficiently far away from the exit of the discharge chamber region to mitigate unphysical behaviour. A hemispherical outlet boundary is chosen as it is equidistant from the discharge chamber exit and isotropic, thus eliminating any directional bias and circulation effects that arise due to unequal distances from boundaries, as well as computational anomalies caused by corners. Additionally, it is more versatile as the simulation domain can represent PR being mounted directly to a vacuum chamber at a given background pressure p_0 [46, 47], or immersed in a space environment [47, 53].

D has a radius of 50 mm, and is split into six trapezoidal sub-regions in order to maintain a relatively orthogonal mesh and minimise skew close to D1. D2 and D4 expand from a linear grid pitch of 0.1 mm to 0.15 mm over a distance of 16 mm, up to 0.5 mm at the top right corner of D3. In D5 and D6, the cells gradually increase to a maximum size of 1.25 mm $\times$ 1.25 mm at 45° of the hemispherical boundary, but are kept narrow at 1.25 mm $\times$ 0.25 mm at the bottom right and top corners as the region near the horizontal and vertical axes are important for resolving axial propellant flow and plasma interactions with the surface of the structure. While this method of manually building the downstream region mesh is rather

labour intensive, following this procedure ensures the accuracy of the simulation results. Creating a mesh by rotating the horizontal edge 90° to the vertical position is not ideal since it creates not only a singularity at the axis of rotation but also cells with a high amount of skew. Generating an unstructured mesh is also not ideal as the triangular cells are not orthogonal, and there is less control over the mesh density in the middle of each region.

In total, there are 36,288 cells in the `PR` simulation mesh shown in Figure 2.8. Overall, the mesh density is significantly higher than what is deemed sufficient by previous mesh independence studies [60, 66] performed with an outlet pressure of $p_0 = 0.75\,\text{Torr}$. Having a higher mesh density is desirable for the CFD-plasma simulations presented in this thesis, as the capabilities of the fluid and plasma numerical techniques are pushed to the limits for modelling $p_0 = 0.1\,\text{Torr}$ and even $p_0 = 0\,\text{Torr}$ vacuum scenarios.

2.2.3 Fluid numerical method

Modelling compressible flows in CFD-ACE+ requires the `Flow` and `Heat Transfer` modules. The `Flow` module numerically solves the Navier-Stokes equations for the flow velocity and pressure field over a given meshed geometry. The simulation domain is discretised and the continuity equations numerically integrated over each cell via the finite volume method (FVM). The result is assigned to the cell centre, and interpolated to the cell faces to determine the flux across each cell interface. Mass conservation is implemented, and pressure is calculated using the iterative Semi-Implicit Method for Pressure Linked Equations-Consistent (SIMPLEC) algorithm until convergence. Fixed value boundary conditions (e.g. inlets, outlets, isothermal walls) are imposed by setting a source term in a fictitious cell on the external boundary of the volume, while zero-flux boundary conditions (e.g. symmetric boundaries, adiabatic walls) are achieved simply by setting the cell interface coefficients to zero. The `Heat Transfer` module keeps track of energy transfers arising from work done on and by the gas during compression and expansion, as well as to impose thermal boundary and initial conditions. Energy conservation is implemented via the total enthalpy equation, and solved similarly to those described above. While not explicitly required for modelling inert fluid flows, the `Chemistry` module can be used to specify species mass flow rates and propellant mixture composition at the inlet instead of a fixed pressure condition.

The CFD simulations are self-consistent, with no artificial source terms or limits used. Apart from the intrinsic volume and boundary conditions, the only extrinsic input parameters are the inlet, outlet, and initial conditions. The CFD simulations are solved iteratively until steady state convergence. There are two ways of determining if the solution has converged.

The first method is by tracking the overall residuals of certain fluid parameters such as the axial and radial velocities u_z and u_r, and static pressure p in the whole simulation domain. For convergence, it is suggested to have a $\sim 10^{-5}$ reduction in the residuals of each parameter by the end of the simulation. However, this measure is not precise as the overall residuals are overrepresented by the downstream region whose $14,352$ cells account for almost $40\,\%$ of the total number of cells in the simulation mesh. The second more rigorous method is by tracking the fluid parameters at the exit of the discharge chamber region, which includes u_z, u_r, p, as well as the mass density ρ and temperature T. Convergence is achieved when these fluid parameters remain stable over ~ 1000 iterations. For the CFD simulations presented in this thesis, $n(i_\mathrm{s}) = 10,000$ steady state iterations are sufficient to achieve converged solutions.

Figure 2.9 plots a few of the tracked fluid parameters (coloured — lines) at the discharge chamber exit, at the coordinates $(z, r) = (0, 0)$ in Figure 2.8, for a CFD simulation of PR with $\dot{m} = 100\,\mathrm{SCCM}$ of Ar cold gas propellant with the outlet boundary static pressure set to $p_0 = 0\,\mathrm{Torr}$. The vertical axis is in units normalised to the final converged value of each parameter, while the horizontal axis is the number of steady state iterations $i_{\mathrm{s}:n}$ from $i_{\mathrm{s}:1}$ up to $i_{\mathrm{s}:10,000}$ in logarithmic scale. $i_{\mathrm{s}:0}$ (not shown on this scale) represents the initial conditions, while $i_{\mathrm{s}:1}$ is the solution at the first iteration from those initial conditions. The solution is already sufficiently converged by $i_{\mathrm{s}:1000}$, but is left to run for the whole $n(i_\mathrm{s}) = 10,000$ to ensure a high degree of convergence and repeatability.

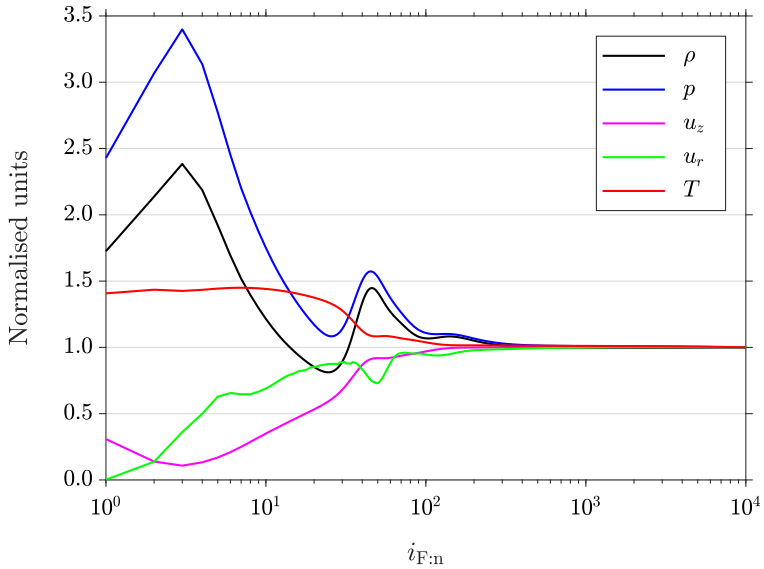

Figure 2.9: CFD simulation steady state convergence of the fluid parameters: mass density ρ (black — line), static pressure p (blue — line), axial velocity u_z (magenta — line), radial velocity u_r (green — line), and temperature T (red — line).

2.2.4 Plasma numerical method

The addition of plasma to the fluid model requires the `Chemistry`, `Electric`, and `Plasma` modules. In addition to the base set of fluid and plasma equations, the presently employed plasma modelling technique also solves for electron partial pressure and electron stochastic heating, as well as for ion momentum, mobility, ohmic heating, and surface heating from ion bombardment.

Unlike purely fluid CFD simulations which have steady state solutions, the CFD-plasma simulations are solved in a transient manner in order to capture the time dependent plasma dynamics within the RF cycle. Two distinct solver time-steps are used in the present CFD-plasma simulations: $\Delta\tau_\mathrm{f} = 1\,\mu\mathrm{s}$ for fluid dynamics, and $\Delta\tau_\mathrm{p} = 1.229\,\mathrm{ns}$ for plasma dynamics, equivalent to 1/60 of the period $\tau_\mathrm{RF} = 73.75\,\mathrm{ns}$ of a 13.56 MHz RF cycle. $\tau_\mathrm{RF}/\Delta\tau_\mathrm{p} = 60$ time-steps per RF cycle is chosen since $\sim 1\,\mathrm{ns}$ is the recommended time-step resolution for resolving plasma dynamics, and performs best with the $V_\mathrm{pwr} = 300\,\mathrm{V}$ waveform used presently without being too excessive. $\Delta\tau_\mathrm{f}$ and $\Delta\tau_\mathrm{p}$ are used for solving their corresponding equations independently, without any intermediate time-stepping, and do not have to be synchronised. Some solvers like COMSOL are limited to using a single time-step for solving the entire system of equations for both electron and heavy particle dynamics [61]. However, doing this or setting $\Delta\tau_\mathrm{f}$ too small (e.g. 1 ns) either causes the fluid to be frozen in time or the solution to be unstable and divergent, while setting $\Delta\tau_\mathrm{f}$ too large (e.g. 1 ms or even 1 s) causes large unphysical fluctuations and divergent behaviour. For best results, $\Delta\tau_\mathrm{f}$ has to be set to a value commensurate with the dynamics of the problem.

The main feature of this dual time-step technique is that different modules run at different rates. Two distinct iterative cycles are used in the CFD-plasma simulations. The first is the 'fluid iteration' i_f, which involves the `Flow`, `Heat Transfer`, and `Chemistry` modules, controlling parameters such as flow velocity and pressure, and are resolved at $\Delta\tau_\mathrm{f}$. The second is the 'plasma iteration' i_p, which involves the `Electric` and `Plasma` modules, controlling parameters such as electron number density, electron energy, and electric potential, and are resolved at $\Delta\tau_\mathrm{p}$. Temperature, chemical reactions, and the mass fractions of heavy species are also controlled by i_f, but these parameters are solved intelligently on a time-step that bridges $\Delta\tau_\mathrm{f}$ and $\Delta\tau_\mathrm{p}$. The number of fluid iterations $n(i_\mathrm{f})$ is selected empirically, with scaling based on the complexity of the flow behaviour and the degree of interaction between the fluid and the plasma, while the number of plasma iterations $n\big(i_\mathrm{p}\big)$ typically scales inversely with pressure.

The present CFD-plasma modelling technique uses $n(i_\mathrm{f}) = 10$ for slip regime supersonic

flow with significant plasma-induced heating, and $n(i_{\mathrm{p}}) = 5$ for a nominal $p \sim 1\,\mathrm{Torr}$ simulation domain. This means that the `Electric` and `Plasma` modules cycle among themselves for five iterations ($i_{\mathrm{p:1}}$ to $i_{\mathrm{p:5}}$) before passing the results at the end of $i_{\mathrm{p:5}}$ to the `Flow`, `Heat Transfer`, and `Chemistry` modules. These modules then cycle once ($i_{\mathrm{f:1}}$), and then return their results to the `Electric` and `Plasma` modules. The process repeats for a total of ten times ($i_{\mathrm{f:1}}$ to $i_{\mathrm{f:10}}$), whereupon the final result at the end of $i_{\mathrm{f:10}}$ constitutes the solution of the first simulation time-step t_1. Between each time-step t_n and t_{n+1}, the electrostatic and plasma parameters advance by $\Delta\tau_{\mathrm{p}}$, while the fluid parameters advance by $\Delta\tau_{\mathrm{f}}$. The algorithm of the present CFD-plasma modelling technique is summarised in Figure 2.10. At the end of t_{60}, the electrostatic and plasma parameters have advanced by τ_{RF} or exactly one RF cycle, while the fluid parameters have advanced by 60 µs. Although $\Delta\tau_{\mathrm{f}}$ is in lock-step with $\Delta\tau_{\mathrm{p}}$, the variation of the fluid parameters at each time-step is to a large extent a consequence of the large $\Delta\tau_{\mathrm{f}}$ rather than an actual response to the variation of the plasma parameters over $\Delta\tau_{\mathrm{p}}$. Hence, the fluid parameters must be averaged over the RF cycle for valid interpretation.

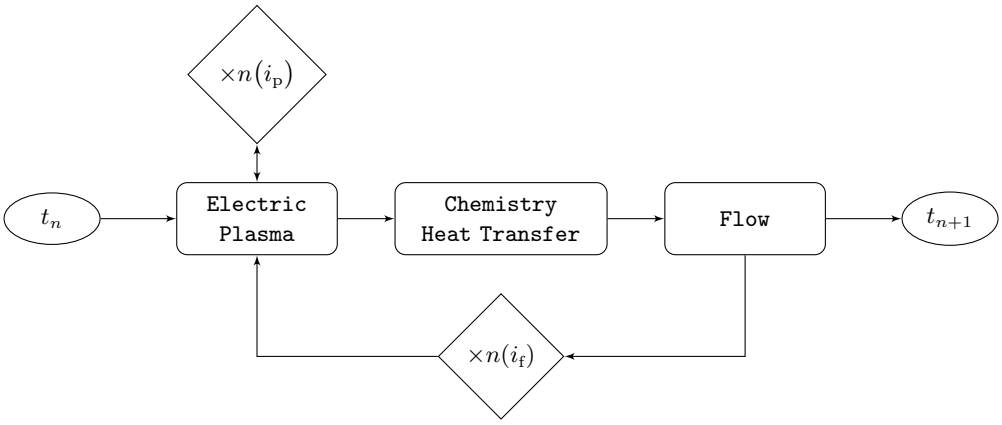

Figure 2.10: CFD-plasma modelling technique algorithm. Between time-step t_n and t_{n+1}, electrostatic and plasma parameters advance by $\Delta\tau_{\mathrm{p}}$, while fluid parameters advance by $\Delta\tau_{\mathrm{f}}$ interdependently.

The present CFD-plasma modelling technique first runs the simulation for 100 RF cycles (6000 time-steps, t'_1 to t'_{6000}) from static initial conditions with $n'(i_{\mathrm{f}}) = 1$ to obtain a quick but inaccurate 'seed solution'. This seed solution t'_{6000} is used as the initial conditions t_0 to start the 'convergence run' which goes for 1000 RF cycles (60,000 time-steps, t_1 to $t_{60{,}000}$). As this process takes about a fortnight on a second generation Intel Core processor clocked at 4.5 GHz, the convergence run is broken into ten stages to mitigate data loss in the event of

failure. The solution at the end of the convergence run $t_{60,000}$ is used as the initial conditions to start the 'final run' of 20 RF cycles (1200 time-steps, $t_{60,001}$ to $t_{61,200}$). The results from first half of the final run are not used, as anomalies have been known to appear when using prior solutions as initial conditions, but these anomalies tend to disappear quickly within a few cycles and the solution returns to equilibrium shortly thereafter. Hence, the latter 10 RF cycles (600 time-steps, $t_{60,600}$ to $t_{61,199}$) constitute the 'final solution' from which the results presented in this thesis are obtained.

It is critical that the simulation settings (e.g. $\Delta\tau_\mathrm{f}$, $\Delta\tau_\mathrm{p}$, $n(i_\mathrm{f})$, and $n\big(i_\mathrm{p}\big)$) are not changed after committing to the convergence run process. Previous CFD-plasma simulations of PR [15, 60, 66] have used only $\tau_\mathrm{RF}/\Delta\tau_\mathrm{p} = 20$ time-steps per RF cycle during the convergence run to reduce computation time. However, subsequent tests of the previous CFD-plasma modelling technique have shown that the solution at the end of the convergence run is of lower quality than using the present settings, with some significant differences in the results. Although $\tau_\mathrm{RF}/\Delta\tau_\mathrm{p} = 60$ time-steps per cycle are used for the final few RF cycles in the previous CFD-plasma simulations, the time is insufficient for capturing any further evolution of the solution, and may thus produce erroneous results. These issues have been resolved in the present CFD-plasma modelling technique.

Figure 2.11 plots a few of the tracked plasma parameters (coloured — lines) in the middle of the discharge chamber, at the coordinates $(z, r) = (-9, 0)$ in Figure 2.8, for a CFD-plasma simulation of PR with $\dot{m} = 100\,\mathrm{SCCM}$ of Ar, $p_0 = 0.349\,\mathrm{Torr}$, and $V_\mathrm{pwr} = 300\,\mathrm{V}$ on the powered electrode. The vertical axis is in units normalised to the final converged value of each parameter while the horizontal axis is the number of RF cycles, where one RF cycle is equivalent to 60 time-steps. The first 100 RF cycles (t'_1 to t'_{6000}) show the course to convergence of the seed solution, while the subsequent 1000 RF cycles (t_1 to $t_{60,000}$) are from the convergence run towards the final solution. The final run of 20 RF cycles are not visible on this logarithmic scale.

The convergence is periodic for both the fluid and plasma parameters as they are solved in lockstep. The solution is asymptotic after a few hundred RF cycles, but is left to run to completion to ensure a high degree of convergence and repeatability. While certain parameters such as the plasma potential Φ_p (green — line) and the electron density n_e (cyan — line) have not completely stagnated at the end of the convergence run, the rates at which these parameters are drifting are significantly smaller than their respective periodic variations and therefore do not have a significant impact on the final solution.

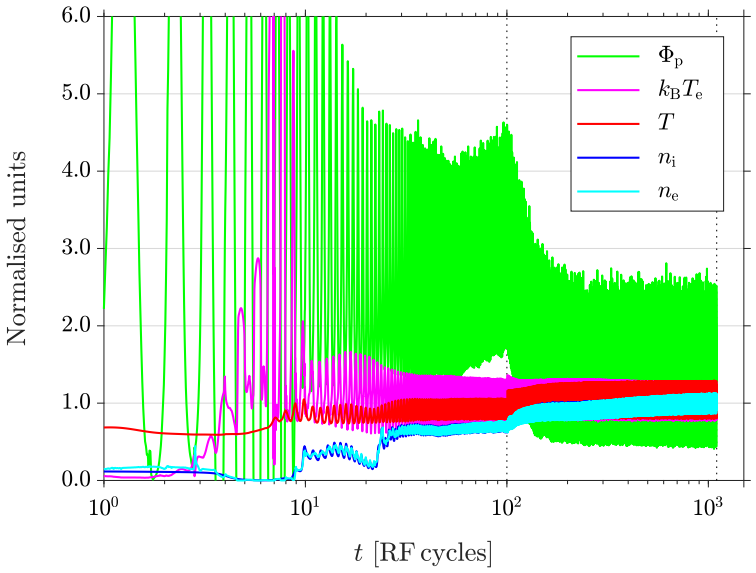

Figure 2.11: CFD–plasma simulation periodic convergence of the plasma parameters: plasma potential Φ_p (green — line), electron energy $k_B T_e$ (magenta — line), neutral gas temperature T (red — line), ion density n_i (blue — line), and electron density n_e (cyan — line).

2.3 Physical properties database

Although CFD-ACE+ has an inbuilt physical properties database, the default entries for the solid materials and fluid species are not sufficiently detailed for the CFD-plasma studies presented in this thesis. In particular, the inbuilt database lists constant values for fluid parameters such as dynamic viscosity μ and thermal conductivity k, when they are in fact functions of temperature. This is especially important in the CFD-plasma simulations of `PR` as the fluid species are subject to a wide range of temperatures from $\sim 100\,\mathrm{K}$ to $\sim 1000\,\mathrm{K}$. Consequently, the physical properties database has to be populated with the appropriate temperature dependent data for each and every solid material and fluid species used in the CFD-plasma simulations. The comprehensive use of temperature dependent physical properties represent a significant improvement of the CFD-plasma modelling technique over previous works [15, 60, 66] which used only constant values.

2.3.1 Solid materials

The solid materials considered are Al_2O_3, Al, Cu, Macor, and zirconia (ZrO_2). The solid phase specific heat c_p is calculated using the Shomate equation:

$$c_p = A_0 + A_1 T + A_2 T^2 + A_3 T^3 + A_4 / T^2 \tag{2.6}$$

with coefficients sourced from [67] within the stated nominal temperature range at a resolution of $\Delta T = 25\,\mathrm{K}$. The other physical properties include mass density ρ, thermal conductivity k, electrical resistivity ρ_{el}, and relative permittivity ε_{r}. These data are sourced from [68–70], and typically have sparse data points. The data is left as is for approximately linear curves, but fitting is required for some parameters to improve smoothness. Figures 2.12 and 2.13 plot the more important physical properties for Al_2O_3 and Cu respectively. For example, $k(T)$ of Al_2O_3 (Figure 2.12, red — line) needs to be fitted at a higher resolution of $\Delta T = 25\,\mathrm{K}$, but $k(T)$ of Cu (Figure 2.13, red — line) is sufficiently well described using the regular piecewise linear interpolation for $T \geq 300\,\mathrm{K}$.

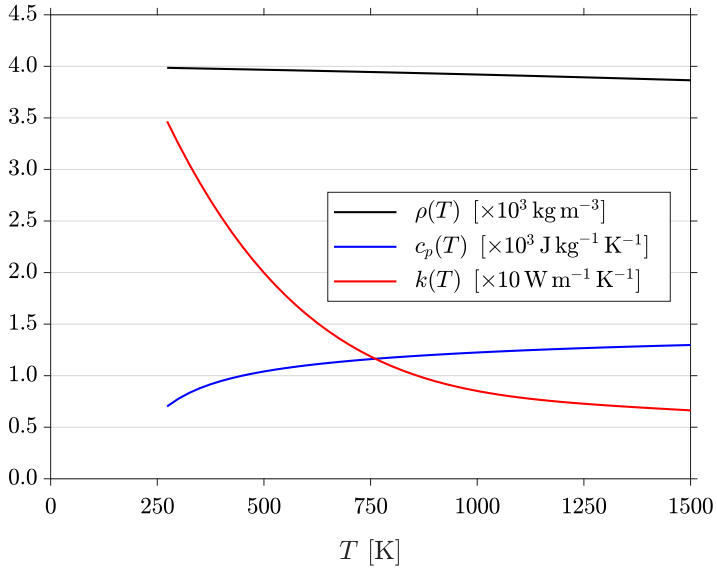

Figure 2.12: Temperature dependent physical properties of Al_2O_3: mass density $\rho(T)$ (black — line), solid phase specific heat $c_p(T)$ (blue — line), and thermal conductivity $k(T)$ (red — line), all fitted at $\Delta T = 25\,\mathrm{K}$ resolution.

The electrical resistivity ρ_{el} for electrically conductive materials such as Al and Cu uses the relation:

$$\rho_{\mathrm{el}}(T) = \rho_{\mathrm{el}}(300\,\mathrm{K}) \cdot [1 + \alpha_{\mathrm{el}}\,(T - 300\,\mathrm{K})] \tag{2.7}$$

where α_{el} is the temperature coefficient for electrical resistivity, fitted to the data points for calculating the temperature dependent $\rho_{\mathrm{el}}(T)$ from the reference value at $T = 300\,\mathrm{K}$. Dielectric materials such as Al_2O_3, Macor, and ZrO_2 are considered as electrical insulators, and therefore the relative permittivity ε_{r} applies instead of ρ_{el}.

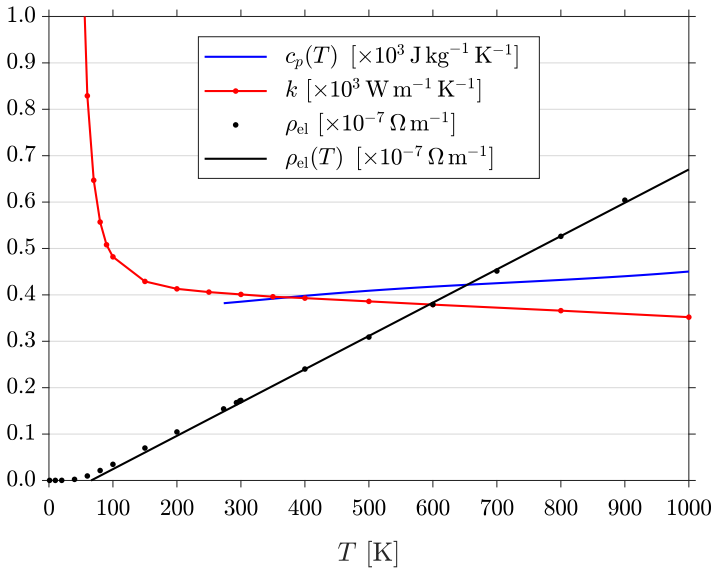

Figure 2.13: Temperature dependent physical properties of Cu: solid phase specific heat $c_p(T)$ (blue — line, fitted at $\Delta T = 25\,\mathrm{K}$ resolution), thermal conductivity k (red • markers) with linear interpolation (red — line), and electrical resistivity ρ_{el} (black • markers) with linear fit $\rho_{el}(T)$ (black — line).

2.3.2 Fluid species

The fluid species considered are Ar, Xe, and N_2. As an example, Figure 2.14 plots the dynamic viscosity μ (blue — line) in units of $[\times 10^{-5}\,\mathrm{Pa\,s}]$ and thermal conductivity k (red — line) in units of $[\times 10^{-2}\,\mathrm{W\,m^{-1}\,K^{-1}}]$ for Ar gas at $p = 1\,\mathrm{Torr}$ over the range $84\,\mathrm{K} \leq T \leq 700\,\mathrm{K}$. These fluid parameters vary considerably with temperature, and thus using default constant values may introduce nonideal deviations from the accurate result. Temperature dependent data for μ, k, and the specific heat at constant pressure c_p are sourced from [67]. As these parameters do not vary significantly with pressure, the isobaric dataset at $p = 1\,\mathrm{Torr}$ and $\Delta T = 1\,\mathrm{K}$ resolution is selected, and is adequate for the $0\,\mathrm{Torr} \leq p \leq 10\,\mathrm{Torr}$ range that the PR CFD-plasma simulations are conducted in. CFD-ACE+ uses piecewise linear interpolation to calculate parameter values between data points.

Figure 2.14 also plots the mass diffusivity $D(T)$ (black — line) in units of $[\times 10^{-2}\,\mathrm{m^2\,s^{-1}}]$. Temperature dependent data for D is sourced from both theoretical calculations of intermolecular forces [71] and potential energy functions [72], as well as diffusion cell experiments with gases doped with tracer isotope species [73–78]. The value of D is usually quoted for $p = 1\,\mathrm{atm}$. Thus, it is necessary to convert D_{atm} to D at the nominal $p = 1\,\mathrm{Torr}$ regime via:

$$D = \frac{\rho_{atm}}{\rho} D_{atm} \tag{2.8}$$

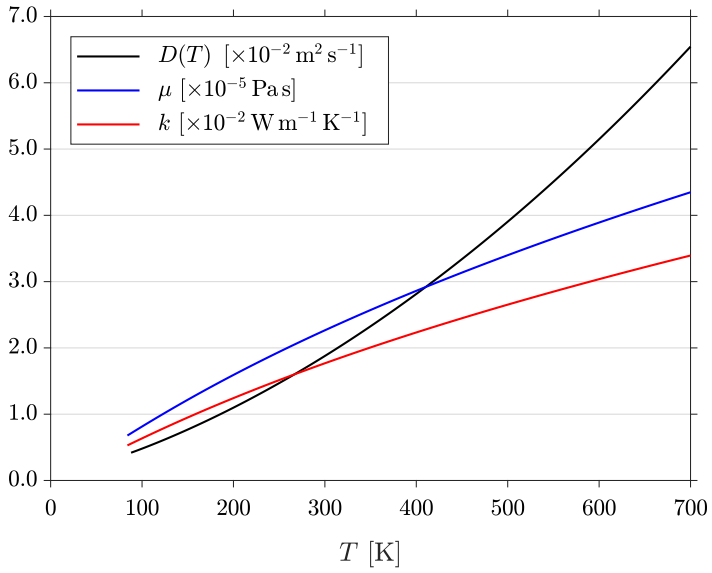

Figure 2.14: Temperature dependent physical properties of Ar at 1 Torr: mass diffusivity $D(T)$ (black — line, fifth order polynomial fit), dynamic viscosity μ (blue — line), and thermal conductivity k (red — line), at $\Delta T = 1\,\mathrm{K}$ resolution.

where ρ_{atm} and ρ are the temperature dependent mass density of the species at $p = 1\,\mathrm{atm}$ and $p = 1\,\mathrm{Torr}$ respectively. Since the D_{atm} measurements are discrete, a fifth order polynomial in T is fitted to the experimental data. The conversion to D is then calculated at finer intervals of $\Delta T = 1\,\mathrm{K}$ with ρ_{atm} and ρ sourced from [67], and a fifth order polynomial in T (Figure 2.14) is fitted to the calculated D values. $D(T)$ is preferred to using a constant Schmidt number Sc in:

$$D = \frac{\mu}{\rho \cdot \mathrm{Sc}} \tag{2.9}$$

as Sc also tends to vary with T.

The first approximation of the Chapman-Enskog theory [79, 80] for calculating D_{12} in $[\mathrm{m^2\,s^{-1}}]$ of two species with molecular masses m_1 and m_2 is:

$$D_{12} = \frac{1.41 \times 10^{-4}}{p\sigma_{12}^2\Omega} \cdot T^{\frac{3}{2}} \left(\frac{1}{m_1} + \frac{1}{m_2}\right)^{\frac{1}{2}} \tag{2.10}$$

where p is the static pressure in [Torr], T is the temperature in [K], and $\sigma_{12} = 1/2\,(\sigma_1 + \sigma_2)$ is the average Lennard-Jones collision diameter of the two species in [Å]. Ω is a dimensionless quantity of order one, characteristic of the integration of the interaction between the two species [80]. Note that for the referenced experiments, the self-diffusion coefficient $D = D_{11}$ is obtained by putting $m_2 = m_1$ even though different isotope species are used. This assumption is generally valid as the mass dependent term in (2.10) is insensitive to

species with molecular mass $m \gtrsim 20\,\mathrm{u}$ [75]. Overall, (2.10) is accurate to $\sim 10\,\%$ [80] when calculating D_{11}, and is also approximately valid for electronically excited species.

Temperature independent parameters for the fluid species include the following. The molecular mass m for each fluid species is a constant, sourced from [81]. For CFD or CFD-plasma simulations involving multiple fluid or neutral plasma species, the Lennard-Jones characteristic energy ϵ_σ and collision diameter σ [82] are used for calculating the Lennard-Jones potential:

$$V_\sigma(r) = 4\epsilon_\sigma \left[\left(\frac{\sigma}{r}\right)^{12} - \left(\frac{\sigma}{r}\right)^{6} \right] \tag{2.11}$$

which describes the interaction between a pair of neutral molecules separated by a distance r. For CFD-plasma simulations, additional parameters such as the electrical resistivity ρ_{el}, relative permittivity ε_{r}, charge exchange cross section σ_q, and polarisability volume α' [83] are required and loaded into the physical properties database.

2.4 Chapter summary

This chapter details the PR experimental apparatus, which includes the PR device itself, as well as the propellant flow and RF electrical circuits that are used in the laboratory or packaged as a miniaturised subsystem. The standard operating conditions are with $\dot{m} = 100\,\mathrm{SCCM}$ of Ar and $V_{\mathrm{pwr}} = 300\,\mathrm{V}$ at $13.56\,\mathrm{MHz}$, targeting $P \sim 5\,\mathrm{W}$ for use on microspacecraft.

The motivation for CFD-plasma modelling stems from the challenges in obtaining precise experimental measurements at high spatial and temporal resolution within the constricted geometry of PR. Simulations are performed to complement experimentation, and work on PR progresses in a leapfrogging manner between these two techniques.

The PR simulation mesh replicates the different components in the physical device at actual scale. A hemispherical downstream region allows vacuum expansion to be modelled without computational anomalies. The CFD and CFD-plasma modelling techniques are outlined, with a description of both the fluid and plasma numerical methods and their respective parameters. The convergence to the final solution is steady state in CFD simulations, and periodic in CFD-plasma simulations. The physical properties database is an integral part of the simulation program, and has been manually populated with highly precise data with a focus on temperature dependent parameters.

Chapter 3

Slip flow

This chapter presents cold gas CFD simulations of *Pocket Rocket* performed in the rarefied slip flow regime [84]. In this regime, boundary layer effects are dominant, and have a significant influence on the overall flow behaviour of the system. The correct flow boundary conditions must be used in the CFD simulations in order to produce results that are physically accurate. Theoretical concepts of rarefied flow dynamics are introduced, followed by a detailed discussion of the slip regime boundary condition and the accommodation coefficients used to implement slip flow. Different flow boundary conditions are tested in a total of 54 CFD simulations performed with two variations of the *Pocket Rocket* geometry (`PR-A` and `PR-Z`), and using Ar and N_2 propellants. The CFD simulation results are compared against experimental measurements to confirm the accuracy of the slip boundary condition across all the tested operating conditions.

3.1 Rarefied gas dynamics

3.1.1 Mean free path

The mean free path λ is the statistical mean distance travelled by a moving particle between collisions with other moving particles. In a fluid medium, λ may be characterised using its dynamic viscosity μ:

$$\lambda_\mu = \frac{\mu}{p}\sqrt{\frac{\pi k_\mathrm{B} T}{2m}} \tag{3.1}$$

where k_B is the Boltzmann constant, p and T are the static pressure and temperature of the fluid, and m is the molecular mass of the constituent fluid molecule.

With sufficient rarefaction, gases begin to act more like individual particles and less like

a cohesive fluid, and the fluid description of λ_μ ceases to be accurate. A kinematic relation is required, characterised using the Lennard-Jones collision diameter σ of the gas molecule [82]:

$$\lambda_\sigma = \frac{k_\mathrm{B}T}{\sqrt{2}\pi p\sigma^2} \tag{3.2}$$

λ_σ preserves its accuracy even in rarefied conditions, and is therefore more appropriate for the present study of PR in the $\lesssim 1\,\mathrm{Torr}$ range. Hereafter, the subscript 'σ' is dropped for convenience, except when it is necessary to distinguish between λ_μ and λ_σ. As a general estimate, $p \sim 1\,\mathrm{Torr}$ and $T \sim 300\,\mathrm{K}$ gives $\lambda \sim 0.06\,\mathrm{mm}$.

3.1.2 Knudsen number

The Knudsen number Kn is a dimensionless parameter which determines whether a flow is better characterised by continuum or statistical mechanics. It is defined as the ratio of the mean free path λ to the characteristic length L of the flow system:

$$\mathrm{Kn} = \frac{\lambda}{L} \tag{3.3}$$

In general, L is the smallest length scale in a particular geometry. For a cylinder, L is typically its radius, unless its length is smaller than its diameter, in which case L is defined to be half the length.

For the PR geometry (Figure 2.8), the respective values are specified to be $L_\mathtt{P} = 6\,\mathrm{mm}$ in the plenum using the latter definition, while $L_\mathtt{C} = 2.1\,\mathrm{mm}$ in the discharge chamber using the former definition. Assuming $p \sim 1\,\mathrm{Torr}$ and $T \sim 300\,\mathrm{K}$, this gives $\mathrm{Kn} \sim 0.03$ in the discharge chamber. The value of $L_\mathtt{D} = 22.5\,\mathrm{mm}$ is selected for the downstream region according to the dimensions of the glass expansion tube using the former definition. The smaller radius of the glass expansion tube sets a stricter criteria for assessing the validity of the solution in the downstream region for low pressure scenarios.

3.1.3 Flow regimes

Flow can be categorised into four regimes according to their respective Kn range: continuum ($\mathrm{Kn} \lesssim 0.01$), slip ($0.01 \lesssim \mathrm{Kn} \lesssim 0.1$), transitional ($0.1 \lesssim \mathrm{Kn} \lesssim 10$), and free molecular ($\mathrm{Kn} \gtrsim 10$).

Continuum flow is dominated by fluid viscosity. Hagen-Poiseuille flow is an example of continuum flow. It is the laminar flow of an incompressible viscous fluid through a high aspect ratio channel induced by a pressure difference between upstream and downstream. The axial

velocity of the fluid in the channel has a peaked parabolic profile, as the fluid in the middle of the channel is moving the fastest while the fluid in contact with the channel wall is stationary with respect to the wall. This observation of the stationary fluid boundary is embodied in the no slip boundary condition. Another continuum flow example that prominently features the no slip boundary condition is Couette flow, where an incompressible viscous fluid flows between two surfaces, with one surface moving tangentially relative to the other. The no slip boundary condition at each surface forces the fluid to shear, resulting in a linear velocity profile between the two surfaces.

In the rarefied slip regime, λ becomes comparable to L, and boundary layer effects begin to dominate flow behaviour. The no slip boundary condition is no longer valid for flow systems where $\mathrm{Kn} \gtrsim 0.01$, which is the case in the discharge chamber of `PR`. For accurate results, the boundary layer must be treated accordingly using the slip boundary condition.

Free molecular flow occurs in near-vacuum conditions where λ becomes very large. At this Kn scale, gas molecules rarely encounter one another. They resemble discrete particles, travelling in straight lines and interacting primarily with the walls of the flow system. Consequently, fluid concepts like pressure and viscosity no longer apply. For example, the interstellar medium exists in the state of free molecular flow. In terrestrial laboratories, the free molecular regime may be attained in vacuum chambers through turbomolecular or cryogenic pumping.

Generally, fluid mechanics break down upon entering the transitional regime. Hence, CFD simulations are limited to modelling continuum flow, and the treatment of rarefied flows with higher Knudsen numbers require modelling techniques such as molecular dynamics (MD) or direct simulation Monte Carlo (DSMC). However, MD simulations are extremely computationally expensive for all but very small systems since it scales by the square of the number of molecules involved. A more practical solution is DSMC simulations which use a characteristic particle to represent a large ensemble of real molecules. While this reduces the scale of the problem, DSMC simulations are nevertheless still very much more computationally expensive than CFD simulations for modelling weakly rarefied flows, particularly in the continuum and slip regimes. Studies seeking to model flows spanning a wide range of Knudsen numbers typically resort to a hybrid CFD/DSMC approach, applying CFD modelling techniques to regions of low Kn, and using the results thus obtained as a boundary condition for the neighbouring regions of high Kn where DSMC modelling techniques are employed [85].

3.2 Slip regime boundary condition

Despite the apparent limitations, CFD modelling techniques can still be used to accurately model rarefied gas dynamics in the slip flow regime, *proviso* of the careful and proper implementation of the slip boundary condition.

The following sections describe the derivation of the slip boundary condition from the fundamental approach of studying the molecular reflection of a gas molecule off a solid wall. Characterising this behaviour requires the concept of the 'accommodation coefficient', which results in a 'slip' in flow velocity and temperature at the rarefied fluid boundary adjacent to the wall. This small but important feature distinguishes the slip boundary condition from the no slip boundary condition, and is essential for treating the dominant boundary layer in slip flow.

3.2.1 Molecular reflection off a solid wall

The state of a rarefied gas flow system is highly dependent on the nature of the interactions of the gas molecules, monatomic or otherwise, with the walls of the system. It is therefore necessary to know the velocity and temperature distribution function of the gas molecules that have been reflected off the solid surface and back into the flow. The following paragraphs summarise the original phenomenological picture of molecular reflection off a solid wall proposed by Maxwell in 1879 [86].

Consider the case of an ideal gas in which the gas molecules are elastic hard spheres of a fixed diameter. Each molecule that is incident on a solid surface is reflected with its tangential velocity remaining the same but its normal velocity reversed. In other words, the reflection is specular. Since no tangential velocity is lost during the collision, the gas does not exert any tangential stress on the surface and likewise experiences no friction with the wall, and so the only force exerted by the gas on the wall is the normal pressure force. However, specular reflection is only possible if the boundary layer is sufficiently devoid of other molecules such as in extremely rarefied or free molecular flows [87].

A more realistic picture of molecular reflection involves a boundary layer populated by a sufficient number of freely moving molecules, such that a gas molecule passing through the layer must strike elastically a random number of molecules, but not so crowded that the layer becomes impenetrable. Each molecule that passes through the boundary layer and is incident on the wall must have a randomised velocity in any direction towards the wall. When the molecule is reflected off the wall and passes through the boundary layer a second

time, its velocity must again be random in magnitude and direction (away from the wall), with a probability given by a half-range Maxwellian distribution in equilibrium with the wall. This is called diffuse reflection.

Let α be the fraction of gas molecules that reflect diffusively, then $1-\alpha$ is the fraction of molecules that reflect specularly. If $\alpha = 1$, then every molecule reflects diffusively, and the flow is said to achieve 'perfect accommodation' at the wall. In reality, molecular reflection is a mixture of diffuse and specular reflection such that $0 < \alpha < 1$. The molecular reflection kernel (also called the scattering kernel) according to Maxwell's picture is therefore a linear combination of the diffuse and specular reflection kernels [88]:

$$R(\boldsymbol{u}_1 \to \boldsymbol{u}_2) = \alpha \cdot \frac{m^2 u_y}{2\pi \left(k_\mathrm{B} T_\mathrm{wall}\right)^2} \cdot \exp\left(-\frac{m u_x^2}{2 k_\mathrm{B} T_\mathrm{wall}}\right) + (1-\alpha)\,\delta\left(\boldsymbol{u}_1 - \boldsymbol{u}_2 + 2\boldsymbol{u}_y\right) \tag{3.4}$$

where $\boldsymbol{u}_1$ and $\boldsymbol{u}_2$ are the incident and reflected velocity vectors, while $u_x = |\boldsymbol{u}_x|$ and $u_y = |\boldsymbol{u}_y|$ are the magnitudes of the velocity vectors parallel and perpendicular to the wall respectively. The first term prefixed by α is the reflection kernel for diffuse reflection in which m is the molar mass of the gas molecule, and T_wall is the wall temperature, where the reflected gas molecule is at thermal equilibrium with the wall with velocity sampled from the half-range Maxwellian distribution. The second term prefixed by $(1-\alpha)$ is the reflection kernel for specular reflection which is simply a Dirac delta function effective when the reflected velocity is the same as the incident velocity but with the normal component of the velocity reversed. Other forms of molecular reflection kernels have been proposed [89], one of the more popular ones being the Cercignani-Lampis kernel [90] which features two separate accommodation coefficients α_x and α_y for the directions tangential and normal to the reflecting surface.

3.2.2 Accommodation coefficients

Tangential momentum accommodation coefficient

$\alpha = \alpha_u$ is also called the 'tangential momentum accommodation coefficient' (TMAC), with reason apparent from the following equation:

$$\alpha_u = \frac{u_1 - u_2}{u_1 - u_\mathrm{wall}} \tag{3.5}$$

where u_1 and u_2 are the velocity components tangential to the surface of reflection for the incident and reflected gas molecule respectively, and u_wall is the tangential velocity of the wall, typically taken to be stationary. In the case where every reflection event is diffuse, u_2 is on average zero relative to the wall over many events since the velocity of each reflected

gas molecule has equal probability in any direction away from the wall. Hence, $\alpha_u = 1$ for fully diffuse reflection. For fully specular reflection, $\alpha_u = 0$ since $u_1 = u_2$ for every molecule.

Measurements of α_u are typically performed by tracking the flow of gas through a microchannel. Experiments by [91–98] use microchannels constructed of various materials (glass, silica, silicon, stainless steel, etc.) with different shapes and diameters spanning the whole µm range, over a wide range of pressures at room temperature. Table 3.1 lists the results for Ar, Xe, and N_2 from these experiments and the flow regime in which they were performed. α_u for each gas species remains roughly constant across different conditions and flow regimes. [98] demonstrates good agreement of their experimental data from the continuum, slip, and transitional regimes with sourced numerical simulations valid for each regime up to the near free molecular regime. Their results are consistent with those of the other references and also very close to the average values. Section 3.4.1 shows that precision in the values for α_u may be disregarded for α_u close to unity, and it is sufficient to use α_u rounded to one decimal place in the CFD simulations. Namely, $\alpha_u(\mathrm{Ar}) = 0.9$, $\alpha_u(\mathrm{Xe}) = 1.0$, and $\alpha_u(\mathrm{N_2}) = 0.9$.

Thermal accommodation coefficient

Similarly, this treatment is also used for deriving the temperature distribution of the reflected gas molecules with the 'thermal accommodation coefficient' (TAC):

$$\alpha_T = \frac{T_1 - T_2}{T_1 - T_{\mathrm{wall}}} \tag{3.6}$$

where T_1 and T_2 are the temperatures of the incident and reflected gas molecule respectively, and T_{wall} is the wall temperature, typically taken to be a fixed value. Gas molecules reflecting diffusively take up a temperature distribution where the mean temperature is at equilibrium with the wall, therefore $T_2 = T_{\mathrm{wall}}$, and $\alpha_T = 1$ for fully diffuse reflection. As before, fully specular reflection gives $\alpha_T = 0$ since $T_1 = T_2$ remains the same.

α_T is in general not the same as α_u for each gas species. Table 3.2 lists the α_T values for Ar, Xe, and N_2 obtained from experiments [99–103] and the temperature range in which the measurements are made. Various methods are employed. [99] measures the conductance of the gas in the gaps between two rough surfaces in contact (the asterisk * denotes interface temperature), while [100] measures the thermomolecular pressure difference in two chambers on either ends of a capillary tube. More traditional methods involve measuring the heat flux through the test gas between two solid surfaces held at separate temperatures T_{w1} and T_{w2}, using either parallel plates [101, 102] or coaxial cylinders [104, 105]. [103] uses a novel experimental technique of observing the temperature-dependent frequency shifts in the

Table 3.1: Tangential momentum accommodation coefficient α_u

Ref.	Flow regime	Ar	Xe	N_2
[91]	Slip	0.927	1.010	0.925
	Free molecular	0.979	1.0	0.977
[92]	Transitional	–	–	0.87
[93]	Slip	–	–	0.93
[94]	Slip	0.871	–	0.908
[95]	All	0.879	–	0.923
[96]	Slip	0.888	–	0.914
[97]	Slip	0.825	–	0.820
[98]	Slip	0.887	–	0.895
	All	0.90	–	0.90
Average		0.89	1.0	0.90

Table 3.2: Thermal accommodation coefficient α_T

Ref.	$T_{w1} : T_{w2}$ [K]	Ar	Xe	N_2
[99]	444*	0.90	–	0.78
[100]	273 : 293	0.74	0.79	0.73
[101]	278 : 318	0.870	–	–
	288 : 308	–	–	0.798
[102]	293 : 303	0.93	–	0.85
[103]	298 : 299	–	–	0.796
Average		0.86	0.79	0.79
[104]	296 : 358	0.876		
	296 : 389	0.859		
	296 : 422	0.840		
	296 : 459	0.791		
	296 : 497	0.724		
	296 : 591	0.682		
[105]	943 : 977	0.800		
	1083 : 1129	0.644		
	1098 : 1136	0.649		
	1148 : 1188	0.624		

whispering-gallery modes of a dielectric optical microresonator as it cools while immersed in the gas. While α_T is roughly constant for each gas species across different surface materials [102] and roughness [101], it appears to decrease as the temperature difference between T_{w1} and T_{w2} increases [104]. [105, 106] further suggest that α_T may be in fact a function of temperature. However, due to the lack of extensive studies on this behaviour, the decision is made to use the constant, average values from the first five references in Table 3.2, with $\alpha_T\,(\mathrm{Ar}) = 0.9$, $\alpha_T\,(\mathrm{Xe}) = 0.8$, and $\alpha_T\,(\mathrm{N_2}) = 0.8$.

3.2.3 Slip velocity & temperature jump

Applying the Maxwellian molecular reflection kernel and the accommodation coefficients α_u and α_T produces the proper boundary conditions required for the solution of the boundary layer flow near a wall. [107] presents a clear conceptual explanation of how the implementation of fictitious velocity and temperature slip boundary conditions, such that when fulfilled, give a solution of the Navier-Stokes equations in the main flow that resembles the flow kinetics in reality. The following section provides a summary.

Slip velocity

Let the velocity of the wall be zero. With a nonzero α, the presence of the stationary wall must slow down the flow. However, there is no *a priori* justification for assuming that the velocity or temperature of the gas at the wall must be zero relative to the wall (*à la* the no slip boundary condition). Let the true tangential flow velocity near the wall be the solid curve in Figure 3.1. The horizontal `--` line delimits the boundary layer, above which in the main flow that the Navier-Stokes solution approximates the real flow to within sufficient accuracy. If the velocity and temperature of the gas is known along that line, then it is possible to extend the Navier-Stokes solution inside the boundary layer, and determine fictitious values of the tangential flow velocity and temperature at the wall. In general, the fictitious velocity and temperature obtained from the Navier-Stokes solution in the boundary layer are not equal to either the true velocity and temperature of the gas at the wall, or the velocity and temperature of the wall itself. The difference between the fictitious tangential flow velocity and the wall velocity is called the 'slip velocity' u_{slip}, and the corresponding temperature difference is called the 'slip temperature' T_{slip}, also more commonly known as the 'temperature jump'.

Maxwell's original formulation for the slip velocity is a first order approximation valid up to the slip regime. In Cartesian coordinates, with x representing the direction tangential

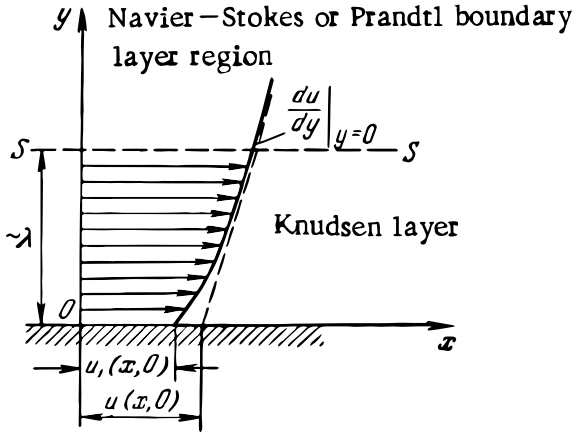

Figure 3.1: Slip flow boundary layer. Image credit [107].

to the wall and y normal to the wall:

$$u_{\text{slip}} = u_{\text{wall}} - \frac{2-\alpha_u}{\alpha_u} \cdot \lambda \left[\frac{\partial u_x}{\partial y} + \frac{\partial u_y}{\partial x} - \frac{3}{2} \frac{\mu}{\rho T_{\text{wall}}} \frac{\partial^2 T}{\partial x \partial y} \right]_{\text{wall}} + \frac{3}{4} \frac{\mu}{\rho T_{\text{wall}}} \left[\frac{\partial T}{\partial x} \right]_{\text{wall}} \tag{3.7}$$

where u_{slip} is the slip velocity, u_{wall} is the tangential velocity of the wall, u_x and u_y are the velocity components tangential and normal to the wall respectively, T is the gas temperature, and T_{wall} is the wall temperature. α_u is the tangential momentum accommodation coefficient as defined earlier, λ is the mean free path of the gas, μ is the gas viscosity, and ρ is the mass density. In (3.7), the terms in the first set of brackets is the contribution to the slip velocity due to the tangential shear stresses in the xy plane, and the final term in the equation accounts for the temperature gradient in the direction of the flow. If there is no inequality of temperature, then the terms involving T may be discarded. To further simplify the equation, $\partial u_y/\partial x$ may be omitted if the wall is planar and nonrotating (a counterexample being cylindrical Couette flow), or has no velocity in the normal direction (unlike a deflecting flap) [108]. Then, the slip velocity is:

$$u_{\text{slip}} = u_{\text{wall}} - \frac{2-\alpha_u}{\alpha_u} \cdot \lambda \left[\frac{\partial u_x}{\partial y} \right]_{\text{wall}} \tag{3.8}$$

which is the expression used in CFD-ACE+.

$\alpha_u = 2$ reduces (3.8) to the no slip boundary condition with $u_{\text{slip}} = u_{\text{wall}}$. In the case of fully diffuse reflection, $\alpha_u = 1$ results in a linear function where the slip velocity is simply the gradient of the tangential flow velocity at the wall (negative in sign since $u > u_{\text{wall}}$) multiplied by λ. In the case of fully specular reflection, the limit $\alpha_u = 0$ causes $(2-\alpha_u)/\alpha_u \to \infty$, which demands that $[\partial u_x/\partial y]_{\text{wall}}$ must necessarily be zero. This resembles frictionless or inviscid flow since the velocity of the gas at the wall is decoupled from u_{wall}.

Temperature jump

The original formulation for the temperature jump is attributed to Smoluchowski [109]. Also to the first order and in the same Cartesian coordinates:

$$T_{\text{slip}} = T_{\text{wall}} - \frac{2-\alpha_T}{\alpha_T}\frac{2\gamma}{\gamma+1}\frac{k}{c_p\mu}\cdot\lambda\left[\frac{\partial T}{\partial y}\right]_{\text{wall}} \tag{3.9}$$

where T_{slip} is the temperature jump, T_{wall} is the wall temperature, and T is the gas temperature. α_T is the thermal accommodation coefficient as defined earlier, λ is the mean free path of the gas, γ is the gas adiabatic index, k is the gas thermal conductivity, c_p is the gas specific heat at constant pressure, and μ is the gas viscosity. The term $\text{Pr} = c_p\mu/k$ is also called the Prandtl number which is essentially the ratio of the viscous diffusivity μ/ρ to the thermal diffusivity $k/\left(c_{\text{p}}\rho\right)$. Generally, γ and Pr are approximately constant over a reasonable range of pressures and temperatures, so $C = 2\gamma/\left[(\gamma+1)\,\text{Pr}\right]$ is also approximately constant. Thus:

$$T_{\text{slip}} = T_{\text{wall}} - \frac{2-\alpha_T}{\alpha_T}\cdot C\lambda\left[\frac{\partial T}{\partial y}\right]_{\text{wall}} \tag{3.10}$$

In a similar manner, $\alpha_T = 2$ reduces (3.10) to the no slip boundary condition with $T_{\text{slip}} = T_{\text{wall}}$. In the case of fully diffuse reflection, $\alpha_T = 1$ results in a linear function where the temperature jump is simply the gradient of the flow temperature at the wall multiplied by λ. The gradient of the flow temperature is negative in sign if the gas is volumetrically heated such that $T > T_{\text{wall}}$, otherwise it is positive in sign with cold gas flows or when the wall is heated such that $T < T_{\text{wall}}$. In the case of fully specular reflection, the limit $\alpha_T = 0$ causes $(2-\alpha_T)/\alpha_T \to \infty$, which demands that $[\partial T/\partial y]_{\text{wall}}$ must necessarily be zero.

Table 3.3: Modified thermal accommodation coefficient α_T'

	Ar	Xe	N_2	Comments
γ	5/3	5/3	7/5	Theoretical values
Pr	0.667	0.660	0.720	Calculated using fluid parameters [67]
C	1.875	1.893	1.620	Calculated using equation given above
α_T	0.86	0.79	0.79	Values from Table 3.2
α_T'	0.89	0.82	0.89	Calculated using (3.11)

CFD-ACE+ uses the expression given in (3.10) but with a fixed value of $C = C' = 2$. Table 3.3 lists the relevant parameters in (3.10) for Ar, Xe, and N_2 at $T = 300\,\text{K}$ and $p = 1\,\text{Torr}$. Since C for each gas species is slightly different, using $C' = 2$ is not only

inaccurate but also produces a slight overestimate of the temperature jump. To compensate for this, a modified thermal accommodation coefficient α'_T is designated such that:

$$\frac{2-\alpha'_T}{\alpha'_T}\cdot C' = \frac{2-\alpha_T}{\alpha_T}\cdot C \tag{3.11}$$

thus giving $\alpha'_T\,(\mathrm{Ar}) = 0.9$, $\alpha'_T\,(\mathrm{Xe}) = 0.8$, and $\alpha'_T\,(\mathrm{N_2}) = 0.9$.

In conclusion, for each gas species in the simulations, the aforementioned values of α_u and α'_T are used based on the recommendations of the references listed in Tables 3.1 and 3.2. These values for α_u and α'_T produce the appropriate fictitious slip velocity and temperature jump at the wall that is required in order for the Navier-Stokes solution in the main flow to accurately reproduce the actual rarefied flow kinetics in the $p \sim 1$ Torr environment of PR.

3.3 CFD simulation setup

The aim of the CFD simulations presented in this chapter is to study the rarefied slip flow behaviour of Ar and N_2 in PR, and compare the simulation results to cold gas experimental results. In order to produce realistic and accurate results, it is imperative that the correct volume and boundary conditions are applied. The PR simulation domain (Figure 3.2) shows the volume regions and the different types of boundaries (coloured lines).

Two versions of the PR geometry are tested in this chapter. The first is the original PR with the 4.2 mm internal diameter and 6.2 mm external diameter Al_2O_3 refractory tube discharge chamber. The second is a modified prototype with a 3.666 mm internal diameter and 5.5 mm external diameter ZrO_2 refractory tube discharge chamber. Apart from the different diameters of the discharge chambers, all other dimensions are unchanged. To differentiate between the two geometries in this chapter, the original Al_2O_3 version is designated as PR-A, while the narrower ZrO_2 version is designated as PR-Z. The PR-Z simulation mesh is very similar to the PR-A simulation mesh, but with the discharge chamber wall (CW, yellow) displaced slightly downwards. The CFD simulations replicate the cold gas experimental setup, with either PR-A or PR-Z mounted on the vacuum chamber via the glass expansion tube (Figures 2.2 and 2.3).

3.3.1 Volume conditions

Solid regions

As these are purely fluid CFD simulations at thermal equilibrium, the powered electrode (E), insulation (I), and structure (S) solid regions (Figure 2.8) may be excluded to reduce

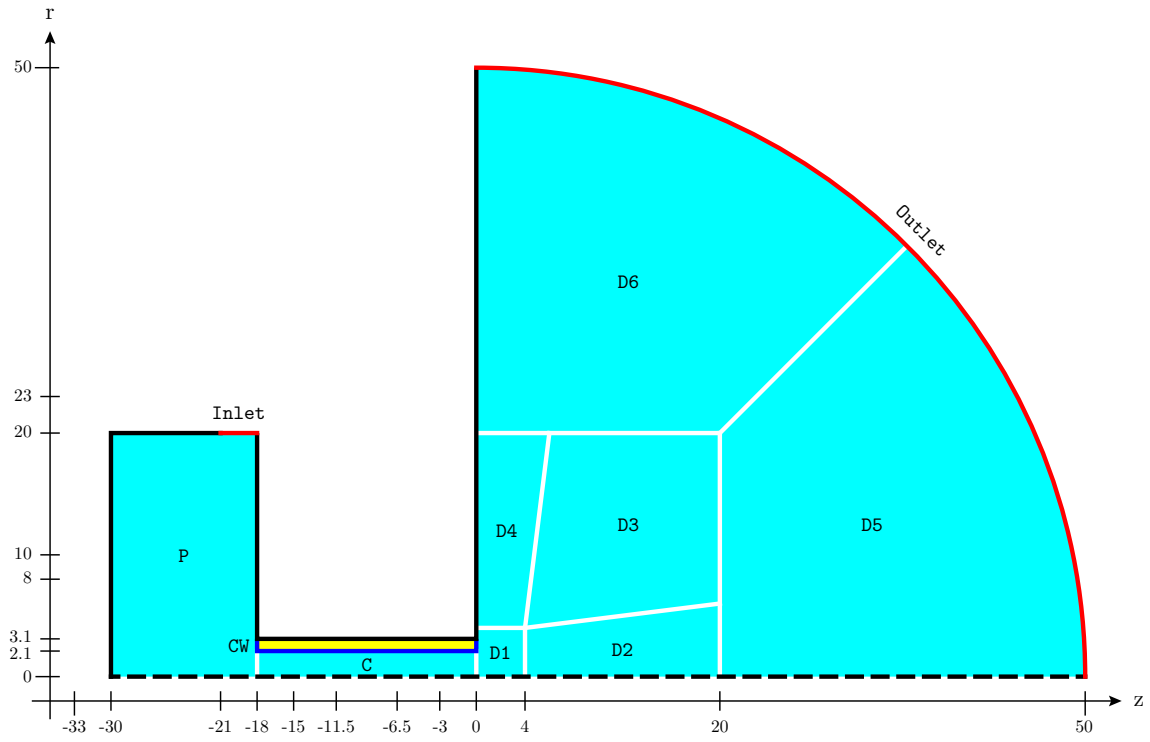

Figure 3.2: PR CFD simulation domain. Fluid regions (aqua): plenum (P), discharge chamber (C), and downstream (D). Solid region: Al_2O_3 discharge chamber wall (CW, yellow). Boundaries: inlet and outlet (red — lines), axis of symmetry (black -- line), wall (black — lines), and solid-fluid interface (blue — line).

computation time without affecting the results. However, the discharge chamber wall (CW) must be included as it acts as a thermally conductive heat exchanger along the length of the discharge chamber (C). The solid material physical properties (Section 2.3.1) of Al_2O_3 and ZrO_2, namely the mass density ρ, thermal conductivity k, and specific heat c_p, are loaded as volume conditions for the solid region CW in PR-A and PR-Z respectively. No artificial source term for heat is used in CW.

Fluid regions

The fluid species physical properties of Ar and N_2, namely the molecular mass m, mass density ρ, dynamic viscosity μ, thermal conductivity k, specific heat at constant pressure c_p, and mass diffusivity D (Section 2.3.2) are loaded as volume conditions for the fluid regions P, C, and D in both PR-A and PR-Z. As the fluid considered is either pure Ar or pure N_2, gas mixing rules are not necessary. No artificial source terms for mass, velocity, or heat are used in the fluid regions.

3.3.2 Boundary conditions

For CFD simulations, the boundary conditions refer to the fluid parameters handled by the `Flow`, `Heat Transfer`, and `Chemistry` modules. There are five types of boundaries: inlet (`i`), outlet (`o`), symmetry, wall (`w`), and interface. In Figure 3.2, the inlet boundary is a 3 mm section (`i-P`, red — line) on the top right edge of the plenum, while the outlet boundary is the hemispherical edge (`o-D5` and `o-D6`, red — arc) of the downstream subregions `D5` and `D6`. The axis of symmetry is horizontally along the base of the `PR` simulation domain (black `--` line). Wall boundaries (`w-P`, `w-CW`, `w-D1`, `w-D4`, and `w-D6`, black — line) are along the external edges of the plenum, discharge chamber wall, and downstream subregions `D1`, `D4`, and `D6`.

Interfaces exist between adjacent regions, allowing the two regions to communicate information. There are three kinds of interfaces: solid-solid, solid-fluid, and fluid-fluid. Solid-solid interfaces are not featured in the `PR-A` or `PR-Z` simulation domain (Figure 3.2) as there is only a single solid region present. Solid-fluid interfaces (blue — lines) exist between a solid region and an adjacent fluid region. Presently, these are between the discharge chamber wall and the plenum (`CW-P`), discharge chamber (`CW-C`), and downstream (`CW-D`). Fluid-fluid interfaces (white — lines) exist between two adjacent fluid regions, such as the plenum and the discharge chamber (`P-C`), the discharge chamber and the downstream region (`C-D`), as well as between each adjacent subregions (`D1` to `D6`) in the downstream region.

Inlet & outlet boundaries

At the inlet boundary (`i-P`), the required fluid boundary conditions are the species mass flow rate $\dot{m}$, static pressure p, and temperature T. The CFD simulations presented in this chapter are run using a range of $\dot{m}$ for both Ar and N_2. Table 3.4 lists $\dot{m}$ in both [SCCM] and [$\mathrm{kg\,s^{-1}}$] to highlight the different mass densities of the respective gas species.

In all the CFD simulations, p at the inlet boundary is calculated automatically from $\dot{m}$ instead of being artificially imposed, and the inflowing propellant is set to $T = 300\,\mathrm{K}$. At the outlet boundary (`o-D5` and `o-D6`), the required fluid boundary conditions are the backflow temperature $T_0 = 300\,\mathrm{K}$ and the static pressure p_0. Due to the small volume of the vacuum chamber and the limited pumping speed, the background pressure in the vacuum chamber rises depending on $\dot{m}$. The outlet boundary static pressure p_0 is set to the experimentally measured background pressure at the respective $\dot{m}$.

Table 3.4: CFD simulation inlet and outlet boundary conditions

Species	$\dot{m}$ [SCCM]	$\dot{m}$ [mg s^{-1}]	p_0 [Torr]
Ar	25	0.74	0.135
	50	1.49	0.219
	75	2.23	0.287
	100	2.97	0.349
	144	4.28	0.450
N_2	25	0.52	0.123
	50	1.04	0.199
	75	1.56	0.262
	100	2.08	0.320

Fluid-fluid interfaces

As fluids are homogeneous and not confined to a single fluid region or subregion, fluid-fluid interfaces do not require any setting, and merely serve to communicate information between the two adjacent fluid regions. The fluid-fluid boundaries are necessary for constructing fluid regions of different shapes in the manner described earlier in Section 2.2.2.

Solid-fluid interfaces

For the purposes of the present study, the most critical settings are for the solid-fluid interfaces, and especially at `CW-C`. Six different flow boundary conditions are considered: no slip, inviscid, $\alpha = 0$, $\alpha = 0.5$, $\alpha = 1$, and finally with the α_u and α_T tangential momentum and thermal accommodation coefficients recommended in Section 3.2.2. Note that the three cases with α refers to setting both α_u and α_T to the given value, while the final case uses the aforementioned specific α_u and α_T values. No artificial source term for heat is used at the solid-fluid interfaces. The chemical boundary condition is set to zero flux, meaning that species incident on the solid-fluid interfaces are unchanged.

A total of 63 CFD simulations are conducted. This includes running the six flow boundary condition cases for each of the nine $\dot{m}$ and corresponding p_0 cases listed in Table 3.4 for `PR-A`, plus an additional nine for each of the $\dot{m}$ cases run using the recommended α_u and α_T values for `PR-Z` ($6 \times 9 + 9 = 63$ total).

Wall boundaries

For the present CFD simulations, all wall boundaries are set to a fixed temperature of $T_{\text{ext}} = 300\,\text{K}$ to replicate the ambient laboratory environment. Wall boundaries adjacent to a fluid region act like solid-fluid interfaces, and the selected flow, heat, and chemical boundary conditions are likewise applied.

3.3.3 Initial conditions

The CFD simulations evolve from the set initial conditions towards steady state convergence. While it may be desirable to use initial conditions that closely resemble the converged solution, it is not strictly necessary as the present CFD modelling technique is sufficiently robust and highly convergent as demonstrated earlier in Figure 2.9. Although the computation time may be slightly longer using the present CFD modelling technique, time and labour is saved since a single coarsely designed set of initial conditions can be used across multiple similar CFD simulation cases with guaranteed convergence. For purely fluid CFD simulations, the initial conditions of the fluid regions require the setting of the fluid species, static pressure p, axial and radial flow velocities u_z and u_r, and temperature T. Table 3.5 lists the general recommendations for the initial conditions used for the 54 `PR-A` and 9 `PR-Z` CFD simulations presented in this chapter.

Table 3.5: CFD simulation initial conditions

Region	Species	p	$u_z\,[\text{m s}^{-1}]$	$u_r\,[\text{m s}^{-1}]$	$T\,[\text{K}]$
`P`	Ar or N_2	p_{st}	0	0	300
`C`		$\sim p_{\text{st}}/2$	~ 100	0	300
`D`		p_0	0	0	300
`CW`	–	–	–	–	300

The initial gas mixture in the contiguous fluid regions `P`, `C`, and `D` are set to be either pure Ar or pure N_2 depending on the particular study. In the plenum (`P`), the initial static pressures is set to the macroscopic plenum pressure p_{st} measured by the capacitance manometer mounted to the `PR-A` or `PR-Z` structure. p_{st} varies with $\dot{m}$ and also depends on the gas species as well as the diameter of the discharge chamber. The initial static pressure in the downstream region (`D`) is set to the outlet pressure p_0 which is equivalent to the background static pressure measured by the capacitance manometer mounted on the vacuum chamber.

An initial pressure of $\sim p_{\mathrm{st}}/2$ is used in the discharge chamber (C) to allow a smoother transition from P to D. As the flow is mostly stationary in P and most of D, the initial axial and radial flow velocities are set to zero in these regions. Only laminar flow is expected in C, so the initial axial flow velocity is set to $\sim 100\,\mathrm{m\,s^{-1}}$ here. This value is chosen as a compromise between mostly stationary flow near the entrance of C and supersonic flow at the exit of C. Finally, as the PR-A and PR-Z cold gas experiments are conducted in a $T_{\mathrm{ext}} = 300\,\mathrm{K}$ environment without any sources of heat, it is reasonable to set the initial temperatures of both the fluid and solid regions to 300 K. Some cooling is expected as the gas expands upon leaving the discharge chamber. This behaviour is captured in the converged solution without needing to account for it in the initial conditions.

3.4 Evaluating boundary conditions

The following sections demonstrate the effects of the different flow boundary conditions on the flow behaviour, in an effort to determine which accommodation coefficients α_u and α_T are most appropriate for the slip flow regime in PR. The CFD simulation results are verified against the theoretical understanding of fluid parameters, as well as against experimental measurements of p_{st} in both PR-A and PR-Z, with both Ar and N_2 cold gas propellants.

3.4.1 Cold gas stagnation pressure

In the experimental setup, the static pressure in PR and the vacuum chamber are both initially at the base pressure of $p \leq 1\,\mathrm{mTorr}$. After the mass flow controller is turned on, propellant gas entering the system at the set mass flow rate $\dot{m}$ over an infinitesimal time period causes the pressure to increase very slightly in the plenum, thereby momentarily setting up a small pressure difference across the discharge chamber between the plenum and the vacuum chamber. The system seeks to return to equilibrium through the movement of the gas from the plenum where the pressure is higher to the vacuum chamber where the pressure is lower. However, the rate at which the gas can be moved is dependent on the steepness of the pressure gradient along the discharge chamber. In the beginning while the pressure difference is still small, $\dot{m}$ through the discharge chamber is less than the imposed $\dot{m}$ into the plenum. Consequently, the pressure in the plenum continues to increase until the pressure gradient in the discharge chamber can support the full $\dot{m}$, at which point the system attains equilibrium. This happens on the time scale of a few seconds.

The stagnation pressure p_{st} in the plenum is a very unambiguous and spontaneous in-

dicator of the flow characteristics in PR. For the CFD simulations to be accurate, they must reproduce the same p_{st} observed in the experimental setup. Figure 3.3 plots the experimentally measured macroscopic plenum pressure p_{st} in PR-A (blue — line) and background static pressure p_0 in the vacuum chamber (black — line) against the set mass flow rate $\dot{m}$ of Ar. Due to the small volume of the 20 L six-way cross vacuum chamber and the limited pumping speed, the static pressure in the vacuum chamber increases with higher $\dot{m}$. At $\dot{m} \gtrsim 25$ SCCM, the increase is approximately linear for both p_{st} and p_0.

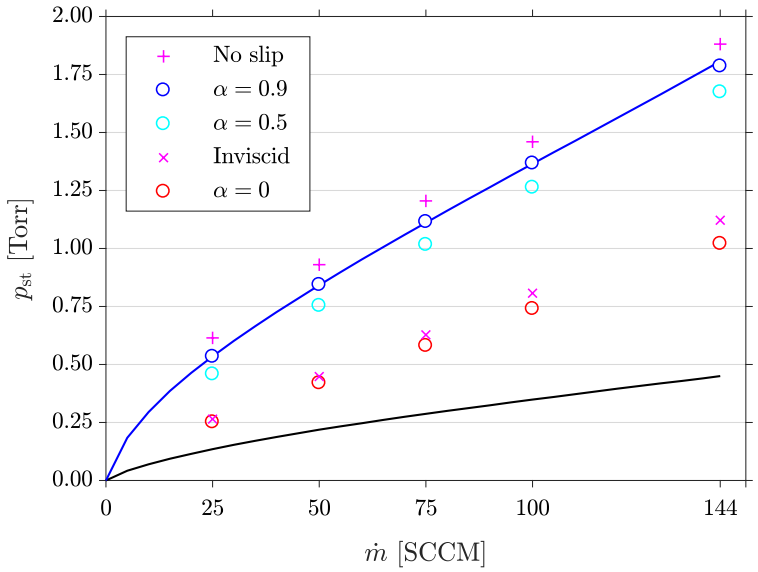

Figure 3.3: Markers represent the computed stagnation pressure p_{st} from CFD simulations performed with different boundary conditions. The blue — line is the experimentally measured macroscopic plenum pressure in PR-A, while the black — line is the background static pressure p_0 in the vacuum chamber.

The CFD simulations are performed with the outlet boundary static pressure p_0 set to the experimentally measured background pressure at the respective $\dot{m}$ (black — line). The computed steady state stagnation pressure p_{st} is calculated by integrating the pressure along the radius at the front of the plenum (left edge of P at $z = -30$ mm in Figure 3.2), and averaging over the whole circular area. Figure 3.3 plots the computed p_{st} for PR-A operating with Ar using no slip (magenta + markers), inviscid (magenta × markers), and slip boundary conditions with $\alpha = 0.9$ (blue ○ markers), $\alpha = 0.5$ (cyan ○ markers) and $\alpha = 0$ (red ○ markers). Here, α refers to setting both α_u and α_T to the listed value.

The computed p_{st} most accurately matches the experimentally measured p_{st} only when a slip boundary condition is used with the recommended values of $\alpha_u = 0.9$ and $\alpha_T = 0.9$ for

Ar (Section 3.2.2). p_{st} is very slightly overestimated with a no slip boundary condition, and severely underestimated with an inviscid boundary condition. Using $\alpha = 0$ produces results similar to the inviscid case, as expected. Notably, $\alpha = 0.5$ gives only slight underestimates, while the results for $\alpha = 1$ (not shown for clarity) are almost indistinguishable from those of $\alpha_u = 0.9$. This is expedient since it means that the CFD simulation results are insensitive to small errors in α for values close to unity.

CFD simulations using N_2 with the same set of flow boundary conditions have also been performed, and the trends are very similar. Likewise, using a slip boundary condition with the recommended values of $\alpha_u = 0.9$ and $\alpha_T = 0.8$ for N_2 (Section 3.2.2) produces the most accurate results in `PR-A`. The investigation is repeated for `PR-Z` in order to confirm that the accuracy of the slip regime CFD simulations are independent of the discharge chamber diameter. Figure 3.4 plots the computed p_{st} from the four sets of CFD simulations performed with Ar (○ markers) and N_2 (□ markers). The experimentally measured p_{st} in `PR-A` (blue lines), p_{st} in `PR-Z` (red lines), and p_0 in the vacuum chamber (black lines) are also plotted. Experiments run with Ar are represented by — lines, while those run with N_2 are represented by the –·– lines. The precise agreement between these CFD simulations and the experimental results validates the slip boundary condition as the most appropriate for `PR`, provided that the correct α_u and α_T values (Section 3.2.2) are used.

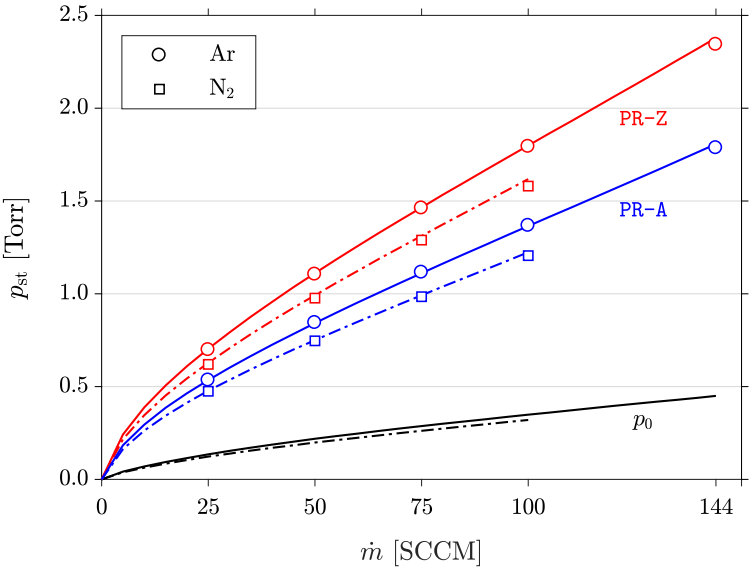

Figure 3.4: The computed stagnation pressure p_{st} from the `PR-A` (blue) and `PR-Z` (red) CFD simulations performed with both Ar (○ markers) and N_2 (□ markers) are in precise agreement with the experimentally measured p_{st} (blue and red — and –·– lines).

3.4.2 Fluid parameter profiles

Before concluding this chapter, it is worthwhile to briefly examine the profiles of a few fluid parameters generated by the different flow boundary conditions, namely those of the static pressure p (Figure 3.5), the axial velocity u_z (Figure 3.6), and the temperature T (Figure 3.7). The profiles are obtained from the `PR-A` CFD simulations run with $\dot{m} = 100\,\text{SCCM}$ of Ar, and plotted along the central z-axis from the front of the plenum at $z = -30\,\text{mm}$ to $z = 10\,\text{mm}$ just beyond the discharge chamber exit. The no slip boundary condition is represented by magenta — lines, while the inviscid boundary condition is represented by magenta -- lines. The slip boundary condition cases are represented by blue — lines for $\alpha = 0.9$, cyan — lines for $\alpha = 0.5$, and red — lines for $\alpha = 0$. The $\alpha = 1$ case is again almost identical to the $\alpha = 0.9$ case, and not shown for clarity.

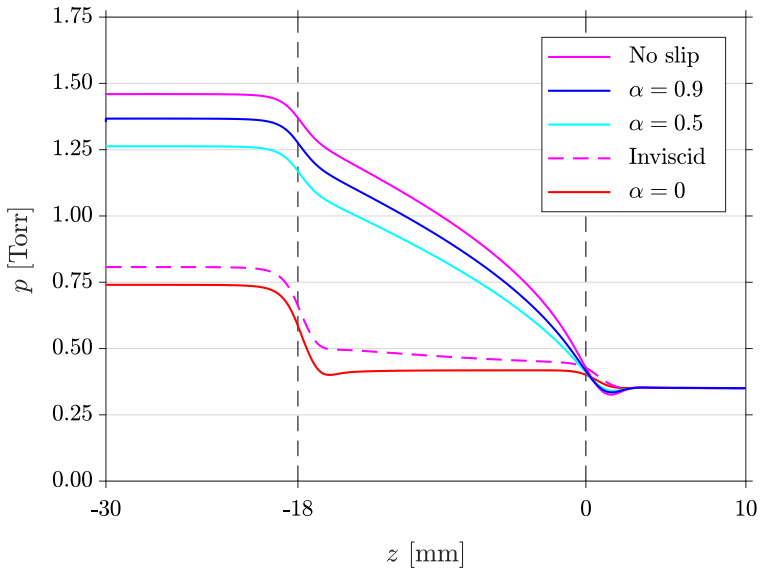

Figure 3.5: Static pressure p along the z-axis with different boundary conditions.

The inviscid and $\alpha = 0$ cases immediately stand out as being unphysical, especially for u_z (Figure 3.6) and T (Figure 3.7). The flat u_z profile in the discharge chamber indicates that the flow is unimpeded, since a boundary layer does not form under those conditions. This results in very low p in the plenum region, as seen in Figure 3.3, that are significantly under the experimentally measured p_{st}. The no slip, $\alpha = 0.9$, and $\alpha = 0.5$ cases on the other hand exhibit the correct properties of compressible flow, and are consistent with each other. Nonetheless, the selection of the value of α must be made according to the gas species used, as doing otherwise produces a small but noticeable discrepancy between the CFD simulation and experimental results.

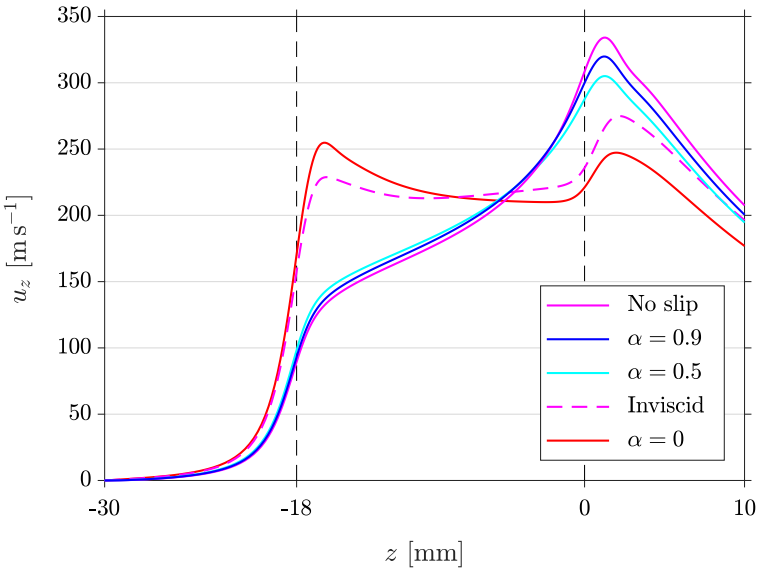

Figure 3.6: Axial velocity u_z along the z-axis with different boundary conditions.

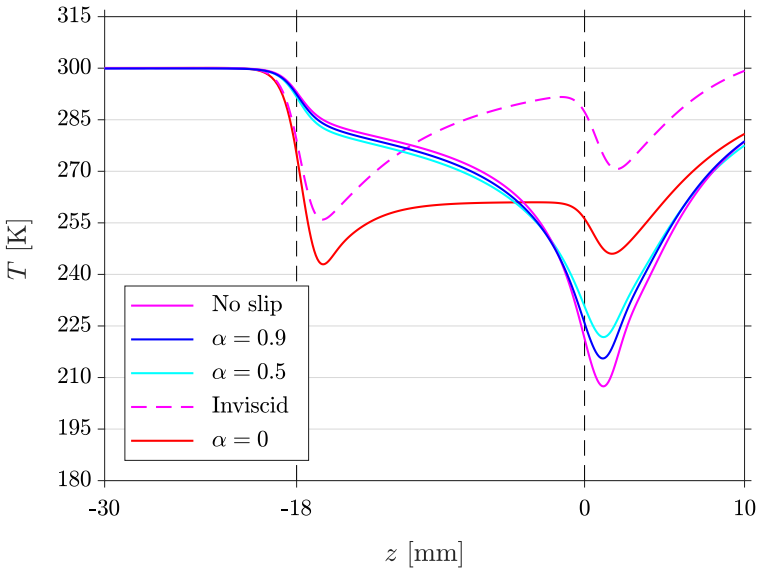

Figure 3.7: Temperature T along the z-axis with different boundary conditions.

Figure 3.8 plots the axial velocity u_z across the diameter of the discharge chamber exit in `PR-A` (along $z = 0\,\mathrm{mm}$) for the different flow boundary condition cases. As mentioned earlier, there is no boundary layer in the inviscid and $\alpha = 0$ cases, and u_z is essentially constant across the diameter of the discharge chamber. In the no slip case, u_z at the discharge chamber wall is exactly $0\,\mathrm{m\,s^{-1}}$ by definition. $u_{\mathrm{slip}} = 31.3\,\mathrm{m\,s^{-1}}$ introduced by $\alpha = 0.9$ produces a solution that best resembles the real behaviour in the main flow. For $\alpha = 0.5$, $u_{\mathrm{slip}} = 47.6\,\mathrm{m\,s^{-1}}$ is not significantly higher, but the flow behaviour is sufficiently deviant from the ideal case. However, $u_{\mathrm{slip}} = 94.5\,\mathrm{m\,s^{-1}}$ in the $\alpha = 0$ case significantly alters the

flow characteristics, and is not appropriate at the present operating conditions.

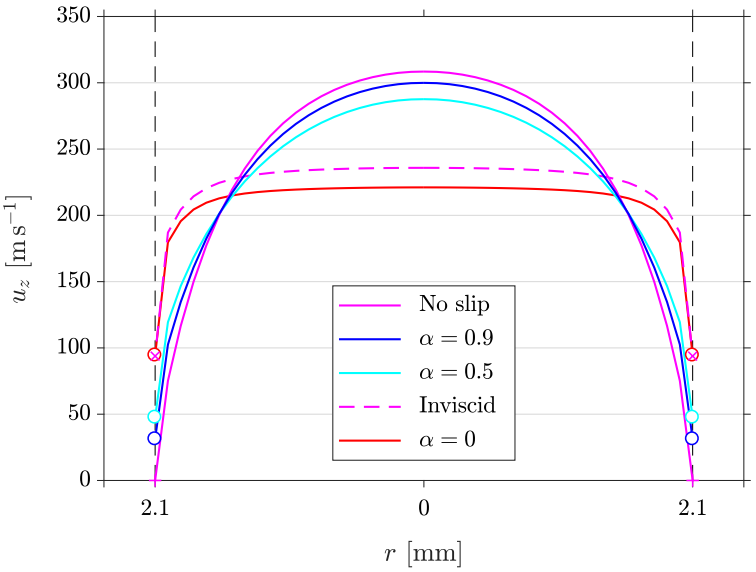

Figure 3.8: Axial velocity u_z across the diameter of the discharge chamber exit in PR-A with different boundary conditions. The slip velocity u_{slip} at the discharge chamber wall ($r = 2.1\,\text{mm}$) is indicated in each case: no slip (magenta + markers), $\alpha = 0.9$ (blue ○ markers), $\alpha = 0.5$ (cyan ○ markers), inviscid (magenta × markers), and $\alpha = 0$ (red ○ markers).

Since the experimentally measured α_u and α_T for most gases are close to unity (Tables 3.1 and 3.2), using $\alpha = 0$ is not a physically accurate representation of real gas flows [87] although the solution is mathematically consistent. Similarly, the applicability of inviscid flow solutions is limited only to frictionless flows (e.g. superfluid He II [110]), and the use of inviscid boundary conditions is therefore strongly discouraged for most conventional problems.

3.5 Chapter summary

This chapter covers slip regime rarefied gas dynamics from a theoretical, experimental, and modelling perspective. First, the theoretical concepts of mean free path, Knudsen number, and flow regimes are introduced, before a more extensive discussion of slip flow is explained with molecular dynamics. The slip boundary conditions are implemented using tangential momentum and thermal accommodation coefficients sourced from various experiments, which introduce a fictitious slip velocity and temperature jump at the wall.

Next, the volume, boundary, and initial conditions for the `PR` CFD simulation domain are detailed. 54 CFD simulations are performed with two geometries `PR-A` and `PR-Z` which have discharge chambers of different diameters, and with Ar and N_2 cold gas propellants. The stagnation pressure in the plenum is either overestimated or underestimated unless the correct tangential momentum and thermal accommodation coefficients are used, making it a clear indicator of the accuracy of the CFD simulation results. The fluid parameter profiles demonstrate how the pressure, axial velocity, and temperature vary along the length of the discharge chamber, while the axial velocity across the diameter of the discharge chamber exit reveals the slip velocity at the discharge chamber wall.

Chapter 4

Plasma-induced heating

Plasmas are used in a wide variety of applications across research, technology, and industry. While the properties of plasmas vary according to each specific application, there is a ubiquitous concern for the temperatures of the species present in the plasma. For weakly ionised plasmas in particular, the neutral gas temperature is an important parameter that can have significant influence on the characteristics of the plasma and its application. For example, microelectronics fabrication require stringent uniformity of the plasma which can be disrupted by gas flow, gradients and variations in gas temperature, as well as ion transport in regions with large voltage biases [111, 112]. Biomedical applications demand minimal heating for the treatment of heat-sensitive materials and soft tissues, and gas temperature affects the rate of chemical reactions as well as the proportion of desired reactive species in the plasma [113]. In electric propulsion, the aim is to maximise heating of the propellant with minimal input power so as to improve thrust performance over cold gas operation.

Many experimental techniques [114] have been used to characterise neutral gas temperatures in plasmas. These include using atomic line profiles from Doppler, Stark, and van der Waals broadening, as well as rotational spectroscopy [49, 51, 55, 115] and laser-induced fluorescence [116]. However, rotational spectroscopy becomes unreliable at low pressures [115, 116], and therefore computational modelling techniques are required. Though immensely useful, there are few successful plasma simulation models [111, 117] due to their complexity and the required expertise to produce accurate results. The biggest challenge lies in modelling plasmas in the $\sim$Torr pressure regime, where the pressure is high enough for collisional effects to be significant but still sufficiently rarefied for thermal conductivity to be ineffective. For example, a model [118] of a microwave plasma chemical vapour deposition (MPCVD) system in COMSOL utilised a heat conduction equation with a single volumetric heat source term for electron-neutral collisions. While the simulation results matched with experiments

at $p = 30\,\text{Torr}$, the gas temperature was overestimated at $p = 10\,\text{Torr}$.

In this chapter, collisional heating of the neutral background gas is modelled in the *Pocket Rocket* Ar discharge at $\sim 1\,\text{Torr}$ pressure. Ion transport and heat transfer mechanisms are examined, and two local models are developed to explain the spatially resolved temperature profile of the neutral gas. Ion-neutral charge exchange collisions are demonstrated to be the dominant heating mechanism. Heating is found to be significantly greater in the plasma bulk than the plasma sheath due to different plasma parameters and ion transport behaviours in these regions. The neutral gas maintains a peak temperature on the central z-axis since radial thermal conduction to the discharge chamber wall is ineffective in this rarefied laminar flow system. The following sections detail the input parameters for the CFD-plasma simulation before moving on to a discussion of the results.

4.1 Plasma chemistry

4.1.1 Plasma species

For the Ar CFD-plasma model, the plasma species considered include not only the ground state neutral Ar but also the excited species grouped under $\text{Ar}(4\text{s}_\text{m})$, $\text{Ar}(4\text{s}_\text{r})$, and $\text{Ar}(4\text{p})$, as well as the positive Ar^+ ion and the electron e^-.

Table 4.1 lists the six plasma species considered for the Ar CFD-plasma model as well as the individual excitation levels grouped under the three excited species. The average excitation energy of the individual excitation levels in each group is used for $\text{Ar}(4\text{s}_\text{m})$, $\text{Ar}(4\text{s}_\text{r})$, and $\text{Ar}(4\text{p})$ while the ionisation energy of Ar^+ is as listed. Accurate values for the atomic energy levels [119] and ionisation potential [120, 121] are necessary for calculating the enthalpy:

$$h = k_\text{B}\left(a_1 T + \frac{a_2 T^2}{2} + \frac{a_3 T^3}{3} + \frac{a_4 T^4}{4} + \frac{a_5 T^5}{5} + a_6\right) \tag{4.1}$$

where k_B is the Boltzmann constant, T is the temperature of the fluid, and a_n are the JANAF coefficients [122]. For Ar, a_6 encodes the excitation and ionisation energies as:

$$a_6 = \left(\frac{q_\text{e}}{k_\text{B}} \cdot \Delta E\right) - 745.375\,\text{K} \tag{4.2}$$

where q_e is the elementary charge and ΔE is the difference in energy between the excited or ionic species and the ground state species in units of [eV]. Two sets of a_n are used for two distinct but contiguous temperature ranges; the first set is valid for $200\,\text{K} \leq T \leq 1000\,\text{K}$, and the second set is valid for $1000\,\text{K} \leq T \leq 6000\,\text{K}$. Note that the temperature constant in (4.2) may be different depending on the considered ground state species and the temperature range.

Table 4.1: Ar plasma species

Species	Description	Level	Energy [eV]	Ref.
Ar	Ground state neutral atom	–	–	–
$Ar(4s_m)$	Metastable levels	$4s[3/2]_2$	11.548	[123]
		$4s'[1/2]_0$	11.723	[123]
$Ar(4s_r)$	Radiatively coupled levels	$4s[3/2]_1$	11.623	[123]
		$4s'[1/2]_1$	11.828	[123]
Ar(4p)	4p manifold levels	$4p[1/2]_1$	12.907	[124]
		$4p[5/2]_3$	13.076	[124]
		$4p[5/2]_2$	13.095	[124]
		$4p[3/2]_1$	13.153	[124]
		$4p[3/2]_2$	13.172	[124]
		$4p[1/2]_0$	13.273	[124]
		$4p'[3/2]_1$	13.283	[124]
		$4p'[3/2]_2$	13.302	[124]
		$4p'[1/2]_1$	13.328	[124]
		$4p'[1/2]_0$	13.480	[124]
Ar^+	Positive ion	–	15.760	[120]
e^-	Electron	–	–	–

4.1.2 Plasma chemical reaction set

Volumetric reactions

The six plasma species Ar, $Ar(4s_m)$, $Ar(4s_r)$, Ar(4p), Ar^+, and e^- constitute a total of 29 individual elementary volumetric reactions, listed as `R1` to `R29` in Tables 4.2a, 4.2b, and 4.2c, collected from various sources [123–134].

The reaction rates are given in the Arrhenius form:

$$k_{\mathtt{R}} = A \cdot p^m T_{\mathtt{R}}^n \cdot e^{-E_a/(k_B T_{\mathtt{R}})} \tag{4.3}$$

where A, m, n, and the activation temperature E_a/k_B are constants for each reaction, while $T_{\mathtt{R}}$ represents either the electron temperature T_e for electron impact reactions, or the gas temperature T for heavy species reactions. For the present Ar plasma volumetric chemical reaction set, the reaction rates are not dependent on the static pressure p, and many of the listed reactions are also not dependent on $T_{\mathtt{R}}$. Certain reactions (`R22`, `R25`, `R28`, and `R29`) do

Table 4.2a: Ar plasma volumetric chemical reaction set

No.	Reaction	Rate coefficient [$m^3\,s^{-1}$]	Ref.
Elastic collision			
R1	$Ar + e^- \longrightarrow Ar + e^-$	Collision cross section	[125, 126]
Excitation / deexcitation			
R2	$Ar + e^- \longrightarrow Ar(4s_m) + e^-$	Collision cross section	[123, 125]
R3	$Ar + e^- \longrightarrow Ar(4s_r) + e^-$	Collision cross section	[123, 125]
R4	$Ar + e^- \longrightarrow Ar(4p) + e^-$	Collision cross section	[124, 125]
R5	$Ar(4s_m) + e^- \longrightarrow Ar + e^-$	$4.3 \times 10^{-16} \cdot T_e^{0.74}$	[128, 129]
R6	$Ar(4s_m) + e^- \longrightarrow Ar(4s_r) + e^-$	3.7×10^{-13}	[128, 130]
R7	$Ar(4s_m) + e^- \longrightarrow Ar(4p) + e^-$	$8.9 \times 10^{-13} \cdot T_e^{0.51} \cdot e^{-1.59/T_e}$	[128, 131]
R8	$Ar(4s_r) + e^- \longrightarrow Ar + e^-$	$4.3 \times 10^{-16} \cdot T_e^{0.74}$	[128, 129]
R9	$Ar(4s_r) + e^- \longrightarrow Ar(4s_m) + e^-$	9.1×10^{-13}	[128, 130]
R10	$Ar(4s_r) + e^- \longrightarrow Ar(4p) + e^-$	$8.9 \times 10^{-13} \cdot T_e^{0.51} \cdot e^{-1.59/T_e}$	[128, 131]
R11	$Ar(4p) + e^- \longrightarrow Ar + e^-$	$3.9 \times 10^{-16} \cdot T_e^{0.71}$	[128, 129]
R12	$Ar(4p) + e^- \longrightarrow Ar(4s_m) + e^-$	$3.0 \times 10^{-13} \cdot T_e^{0.51}$	[128, 129]
R13	$Ar(4p) + e^- \longrightarrow Ar(4s_r) + e^-$	$3.0 \times 10^{-13} \cdot T_e^{0.51}$	[128, 129]
Quenching			
R14	$2\,Ar(4s_m) \longrightarrow 2\,Ar$	2.0×10^{-13}	[128]
R15	$Ar(4s_m) + Ar \longrightarrow 2\,Ar$	2.1×10^{-21}	[128, 132]

Table 4.2b: Ar plasma volumetric chemical reaction set (cont'd)

No.	Reaction	Rate coefficient [s^{-1}]	Ref.
Radiative decay			
R16	$Ar(4s_r) \longrightarrow Ar + \hbar\omega$	1.0×10^5	[128, 133]
R17	$Ar(4p) \longrightarrow Ar + \hbar\omega$	3.2×10^7	[128, 129]
R18	$Ar(4p) \longrightarrow Ar(4s_m) + \hbar\omega$	3.0×10^7	[128, 134]
R19	$Ar(4p) \longrightarrow Ar(4s_r) + \hbar\omega$	3.0×10^7	[128, 134]

not have explicitly documented rate coefficients, and so their reaction rates are estimated using the closest similar reaction.

Reaction rates for electron-neutral elastic collision (R1), excitation from the ground state (R2, R3, and R4), and direct ionisation from the ground state (R20) are calculated using

Table 4.2c: Ar plasma volumetric chemical reaction set (cont'd)

No.	Reaction	Rate coefficient $[\mathrm{m^3\,s^{-1}}]$	Ref.
Direct / stepwise / Penning ionisation			
R20	$\mathrm{Ar} + \mathrm{e^-} \longrightarrow \mathrm{Ar^+} + 2\,\mathrm{e^-}$	Collision cross section	[125, 127]
R21	$\mathrm{Ar(4s_m)} + \mathrm{e^-} \longrightarrow \mathrm{Ar^+} + 2\,\mathrm{e^-}$	$6.8 \times 10^{-15} \cdot T_\mathrm{e}^{0.67} \cdot e^{-4.20/T_\mathrm{e}}$	[128, 131]
R22	$\mathrm{Ar(4s_r)} + \mathrm{e^-} \longrightarrow \mathrm{Ar^+} + 2\,\mathrm{e^-}$	$6.8 \times 10^{-15} \cdot T_\mathrm{e}^{0.67} \cdot e^{-4.20/T_\mathrm{e}}$	R21
R23	$\mathrm{Ar(4p)} + \mathrm{e^-} \longrightarrow \mathrm{Ar^+} + 2\,\mathrm{e^-}$	$1.8 \times 10^{-13} \cdot T_\mathrm{e}^{0.61} \cdot e^{-2.61/T_\mathrm{e}}$	[128, 131]
R24	$2\,\mathrm{Ar(4s_m)} \longrightarrow \mathrm{Ar^+} + \mathrm{Ar} + \mathrm{e^-}$	6.4×10^{-16}	[128, 130]
R25	$2\,\mathrm{Ar(4s_r)} \longrightarrow \mathrm{Ar^+} + \mathrm{Ar} + \mathrm{e^-}$	6.4×10^{-16}	R24
R26	$2\,\mathrm{Ar(4p)} \longrightarrow \mathrm{Ar^+} + \mathrm{Ar} + \mathrm{e^-}$	5.0×10^{-16}	[128, 131]
R27	$\mathrm{Ar(4s_m)} + \mathrm{Ar(4s_r)} \longrightarrow \mathrm{Ar^+} + \mathrm{Ar} + \mathrm{e^-}$	2.1×10^{-15}	[128, 132]
R28	$\mathrm{Ar(4s_m)} + \mathrm{Ar(4p)} \longrightarrow \mathrm{Ar^+} + \mathrm{Ar} + \mathrm{e^-}$	5.0×10^{-16}	R26
R29	$\mathrm{Ar(4s_r)} + \mathrm{Ar(4p)} \longrightarrow \mathrm{Ar^+} + \mathrm{Ar} + \mathrm{e^-}$	5.0×10^{-16}	R26

collision cross sections σ_R [123–127]. Note that $\sigma_\mathrm{R2} = \sigma_{4\mathrm{s}[3/2]_2} + \sigma_{4\mathrm{s}'[1/2]_0}$ since the reaction rate of R2 represents the total probability of excitation from ground state Ar to either $\mathrm{Ar(4s[3/2]_2)}$ or $\mathrm{Ar(4s'[1/2]_0)}$ excitation levels which are both considered to be $\mathrm{Ar(4s_m)}$. Similarly, $\sigma_\mathrm{R3} = \sigma_{4\mathrm{s}[3/2]_1} + \sigma_{4\mathrm{s}'[1/2]_1}$ for excitation from Ar to $\mathrm{Ar(4s_r)}$, and $\sigma_\mathrm{R4} = \sigma_{4\mathrm{p}[1/2]_1} + \ldots + \sigma_{4\mathrm{p}'[1/2]_0}$ for excitation from Ar to Ar(4p). Figure 4.1 plots σ_R1 (blue — line) and σ_R20 (red — line) over the range of electron energy $k_\mathrm{B}T_\mathrm{e}$ for which experimental data is available. Figure 4.2 plots σ_R2 (blue — line), σ_R3 (red — line), and σ_R4 (black — line) as the sum of the collision cross sections of the excitation levels grouped under the respective excited species (blue, red, and black – · – lines). While cross section data for higher excitation levels (e.g. Ar(3d), Ar(5p), Ar(4d), and Ar(6s)) are available, these rarer species are omitted so as to limit the total number of reactions in the volumetric reaction set. This ensures that the CFD-plasma simulations remain tractable as the computation time typically scales with the square of the total number of reactions.

Surface reactions

Surface reactions are use to effect the deexcitation of the three excited species $\mathrm{Ar(4s_m)}$, $\mathrm{Ar(4s_r)}$, and Ar(4p), and $\mathrm{Ar^+}$ ion recombination at the plasma-facing solid surfaces in the PR simulation domain. For simplicity, a sticking coefficient of unity is used for each of the four elementary surface reactions, transforming any incident $\mathrm{Ar(4s_m)}$, $\mathrm{Ar(4s_r)}$, Ar(4p), and $\mathrm{Ar^+}$ species into the ground state neutral Ar.

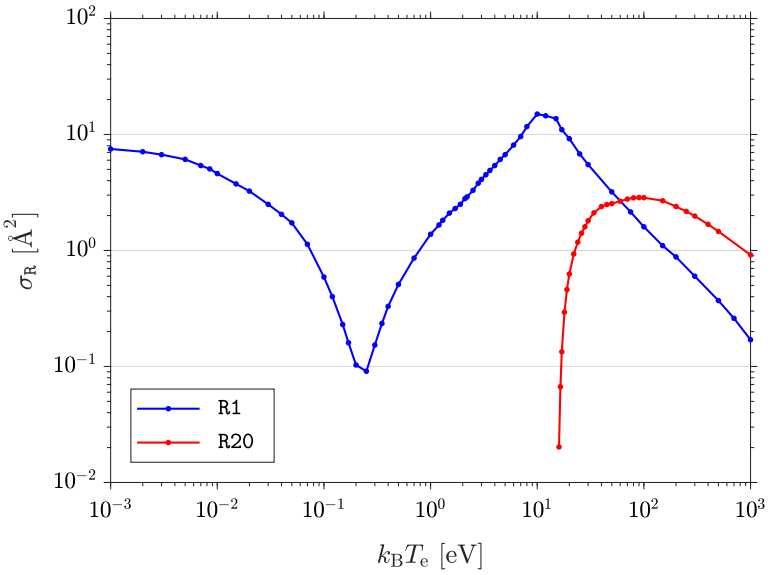

Figure 4.1: Cross sections for electron-neutral elastic collisions (R1) and direct ionisation (R20).

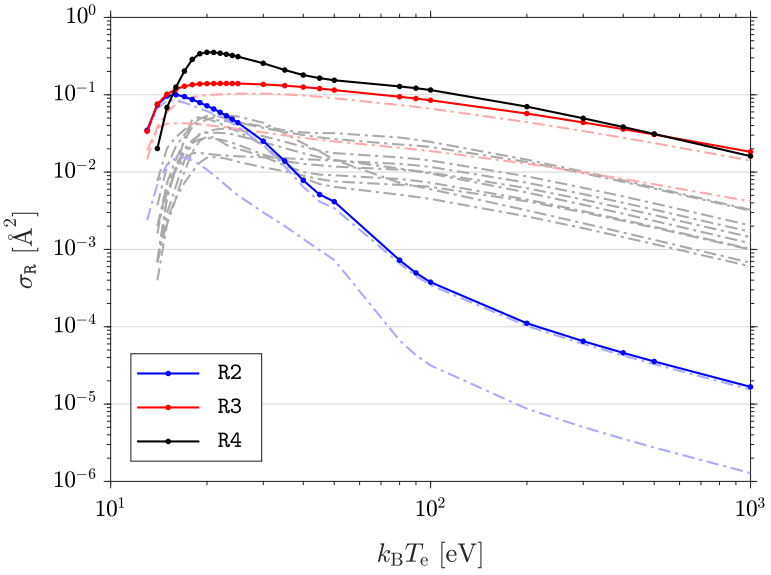

Figure 4.2: Aggregate cross sections for excitation reactions R2, R3, and R4. The light coloured -·- lines represent the cross section of each excitation reaction to the various energy levels of Ar($4s_m$), Ar($4s_r$), and Ar(4p) (Table 4.1).

4.2 Plasma dynamics

Plasma dynamics involve solving for electron, ion, and neutral dynamics that are separate from fluid dynamics. The equations for most of these processes are documented in [60, 62, 66] and extensively in other literature [135], and are not repeated here.

For electrons, this includes particle and energy conservation, drift and diffusion transport, diffusivity and mobility as well as ohmic, inductive, and collisionless stochastic sheath heating. For stochastic heating in particular, CFD-ACE+ uses a 'self-aware' approach that automatically detects sheath regions near powered electrode surfaces. In PR, ohmic heating is dominant due to the presence of a steep potential gradient in the powered sheath, while stochastic heating is comparatively negligible at the $p \sim 1\,\text{Torr}$ operating pressure. Given the high collision frequency in the high pressure discharge, the electron energy distribution function (EEDF) is assumed to be a single temperature Maxwellian with a mean electron temperature of $3/2 \cdot T_\text{e}$. In addition to the usual electron dynamics, e^- species also contribute to the fluid static pressure by the electron partial pressure:

$$p_\text{e} = n_\text{e} k_\text{B} T_\text{e} \tag{4.4}$$

where n_e is the electron number density and $k_\text{B}T_\text{e}$ is the electron energy.

Ion dynamics include drift and diffusion transport, diffusivity and mobility, as well as inertia. The most important processes are the heat transfer mechanisms from the plasma species Ar^+ and e^- to the neutral Ar species, and from Ar^+ to the plasma-facing solid surfaces in PR. Three heat transfer mechanisms are considered in the CFD-plasma model, namely ion-neutral charge exchange collisions, electron-neutral elastic collisions, and ion bombardment of surfaces. These processes are discussed in more detail in Section 4.5, with reference to the CFD-plasma simulation results.

4.3 CFD-plasma simulation setup

The CFD-plasma simulation is performed using the original PR simulation mesh, with all the solid and fluid volume regions. The different types of boundaries (coloured lines) are highlighted in Figure 4.3. Modelling plasmas requires the `Electric` and `Plasma` modules in addition to the `Flow`, `Heat Transfer`, and `Chemistry` modules used for the CFD simulations presented in Chapter 3. The additional volume and boundary conditions handled by the `Chemistry`, `Electric`, and `Plasma` modules are detailed in the following sections.

4.3.1 Volume conditions

Solid regions

The solid material physical properties (Section 2.3.1) of Al_2O_3, Cu, Macor, and Al, namely the mass density ρ, thermal conductivity k, and specific heat c_p, are loaded as volume con-

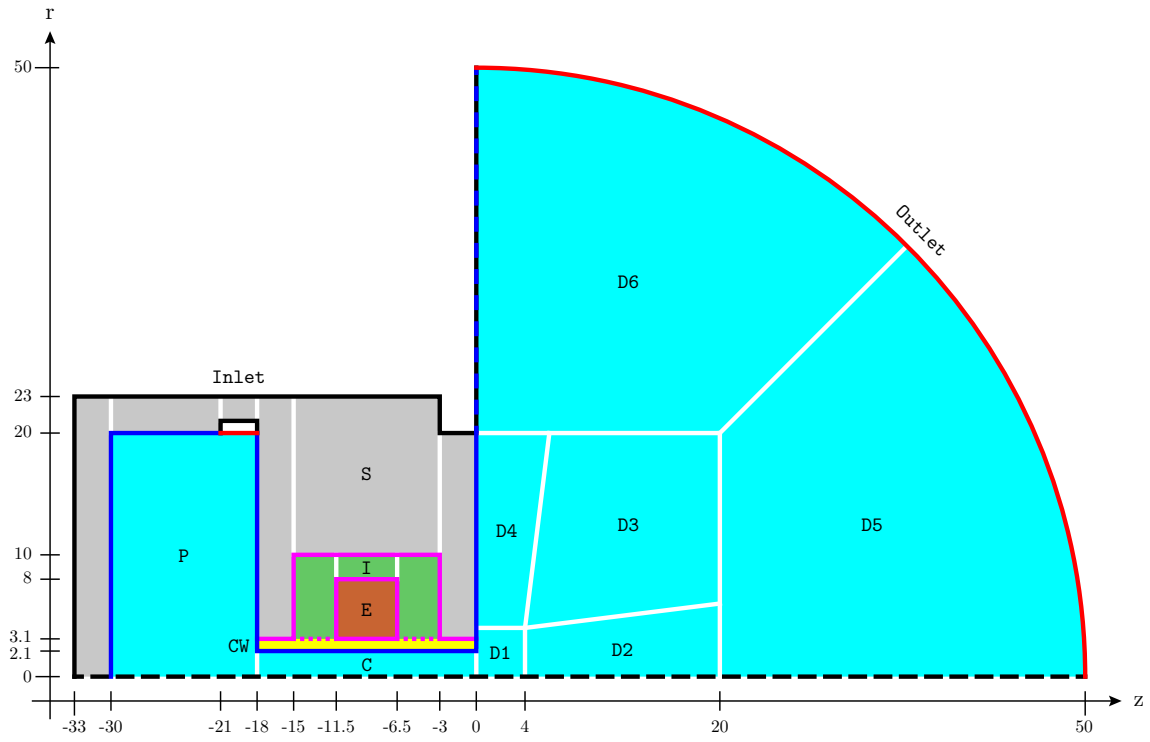

Figure 4.3: PR CFD-plasma simulation domain. Fluid regions (aqua): plenum (P), discharge chamber (C), and downstream (D). Solid regions: Al structure (S, grey), Macor insulation (I, dark green), Cu powered electrode (E, brown), and Al_2O_3 discharge chamber wall (CW, yellow). Boundaries: inlet and outlet (red — lines), axis of symmetry (black -- line), wall (black — lines), solid-solid interfaces (magenta — and ····· lines), and solid-plasma interfaces (blue — lines).

ditions for the discharge chamber wall (CW, yellow), powered electrode (E, brown), insulation (I, dark green), and structure (S, grey) solid regions respectively. Additionally, the electrical resistivity ρ_{el} (2.7) for the electrically conductive Cu and Al, and the relative permittivity ε_{r} for the dielectric Al_2O_3 and Macor are necessary for the Electric module. No artificial source term for heat is used in these solid regions.

Plasma regions

The plasma regions (aqua) are the same as the fluid regions, and the CFD-plasma volume conditions are a superset of the CFD volume conditions discussed earlier in Section 3.3.1.

Other than the parameters mentioned in Section 4.1.1 (JANAF coefficients a_n and the excitation and ionisation energies ΔE), the heavy species $Ar(4s_m)$, $Ar(4s_r)$, $Ar(4p)$, and Ar^+ share the same physical properties as Ar, which are loaded as volume conditions for the

plasma regions `P`, `C`, and `D`. These include all of the fluid species physical properties mentioned in Section 2.3.2, namely the molecular mass m, mass density ρ, dynamic viscosity μ, thermal conductivity k, specific heat at constant pressure c_p, mass diffusivity D, Lennard-Jones characteristic energy ϵ_σ, Lennard-Jones collision diameter σ [82], relative permittivity ε_r, charge exchange cross section σ_q, and polarisability volume α' [83]. The electrical resistivity of Ar is set to a constant value of $\rho_\mathrm{el} = 10^6\,\Omega\,\mathrm{m}$ such that the electrical conductivity is a small but nonzero value. Gas mixing rules take effect as there are multiple heavy species present, and uses the parameters in the physical properties database for each heavy species. The Ar plasma volumetric chemical reaction set listed in Tables 4.2a, 4.2b, and 4.2c take effect in the plasma regions. No artificial source terms for mass, velocity, heat, electron energy, or ionisation are used in the plasma regions.

4.3.2 Boundary conditions

The CFD-plasma boundary conditions are a superset of the CFD boundary conditions discussed earlier in Section 3.3.2. In addition to the fluid parameters, the boundary conditions now include the electrostatic and plasma parameters handled by the `Electric`, `Chemistry`, and `Plasma` modules. The same five types of boundaries are present: inlet (`i`), outlet (`o`), symmetry, wall (`w`), and interface. While the inlet (`i-P`, red — line) and outlet (`o-D5` and `o-D6`, red — arc) boundaries of the CFD-plasma simulation domain (Figure 4.3) are the same as those in the CFD simulation domain (Figure 3.2), the axis of symmetry (black `--` line) in the CFD-plasma simulation domain extends to $z = -33\,\mathrm{mm}$. The wall (black — line) and interface boundaries are also different due to the inclusion of the powered electrode (`E`), insulation (`I`), and structure (`S`) solid regions.

Plasma-plasma interfaces

Like fluid-fluid interfaces, plasma-plasma interfaces (white — lines within aqua) do not require any setting, and merely serve to communicate information between the two adjacent plasma regions. Critical plasma regions such as the discharge chamber (`C`) are ideally kept whole and not broken up into subregions, since the presence of redundant plasma-plasma interfaces may give rise to numerical anomalies and therefore produce inaccurate results.

Solid-solid interfaces

There are three kinds of solid-solid interfaces. The first is the interface between solid subregions within a contiguous solid region of the same material (white — lines within `S` and `I`).

Like fluid-fluid interfaces, this kind of solid-solid interfaces do not require any setting, but are necessary for constructing the geometry of the respective solid regions.

The second is the interface between adjacent dielectric solid regions of different materials (magenta ····· lines), namely `CW-I` between the Al_2O_3 discharge chamber wall and the Macor insulation. For this kind of interface, the surface electric potential is set with a dielectric boundary condition, whereby CFD-ACE+ solves for the surface electric potential and surface charge.

The third is the interface between an electrically conductive solid region and a dielectric solid region (magenta — lines). In this case, the surface electric potential of the electrically conductive solid region takes priority. For `S-CW` and `S-I`, the surface electric potential is set to $\Phi_{\mathrm{gnd}} = 0\,\mathrm{V}$ since the surfaces of the dielectric discharge chamber wall and insulation are in contact with the electrically grounded structure. For `E-CW` and `E-I`, the surface electric potential of the powered electrode is set to a sinusoidal waveform $\Phi_{\mathrm{pwr}} = V_{\mathrm{pwr}} \sin(\omega t)$, with voltage amplitude $V_{\mathrm{pwr}} = 300\,\mathrm{V}$ and angular frequency $\omega = 2\pi \cdot 13.56\,\mathrm{MHz}$.

Solid-plasma interfaces

There are two kinds of solid-plasma interfaces (blue — lines), depending on whether the plasma-facing solid surface is electrically conductive or dielectric. The surface of the structure around the plenum (`S-P`) and facing the downstream region (`S-D1`, and `S-D4`) belong to the former kind, and the surface electric potential is set to $\Phi_{\mathrm{gnd}} = 0\,\mathrm{V}$. The surface of the discharge chamber wall facing the plenum, (`CW-P`), discharge chamber (`CW-C`), and the downstream region (`CW-D1`) belong to the latter kind, and the surface electric potential is set with a dielectric boundary condition.

The slip boundary condition is applied to all solid-plasma interfaces, with the recommended $\alpha_u = 0.9$ and $\alpha_T = 0.9$ tangential momentum and thermal accommodation coefficients for Ar. The chemical boundary condition is set to induce the deexcitation of $\mathrm{Ar}(4s_m)$, $\mathrm{Ar}(4s_r)$, and Ar(4p) as well as the recombination of Ar^+ to ground state neutral Ar. Plasma boundary conditions required are the electron number density n_e and electron energy $k_B T_e$, which are set to a thermal flux balance boundary condition, while a secondary electron emission coefficient of $\gamma_{e'} = 0.1$ is used for all plasma-facing solid surfaces, regardless of the material. Presently, using this value of $\gamma_{e'}$ in the CFD-plasma simulation produces results that are in good agreement with `PR` experiments at $V_{\mathrm{pwr}} = 300\,\mathrm{V}$, but may require adjustment for different V_{pwr}, discharge impedances $Z_{\mathtt{PR}}$, or operating pressures p. No artificial source term for heat is used at the solid-plasma interfaces.

Wall boundaries

The wall boundaries for the CFD-plasma simulation domain are along the external edges of the structure (`w-S`, black — line). Instead of setting an artificially fixed temperature, the wall boundaries are allowed to freely radiate and exchange thermal energy with the surrounding air by convection, in an ambient $T_{\text{ext}} = 300\,\text{K}$ atmospheric pressure environment that replicates the laboratory condition of the `PR` experiment. This allows for more accurate accounting of energy throughout the simulation domain, and also error checking as the temperature of the `PR` structure is not expected to rise by any significant amount during the time frame of the simulation. A grey body emissivity coefficient of 0.1 is used for the Al structure, while a heat transfer coefficient of $10\,\text{W}\,\text{m}^{-2}\,\text{K}^{-1}$ is used for the ambient air. These values are rough estimates, and are negligibly consequential to the CFD-plasma simulation results. Finally, as `w-S` borders the electrically grounded structure, the surface electric potential is set to $\Phi_{\text{gnd}} = 0\,\text{V}$.

The left edge of `D6` (blue and black `--` line) is also considered to be a wall boundary. However, as it is adjacent to a plasma region, the boundary conditions of `w-D6` resemble that of a solid-plasma interface, and the same slip, chemical, and plasma boundary conditions are applied. On a spacecraft, this area is likely to be a metallic panel attached to the structure, and therefore the surface electric potential is set to $\Phi_{\text{gnd}} = 0\,\text{V}$. The surface temperature of `w-D6` is allowed to float so as to not place any artificial constraints on the plasma region `D6`.

Inlet & outlet boundaries

At the inlet boundary (`i-P`), the required fluid boundary conditions are the species mass flow rate $\dot{m}$, static pressure p, and temperature T. The CFD-plasma simulation presented in this chapter is run using $\dot{m} = 100\,\text{SCCM}$ of Ar at $T = 300\,\text{K}$, and an automatically calculated p. At the outlet boundary (`o-D5` and `o-D6`), the required fluid boundary conditions are the background pressure $p_0 = 0.349\,\text{Torr}$ and the backflow temperature $T_0 = 300\,\text{K}$. These settings are the same as those used for the CFD simulations presented in Chapter 3.

It is also necessary to specify the surface electric potential at the inlet and outlet boundaries. The inlet boundary traces out a cylinder when the simulation mesh is rotated about the axis of symmetry. Since most of this area in the `PR` device is the surface of the electrically grounded structure, the inlet boundary is set to a fixed surface electric potential of $\Phi_{\text{gnd}} = 0\,\text{V}$. For the outlet boundary, the surface electric potential is allowed to float such that the normal electric field is zero, since there is no object downstream that influences the electric potential Φ.

The plasma boundary conditions for the inlet boundary `i-P` are the same as those used for the solid-plasma interfaces `S-P`. For the outlet boundary on the other hand, the electron energy $k_B T_e$ and the electron number density n_e are allowed to float such that the normal gradient is zero at the outlet boundary, thus placing no artificial constraints on either of these parameters.

4.3.3 Initial conditions

While it is possible to use the converged steady state solution of a CFD simulation as the initial condition of a CFD-plasma simulation, plasma parameters that are absent in the CFD simulation nonetheless have to be configured separately. Additionally, starting a transient CFD-plasma simulation from converged steady state solution discourages deviation from the initial state, and may cause certain fluid and plasma parameters to become artificially constrained or frozen. Hence, the CFD-plasma modelling technique is designed in the manner detailed in Section 2.2.4.

The CFD-plasma simulations are first set to start from static initial conditions to produce a quick but inaccurate seed solution. The fluid parameters in these initial conditions are the same as those listed in Table 3.5, except the discharge chamber (`C`) is seeded with a mixture consisting of 99.9996 % Ar and 0.0001 % each of $Ar(4s_m)$, $Ar(4s_r)$, Ar(4p), and Ar^+ by concentration, and e^- is set to the same number density as Ar. The electron energy is set to 1 eV in the plasma regions (`P`, `C`, and `D`), while the electric potential is set to 0 V everywhere. These are simple and straightforward initial conditions, and no parameters have been cherry-picked. The convergence of the CFD-plasma simulation is entirely dependent on the CFD-plasma simulation algorithm (Figure 2.10), thereby ensuring that the converged final solution is impartial to the selected initial conditions.

4.4 Validating benchmark parameters

Several metrics are used to validate the accuracy of the CFD-plasma simulation with respect to the `PR` experiment. These are the stagnation pressure in the plenum, the power supplied to the discharge, the ion density, and the neutral gas temperature. The close agreement of these parameters gives confidence to the other parameters from the CFD-plasma simulation results that cannot be experimentally measured.

4.4.1 Stagnation pressure

Figure 4.4 plots the experimentally measured stagnation pressure $p_{\mathrm{st}}(t)$ in the PR plenum during plasma operation. Initially, Ar is flowing through PR at a mass flow rate of $\dot{m} = 100\,\mathrm{SCCM}$, and $p_{\mathrm{st}}(t)$ holds steady at the cold gas stagnation pressure of 1.365 Torr. The RF power is switched on precisely at $t = 0\,\mathrm{s}$, putting $V_{\mathrm{pwr}} = 300\,\mathrm{V}$ on the powered electrode. The plasma is ignited in the discharge chamber, and $p_{\mathrm{st}}(t)$ in the plenum rises almost instantaneously. The hot propellant and the discharge chamber wall moves towards thermal equilibrium over the next $\sim 10\,\mathrm{s}$, and this is reflected in the gradient of $p_{\mathrm{st}}(t)$ approaching a constant value. The entire PR device gradually heats up as plasma operation continues, and the increase in temperature is again reflected in the slow rise of $p_{\mathrm{st}}(t)$ on the $\sim 100\,\mathrm{s}$ time scale.

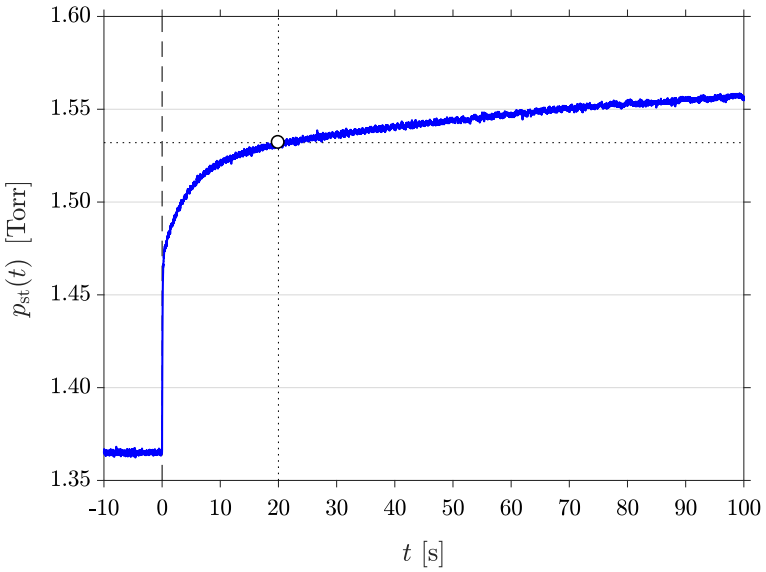

Figure 4.4: Measured stagnation pressure $p_{\mathrm{st}}(t)$ during PR plasma operation (blue — line). The black ○ marker shows the computed $p_{\mathrm{st}} = 1.532\,\mathrm{Torr}$ from the CFD-plasma simulation, corresponding to $t \approx 20\,\mathrm{s}$ after plasma ignition.

Unlike temperature, p_{st} can be measured spontaneously, unambiguously, and with high precision and temporal resolution. The capacitance manometer used in the experimental setup is accurate to 0.25 % of the reading [136], and is able to log measurements at 100 Hz. p_{st} is therefore a very good proxy for inferring the propellant temperature T in PR. However, there are two criteria to verify before this is possible. First, the temporal evolution of the experimentally measured $p_{\mathrm{st}}(t)$ must be the same or at least comparable to the experimentally measured $T(t)$. Second, the computed p_{st} from the CFD-plasma simulation must match

the experimentally measured p_{st}. Only when these two conditions are met can the computed neutral gas temperature be considered to be an accurate estimate of the propellant temperature in reality.

Plotting the time axis in logarithmic scale (Figure 4.5) enables the initial rise of $p_{st}(t)$ to be examined more closely. There is a rapid increase in $p_{st}(t)$ in the first ~ 0.1 s after plasma ignition due to the fast heating via ion-neutral charge exchange collisions. $p_{st}(t)$ then levels off until $t \sim 1$ s. The plateauing indicates that the background neutral gas has attained local thermal equilibrium, but the discharge chamber wall is still close to the initial temperature of $T = 300$ K. $p_{st}(t)$ resumes a linear increase thereafter as the discharge chamber wall heats up over time. The temporal evolution of the measured $p_{st}(t)$ in Figure 4.5 has the same shape and time scales as the previously measured $T(t)$ of N_2 propellant in the PR discharge obtained via rotational spectroscopy [55, 60]. Although $p_{st}(t)$ is measured with Ar propellant in the present case, the conformity of the trends between these two parameters confirms the first condition, and proves that $p_{st}(t)$ is a reliable proxy for $T(t)$.

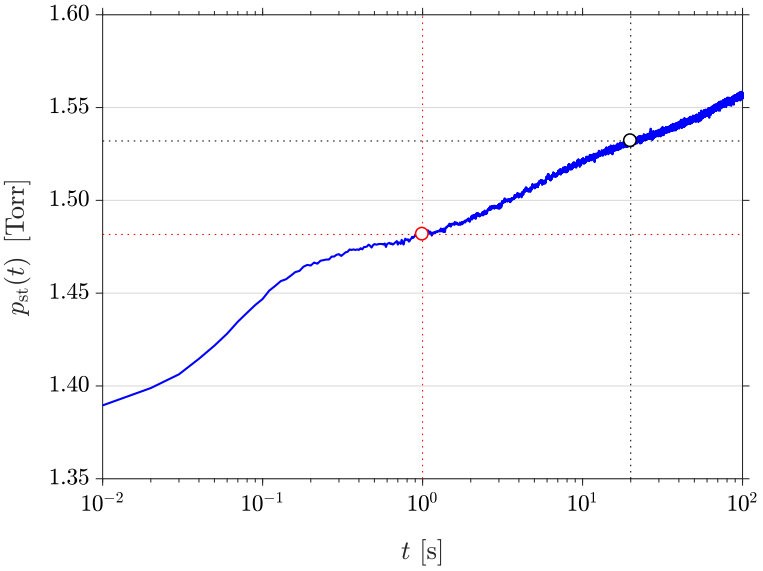

Figure 4.5: Time scales of rising stagnation pressure $p_{st}(t)$ during PR plasma operation. $p_{st}(t)$ increases rapidly in the first ~ 0.1 s, plateaus at $t \sim 1$ s, and resumes the rise thereafter. The computed $p_{st} = 1.532$ Torr (black ○ marker) is 3.4 % higher than the target $p_{st}(t = 1\,\text{s}) = 1.482$ Torr (red ○ marker).

The second condition requires $p_{st}(t)$ from the CFD-plasma simulation to match experimental measurements. Due to the dual time-step nature of the CFD-plasma modelling technique where plasma dynamics are solved in lockstep with fluid dynamics, the fluid dynamics

solver time-step $\Delta\tau_{\mathrm{f}}$ cannot be interpreted as a progression of the CFD-plasma simulation results in real time. Instead, the periodic converged result at the end of the CFD-plasma simulation (Figure 2.11) represents a transient equilibrium state. In the present CFD-plasma simulation of PR, the temperature of the discharge chamber wall is still close to the initial temperature of $T = 300\,\mathrm{K}$. This time scale corresponds to $t \sim 1\,\mathrm{s}$ in the PR experiment where $p_{\mathrm{st}}(t)$ plateaus, shown as the red ○ marker in Figure 4.5. This is a more accurate indicator of the time scale of the CFD-plasma simulation results, instead of simply comparing the computed p_{st} to the experimentally measured p_{st}.

The computed stagnation pressure $p_{\mathrm{st}}(t)$ at each time-step of the RF cycle is calculated by integrating the pressure along the radius at the front of the plenum (left edge of P at $z = -30\,\mathrm{mm}$ in Figure 4.3), and averaging over the whole axisymmetric circular area. The average over the 600 time-steps of the 10 RF cycles that constitute the converged final solution (Section 2.2.4) gives the cycle average $p_{\mathrm{st}} = 1.532\,\mathrm{Torr}$, shown as the black ○ marker in Figures 4.4 and 4.5. This value is 3.4 % higher than the measured $p_{\mathrm{st}}(t = 1\,\mathrm{s}) = 1.482\,\mathrm{Torr}$ (Figure 4.5, red ○ marker), indicating a slight overestimation in the computed p_{st}.

To summarise, the temporal evolution of the measured $p_{\mathrm{st}}(t)$ matches that of the measured $T(t)$. This indicates that $p_{\mathrm{st}}(t)$, which can be obtained more conveniently, is a reliable proxy for determining $T(t)$. In these profiles, the inflection point at $t \sim 1\,\mathrm{s}$ is the most distinctive. It is also the most appropriate to be modelled in the CFD-plasma simulation since it represents the state of the PR discharge when the neutral gas temperature has stabilised, but the discharge chamber wall has yet to heat up. The computed $p_{\mathrm{st}} = 1.532\,\mathrm{Torr}$ is very close to the target $p_{\mathrm{st}}(t = 1\,\mathrm{s}) = 1.482\,\mathrm{Torr}$. Hence, the CFD-plasma simulation results can be considered to be an accurate model of the PR discharge at $t \sim 1\,\mathrm{s}$ after plasma ignition not only in terms of the computed stagnation pressure, but also the computed neutral gas temperature.

4.4.2 Power draw

The computed cycle average power absorbed by the PR discharge is $P = 5.010\,\mathrm{W}$, calculated by integrating the volumetric and surface energy in the PR simulation domain averaged over 10 RF cycles. This is in good agreement with the constant $P_{\mathrm{PR}} = 4.725\,\mathrm{W}$ of power supplied to the PR experiment, measured using the post-match digital in-line voltage/current (V/I) probe between the impedance matching network and the powered electrode. The secondary electron emission coefficient $\gamma_{\mathrm{e}'}$ may be adjusted slightly to bring the computed value more in line with the measured value. Presently, this is not necessary since the discrepancy is

small, and doing so does not alter the general characteristics of the CFD-plasma simulation results. Power deposition in the PR discharge is discussed in more detail in Section 4.5 from a plasma dynamics perspective, and also separately in Chapter 5 from an electrical circuit perspective.

4.4.3 Ion density

The ion density in the PR discharge chamber has been determined previously by Langmuir probe (LP) measurements of the ion saturation current while operating with $V_{\text{pwr}} = 250\,\text{V}$ on the powered electrode [14]. The pre-match power was reported to be 9.5 W, corresponding to $P_{\texttt{PR}} \approx 4\,\text{W}$ post-match. The LP was inserted into PR from the KF-25 port at the front of the plenum (left edge of P at $z = -30\,\text{mm}$ in Figure 4.3), and measurements were taken in the range of $-22\,\text{mm} \leq z \leq 9\,\text{mm}$. The LP had a 1 mm in diameter circular nickel (Ni) tip set at the end of a cylindrical shaft. When the LP was inserted into the discharge chamber by more than 8 mm, the static pressure in the plenum rose by 0.1 Torr every 2 mm due to flow constriction. Additionally, the LP in this position displaces the plasma from under the powered electrode, and changes the operating conditions considerably. As such, measurements taken beyond $z \geq -10\,\text{mm}$ are prone to greater errors [14].

The ion density obtained from the CFD-plasma simulation results is plotted in Figure 4.6, showing both the cycle average n_{i} (blue — line) as well as the temporal variation of $n_{\text{i}}(t)$ (light blue — lines) at each time-step within the RF cycle. The n_{i} profile has a strong central peak with $n_{\text{i}} = 5.373 \times 10^{17}\,\text{m}^{-3}$ at $z = -9.9\,\text{mm}$, with two shoulder plateaus on either side near the entrance and exit of the discharge chamber. The upstream half of the n_{i} profile is in good agreement with the measured ion saturation current profile, which had a plateau near the entrance of the discharge chamber, followed by a peak at $z = -8.0\,\text{mm}$ under the powered electrode. A LP characteristic collected at $z = -14\,\text{mm}$ gave an estimated $n_{\text{i}} \approx 2.8 \times 10^{17}\,\text{m}^{-3}$ while operating with $P_{\texttt{PR}} \approx 11\,\text{W}$ post-match (19.7 W pre-match) [14]. The present CFD-plasma simulation results give $n_{\text{i}} = 1.601 \times 10^{17}\,\text{m}^{-3}$ at the same position, which is a reasonable value at the lower power of $\sim 5\,\text{W}$.

The previous experimental investigation inferred the peak ion density to be $n_{\text{i}} \sim 1.8 \times 10^{18}\,\text{m}^{-3}$ at $P_{\texttt{PR}} \approx 5\,\text{W}$ post-match (9.5 W pre-match) based on scaling the ion saturation current measurements with power [14]. The discrepancy between this value and the peak n_{i} obtained from the present CFD-plasma simulation results may be due to a combination of factors such as imprecise experimental results caused by the aforementioned physical flow constriction and electrical interference from the LP when placed within the narrow discharge

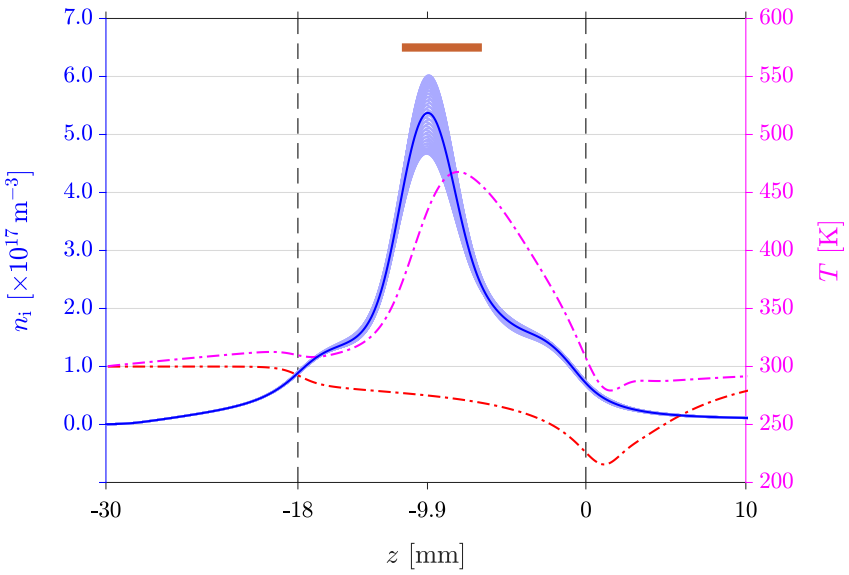

Figure 4.6: Cycle average ion density n_i (blue — line) and neutral gas temperature T during plasma operation (magenta –·– line) and cold gas operation (red –·– line)) along the z-axis. The temporal variation of the ion density $n_i(t)$ is represented by the light blue — lines. The vertical – – lines demarcate the plenum ($-30\,\text{mm} \leq z \leq -18\,\text{mm}$), discharge chamber ($-18\,\text{mm} \leq z \leq 0\,\text{mm}$), and downstream ($z \geq 0\,\text{mm}$) regions. The brown bar shows the position of the powered electrode ($-11.5\,\text{mm} \leq z \leq -6.5\,\text{mm}$). n_i peaks at $5.373 \times 10^{17}\,\text{m}^{-3}$ at $z = -9.9\,\text{mm}$, while T peaks at 467.7 K, slightly further downstream at $z = -8.0\,\text{mm}$.

chamber, and the application of the scaling relation to the nonuniform plasma. Thus, in the absence of more more definitive experimental measurements, the ion density from the CFD-plasma simulation may be relied upon *proviso* of the verification of other more easily measurable parameters. Additionally, $\gamma_{e'}$ may be adjusted [66] to achieve better agreement with experimental results if necessary.

4.4.4 Neutral gas temperature

Figure 4.6 also plots the cycle average neutral gas temperature T during plasma operation (magenta –·– line) from the CFD-plasma simulation results and during cold gas operation (red –·– line) from the CFD simulation results. Although results for $T(t)$ are produced at every time-step in the RF cycle in the CFD-plasma simulation, $T(t)$ must not be taken to represent real temperature variation due to the nature of the dual time-step technique employed. Instead, $T(t)$ serves to produce an accurate context for the solution of other fluid and plasma parameters, and exist on a time scale separate to the plasma time-step $\Delta\tau_p$ or the fluid time-step $\Delta\tau_f$. The variation of $T(t)$ from the cycle average T is dependent on the size of

$\Delta\tau_f$: using a larger $\Delta\tau_f$ increases the variation while using a smaller $\Delta\tau_f$ reduces it. However, using a value that is larger or smaller than the optimal value of $\Delta\tau_f = 1\,\mu s$ exacerbates divergence. At any $\Delta\tau_f$ setting, only the cycle average T profile can be interpreted as realistic.

The peak temperature of $T = 467.7\,K$ is attained at $z = -8.0\,mm$, slightly downstream of the n_i peak. This is in agreement with the reported $T \sim 400\,K$ measured in a N_2 plasma by rotational spectroscopy at $\sim 1\,s$ after plasma ignition [49, 55]. However, the photons in the collected spectra originate from various points in the discharge chamber along the line of sight (z-axis), and resolution in the r-axis is also poor [51]. The present CFD-plasma modelling technique is able to resolve the T profile along both the z- and r-axes at 0.1 mm spatial resolution. This is a significant advantage as the plasma-induced heating in PR is highly localised, and produces a nonuniform T profile in the discharge chamber. The shape and nature of the T profile are discussed in more detail in the following sections. $T(t)$ is also discussed separately in Section 7.5.1.

4.5 Heat transfer mechanisms

In order to understand and critique the T profile produced by the CFD-plasma simulation, the following sections provide an analysis of the three explicit heat transfer mechanisms, in addition to the implicit thermal conduction, considered in the CFD-plasma simulation: volumetric heating of neutral Ar species happening through (i) electron-neutral elastic collisions and (ii) ion-neutral charge exchange collisions, and surface heating occurring via (iii) ion bombardment on the plasma-facing solid surfaces of the PR simulation domain.

4.5.1 Electron-neutral elastic collisions

The first mechanism for heat transfer in the CFD-plasma simulation is through electron-neutral elastic collisions. The amount of energy transferred from a Maxwellian electron to an Ar neutral in an elastic collision is calculated as:

$$\epsilon_e = \frac{2m_e}{m} \cdot \frac{3}{2} k_B (T_e - T) \tag{4.5}$$

where k_B is the Boltzmann constant, m represents the mass and T is the temperature of an Ar neutral, and those with the subscript 'e' are the corresponding values for the electrons in units of [K]. The collision rate is calculated using the cross section obtained from [125]. The power deposition density for electron-neutral elastic collisions peaks at $\sim 0.051\,W\,cm^{-3}$, momentarily in the RF cycle, in the middle of the discharge chamber. Using this peak

value for the whole discharge chamber (C in Figure 4.3) gives a generous overestimate of $\sum_{\mathtt{C}} \epsilon_\mathrm{e} \lesssim 0.013\,\mathrm{W}$. The rate of electron-neutral elastic collisions is much lower in the plenum and downstream (P and D respectively in Figure 4.3) due to the low electron density in these regions and thus may be neglected.

4.5.2 Ion-neutral charge exchange collisions

The amount of energy transferred from an Ar^+ ion to an Ar neutral in a charge exchange collision can be modelled as ohmic heating which is defined to be:

$$\epsilon_\mathrm{i} = \frac{q_\mathrm{e}}{\mu_\mathrm{i}} n_\mathrm{i} v_\mathrm{i}^2 \tag{4.6}$$

where q_e is the elementary charge representing singly charged Ar^+, μ_i is the ion mobility, n_i is the ion density, and v_i is the magnitude of the velocity of an individual ion.

In the collisional plasma sheath where a strong radial electric field E_r is present, the collective motion of the ions can be simplified as the radial ion drift velocity where $v_\mathrm{i} = \sqrt{u_{z,\mathrm{i}}^2 + u_{r,\mathrm{i}}^2} \approx u_{r,\mathrm{i}} = \mu_\mathrm{i} E_r$ according to Ohm's law, thus giving:

$$\epsilon_{\mathrm{i,sheath}} \approx q_\mathrm{e} \mu_\mathrm{i} n_\mathrm{i} E_r^2 \tag{4.7}$$

However, this approximation is not valid in the plasma bulk where the plasma potential Φ_p is mostly flat and $E = -\nabla\Phi_\mathrm{p}$ is small. For a hot ion of temperature T_i in the plasma bulk prior to giving up its energy, its thermal velocity $u_{T,\mathrm{i}} = \sqrt{3k_\mathrm{B}T_\mathrm{i}/m_\mathrm{i}}$ is comparable or greater than $u_{r,\mathrm{i}}$, and thus:

$$\epsilon_{\mathrm{i,bulk}} \approx \frac{q_\mathrm{e}}{\mu_\mathrm{i}} n_\mathrm{i} u_{T,\mathrm{i}}^2 \tag{4.8}$$

This means that in the plasma bulk, heat transfer via ion-neutral charge exchange collisions occur effectively and quickly in locations where hot ions are numerous. The collision rate is dependent on the charge exchange cross section and polarisability volume, which for Ar are $\sigma_q = 49.0\,\text{Å}^2$ and $\alpha' = 1.664\,\text{Å}^3$ respectively [83]. Note that while σ_q is dependent on ion energy [137], a constant value is used due to the limitations of CFD-ACE+.

Once an ion has given up its energy to a neutral, subsequent neutral-neutral collisions facilitate local thermalisation. The ion then takes on the temperature of the local neutrals, and eventually drift out of the plasma bulk. (4.8) can be simplified by recognising that $u_{T,\mathrm{i}}^2$ is linear with T_i. Since μ_i is on the order of unity and within a tight range across the radius of the discharge chamber, it may be ignored for simplicity.

Thus, heat transfer from Ar^+ ions to Ar neutrals via ion-neutral charge exchange collisions can be approximated by two local models. Since radial thermal conduction through the

rarefied laminar flow system is insignificant on the time scale of the ion transit time across the radius of the discharge chamber, the temperature of the Ar neutral gas must therefore closely track the energy that was initially transferred to the neutrals, with $T \propto \epsilon_{\mathrm{i}}$, whereby $\epsilon_{\mathrm{i,bulk}} \propto n_{\mathrm{i}}$ in the plasma bulk, and $\epsilon_{\mathrm{i,sheath}} \propto n_{\mathrm{i}} E_{\mathrm{r}}^2$ in the plasma sheath.

The left half of Figure 4.7 plots the cycle average ion density n_{i} (blue — line) and the cycle average electron density n_{e} (blue –·– line) across the radius of the discharge chamber at $z = -9.9\,\mathrm{mm}$ where the ion density peaks. A charge imbalance is visible in the plasma sheath, which is expected due to the higher mobility of electrons as compared to that of ions [135]. Also shown is the product term $n_{\mathrm{i}} E_r^2$ (magenta – – line) scaled to arbitrary units. The temporal variation of $n_{\mathrm{i}}(t)\, E_r^2(t)$ within the RF cycle is included to illustrate the oscillatory nature of $E_r(t)$ in the plasma sheath. Despite the strong n_{i} peak, the cycle average $n_{\mathrm{i}} E_r^2$ is close to zero and flat in the plasma bulk since $E_r^2 \to 0$ given the relative flatness of Φ_{p} there.

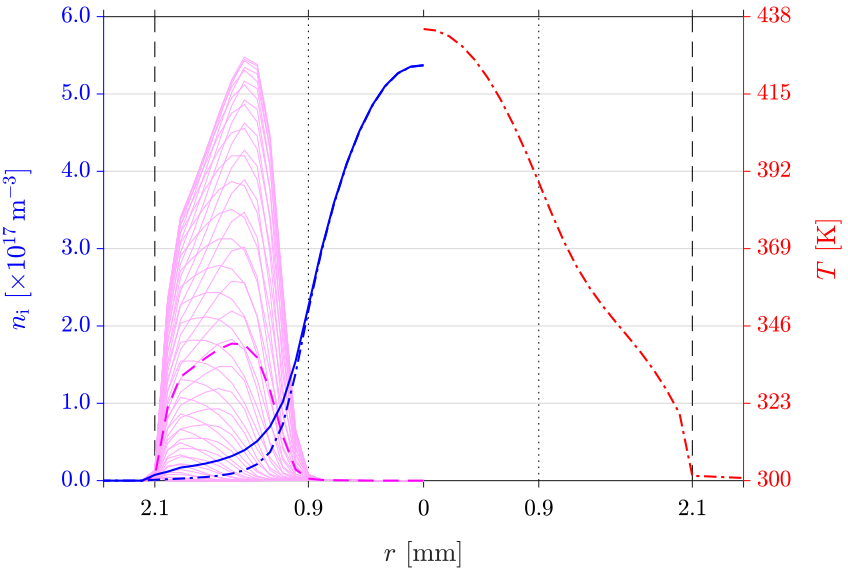

Figure 4.7: Cycle average ion density n_{i} (blue — line), electron density n_{e} (blue –·– line), and neutral gas temperature T (red –·– line) along $z = -9.9\,\mathrm{mm}$. Also plotted is $n_{\mathrm{i}}(t)\, E_r^2(t)$ (light magenta — lines, arbitrary units) and its cycle average $n_{\mathrm{i}} E_r^2$ (magenta – – line, arbitrary units). The vertical ····· lines delimit the extent of the plasma bulk ($0\,\mathrm{mm} \leq r \leq 0.9\,\mathrm{mm}$) and the plasma sheath ($0.9\,\mathrm{mm} \leq r \leq 2.1\,\mathrm{mm}$). The shape of the T profile follows that of n_{i} in the plasma bulk, and $n_{\mathrm{i}} E_r^2$ in the plasma sheath.

In the plasma sheath however, the large variations in $n_{\mathrm{i}}(t)\, E_r^2(t)$ is due to the large amplitude of the oscillating plasma sheath potential. The right half of the figure plots the radial profile of T (red –·– line). Demonstrably, T is proportional to n_{i} in the plasma bulk

($0 \leq r \leq 0.9$) and proportional to $n_\mathrm{i} E_r^2$ in the plasma sheath ($0.9 \leq r \leq 2.1$). These observations are in line with the two local models for heat transfer via ion-neutral charge exchange collisions. At $z = -9.9\,\mathrm{mm}$, the neutral gas temperature is highest at $T = 434.3\,\mathrm{K}$ at $r = 0\,\mathrm{mm}$, and decreases along r. There is a minor inflection near the inner edge of the plasma sheath before resuming the concave down profile, indicating a transition between the two local heat transfer models. Since slip boundary conditions are used, there is a temperature jump (Section 3.2.3) of $T_\mathrm{s} = 18.5\,\mathrm{K}$ from $319.9\,\mathrm{K}$ to $301.4\,\mathrm{K}$ across one cell before the surface of the discharge chamber wall. Within the discharge chamber wall and beyond, T is essentially flat and goes to $300.0\,\mathrm{K}$ on the external surface of the PR structure. The CFD-plasma simulation results are consistent with the initial state of PR discharge on a time scale of $\sim 1\,\mathrm{s}$, before any significant heating of the PR device.

At the local pressure of $p = 1.106\,\mathrm{Torr}$, the mean free path of an Ar neutral, using the kinematic definition in this rarefied flow regime with the Lennard-Jones collision diameter σ, is $\lambda = 72.6\,\mu\mathrm{m}$ on the central z-axis. The $0.9\,\mathrm{mm}$ radius of the plasma bulk is equivalent to $\sim 12.4\,\lambda$. Traversing this distance, perpendicular to the direction of flow, by random walk requires on the order of $n^2 \approx 154$ collisions. At the local thermal velocity of $u_T = \sqrt{3 k_\mathrm{B} T / m} = 519.1\,\mathrm{m\,s^{-1}}$, this corresponds to a duration of $\sim 21.5\,\mu\mathrm{s}$ for thermal equilibrium to be achieved across the plasma bulk. However, since this is already sufficient time for the Ar neutral to travel $\sim 3.9\,\mathrm{mm}$ downstream in the z direction given the high axial velocity u_z of the gas (Figure 3.6, blue — line), thermalisation can only occur locally in the r direction. Hence, the T profile is radially nonuniform as the rarefied medium renders thermal conduction ineffective in the laminar flow.

By integrating over all the plasma regions in the PR simulation domain and taking the average over the 10 RF cycles of the final solution, the total power deposited volumetrically via ion-neutral charge exchange collisions and electron-neutral elastic collisions is $P_\mathrm{V} = \sum_{\mathtt{P,C,D}} \epsilon_\mathrm{V} = \sum_{\mathtt{P,C,D}} (\epsilon_\mathrm{e} + \epsilon_\mathrm{i}) = 0.344\,\mathrm{W}$. The discharge chamber alone accounts for $\sum_{\mathtt{C}} \epsilon_\mathrm{V} = 0.263\,\mathrm{W}$ or $76.3\,\%$ of the total amount. This amount of power applied uniformly to Ar gas flowing at a rate of $\dot{m} = 100\,\mathrm{SCCM}$ through the cross sectional area of the discharge chamber can raise the propellant temperature by $\Delta T = +170.0\,\mathrm{K}$, assuming a specific heat capacity of $520.3\,\mathrm{J\,K^{-1}\,kg^{-1}}$ for Ar. In the CFD-plasma simulation, the peak of $T = 467.7\,\mathrm{K}$ at $z = -8.0$ in Figure 4.6 is $\Delta T = +195.9\,\mathrm{K}$ above the cold gas operation case where $T = 271.9\,\mathrm{K}$ at the same position (Figure 3.7, blue — line). The slightly greater ΔT from the CFD-plasma simulation can be explained by accounting for the peaked T profile due to the highly localised plasma-induced heating, as well as the factors responsible for cooling, such as the work done by the gas during expansion and conductive thermal losses to the

discharge chamber wall and the neighbouring plenum and downstream regions.

Ion-neutral charge exchange collisions are responsible for $\gtrsim 95.1\,\%$ of P_V, with values estimated at $0.332\,\mathrm{W} \lesssim \sum_{\mathtt{P,C,D}} \epsilon_\mathrm{i} < 0.344\,\mathrm{W}$ across all the plasma regions in the PR simulation domain, or $0.250\,\mathrm{W} \lesssim \sum_{\mathtt{C}} \epsilon_\mathrm{i} < 0.263\,\mathrm{W}$ in the discharge chamber. These values, along with the conformity of the T profile in Figure 4.7 to the two local heat transfer models, confirm that volumetric plasma-induced heating of the neutral gas in PR is primarily the consequence of ion-neutral charge exchange collisions in the plasma bulk, and that the CFD-plasma simulation produces a spatially resolved neutral gas temperature profile that is reasonable and accurate.

4.5.3 Surface heating via ion bombardment

Finally, surface heating is the result of energy transfer from the plasma species ($\mathrm{Ar}(4\mathrm{s_m})$, $\mathrm{Ar}(4\mathrm{s_r})$, $\mathrm{Ar}(4\mathrm{p})$ and Ar^+) to the plasma-facing solid surfaces of the PR simulation domain (blue — lines in Figure 4.3). The dominant mechanism is via ion bombardment, but the contribution from surface recombination and deexcitation reactions are also included, and calculated in the CFD-plasma simulation as:

$$\epsilon_\mathrm{S} = \epsilon_\mathrm{k} + \epsilon_\mathrm{c} = \varphi_\mathrm{i} \cdot \frac{1}{2} m_\mathrm{i} v_\mathrm{i}^2 + \sum_\mathrm{n} h_\mathrm{n} \varphi_\mathrm{n} \tag{4.9}$$

where ϵ_k represents the kinetic energy released by the impacting ions with speed v_i, while ϵ_c represents the chemical energy released by the impacting species via surface recombination or deexcitation reactions; $\varphi = nv$ is the particle flux, and h_n is the excitation or ionisation energy for the respective Ar species.

Near the discharge chamber wall, the number density of the excited species ($\mathrm{Ar}(4\mathrm{s_m})$, $\mathrm{Ar}(4\mathrm{s_r})$, and $\mathrm{Ar}(4\mathrm{p})$) combined is ~ 50 times of n_i. However, the radial velocity of the excited species towards the discharge chamber wall is several orders of magnitude lower than the radial ion drift velocity $u_{r,\mathrm{i}}$ since the uncharged species are only transported by diffusion. Hence, the particle flux of the excited species is negligible compared to the ion flux $\varphi_\mathrm{i} = n_\mathrm{i} u_{r,\mathrm{i}}$, and the contribution from Ar^+ surface recombination reactions provides an adequate estimation for ϵ_c. With the ionisation energy of Ar^+ at $h_\mathrm{i} = 15.760\,\mathrm{eV}$, integrating φ_i along the internal cylindrical surface of the discharge chamber wall gives $\sum_{\mathtt{CW}} \epsilon_\mathrm{c} = 0.098\,\mathrm{W}$. ϵ_c at the other plasma-facing solid surfaces may be neglected since φ_i is significantly lower far away from the powered electrode.

In the whole PR simulation domain, the total amount of power going into surface heating is $P_\mathrm{S} = \sum_{\mathtt{S,CW}} \epsilon_\mathrm{S} = 4.666\,\mathrm{W}$. Of this value, $\sum_{\mathtt{CW}} \epsilon_\mathrm{S} = 4.641\,\mathrm{W}$ or $99.5\,\%$ of the power is deposited

on the internal cylindrical surface of the discharge chamber wall. Hence, $\sum_{\mathtt{CW}} \epsilon_\mathrm{k} = 4.543\,\mathrm{W}$ is released via ion bombardment on the surface of the discharge chamber wall. As this represents a significant portion of the total applied power (90.7 % of $P = 5.010\,\mathrm{W}$), it is important to thoroughly understand the process of ion transport in the plasma sheath.

4.6 Ion transport in the plasma sheath

4.6.1 Ion velocity

Figure 4.8 shows the temporal variation of the radial ion drift velocity $u_{r,\mathrm{i}}(t)$ (left, light blue — lines) and the plasma potential $\Phi_\mathrm{p}(t)$ (right, light red — lines), and the respective cycle average profiles $u_{r,\mathrm{i}}$ (blue — line) and Φ_p (red — line) across the radius of the discharge chamber along $z = -9.9\,\mathrm{mm}$ underneath the powered electrode. In the plasma bulk at $r = 0\,\mathrm{mm}$, $\Phi_\mathrm{p}(t)$ oscillates between $\Phi_\mathrm{p}^- = 12.0\,\mathrm{V}$ and $\Phi_\mathrm{p}^+ = 60.9\,\mathrm{V}$, with a mostly flat cycle average value of $\Phi_\mathrm{p} = 27.0\,\mathrm{V}$. In the plasma sheath however, $\Phi_\mathrm{p}(t)$ goes from flat during the positive peak of the RF cycle, to an extremely steep gradient during the negative peak. At $r = 2.1\,\mathrm{mm}$, the electric potential at the plasma-facing surface of the discharge chamber wall oscillates between $\Phi_\mathrm{wall}^- = -458.1\,\mathrm{V}$ and $\Phi_\mathrm{wall}^+ = 52.7\,\mathrm{V}$, with $\Phi_\mathrm{wall} = -193.0\,\mathrm{V}$.

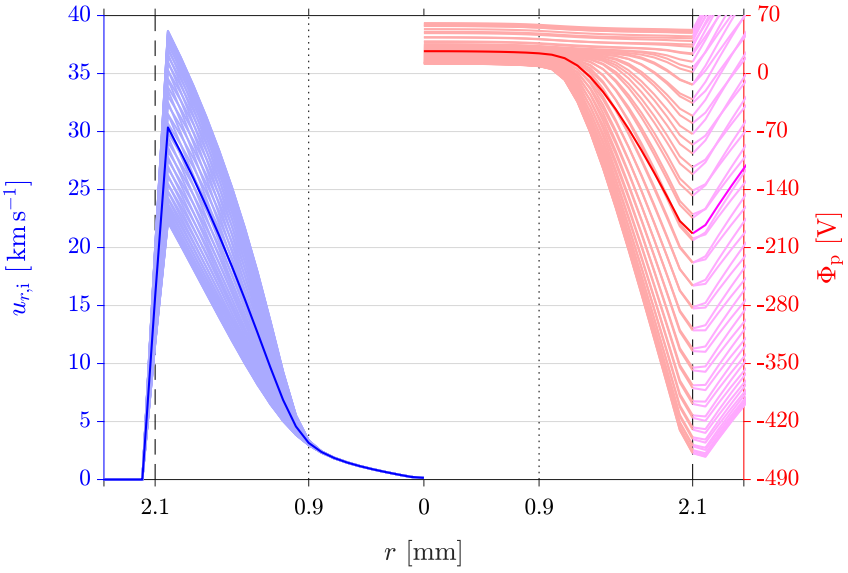

Figure 4.8: Radial ion drift velocity $u_{r,\mathrm{i}}$ (blue — line) and plasma potential Φ_p (red — line) along $z = -9.9\,\mathrm{mm}$. The temporal variation of $u_{r,\mathrm{i}}(t)$ (light blue — lines) and $\Phi_\mathrm{p}(t)$ (light red — lines) are also shown. $u_{r,\mathrm{i}}$ is rendered over the width of two whole cells at the solid-plasma interface at the discharge chamber wall ($r = 2.1\,\mathrm{mm}$).

The geometrical asymmetry of the PR discharge creates a negative self-bias (Chapter 5) in the section of the discharge chamber wall underneath the powered electrode. As such, $\Phi_{\mathrm{p}}(t)$ in the plasma bulk is always higher than $\Phi_{\mathrm{wall}}(t)$, and ions are continuously accelerated from the plasma bulk into the self-biased section of the discharge chamber wall throughout the whole RF cycle. Along $z = -9.9\,\mathrm{mm}$, the cycle average radial ion drift velocity attains a high of $u_{r,\mathrm{i}} = 30.35\,\mathrm{km\,s^{-1}}$ at $r = 2.0\,\mathrm{mm}$, one cell away from the solid-plasma interface CW-C between the discharge chamber wall and the discharge chamber. This behaviour is due to CFD-ACE+ rendering the solid-plasma interface over the width of two whole cells on either side of the interface for certain parameters. For most other parameters, the solid-plasma interface is treated normally at the shared boundary of the adjacent solid and plasma regions.

Let v_0 be the ion velocity at the inner edge of the plasma sheath and $v_{\mathrm{i}}(z,r)$ be the ion velocity at any point in the plasma. Typically, the plasma sheath is considered to be collisionless, and v_{i} represents the actual velocity of the ion. The same analysis can be applied with equivalent validity to a collisional plasma sheath in the PR discharge, but with v_{i} representing the radial ion drift velocity $u_{r,\mathrm{i}}$ instead. The energy gained by an ion drifting through a potential drop of $\Delta\Phi = \Phi_{\mathrm{p}}(z,r) - \Phi_0$ is:

$$\frac{1}{2} m_{\mathrm{i}} \left(v_{\mathrm{i}}^2 - v_0^2 \right) = -q_{\mathrm{e}} \Delta\Phi \tag{4.10}$$

which rearranges to:

$$v_0 = v_{\mathrm{i}} \left(1 + \frac{2 q_{\mathrm{e}} \Delta\Phi}{m_{\mathrm{i}} v_{\mathrm{i}}^2} \right)^{\frac{1}{2}} \tag{4.11}$$

where q_{e} is the elementary charge and m_{i} is the molecular mass of an Ar^+ ion.

Correspondingly, let n_0 be the ion density at the inner edge of the plasma sheath and $n_{\mathrm{i}}(z,r)$ be the ion density at any point in the plasma. The ion flux is conserved by the continuity relation $\varphi_{\mathrm{i}} = n_{\mathrm{i}} v_{\mathrm{i}} = n_0 v_0$ which upon substitution of (4.11) gives:

$$n_{\mathrm{i}} = \frac{n_0 v_0}{v_{\mathrm{i}}} = n_0 \left(1 + \frac{2 q_{\mathrm{e}} \Delta\Phi}{m_{\mathrm{i}} v_{\mathrm{i}}^2} \right)^{\frac{1}{2}} \tag{4.12}$$

The electron density $n_{\mathrm{e}}(z,r)$ on the other hand is given by the Boltzmann relation [135]:

$$n_{\mathrm{e}} = n_0 \cdot \exp\left(-\frac{q_{\mathrm{e}} \Delta\Phi}{k_{\mathrm{B}} T_{\mathrm{e}}} \right) \tag{4.13}$$

where $k_{\mathrm{B}} T_{\mathrm{e}}$ is the electron energy.

A charge imbalance exists in the plasma sheath, where the ion density n_{i} falls more slowly than the electron density n_{e}. This can be seen in Figure 4.7 as the bifurcation of the n_{i} (blue

— line) and n_e (blue -·- line) profiles for $r \gtrsim 0.9\,\text{mm}$. Therefore, the condition:

$$|\nabla n_i| \leq |\nabla n_e| \tag{4.14}$$

is imposed where ∇ is the del operator, with equality attained only at the inner edge of the plasma sheath. Since the gradients are negative with increasing distance from the plasma bulk, their absolute values are used for mathematical consistency. Substituting (4.12) and (4.13) into (4.14) eventuates in a second order polynomial inequality in v_i^2 of the form:

$$v_i^4 + Av_i^2 - B \geq 0 \tag{4.15}$$

where the contracted coefficients are:

$$A = \frac{2q_e\Delta\Phi}{m_i} \tag{4.16}$$

$$B = \left(\frac{k_B T_e}{m_i}\right)^2 \cdot \exp\left(\frac{2q_e\Delta\Phi}{k_B T_e}\right) \tag{4.17}$$

If the electron energy $k_B T_e$ is taken to be a constant for the particular plasma in consideration, then (4.15) is ultimately only dependent on $\Delta\Phi$.

The ion sound speed $c_{s,i}$ is the minimum velocity an ion exiting the plasma bulk is allowed to have before entering the plasma sheath. The traditional derivation of $c_{s,i}$ is for the specific case $\Delta\Phi = 0\,\text{V}$, or exactly at the inner edge of the plasma sheath. This reduces (4.15) to $v_i^4 = B$ where $v_i = v_0 = c_{s,i}$, thus producing the familiar expression for the ion sound speed:

$$c_{s,i} = \sqrt{\frac{k_B T_e}{m_i}} \tag{4.18}$$

In the PR Ar discharge at the coordinates $(z, r) = (-9.9, 0.9)$, $k_B T_e = 2.92\,\text{eV}$ gives $c_{s,i} = 2.65\,\text{km s}^{-1}$. In Figure 4.8, $u_{r,i}$ surpasses $c_{s,i}$ at $r \approx 0.94\,\text{mm}$, which is consistent with the stated position of the inner edge of the plasma sheath. A weak radial electric field in the presheath, originating from the small potential drop of $\Delta\Phi = -2.6\,\text{V}$ between $r = 0\,\text{mm}$ and $r = 0.9\,\text{mm}$, is responsible for accelerating the ions to $c_{s,i}$ as they leave the plasma bulk.

For the more general case with arbitrary $\Phi_p(z, r)$, (4.18) is substituted into (4.10) in place of v_0, and solved to yield a single real root. To verify that the $u_{r,i}$ profile produced by the CFD-plasma simulation is accurate, it is sufficient to check $v_i(z, r)$ at two selected points: $v_i(-9.9, 2.0) = 31.58\,\text{km s}^{-1}$ and $v_i(-9.9, 1.5) = 18.62\,\text{km s}^{-1}$. The respective values from Figure 4.8 are: $u_{r,i}(-9.9, 2.0) = 30.35\,\text{km s}^{-1}$ and $u_{r,i}(-9.9, 1.5) = 18.38\,\text{km s}^{-1}$, which are in excellent agreement with the theoretical calculations. Thus, the CFD-plasma simulation accurately resolves the plasma sheath and ion dynamics even without an explicit plasma sheath model.

Integrating the ion flux φ_i across the internal cylindrical surface of the discharge chamber wall reveals that it is necessary for the ion impact speed to be $v_\mathrm{i} \approx 2.19 \cdot \sqrt{u_{z,\mathrm{i}}^2 + u_{r,\mathrm{i}}^2}$ in order to match the value of $\sum_{\mathtt{CW}} \epsilon_\mathrm{k}$ (4.9). This implies that the path length d of an ion travelling through the collisional plasma sheath has to be correspondingly ~ 2.19 times the width of the plasma sheath, or $d \approx 2.19 \cdot 1.2\,\mathrm{mm} = 2.6\,\mathrm{mm}$. Taking a simplistic view, this can be visualised as a hot Ar^+ ion traversing through the plasma sheath towards the discharge chamber wall along a zigzagging path with an average deflection angle of $\sim \cos^{-1}(1/2.19) = 62.8°$ from the r unit vector.

The average collisional mean free path of an Ar neutral in the region of the plasma sheath is $\lambda_\mathrm{LJ} \approx 58.4\,\mu\mathrm{m}$ (3.2), calculated using the local temperature T of the neutral gas. An Ar neutral covering a distance of d thus undergoes $n = d/\lambda_\mathrm{LJ} \approx 45$ collisions. For a hot Ar^+ ion, the average collisional mean free path is $\lambda_{\mathrm{LJ,i}} = T_\mathrm{i}/T \cdot \lambda_\mathrm{LJ}$. If T_i/T is large, then hot Ar^+ ions undergo correspondingly fewer collisions with Ar neutrals as they transit the plasma sheath, with perhaps on the order of $n \lesssim 10$ collisions. It is important to recognise that the path of an ion through the plasma sheath is unlike the aforementioned random walk in the plasma bulk. Instead, the ion momentum is strongly directed due to the strong radial electric field E_r, and therefore the transfer of momentum during ion-neutral charge exchange collisions in the plasma sheath is primarily kinetic rather than thermal.

Hence, while volumetric heating via ion-neutral charge exchange collisions is still present in the plasma sheath as visible in the shape of the T profile matching the $n_\mathrm{i}E_r^2$ profile in Figure 4.7, it is considerably less effective in the plasma sheath than in the plasma bulk. As such, the ions retain most of the energy gained in the plasma sheath, which is eventually transferred to the discharge chamber wall upon impact ($\sum_{\mathtt{CW}} \epsilon_\mathrm{k}$). This energy is not wasted *per se*, as ion bombardment is a necessary process for the creation of the secondary electrons that are ultimately responsible for sustaining the gamma mode discharge in PR.

4.6.2 Ion transit time

The average ion transit time through the plasma bulk ($\tau_{\mathrm{i,bulk}}$) and plasma sheath ($\tau_{\mathrm{i,sheath}}$) can be used as a gauge for the degree of thermalisation achieved through ion-neutral charge exchange collisions in the respective regions. This is done by performing a fourth order Runge-Kutta analysis on the cycle average radial ion drift velocity $u_{r,\mathrm{i}}$ to obtain $r_\mathrm{i}(t)$, the cycle average radial drift position of the ion as a function of time. Figure 4.9 plots $r_\mathrm{i}(t)$ for ions originating from various points along the radius of the discharge chamber, with t given in terms of the RF period $\tau_\mathrm{RF} = 73.75\,\mathrm{ns}$. Highlighted, in particular, are the paths originating

from $r = 0\,\text{mm}$ in the middle of the plasma bulk (blue — line) and from $r = 0.9\,\text{mm}$ on the inner edge of the plasma sheath (red — line).

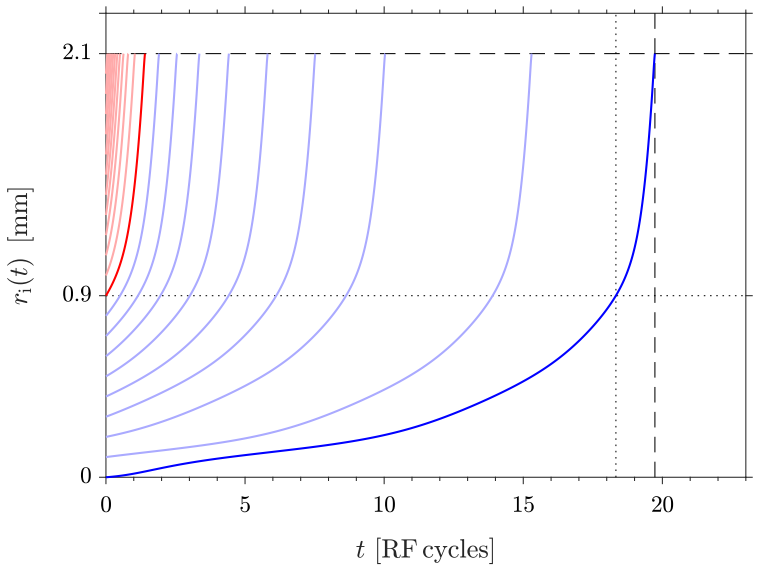

Figure 4.9: Average ion transit time across the radius of the discharge chamber. The horizontal ····· line delimits the extent of the plasma bulk ($0\,\text{mm} \leq r \leq 0.9\,\text{mm}$) and the plasma sheath ($0.9\,\text{mm} \leq r \leq 2.1\,\text{mm}$). The blue — line shows the average path of an ion originating from $r = 0\,\text{mm}$ ($\tau_\text{i,bulk} = 19.25 \cdot \tau_\text{RF}$), while the red — line shows the average path of an ion through the plasma sheath ($\tau_\text{i,sheath} = 1.4 \cdot \tau_\text{RF}$).

The average time taken for an ion to transit the 0.9 mm radius of the plasma bulk is $\tau_\text{i,bulk} = 19.25 \cdot \tau_\text{RF} = 1.419\,\mu\text{s}$. Since $\tau_\text{i,bulk}$ is many times of τ_RF, ions in the plasma bulk only respond to the cycle average plasma potential Φ_p. This is also evidenced by the coinciding $u_{r,\text{i}}(t)$ profiles (light blue — lines) in Figure 4.8 for $r \leq 0.9\,\text{mm}$ despite the variation of $\Phi_\text{p}(t)$ (light red — lines) within the RF cycle. The average time taken for an ion to transit the 1.2 mm width of the plasma sheath is $\tau_\text{i,sheath} = 1.4 \cdot \tau_\text{RF} = 103\,\text{ns}$. Since $\tau_\text{i,sheath}$ is on the order of τ_RF, ions in the plasma sheath are responsive to the oscillating $\Phi_\text{p}(t)$, as seen in the spread of $u_{r,\text{i}}(t)$ for $0.9\,\text{mm} \leq r \leq 2.1\,\text{mm}$. The disparity between $\tau_\text{i,bulk}$ and $\tau_\text{i,sheath}$ shows that an ion starting at $r = 0\,\text{mm}$ spends 93.3 % of the total transit time in the plasma bulk, and only 6.7 % in the plasma sheath. This alternatively confirms that heat transfer via ion-neutral charge exchange collisions and thermalisation happens much more effectively in the plasma bulk than in the plasma sheath.

4.7 Chapter summary

This chapter investigates the plasma-induced heating in the PR discharge. Six plasma species (Ar, Ar($4s_m$), Ar($4s_r$), Ar(4p), Ar^+, and e^-) are considered in the CFD-plasma model, with a total of 29 volumetric chemical reactions. The volume, boundary, and initial conditions of the PR CFD-plasma simulation domain are a superset of those used in the CFD simulation domain, with additional settings for electrical and plasma parameters.

Several metrics are used to validate the accuracy of the CFD-plasma simulation with respect to the PR experiment. The computed stagnation pressure in the plenum is in agreement with experimental measurements, and corresponds to the inflection point at ~ 1 s after plasma ignition, when the neutral gas attains local thermal equilibrium but before the discharge chamber wall begins to heat up. The stagnation pressure can be used as a reliable proxy for measuring the temperature since it responds on the same time scale. The computed power is also in agreement with the power draw of the PR experiment at the standard operating conditions. The ion density produced by the CFD-plasma simulation has a higher spatial and temporal resolution than that which was obtained from Langmuir probe experiments, and is a reliable estimate due to its noninvasive nature.

Three mechanisms for heat transfer have been examined in detail, namely electron-neutral elastic collisions, ion-neutral charge exchange collisions, and surface heating via ion bombardment. Plasma-induced heating of the neutral gas in the PR Ar discharge is verified to be primarily due to ion-neutral charge exchange collisions. The neutral gas temperature profile follows two local models, with heating being significantly more effective in the plasma bulk than in the plasma sheath, corroborated by the ion transit time in the respective regions. The power deposition in each of these mechanisms is quantified. A significant fraction of the total applied power is released via ion bombardment on the discharge chamber wall and is responsible for creating the secondary electrons that sustain the PR gamma mode discharge.

Chapter 5

Self-bias

Radiofrequency (RF) discharges are used in a wide variety of high technology industry applications, ranging from plasma processes such as reactive ion etching (RIE) and plasma enhanced chemical vapour deposition (PECVD) of thin films on substrate wafers for microelectronics fabrication, to ion and electrothermal thrusters for electrically powered spacecraft propulsion. Ion bombardment is often a crucial process in these applications. In plasma processing for example, there is a desire to understand and model ion bombardment to control etch profiles and etching rates [138], reduce sputtering and compositional or structural damage to the wafer surface [139], as well as to address a range of other undesirable RIE-related effects [140]. For spacecraft propulsion, hollow cathode thrusters [22] rely on ion bombardment for heating and sustaining temperatures for thermionic emission, but sputtering and erosion of the insert and keeper electrode through the same process can severely limit the lifetime of the thruster. In the *Pocket Rocket* radiofrequency plasma electrothermal microthruster, ion bombardment plays a crucial role in the generation of secondary electrons for sustaining a gamma mode discharge.

In general, ion bombardment is a result of the acceleration of positive ions through a plasma sheath that spans a large potential drop, from the positive electric potential in the plasma bulk to the target surface that is at a lower electric potential. The target surface is often negatively biased, either by imposing a DC voltage or via the formation of a self-bias. A self-bias can arise in a plasma system due to one or a combination of the following three scenarios: the secondary electron asymmetry effect (SEAE) resulting from the use of electrode materials with different affinities for secondary electron emission [141]; the electrical asymmetry effect (EAE) due to the use of tailored waveforms at the powered electrode [142, 143] or from fluctuations in the plasma potential [144]; or most commonly, the use of grounded and powered electrodes with a large area asymmetry ratio.

The self-bias phenomenon due to the geometrical area asymmetry of the grounded and powered electrodes has been extensively documented in experiments [145–149], simulations [150–152], and other literature [135]. Essentially, when the ratio of the grounded and powered electrode areas is far from unity, the capacitance of the plasma sheath at the larger electrode is greater than that at the smaller electrode. In most plasma systems, the grounded electrode is often much larger than the powered electrode, resulting in a negative DC bias on the powered electrode that is maintained by a build-up of negative charge in a blocking capacitor, usually located in an external impedance matching network circuit just before the powered electrode.

It is necessary to have an accurate characterisation of the self-bias behaviour in order to fully understand and control the ion bombardment process. However, performing measurements with invasive probes can be undesirable during plasma operation, or difficult due to geometry or size limitations in many plasma systems. For these situations, CFD-plasma simulation is an especially useful tool for constructing a comprehensive model of the plasma system, that is capable of providing highly detailed data at high spatial and temporal resolutions.

5.1 Sheath circuit models

Capacitively coupled plasma (CCP) systems are often modelled as an electrical circuit consisting of two capacitors, representing the plasma sheaths at the grounded and powered electrodes, in series with a blocking capacitor and a RF source. The circuit resembles a capacitive voltage divider, allowing for simple calculation of the root mean square (RMS) voltage drop across each capacitive component. However, this type of quasi-steady-state sheath circuit model [153–157] is only valid in the regime where the ion transit time across the sheath is much greater than the RF period ($\tau_\mathrm{i} \gg \tau_\mathrm{RF}$). In this regime, heavy ions do not respond to the time-varying high frequency RF electric field but rather to its time-average value.

Sheath circuit models [157–160] also exist for the opposite case of $\tau_\mathrm{i} \ll \tau_\mathrm{RF}$ in low frequency or high density (thin sheath) RF plasmas, where ion motion in the sheath is inertialess and responds rapidly to the oscillating RF electric field. In this regime, each sheath is modelled as a diode, current source, and capacitor in parallel [138, 157], representing the electron current, ion current, and displacement current respectively. Such a circuit has a very different voltage division outcome than the former case, and the calculation of the voltages across the sheaths as well as the blocking capacitor must take into account the electron and

ion currents at each electrode during the positive and negative periods of the RF cycle.

The following is a summary of the derivation presented in [157] of the self-bias voltage V_{bias} developed at the blocking capacitor in an ideal asymmetric RF discharge with a large grounded electrode, and a small powered electrode with a time-varying voltage waveform $\Phi_{\text{pwr}}(t)$.

Due to the blocking capacitor, no DC current can flow to either electrode. For this to be true, the plasma potential $\Phi_{\text{p}}(t)$ must be positive relative to both electrodes, otherwise more electrons arrive at the electrodes than ions due to their greater mobility. Additionally, for an asymmetric system, the smaller powered electrode must be negatively biased relative to the larger grounded electrode. This necessitates $\Phi_{\text{p}}(t)$ and the voltage across the powered sheath $\Phi_{\text{p}}(t) - \Phi_{\text{pwr}}(t)$ to be alternately positive and clamped near zero. Consequently, the electron currents can only reach the electrodes when either sheath voltages are near zero, and one or the other sheath alternately admits a pure ion current.

In the limit where $\tau_{\text{i}} \ll \tau_{\text{RF}}$, the plasma sheaths become resistive instead of capacitive as conduction currents dominate over displacement currents. Over one RF cycle, the total electron charge $Q_{\text{e,pwr}}$ collected by the powered electrode must equal the total ion charge collected:

$$Q_{\text{e,pwr}}(\tau_{\text{RF}}) = Q_{\text{i,pwr}}(\tau_{\text{RF}}) \tag{5.1}$$

$$= q_{\text{e}} c_{\text{s,i}} n_{\text{i,pwr}} A_{\text{pwr}} \cdot \tau_{\text{RF}} \tag{5.2}$$

where q_{e} is the elementary charge, $c_{\text{s,i}}$ is the local ion sound speed, $n_{\text{i,pwr}}$ is the ion density at the inner edge of the powered sheath, A_{pwr} is the area of the powered electrode, and τ_{RF} is the RF period.

Additionally, because the plasma must maintain quasineutrality during the positive period τ_+ of $\Phi_{\text{pwr}}(t)$, the total electron charge collected by the powered electrode must be equal to the total ion charge collected by both the grounded and powered electrodes during τ_+:

$$Q_{\text{e,pwr}}(\tau_+) = Q_{\text{i,gnd}}(\tau_+) + Q_{\text{i,pwr}}(\tau_+) \tag{5.3}$$

$$= \left(q_{\text{e}} c_{\text{s,i}} n_{\text{i,gnd}} A_{\text{gnd}} + q_{\text{e}} c_{\text{s,i}} n_{\text{i,pwr}} A_{\text{pwr}}\right) \cdot \tau_+ \tag{5.4}$$

where $n_{\text{i,gnd}}$ is the ion density at the inner edge of the grounded sheath, and A_{gnd} is the area of the grounded electrode.

Given that $\tau_{\text{RF}} = \tau_+ + \tau_-$, combining (5.2) and (5.4) gives:

$$\frac{\tau_+}{\tau_-} = \frac{c_{\text{s,i}} n_{\text{i,pwr}} A_{\text{pwr}}}{c_{\text{s,i}} n_{\text{i,gnd}} A_{\text{gnd}}} \tag{5.5}$$

specifying that the ratio of the positive period to the negative period of $\Phi_{\mathrm{pwr}}(t)$ is proportional to the ratio of the ion current collected at each electrode. Finally, the solution for $\Phi_{\mathrm{pwr}}(t)$ to preserve τ_+ and τ_- requires it to be displaced by the amount of:

$$V_{\mathrm{bias}} = -V_{\mathrm{pwr}} \cdot \sin\left(\frac{\pi}{2} \cdot \frac{c_{\mathrm{s,i}} n_{\mathrm{i,gnd}} A_{\mathrm{gnd}} - c_{\mathrm{s,i}} n_{\mathrm{i,pwr}} A_{\mathrm{pwr}}}{c_{\mathrm{s,i}} n_{\mathrm{i,gnd}} A_{\mathrm{gnd}} + c_{\mathrm{s,i}} n_{\mathrm{i,pwr}} A_{\mathrm{pwr}}}\right) \tag{5.6}$$

In a highly asymmetric system, assuming $A_{\mathrm{gnd}} \gg A_{\mathrm{pwr}}$ and $A_{\mathrm{gnd}}/A_{\mathrm{pwr}} \gg c_{\mathrm{s,i}} n_{\mathrm{i,pwr}}/c_{\mathrm{s,i}} n_{\mathrm{i,gnd}}$ reduces (5.6) to the familiar $V_{\mathrm{bias}} = -V_{\mathrm{pwr}}$.

This negative DC bias develops on the blocking capacitor such that the voltage waveform on the powered electrode is:

$$\Phi_{\mathrm{pwr}}(t) = -V_{\mathrm{pwr}} \cdot \sin(\omega t) + V_{\mathrm{bias}} \tag{5.7}$$

where V_{pwr} is the peak voltage of the sinusoidal RF waveform oscillating at the angular frequency $\omega = 2\pi f$. Since the DC V_{bias} is negative and constant, $\Phi_{\mathrm{pwr}}(t)$ is displaced negatively relative to the supplied RF waveform by a fixed value, and oscillates in the range $-V_{\mathrm{pwr}} - |V_{\mathrm{bias}}| \leq \Phi_{\mathrm{pwr}}(t) \leq V_{\mathrm{pwr}} - |V_{\mathrm{bias}}|$.

The vital implication of this derivation for the $\tau_{\mathrm{i}} \ll \tau_{\mathrm{RF}}$ regime is that the V_{bias} that develops on the blocking capacitor serves to preserve τ_+ and τ_-, and results in a voltage division behaviour that is very different from the simpler capacitive sheath circuit model in the $\tau_{\mathrm{i}} \gg \tau_{\mathrm{RF}}$ regime. In a numerical study [160], the $\tau_{\mathrm{i}} \ll \tau_{\mathrm{RF}}$ regime sheath circuit model is used to calculate the ion energy distribution (IED) for varying capacitances and inductances in the external RF circuit while keeping the RF frequency and power fixed. The study finds that the IED is bimodal as expected, but the low energy peak remains constant and V_{bias} stays approximately constant despite changes in the impedances of the external RF circuit. Only the high energy peak is shifted when different capacitances and inductances are used, but does not correlate with V_{bias}. This means that the positive peak of $\Phi_{\mathrm{pwr}}(t)$, corresponding to the minimum potential drop at the powered sheath, responsible for the low energy peak of the IED, does not depend on the size of the blocking capacitor or other impedances in the external RF circuit, but is instead characteristic of the plasma parameters and the geometry of the plasma system. On the contrary, the negative peak of $\Phi_{\mathrm{pwr}}(t)$, corresponding to the maximum potential drop at the powered sheath, responsible for the high energy peak of the IED, is sensitive to the impedances of the external RF circuit [157]. In an industrial RIE system for example, shifts in the ion bombardment energies might lead to undesirable process control [161]. Even if the IED can be monitored with a retarding field energy analyser (RFEA), measurements taken in the $\tau_{\mathrm{i}} \ll \tau_{\mathrm{RF}}$ regime can be significantly affected by the RF modulated plasma sheath in front of the RFEA, and thus do not reflect the true IED [162].

Up until now, V_{bias} is defined to be the mean of the $\Phi_{\text{pwr}}(t)$ waveform. However, since $\Phi_{\text{pwr}}(t)$ responds asymmetrically to extraneous impedances in the RF circuit, using a more stable baseline like the maxima envelope $\Phi^{+}_{\text{pwr}} = V_{\text{pwr}} - \left|V'_{\text{bias}}\right|$ instead can provide a more rigorous definition of the self-bias voltage (Section 5.3.4). This chapter uses the geometrically asymmetric CCP PR discharge to demonstrate this phenomenon in the $\tau_{\text{i}} \sim \tau_{\text{RF}}$ regime, where the radial ion drift velocity in the collisional powered sheath varies by $\Delta u_{r,\text{i}} = \pm 27.1\,\%$ within the RF cycle as a response to the oscillating RF electric field (Figure 4.8). In this regime, some assumptions of the $\tau_{\text{i}} \ll \tau_{\text{RF}}$ regime sheath circuit model are not explicitly valid [163, 164], and a complete time-dependent treatment of ion inertial effects is required.

5.2 CFD-plasma simulation setup

Results from three separate CFD-plasma simulations are discussed in this chapter. Comparisons are made between the original PR with the 1 mm thick discharge chamber wall and two other PR geometries with thinner (0.5 mm) and thicker (1.5 mm) discharge chamber walls. Only the external radius of the discharge chamber wall is modified, so as to preserve the internal dimensions of the discharge chamber. The CFD-plasma simulations are designated as PR-05, PR-10, and PR-15 according to the respective thickness of their discharge chamber wall. All three CFD-plasma simulations are set up using the same procedure detailed in Section 4.3, with the same volume, boundary, and initial conditions.

5.3 PR discharge RF circuit model

The CFD-plasma simulation results are detailed in the following sections, with a particular focus on the electrical parameters which are used to derive a RF circuit model of the PR discharge. The high temporal resolution of the CFD-plasma simulation allows the electrical and plasma dynamics within the RF cycle to be examined. The observed behaviour of the electric potential in the discharge chamber wall leads to a more rigorous definition of the self-bias voltage (Section 5.3.4) in the thin sheath regime.

5.3.1 Electric potential

Figure 5.1 shows a spatiotemporal overview of the electric potential $\Phi(t)$ along the radial cross section of PR at $z = -9.9\,\text{mm}$, across the different regions: the discharge chamber (aqua, $r \leq 2.1\,\text{mm}$), discharge chamber wall (yellow, $2.1\,\text{mm} \leq r \leq 3.1\,\text{mm}$), powered

electrode (brown, 3.1 mm $\leq r \leq$ 8 mm), insulation (dark green, 8 mm $\leq r \leq$ 10 mm), and structure (grey, $r \geq$ 10 mm). The 10 RF cycles in the final solution (Section 2.2.4) are averaged to give a single characteristic RF cycle with 60 time-steps. There are 60 light blue — lines in the profile representing $\Phi(t)$ evaluated at each time-step of the characteristic RF cycle, while the single blue — line in the middle of the profile represents the average Φ over the period of the characteristic RF cycle.

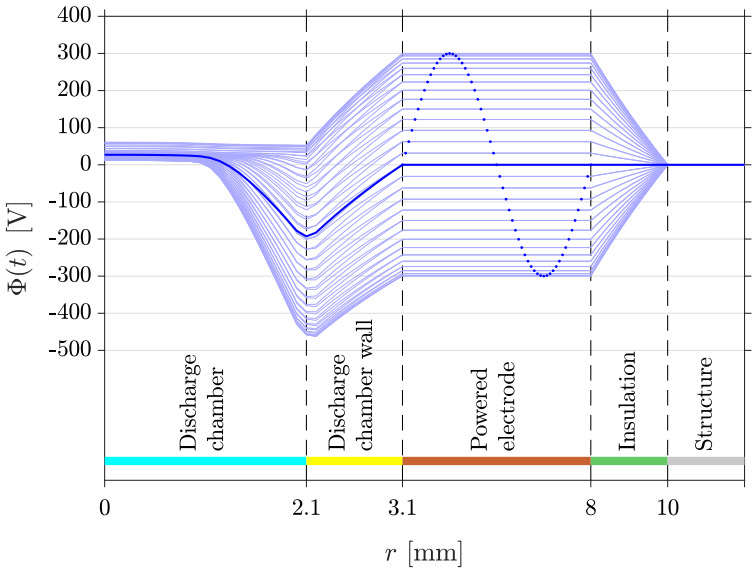

Figure 5.1: Spatially and temporally resolved electric potential $\Phi(t)$ profile along the radial cross section of PR at $z = -9.9$ mm (light blue — lines). The blue — line denotes the cycle average Φ, while the blue ····· sinusoidal wave illustrates the oscillation of $\Phi_{\text{pwr}}(t)$ in the powered electrode over one RF cycle.

The structure (grey) is defined to be electrically grounded, and therefore $\Phi(t)$ is always zero in the electrically conductive Al region. In the powered electrode (brown), the imposed sinusoidal voltage waveform $\Phi_{\text{pwr}}(t)$ causes the whole electrically conductive Cu region to oscillate between ±300 V. A layer of dielectric insulation (dark green) separates the powered electrode from the grounded structure. An electric displacement field is created in the dielectric Macor region that bridges $\Phi(t)$ between the powered electrode and the grounded structure. In these solid regions, the cycle average electric potential Φ (blue — line) is zero.

The discharge chamber wall (yellow) exhibits a rather different behaviour. The displacement field in the dielectric Al_2O_3 region, as evidenced by the gradient $\nabla_r \Phi(t)$, appears to be approximately constant over the whole RF cycle, with the electric potential at the plasma-facing surface of the discharge chamber wall $\Phi_{\text{wall}}(t)$ being biased negatively relative

to $\Phi_{\text{pwr}}(t)$ on the powered electrode side. This is the manifestation of the self-bias due to the geometrical asymmetry of the plasma system. At the coordinates $(z, r) = (-9.9, 2.1)$, the mean electric potential is $\Phi_{\text{wall}} = -193.0\,\text{V}$, while the minimum and maximum values are $\Phi^{-}_{\text{wall}} = -458.2\,\text{V}$ and $\Phi^{+}_{\text{wall}} = 52.6\,\text{V}$ respectively. This gives a peak-to-peak range of $\left|\Phi^{+}_{\text{wall}} - \Phi^{-}_{\text{wall}}\right| = 510.8\,\text{V}$, equivalent to 85.1 % of the supplied 600 V.

In the discharge chamber (aqua), the plasma potential $\Phi_{\text{p}}(t)$ peaks at the same location as the ion density peak. At the coordinates $(z, r) = (-9.9, 0)$, the mean plasma potential is $\Phi_{\text{p}} = 27.0\,\text{V}$, while $\Phi^{-}_{\text{p}} = 12.0\,\text{V}$ and $\Phi^{+}_{\text{p}} = 60.9\,\text{V}$, indicating that $\Phi_{\text{p}}(t)$ oscillates by $\left|\Phi^{+}_{\text{p}} - \Phi^{-}_{\text{p}}\right| = 48.9\,\text{V}$ within the RF cycle. $\Phi_{\text{p}}(t)$ is positive and higher than $\Phi_{\text{pwr}}(t)$ during τ_{+}, and clamped near zero during τ_{-}. Conversely, the potential difference across the powered sheath $\Phi_{\text{p}}(t) - \Phi_{\text{pwr}}(t)$ is clamped near zero during τ_{+}, and greatly positive during τ_{-}. On the other hand, the potential difference across the grounded sheath along the plasma-facing surfaces of the structure (not shown in Figure 5.1), is much smaller in this highly asymmetric plasma system. These results are in agreement with the theoretical analysis outlined in Section 5.1.

5.3.2 Dielectric wall & sheath capacitances

To study the effects of varying the dielectric wall capacitance on the self-bias, two additional CFD-plasma simulations of PR are performed with 0.5 mm and 1.5 mm thick discharge chamber walls. To distinguish between the three CFD-plasma simulations, the default geometry with a 1 mm thick wall is designated as PR-10, while the two other geometries are designated as PR-05 and PR-15. Only the external radius of the discharge chamber wall is modified in the PR-05 and PR-15 simulation meshes, so as to preserve $A_{\text{gnd}}/A_{\text{pwr}}$ (2.3), (2.4).

The capacitance of a cylindrical dielectric capacitor is given by:

$$C = \frac{2\pi\varepsilon_0\varepsilon_{\text{r}}L}{\ln\left(\frac{R}{r}\right)} \tag{5.8}$$

where ε_0 is the vacuum permittivity, ε_{r} is the relative permittivity of the dielectric, L is the length of the cylinder, and R and r are its external and internal radii respectively. Hence, the capacitances of the section of the $\varepsilon_{\text{r}} = 9.6$ Al_2O_3 wall immediately in front of the $L = 5\,\text{mm}$ powered electrode in PR-05, PR-10, and PR-15 are: $C_{\text{wall}} = 12.5\,\text{pF}$, 6.9 pF, and 5.0 pF respectively, which equates to an impedance of $|Z_{\text{wall}}| = |-1/\omega C_{\text{wall}}| = 0.94\,\text{k}\Omega$, 1.7 kΩ, and 2.4 kΩ respectively. For comparison, the capacitance of the blocking capacitor used in the PR RF circuit (Section 2.1.4) is $C_{\text{block}} = 100\,\text{pF}$.

Equivalent capacitance values can also be calculated for the powered sheath using (5.8)

and $\varepsilon_r = 1$ to give $C'_{s,pwr} \approx 3.2\,\text{pF}$. This calculation uses the external and internal radii of the powered sheath in PR-10 (Figure 4.7) with $r = 2.1\,\text{mm}$ and $r = 0.9\,\text{mm}$, but remains approximately valid in PR-05 and PR-15 where the powered sheath widths are only very slightly different. Due to the larger size of the grounded sheath, it may be approximated by a parallel plate capacitor with an area equivalent to the internal grounded surface of the structure of the plenum plus the surface of the end wall facing the downstream region. The width of the grounded sheath at the front wall of the plenum is approximately $d = 1.94\,\text{mm}$, so $C'_{s,gnd} = \varepsilon_0 A_{gnd}/d \approx 229\,\text{pF}$, with a slight variation of $\lesssim 1\,\text{pF}$ between the three geometries due to different internal radii of the rear (S-P) and end (S-D1) walls as a result of the modified external radius of the discharge chamber wall. The collisional sheath capacitance equation $C_{s,sym} \approx 0.76 \cdot \varepsilon_0 A_{sym}/d$ is not able to be used for PR as it is only valid for symmetric plasma systems [154, 156].

The $C'_{s,pwr}$ and $C'_{s,gnd}$ values quoted above are not necessarily accurate in reality, especially in the $\tau_i \ll \tau_{RF}$ regime where the plasma sheaths become resistive instead of capacitive. Instead, it is more appropriate to quantify their impedances, which in the $\tau_i \sim \tau_{RF}$ regime is some combination of resistance R and capacitive reactance $X_C = -1/\omega C$. Since $R \propto d/A$ uses the same geometrical parameters as $X_C \propto d/A$, the effective impedance is therefore $|Z| = \sqrt{R^2 + X_C^2} \propto |X_C|$. Hence, the powered and grounded sheath impedances are $\left|Z'_{s,pwr}\right| \approx \zeta \cdot 3.7\,\text{k}\Omega$ and $\left|Z'_{s,gnd}\right| \approx \zeta \cdot 51\,\Omega$ respectively, where ζ is an unknown proportionality constant.

Figures 5.2 and 5.3 give a closer look at the electric potential Φ^- and Φ^+ during the negative (τ_-) and positive (τ_+) peaks of the RF cycle respectively, averaged over the 10 RF cycles in the final solution. Φ^- and Φ^+ from PR-05 are represented by red — lines, PR-10 by green — lines, and PR-15 by blue — lines. The horizontal axes are labelled according to the plasma and RF circuit features, tracing a path from the plasma bulk (aqua), through the powered sheath (magenta), dielectric wall (colour coded according to each geometry), to the powered electrode (brown). Note that the vertical axes are at different scales in the two figures. Despite significant changes in the dielectric wall capacitance C_{wall}, the minima and maxima plasma potential Φ_p^- and Φ_p^+ profiles remain largely similar across the three geometries. Figures 5.2 and 5.3 also demonstrate the alternately positive (Φ_p^+ and $\Phi_p^- - \Phi_{wall}^-$) and clamping (Φ_p^- and $\Phi_p^+ - \Phi_{wall}^+$) behaviour of the plasma potential and the potential difference across the powered sheath, as well as the $\Phi_p(t) > \Phi_{wall}(t)$ behaviour mentioned in Section 5.1. The maxima, minima, peak-to-peak, and cycle average values of $\Phi_p(t)$ for the three geometries are summarised in Table 5.1. The values for PR-05 tend to be slightly higher than the other two geometries, but overall the results are very close.

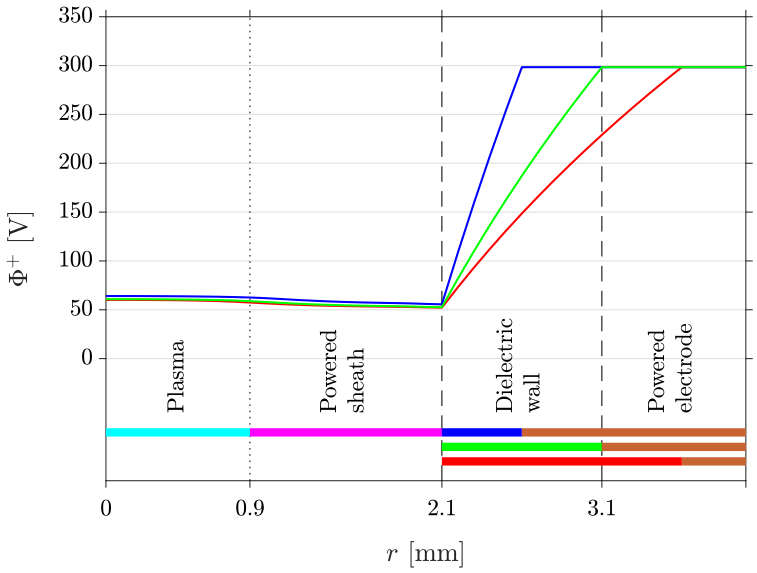

Figure 5.2: Electric potential Φ^+ during the positive peak of the RF cycle through different regions of `PR-05` (blue — line), `PR-10` (green — line), and `PR-15` (red — line). The plasma potential Φ_p^+ profile remain largely similar across the three geometries. The blue, green, and red bars on the bottom of the plot denotes the thickness of the dielectric wall in the respective geometries.

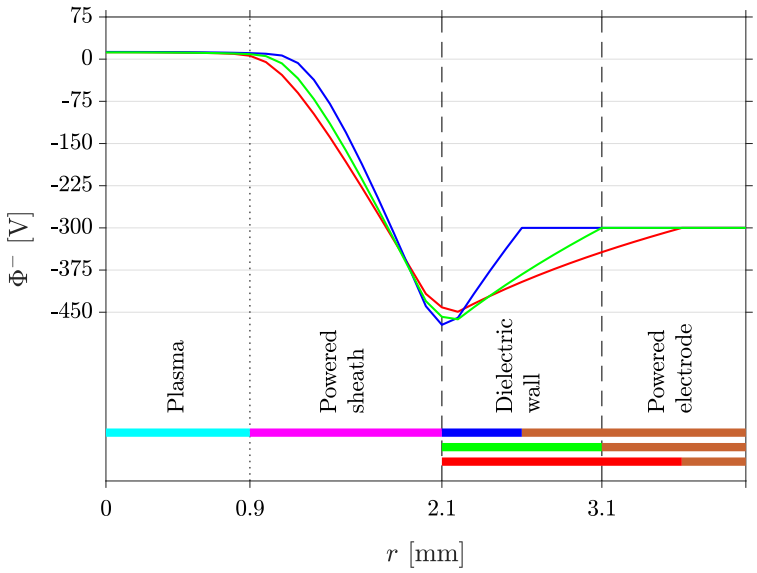

Figure 5.3: Electric potential Φ^- during the negative peak of the RF cycle through different regions of `PR-05` (blue — line), `PR-10` (green — line), and `PR-15` (red — line). The plasma potential Φ_p^- profile remain largely similar across the three geometries, but the gradient $\nabla_r \Phi_\mathrm{p}^-$ in the powered sheath and the electric potential at the plasma-facing surface of the discharge chamber wall Φ_wall^- are slightly different due to the different dielectric wall capacitances C_wall.

The most conspicuous differences between the three geometries are visible in Figure 5.3: namely the gradient of the plasma potential $\nabla_r \Phi_\mathrm{p}^-$ in the powered sheath and the electric potential at the plasma-facing surface of the discharge chamber wall during the negative peak of the RF cycle. These differences are in response to the different extraneous impedances in the RF circuit, in this case the capacitance C_wall of the dielectric discharge chamber wall, described earlier in Section 5.1. Ions falling through the powered sheath at the negative peak of the RF cycle are accelerated to very high velocities by the radial electric field $E_r = -\nabla_r \Phi_\mathrm{p}^-$, therefore differences in the gradient of Φ_p^- or the magnitude of the potential drop in the powered sheath are expected to shift the position of the high energy peak of the IED in the powered sheath. Since Φ_p^+ is unaffected by the change in the dielectric wall capacitance, the low energy peak of the IED in the powered sheath is expected to remain constant. As the dimensions of the `PR` discharge chamber are too small to admit a RFEA or other invasive probes, the only way to gain valuable insight into the ion dynamics in the powered sheath is through CFD-plasma simulations.

Table 5.1: Plasma potential [V]

Geometry	Φ_p^-	Φ_p^+	$\Phi_\mathrm{p}^+ - \Phi_\mathrm{p}^-$	Φ_p
`PR-05`	$12.8\ ^{+0.2}_{-0.2}$	$64.1\ ^{+1.9}_{-3.3}$	$51.3\ ^{+2.1}_{-3.6}$	$28.8\ ^{+0.4}_{-0.3}$
`PR-10`	$12.0\ ^{+0.3}_{-0.7}$	$60.9\ ^{+4.3}_{-4.1}$	$48.9\ ^{+4.4}_{-3.4}$	$27.0\ ^{+0.4}_{-0.9}$
`PR-15`	$12.3\ ^{+0.5}_{-0.6}$	$60.2\ ^{+3.9}_{-2.1}$	$47.8\ ^{+3.6}_{-2.5}$	$26.8\ ^{+0.6}_{-0.9}$

5.3.3 Dielectric wall surface potential

Figure 5.4 plots the electric potential on the plasma-facing surface of the dielectric discharge chamber wall $\Phi_\mathrm{wall}(t)$ at the coordinates $(z, r) = (-9.9, 2.1)$ in `PR-05` (blue — line), `PR-10` (green — line), and `PR-15` (red — line). Also plotted on the same scale is the electric potential in the powered electrode $\Phi_\mathrm{pwr}(t)$ (magenta — line). The supplied RF waveform is the same for all three geometries. Only four of the total 10 RF cycles of the final solution are shown for clarity. The coloured `--` lines denote the mean of each waveform over all 10 RF cycles. Figure 5.4 clearly shows the asymmetric response of $\Phi_\mathrm{wall}(t)$ to the different discharge chamber wall impedances. These $\Phi_\mathrm{wall}(t)$ profiles suggest for the powered sheath an IED with a constant low energy peak given the constant maxima Φ_wall^+, and a high energy peak that is shifted depending on the value of the minima Φ_wall^-.

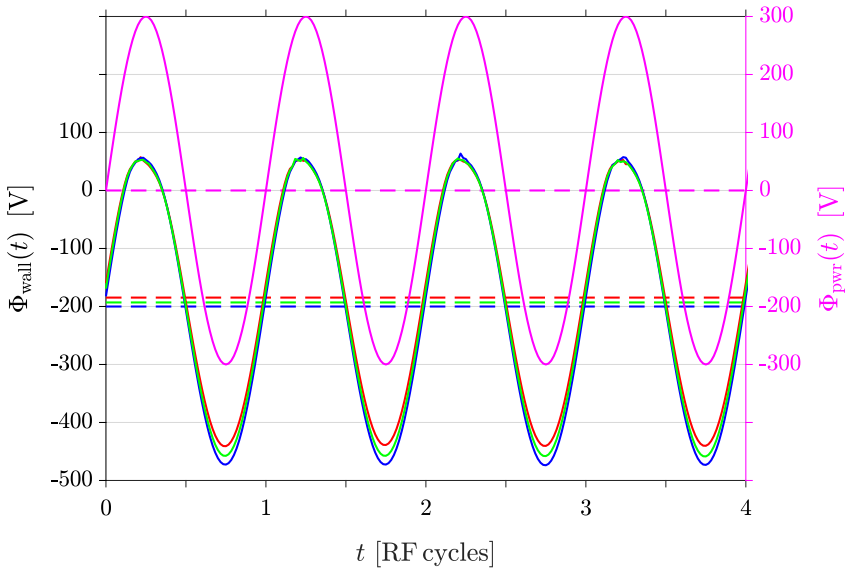

Figure 5.4: Electric potential on the plasma-facing surface of the dielectric discharge chamber wall $\Phi_{\text{wall}}(t)$ in `PR-05` (blue — line), `PR-10` (green — line), and `PR-15` (red — line), and the electric potential in the powered electrode $\Phi_{\text{pwr}}(t)$ (magenta — line). Coloured `--` lines denote the respective mean values. $\Phi_{\text{wall}}(t)$ responds asymmetrically to the different discharge chamber wall impedances, affecting only the negative peaks and minima Φ^{-}_{wall}.

For clearer comparison of the shapes of the $\Phi_{\text{wall}}(t)$ waveforms, Figure 5.5 plots $\Phi'_{\text{wall}}(t) = \Phi_{\text{wall}}(t) - \Phi_{\text{wall}}$, or the original waveform relative to its mean, alongside $\Phi_{\text{pwr}}(t)$ (magenta — line). The profiles have a similar shape across `PR-05` (blue — line), `PR-10` (green — line), and `PR-15` (red — line). $\Phi'_{\text{wall}}(t)$ mostly preserves the sinusoidal waveform of $\Phi_{\text{pwr}}(t)$, but is asymmetric about its mean, with a diminished trailing edge at each positive peak [145]. The peak-to-peak voltages are greatest in `PR-05` and least in `PR-15`.

Table 5.2 lists the maxima, minima, peak-to-peak, and mean values of $\Phi_{\text{wall}}(t)$ for each geometry, including the degree of variation in each parameter. Φ^{-}_{wall} in the second column of Table 5.2 quantifies the asymmetric response exhibited by the negative peaks in the $\Phi_{\text{wall}}(t)$ waveforms to different extraneous impedances in the RF circuit, in this case the dielectric wall capacitance, described earlier in Section 5.1 and visible in Figures 5.3 and 5.4. In `PR`, the affected parameter is $\Phi_{\text{wall}}(t)$ instead of $\Phi_{\text{pwr}}(t)$ because the plasma is in contact with the discharge chamber wall instead of the powered electrode. Essentially, the dielectric wall functions as a blocking capacitor with capacitance C_{wall} (Section 5.3.2) instead of the $C_{\text{block}} = 100\,\text{pF}$ blocking capacitor which is positioned before the powered electrode in the `PR` RF circuit (Figure 2.4). Since the self-bias manifests in $\Phi_{\text{wall}}(t)$ after the powered electrode, $\Phi_{\text{pwr}}(t)$ maintains the electric potential of the supplied RF waveform.

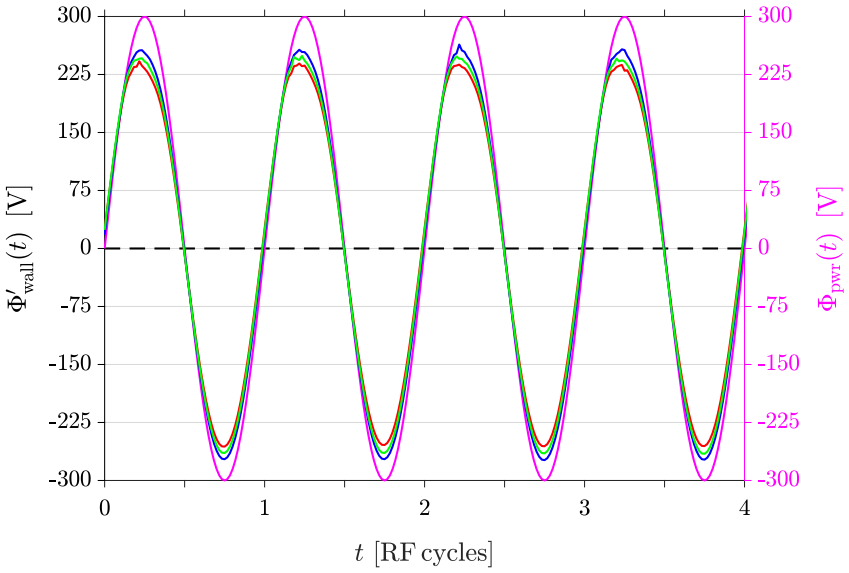

Figure 5.5: When plotting $\Phi_{\text{wall}}(t)$ relative to its mean, $\Phi'_{\text{wall}}(t)$ across the three geometries mostly preserve the sinusoidal waveform of $\Phi_{\text{pwr}}(t)$, but are asymmetric with a diminished trailing edge at each positive peak.

Table 5.2: Discharge chamber wall electric potential [V]

Geometry	Φ^-_{wall}	Φ^+_{wall}	$\Phi^+_{\text{wall}} - \Phi^-_{\text{wall}}$	Φ_{wall}
PR-05	$-472.4\ ^{+2.0}_{-1.4}$	$55.6\ ^{+1.9}_{-3.2}$	$528.0\ ^{+2.7}_{-5.3}$	$-200.1\ ^{+1.5}_{-0.9}$
PR-10	$-458.1\ ^{+1.0}_{-1.9}$	$52.7\ ^{+4.3}_{-3.8}$	$510.8\ ^{+3.9}_{-2.6}$	$-193.0\ ^{+0.9}_{-1.8}$
PR-15	$-441.3\ ^{+2.5}_{-1.8}$	$52.2\ ^{+3.8}_{-2.2}$	$493.5\ ^{+3.8}_{-3.6}$	$-184.7\ ^{+2.0}_{-1.5}$

Of particular interest is the alignment of the positive peaks of $\Phi_{\text{wall}}(t)$ for all three geometries in Figure 5.4. The positive peaks have an average maximum of $\left\langle \Phi^+_{\text{wall}} \right\rangle = 53.5\,\text{V}$ (Table 5.2) with a standard deviation of $\sigma = 2.7\,\text{V}$, and $\tau_+/\tau_- = 14/46$ (out of 60 time-steps) is approximately constant. Since $A_{\text{gnd}}/A_{\text{pwr}}$ is unchanged, (5.5) implies that $c_{\text{s,i}} n_{\text{i,pwr}}/c_{\text{s,i}} n_{\text{i,gnd}}$ is approximately constant in each of the three geometries. While it is possible to verify this by integrating over all the plasma-facing powered (section of the discharge chamber wall) and grounded electrode surfaces over each RF cycle with the present CFD-plasma simulation results, it is a nontrivial task given the size of the dataset and the presence of other non-electrode surfaces in PR.

Nonetheless, Figures 5.6 and 5.7 are provided for reference. Figure 5.6 plots the cycle average ion density n_{i} (— lines) and the cycle average radial ion drift velocity $u_{r,\text{i}}$ (– · – lines) radially along $z = -9.9\,\text{mm}$ under the powered electrode in the discharge chamber,

over the 10 RF cycles in the final solution, in PR-05 (blue), PR-10 (green), and PR-15 (red). n_i peaks on the z-axis, and falls sharply in the powered sheath as $u_{r,\mathrm{i}}$ increases to $u_{r,\mathrm{i}} \approx 30\,\mathrm{km\,s^{-1}}$ due to the steep potential drop from Φ_p to Φ_wall across the powered sheath (Figure 4.8). Figure 5.7 plots the cycle average axial ion density n_i (— lines) and the cycle average axial ion drift velocity $u_{z,\mathrm{i}}$ (-·- lines) along the z-axis at $r = 0\,\mathrm{mm}$ using the same colours for each geometry. The position of the powered electrode is shown by the brown bar at the top. n_i peaks under the powered electrode at the coordinates $(z, r) = (-9.9, 0)$ in all three geometries, with similarly shaped profiles featuring a strong central gamma mode peak and two shoulder alpha mode plateaus. The peak values are $n_\mathrm{i} = 7.010 \times 10^{17}\,\mathrm{m^{-3}}$, $5.373 \times 10^{17}\,\mathrm{m^{-3}}$, and $4.271 \times 10^{17}\,\mathrm{m^{-3}}$ for PR-05, PR-10, and PR-15 respectively. The left edge of the plot at $z = -30\,\mathrm{mm}$ is the grounded electrode, where ions impact onto the front wall of the plenum at $u_{z,\mathrm{i}} \approx -5.0\,\mathrm{km\,s^{-1}}$. Along the z-axis, ions are on average moving away from the central n_i peak, which is expected since the plasma potential Φ_p is most positive at the peak. Figures 5.6 and 5.7 show a consistent $u_{r,\mathrm{i}} n_{\mathrm{i,pwr}} / u_{z,\mathrm{i}} n_{\mathrm{i,gnd}}$ across the three geometries in the powered sheath and front wall grounded sheath respectively, which is a reasonable indication of similar behaviour for the plasma sheaths at all of the grounded electrode surfaces in general. Regardless, the high degree of alignment of the positive peaks and the preservation of a constant τ_+/τ_- in Figure 5.4 is sufficient evidence to prove it so.

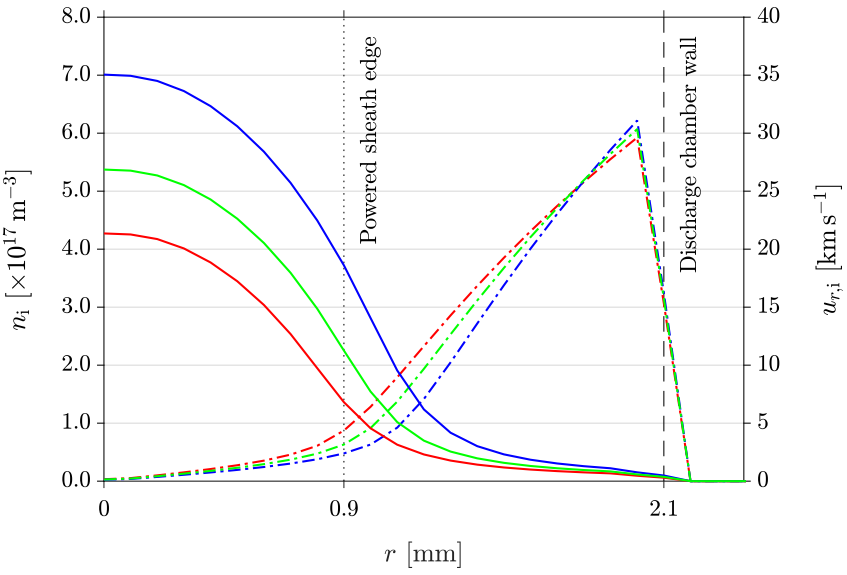

Figure 5.6: Radial profile along $z = -9.9\,\mathrm{mm}$ of the cycle average ion density n_i (— lines) and the cycle average radial ion drift velocity $u_{r,\mathrm{i}}$ (-·- lines) in the discharge chamber of PR-05 (blue), PR-10 (green), and PR-15 (red). The internal radius of the discharge chamber is kept constant at 2.1 mm, and only the external radius is changed in PR-05 and PR-15.

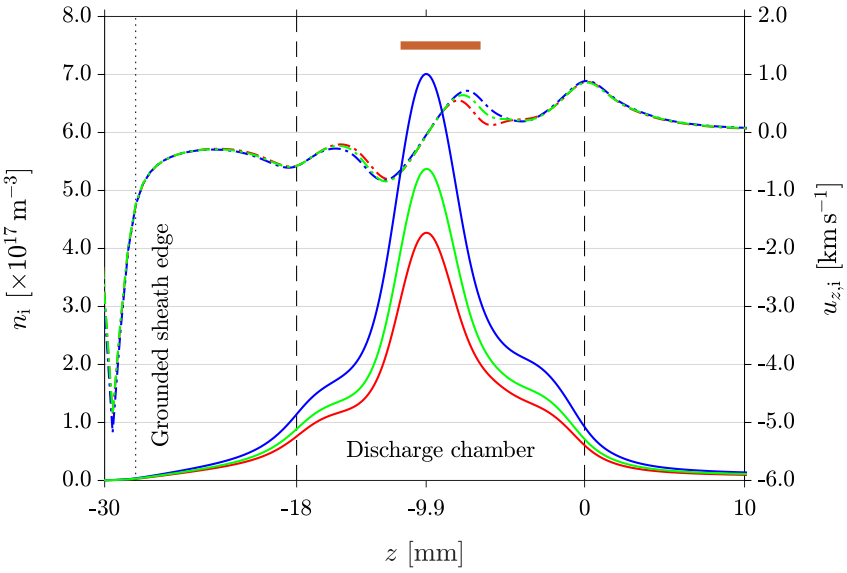

Figure 5.7: Axial profile of the cycle average ion density n_i (— lines) and the cycle average axial ion drift velocity $u_{z,i}$ (-·- lines) along the z-axis for `PR-05` (blue), `PR-10` (green), and `PR-15` (red). n_i peaks at $(z, r) = (-9.9, 0)$ in all three geometries, with similarly shaped profiles featuring a strong central gamma mode peak and two shoulder alpha mode plateaus.

The final assumptions to be verified before calculating the self-bias voltage V_{bias} are the ion transit time τ_i and the variation in the ion drift velocity $\Delta u_{r,i}$ in the powered sheath. The radial transit time is calculated by performing a fourth order Runge-Kutta analysis on $u_{r,i}$ to obtain the cycle average radial drift position of the ion $r_i(t)$ as a function of time (Section 4.6.2). The ion transit times across the powered sheath are: $\tau_i = 134\,\text{ns} = 1.8 \cdot \tau_{RF}$ in `PR-05`, $\tau_i = 103\,\text{ns} = 1.4 \cdot \tau_{RF}$ in `PR-10`, and $\tau_i = 86\,\text{ns} = 1.2 \cdot \tau_{RF}$ in `PR-15`. Given that $\tau_i \sim \tau_{RF}$, $\Delta u_{r,i}$ is expected to be somewhat similar across the three geometries, at $\Delta u_{r,i} = \pm 29.9\,\%$, $\pm 27.1\,\%$, and $\pm 24.6\,\%$ respectively. Since $\Delta u_{r,i}$ is significant in all three geometries, the assumptions made for the $\tau_i \ll \tau_{RF}$ regime are reasonably valid for `PR`.

5.3.4 Self-bias voltage

Finally, substituting $\tau_+/\tau_- = 14/46$ into (5.6) gives:

$$V_{bias} = -V_{pwr} \cdot \sin\left(\frac{\pi}{2} \cdot \frac{46 - 14}{46 + 14}\right) = -0.743 \cdot V_{pwr} \tag{5.9}$$

which for $V_{pwr} = 300\,\text{V}$ results in $V_{bias} = -223\,\text{V}$. However, (5.6) is only accurate for a plasma that is in direct electrically conductive contact with the powered electrode and exposed to the full V_{pwr} amplitude of $\Phi_{pwr}(t)$. This is no longer true in plasma systems where the powered electrode is shielded from the plasma by a component with a non-negligible impedance.

A portion of the RMS RF voltage is dropped across the component, and the resultant RF voltage amplitude on the plasma is $< V_{\text{pwr}}$. In PR, this component is the capacitive discharge chamber wall. In an industrial RIE system, this is the wafer impedance, which includes wafer bulk and spreading resistances, oxide and insulating film capacitances, as well as gap capacitance and contact resistance between the wafer and the powered electrode chuck [165]. The plasma in these systems are exposed to $\Phi_{\text{wall}}(t)$ or $\Phi_{\text{wafer}}(t)$, which have amplitudes $< V_{\text{pwr}}$.

For this type of shielded plasma systems, in particular those operating in the $\tau_{\text{i}} \sim \tau_{\text{RF}}$ or $\tau_{\text{i}} \ll \tau_{\text{RF}}$ regimes, V_{bias} can be defined in a manner that is unaffected by the extra impedances between the powered electrode and the plasma, by using the maxima envelope of the waveform on the plasma-facing surface of the shielding component:

$$V'_{\text{bias}} = \Phi^{+}_{\text{shield}} - V_{\text{pwr}} \tag{5.10}$$

This definition of V'_{bias} is straightforward, and applicable to non-sinusoidal waveforms in general. Most importantly, it is rigorous since Φ^{+}_{shield} is directly correlated with the measurable low energy peak of the IED in the powered sheath. V'_{bias} from (5.10) may also be compared with V_{bias} from (5.6) to quantify any deviances of the plasma system from the ideal case. For PR, (5.10) takes advantage of the asymmetric response of $\Phi_{\text{wall}}(t)$ to the different discharge chamber wall impedances. The result is a constant $V'_{\text{bias}} = \left\langle \Phi^{+}_{\text{wall}} \right\rangle - V_{\text{pwr}} = 53.5\,\text{V} - 300\,\text{V} = -246.5\,\text{V}$ across PR-05, PR-10, and PR-15 on average, which is expected since the root cause of the self-bias, the geometrical area asymmetry of the grounded and powered electrodes, is the same across all three geometries.

Using the traditional definition of $V''_{\text{bias}} = \Phi_{\text{wall}}$ is misleading as it gives erroneous and different values (last column in Table 5.2) for each geometry despite them having the same $A_{\text{gnd}}/A_{\text{pwr}}$ area ratio. Moreover, V''_{bias} is not meaningful since there is no direct correlation between its value and the discharge chamber wall impedances, and does not give accurate insight into the IED in the powered sheath. In earlier works [60, 66] where the imposed voltage on the powered electrode was $V_{\text{pwr}} = 240\,\text{V}$, $\Phi_{\text{wall}}(t)$ was reported to oscillate between $\Phi^{-}_{\text{wall}} = -180\,\text{V}$ and $\Phi^{+}_{\text{wall}} = 70\,\text{V}$. This means that the RMS RF voltage drop across the discharge chamber wall is 81 V, which is a significant 48 % of the original 170 V. The raised negative peaks of $\Phi_{\text{wall}}(t)$ due to such a drastic attenuation causes the mean Φ_{wall} to be artificially raised. This ultimately results in an erroneous $V''_{\text{bias}} = -33\text{V}$, which is unphysical as it is much smaller than the difference in the electric potentials $\Phi^{+}_{\text{wall}} - V_{\text{pwr}} = -170\,\text{V}$ during the positive peaks of the RF cycle. These issues have been remedied in the present generation of CFD-plasma simulations.

If V'_{bias} is constant, then the self-bias charge $Q_{\text{bias}} = C_{\text{wall}} V'_{\text{bias}}$ that accumulates on the capacitive discharge chamber wall must be proportional to C_{wall}. The negative charging of the discharge chamber wall happens during plasma breakdown, and occurs on a time scale of several RF cycles, limited by the speed of positive ions flowing into the grounded electrode [151]. While the CFD-plasma simulations do indeed capture the self-bias charging behaviour during this period, the solutions in the beginning are still evolving from the initial conditions, and are far from being converged. Hence, the data required to calculate Q_{bias} is not explicitly available. However, $Q_{\text{bias}} \propto C_{\text{wall}} \propto n_{\text{i}}$ is a reasonable estimate if the charging duration during plasma breakdown is roughly similar across the three geometries. The values of C_{wall} and n_{i} given in earlier sections are positively correlated, and therefore support this estimate.

5.3.5 Power & voltage division

As shown in Figures 5.6 and 5.7, the cycle average ion density n_{i} is highest in `PR-05` and lowest in `PR-15`. It is known from the plasma energy balance equation [135] that n_{i} is dependent on the total power absorbed by the plasma. The steady state power P may be calculated by integrating the volumetric and surface energy (Section 4.5) in the `PR` simulation domain over the 10 RF cycles in the final solution. This gives $P = 6.984\,\text{W}$, $5.010\,\text{W}$, and $3.834\,\text{W}$ in `PR-05`, `PR-10`, and `PR-15` respectively. P for `PR-10` is in close agreement with the value of $P_{\texttt{PR}} = 4.725\,\text{W}$ measured with a digital inline voltage/current (V/I) probe on the `PR` experimental setup. The cycle average ion density peaks have the respective values: $n_{\text{i}} = 7.010 \times 10^{17}\text{m}^{-3}$, $5.373 \times 10^{17}\text{m}^{-3}$, and $4.271 \times 10^{17}\text{m}^{-3}$, which has a linear correlation coefficient of 0.9995 with P using these three data points and an approximately constant ionisation to power ratio of $n_{\text{i}}/P = 1.1 \times 10^{17}\,\text{m}^{-3}\,\text{W}^{-1}$ across the three cases. The shape of the n_{i} profiles are also in good agreement with previous Langmuir probe experimental measurements [14].

Figure 5.8 plots $\Delta\Phi_{\text{wall}}(t) = \left|\Phi_{\text{pwr}}(t) - \Phi'_{\text{wall}}(t)\right|$, the absolute RF potential difference across the dielectric wall after correcting for the mean negative DC bias of Φ_{wall}. The profiles are similarly shaped across `PR-05` (blue — line), `PR-10` (green — line), and `PR-15` (red — line). The asymmetric waveform is highlighted by the leading peaks resulting from a greater RF potential difference between $\Phi_{\text{pwr}}(t)$ and the diminished trailing edge of the positive peaks in $\Phi'_{\text{wall}}(t)$. The asymmetry also causes the points of intersection between the two waveforms to be displaced from the expected times at every 0.5 RF cycle. The RMS value of the $\Delta\Phi_{\text{wall}}(t)$ profiles (`--` lines) are $\bar{V}_{\text{wall}} = 25.7\,\text{V}$, $32.6\,\text{V}$, and $38.6\,\text{V}$ for `PR-05`, `PR-10`, and `PR-15` respectively.

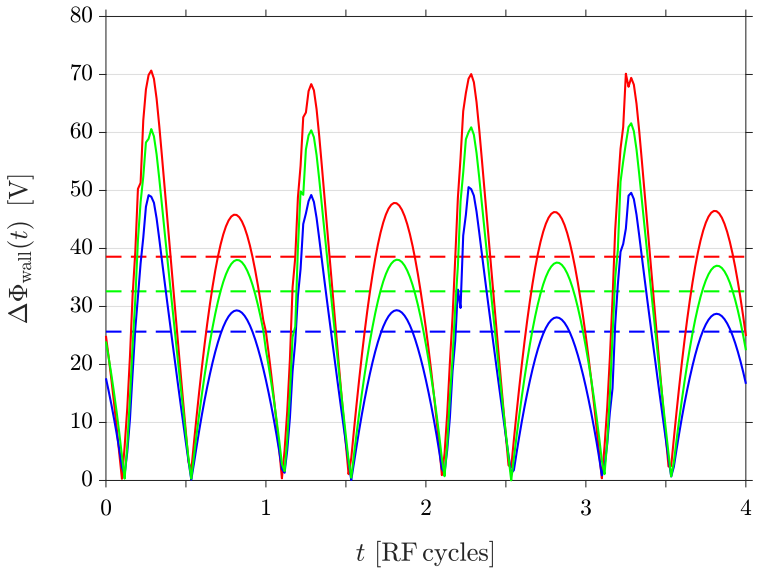

Figure 5.8: Absolute RF potential difference across the dielectric wall $\Delta\Phi_{\text{wall}}(t)$ in `PR-05` (blue — line), `PR-10` (green — line), and `PR-15` (red — line). The coloured `--` lines denote the RMS voltage $\bar{V}_{\text{wall}}$ of each profile. Only four RF cycles are shown for clarity.

Similar calculations can also be performed for the powered and grounded sheaths by tracking the RF potential difference across the widths of the sheaths. For the powered sheath, $\Delta\Phi_{\text{s,pwr}}(t) = \left|\Phi'_{\text{p,pwr}}(t) - \Phi'_{\text{wall}}(t)\right|$ is evaluated between the inner edge of the powered sheath at the coordinates $(z, r) = (-9.9, 0.9)$ and the plasma-facing surface of the discharge chamber wall at $(-9.9, 2.1)$. For the grounded sheath, $\Delta\Phi_{\text{s,gnd}}(t) = \left|\Phi'_{\text{p,gnd}}(t) - \Phi'_{\text{gnd}}(t)\right|$ is evaluated between the inner edge of the grounded sheath at the coordinates $(z, r) = (-28.06, 0)$ and the plasma-facing surface of the front wall at $(z, r) = (-30, 0)$. The RMS values of $\Delta\Phi_{\text{s,pwr}}(t)$ are $\bar{V}_{\text{s,pwr}} = 176.1\,\text{V}$, $170.9\,\text{V}$, and $164.2\,\text{V}$ for `PR-05`, `PR-10`, and `PR-15` respectively, while the RMS values of $\Delta\Phi_{\text{s,gnd}}(t)$ are $\bar{V}_{\text{s,gnd}} = 9.2\,\text{V}$, $8.0\,\text{V}$, and $7.7\,\text{V}$ given in the same order. $\bar{V}_{\text{wall}} + \bar{V}_{\text{s,pwr}} + \bar{V}_{\text{s,gnd}}$ do not exactly add up to the RMS voltage across the `PR` discharge $\bar{V}_{\texttt{PR}} = \bar{V}_{\text{pwr}} = 212.1\,\text{V}$ due to the irregular shapes of the waveforms, but the errors are only on the order of $\sim 1\,\text{V}$.

The $\bar{V}_{\text{s,pwr}}$ and $\bar{V}_{\text{s,gnd}}$ values may be checked against the powered and grounded sheath impedances calculated earlier in Section 5.3.2. The capacitive discharge chamber wall, powered sheath, and grounded sheath may be represented by a voltage divider circuit with their respective impedances $|Z_{\text{wall}}|$, $\left|Z'_{\text{s,pwr}}\right|$, and $\left|Z'_{\text{s,gnd}}\right|$ in series between $\bar{V}_{\text{pwr}} = 212.1\,\text{V}$ and ground. However, due to the unknown proportionality constant ζ, the powered and grounded sheath section of the voltage divider circuit must be considered separately from the capacitive discharge chamber wall.

For convenience of calculation, assume a sinusoidal waveform for $\Delta\Phi_{\text{wall}}(t)$ instead of its actual shape shown in Figure 5.8. Then, $\bar{V}_{\texttt{PR}} - \bar{V}'_{\text{wall}} = \bar{V}'_{\text{p}}$ gives the total RMS RF voltage across both sheaths. Thus, the RMS RF voltage drop across each sheath in a voltage divider circuit is given by:

$$\bar{V}'_{\text{s}} = \bar{V}'_{\text{p}} \cdot \frac{\left|Z'_{\text{s}}\right|}{\left|Z'_{\text{p}}\right|} \tag{5.11}$$

where $\left|Z'_{\text{s}}\right|$ represents either $\left|Z'_{\text{s,pwr}}\right|$ or $\left|Z'_{\text{s,gnd}}\right|$, $\left|Z'_{\text{p}}\right| = \left|Z'_{\text{s,pwr}}\right| + \left|Z'_{\text{s,gnd}}\right|$, and the proportionality constant ζ is eliminated. With $\left|Z'_{\text{s,pwr}}\right| \approx \zeta \cdot 3.7\,\text{k}\Omega$ and $\left|Z'_{\text{s,gnd}}\right| \approx \zeta \cdot 51\,\Omega$, the RMS RF voltage drop across the powered sheath is $\bar{V}'_{\text{s,pwr}} = 183.9\,\text{V}$, $177.1\,\text{V}$, and $171.2\,\text{V}$ for `PR-05`, `PR-10`, and `PR-15` respectively, while the RMS RF voltage drop across the grounded sheath is $\bar{V}'_{\text{s,gnd}} = 2.5\,\text{V}$, $2.4\,\text{V}$, and $2.4\,\text{V}$ in the same order. In this case, the RMS RF voltages sum up to $\bar{V}_{\text{wall}} + \bar{V}'_{\text{s,pwr}} + \bar{V}'_{\text{s,gnd}} = \bar{V}_{\texttt{PR}} = 212.1\,\text{V}$. These values are summarised in Table 5.3.

Table 5.3: Voltage division [V]

Geometry	$\bar{V}_{\text{wall}}$	$\bar{V}_{\text{s,pwr}}$	$\bar{V}'_{\text{s,pwr}}$	$\bar{V}_{\text{s,gnd}}$	$\bar{V}'_{\text{s,gnd}}$
`PR-05`	25.7	176.1	183.9	9.2	2.5
`PR-10`	32.6	170.9	177.1	8.0	2.4
`PR-15`	38.6	164.2	171.2	7.7	2.4

The most obvious discrepancy is $\bar{V}'_{\text{s,gnd}}$ being much lower than $\bar{V}_{\text{s,gnd}}$. This is because the calculation of $\left|Z'_{\text{s,gnd}}\right|$ and $C'_{\text{s,gnd}}$ have not taken into account the variation in distance between the grounded sheath and the plasma bulk due to the geometry of the plenum and the end wall (`S-D`). Areas of the grounded sheath further away from the plasma bulk and the powered electrode are less affected by the oscillating RF potential. The reduction in the effective area results in a smaller $C'_{\text{s,gnd}}$, and therefore a larger $\left|Z'_{\text{s,gnd}}\right|$, which then increases the share of $\bar{V}'_{\text{s,gnd}}$ and decreases $\bar{V}'_{\text{s,pwr}}$. $\bar{V}_{\text{s,pwr}}$ and $\bar{V}_{\text{s,gnd}}$ are not significantly affected by geometry as they are measured along closely adjacent electric field lines, instead of over the electrode surface areas. Overall, the two methods of calculating the RMS RF voltage division are in good agreement.

With these values of $\bar{V}_{\text{wall}}$, $\bar{V}_{\text{s,pwr}}$, and $\bar{V}_{\text{s,gnd}}$, it is possible to calculate the equivalent powered and grounded sheath impedances using:

$$\left|Z_{\text{s}}\right| = \left|Z_{\text{wall}}\right| \cdot \frac{\bar{V}_{\text{s}}}{\bar{V}_{\text{wall}}} \tag{5.12}$$

This gives $\left|Z_{\text{s,pwr}}\right| = 6.4\,\text{k}\Omega$, $9.0\,\text{k}\Omega$, and $10.1\,\text{k}\Omega$, and $\left|Z_{\text{s,gnd}}\right| = 0.34\,\text{k}\Omega$, $0.42\,\text{k}\Omega$, and $0.47\,\text{k}\Omega$ for `PR-05`, `PR-10`, and `PR-15` respectively. Following on from this, it is also possible

to calculate the RMS RF plasma current via Ohm's law, which gives $\bar{I}_{\mathrm{RF}} = 27\,\mathrm{mA}$, 19 mA, and 16 mA for the three respective geometries. The accuracy of these values may be checked by calculating the power $P_{\mathrm{RF}} = \bar{V}_{\mathtt{PR}}\bar{I}_{\mathrm{RF}}$, which gives 5.8 W, 4.0 W, and 3.5 W for `PR-05`, `PR-10`, and `PR-15` respectively. P_{RF} only accounts for the power involved in the movement of the electrically charged species Ar^+ and e^- at the grounded and powered electrodes, and excludes the power sunk into non-electrical processes such as plasma-induced heating of the neutral gas and chemical reactions (Section 4.5). P_{RF} is therefore in good agreement with the integrated steady state power P for each geometry listed earlier in this section.

5.3.6 Powered electrode current

By Ohm's law, the RMS voltage drop across the capacitive discharge chamber wall is equal to the product of the RMS current and its impedance, or $\bar{V}_{\mathrm{wall}} = \bar{I}_{\mathrm{wall}}\,|Z_{\mathrm{wall}}|$. However, obtaining and integrating the spatiotemporal electrical current in `PR` is nontrivial, so the following is an attempt to estimate $\bar{I}_{\mathrm{wall}}$, the RMS current at the plasma-facing surface of the discharge chamber wall directly underneath the powered electrode.

$I_{\mathrm{wall}}(t)$ is a combination of three different charged species fluxes: (i) $I_{\mathrm{i}}(t)$ from the ion flux, which is continuous DC into the wall with a small varying $\Delta u_{r,\mathrm{i}}$ over it, (ii) $I_{\mathrm{e}}(t)$ from the primary electron flux, which is a large diodic spike into the wall during τ_+, and (iii) $I_{\mathrm{e}'}(t)$ from the secondary electron flux, which is a diodic current proportional to the ion flux by the secondary electron emission coefficient $\gamma_{\mathrm{e}'}$, out of the wall during τ_-. These currents are visualised in Figure 5.9. $\Phi_{\mathrm{wall}}(t)$ (black -·- line) is plotted showing the positive period τ_+ and the negative period τ_- of the RF cycle on the horizontal axis. The vertical axes are normalised to the mean $I_{\mathrm{i}} = 1.0$ (blue area), with $I_{\mathrm{i}}(t)$ (blue — line) assumed to have a sinusoidal variation of amplitude proportional to $\Delta u_{r,\mathrm{i}}$ on top of I_{i}, in phase with $-\Phi_{\mathrm{wall}}(t)$.

The CFD-plasma simulations use $\gamma_{\mathrm{e}'} = 0.1$, which means that $I_{\mathrm{e}'}(t) = 0.1 \cdot I_{\mathrm{i}}(t)$ (magenta area), but only during τ_-. $I_{\mathrm{i}}(t)$ and $I_{\mathrm{e}'}(t)$ are positive as they represent a positive ion current into the wall and a negative secondary electron current out of the wall respectively. Over one RF cycle, the total negative charge collected by the wall at the powered electrode must be equal to the total positive charge (5.2). Hence, the negative region bound by $I_{\mathrm{e}}(t)$ (red area) must be equal to the positive area bound by $I_{\mathrm{i}}(t) + I_{\mathrm{e}'}(t)$ over τ_{RF}. Since $I_{\mathrm{e}}(t)$ is limited to τ_+, its vertical amplitude is much larger at $I_{\mathrm{e}}^- = -7.3$, approximately the same for all three geometries, assuming a shape resembling a single negative rectified sinusoidal peak. This number is approximately constant for all three geometries as their $\Delta u_{r,\mathrm{i}}$ are quite similar. Thus, $I_{\mathrm{wall}}(t) = I_{\mathrm{i}}(t) + I_{\mathrm{e}}(t) + I_{\mathrm{e}'}(t)$ is the black — line in Figure 5.9, giving the total RMS

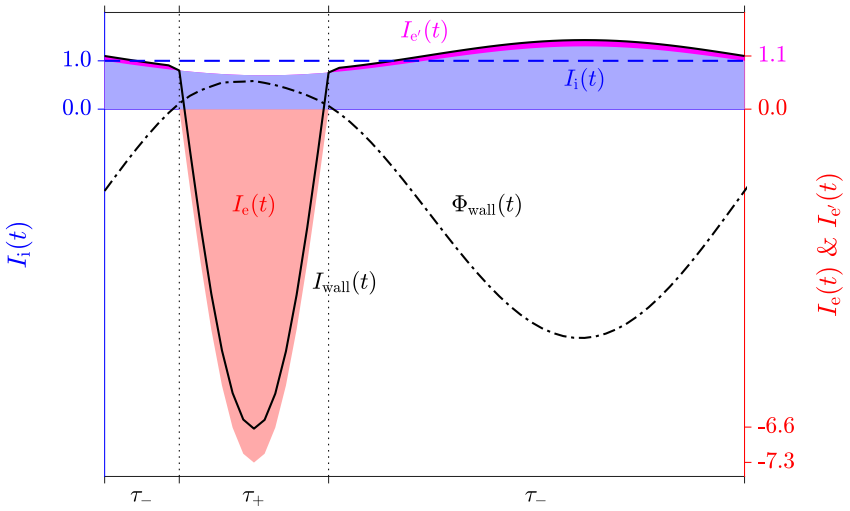

Figure 5.9: Representation of the electron current $I_e(t)$ (red area), ion current $I_i(t)$ (blue area), and secondary electron current $I_{e'}(t)$ (magenta area) at the surface of the discharge chamber wall. The total current $I_{wall}(t)$ (black — line) is the sum of these individual currents. The vertical axes are normalised to $I_i = 1.0$ (blue -- line). $\Phi_{wall}(t)$ (black -·- line) is also plotted to show the positive period τ_+ and the negative period τ_- in the RF cycle.

current $\bar{I}_{wall} = \iota \cdot \bar{I}_i$, with a proportionality constant $\iota \approx 2.4$ for all three geometries.

Now with this estimate for $\bar{I}_{wall}$, Ohm's law in the discharge chamber wall may be roughly approximated as:

$$\bar{V}_{wall} = \nu \cdot \iota \cdot \bar{I}_i \, |Z_{wall}| = \nu \cdot \iota \cdot \frac{q_e \overline{u_{r,i} n_i} A_{wall}}{\omega C_{wall}} \tag{5.13}$$

by assuming $\bar{I}_i = q_e \overline{u_{r,i} n_i} A_{wall}$, where $\overline{u_{r,i} n_i}$ is the RMS ion density flux evaluated at the coordinates $(z, r) = (-9.9, 0.9)$ at the inner edge of the powered sheath, and A_{wall} is the area of the plasma-facing surface of the discharge chamber wall directly underneath the powered electrode. Using $\bar{V}_{wall}$ from Figure 5.8 and the values of the various parameters quoted earlier, the dimensionless proportionality constant for (5.13) is calculated to be $\nu \approx 1.20$, 1.06, and 1.09 for the three respective geometries. The close proximity of ν to unity determines that the derivation of $\bar{I}_{wall} = \iota \cdot \bar{I}_i$ and (5.13) are sound and accurate.

5.4 Secondary electron emission

Figure 5.10 plots the temporal variation of the electron energy $k_B T_e(t)$ at the coordinates $(z, r) = (-9.9, 2.0)$, in the discharge chamber one cell away from the plasma-facing surface

of the discharge chamber wall. This is necessary as the fluid-solid interface is rendered across two cells on either side of the boundary for certain parameters such as $k_{\mathrm{B}}T_{\mathrm{e}}$ and $u_{r,\mathrm{i}}$ (Figure 5.6). The $k_{\mathrm{B}}T_{\mathrm{e}}(t)$ profiles for `PR-05` (blue — line), `PR-10` (green — line), and `PR-15` (red — line) are similar in shape and only differ in peak magnitude. Figure 5.10 also plots the electric potential $\Phi_{\mathrm{wall}}(t)$ (black -·- line) at the surface of the discharge chamber wall at the coordinates $(z, r) = (-9.9, 2.1)$. Only the positive peaks of $\Phi_{\mathrm{wall}}(t)$ are shown for reference.

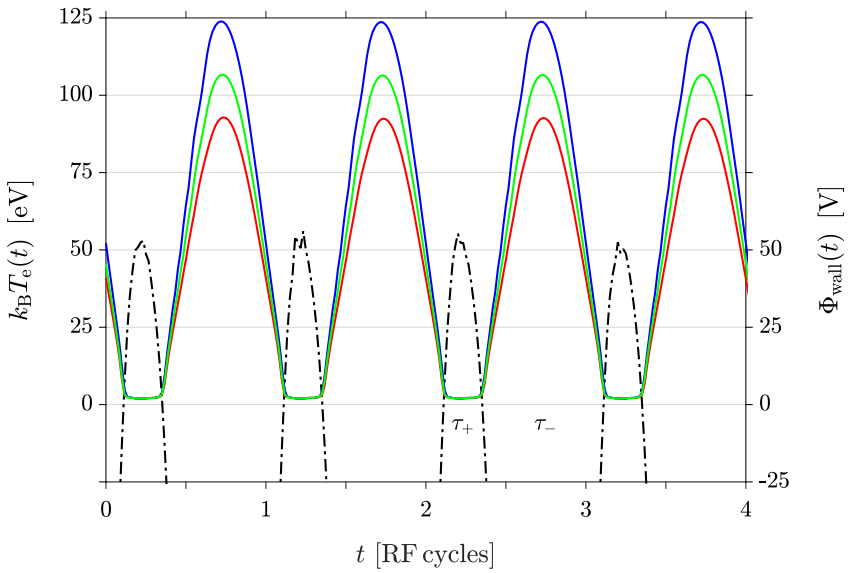

Figure 5.10: Temporal variation of the electron energy $k_{\mathrm{B}}T_{\mathrm{e}}(t)$ at $(z, r) = (-9.9, 2.0)$, in `PR-05` (blue — line), `PR-10` (green — line), and `PR-15` (red — line). Secondary electrons are emitted only during the negative period τ_- of $\Phi_{\mathrm{wall}}(t)$ (black -·- line). Only four RF cycles are shown for clarity.

During τ_+ when $\Phi_{\mathrm{wall}}(t)$ is positive, $k_{\mathrm{B}}T_{\mathrm{e}}(t)$ is low at approximately 2.0 eV for all three geometries, indicating the presence of mainly primary electrons from the plasma bulk. During τ_- however when $\Phi_{\mathrm{wall}}(t)$ is at its most negative, $k_{\mathrm{B}}T_{\mathrm{e}}(t)$ peaks at 123 eV, 106 eV, and 92 eV for `PR-05`, `PR-10`, and `PR-15` respectively, indicating the presence of non-Maxwellian high energy secondary electrons that have been emitted from the surface of the discharge chamber wall due to ion bombardment. The height of the $k_{\mathrm{B}}T_{\mathrm{e}}(t)$ peak is not only dependent on the magnitude of the potential drop across the powered sheath, but also a number of other factors (e.g. RF driving frequency, gradient of the plasma potential, neutral density, etc.) that affect the temporally varying ion drift velocity $u_{r,\mathrm{i}}(t)$ in the collisional powered sheath and the ion bombardment energy. Hence, a fully self-consistent plasma model is required to accurately resolve ion bombardment behaviour and secondary electron emission characteristics in `PR`.

These high energy secondary electrons are the primary source of ionisation in the discharge chamber, driving the strong central gamma mode peak in the ion density (Figure 5.7). Since the high energy secondary electrons are only emitted during τ_- and localised to the region under the powered electrode, the ionisation rate (`R20` in Table 4.2c) is highest in the middle of the discharge chamber during this time. During τ_+, there are no high energy secondary electrons. Instead, bulk electrons from the plenum and the second half of the discharge chamber are drawn towards the positive powered electrode, and the ionisation rate is highest in the first and last thirds of the discharge chamber where the electric field lines are tightest, creating the shoulder alpha mode plateaus seen in Figure 5.7.

5.4.1 Spatiotemporal variation

Figure 5.11 plots the spatiotemporal variation of $k_\mathrm{B}T_\mathrm{e}(t)$ radially along $z = -9.9\,\mathrm{mm}$ in the discharge chamber for `PR-05` (light blue — lines), `PR-10` (light green — lines), and `PR-15` (light red — lines). The — line in the middle of each profile denotes the cycle average $k_\mathrm{B}T_\mathrm{e}$. Notice that the actual peak of the $k_\mathrm{B}T_\mathrm{e}$ radial profiles occurs at two or three cells away from the plasma-facing surface of the discharge chamber wall ($r = 2.1\,\mathrm{mm}$). During $\tau+$, the $k_\mathrm{B}T_\mathrm{e}(t)$ radial profiles are low and flat across the whole radius of the discharge chamber, indicating the collapse of the powered sheath. During τ_-, the $k_\mathrm{B}T_\mathrm{e}(t)$ radial profiles start to rise near the discharge chamber wall as ion bombardment begins to liberate high energy secondary electrons. As the $k_\mathrm{B}T_\mathrm{e}(t)$ radial profiles rise, they also start to extend further from the discharge chamber wall, indicating the formation of the powered sheath. The set of 60 lines representing the 60 time-steps per RF cycle illustrates the oscillatory behaviour of $k_\mathrm{B}T_\mathrm{e}(t)$ and the powered sheath.

The high energy secondary electrons emitted from the discharge chamber wall are depleted mainly via gamma mode ionisation collisions with the ground state neutral Ar as they transit the powered sheath. The electron population in the plasma bulk is predominantly low energy primary electrons at a stable $k_\mathrm{B}T_\mathrm{e} = 2.9\,\mathrm{eV}$ on average across the three geometries.

Additionally, there is spatial variation in the distribution of the negative self-bias charge in the discharge chamber wall, mainly localised to the ungrounded section of the wall near the powered electrode. Figure 5.12 plots the spatiotemporal variation of $\Phi_\mathrm{wall}(t)$ (top) axially along $r = 2.1\,\mathrm{mm}$ between $-18 \leq z \leq 0$, and $k_\mathrm{B}T_\mathrm{e}(t)$ (bottom) axially along $r = 2.0\,\mathrm{mm}$, one cell away from the plasma-facing surface of the discharge chamber wall in the same range of z. `PR-05`, `PR-10`, and `PR-15` are represented by the colours blue, green, and red respectively. The — line in the middle of each plot denotes the cycle average, while the ····· curve shows

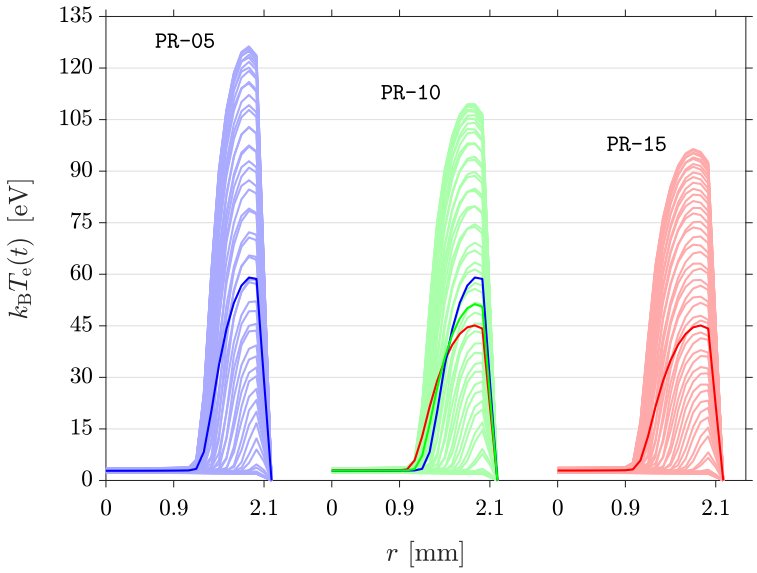

Figure 5.11: Spatially and temporally resolved electron energy $k_B T_e(t)$ profiles across the radius of the discharge chamber along $z = -9.9\,\text{mm}$ in PR-05 (light blue — lines), PR-10 (light green — lines), and PR-15 (light red — lines). The cycle average electron energy $k_B T_e$ for PR-05 (blue — line) and PR-15 (red — lines) are superimposed onto the PR-10 profile for comparison.

the temporal variation of each profile over the RF cycle. The axial position of the powered electrode is shown by the brown bar at the middle for each geometry, while the rear and end walls of the grounded structure are represented by the grey bars. The uncoloured space between the bars denote the sections of the discharge chamber wall that are electrically insulated by the Macor discs from both the powered electrode and the grounded structure (Figure 4.3).

During τ_-, the $\Phi_{\text{wall}}(t)$ axial profiles have a plateau shape where $\Phi_{\text{wall}}(t)$ is greatly negative in the region underneath the powered electrode. The electric potential at the sections of the discharge chamber wall underneath the grounded structure is close to zero but slightly positive (6.7 V on average) due to the presence of the positive plasma potential. There is a steep gradient in $\Phi_{\text{wall}}(t)$ across the surface of the insulated section of the discharge chamber wall, suggesting that ions are drawn towards the negatively biased wall from a wider angle in the discharge chamber instead of only in the radial direction. During τ_+, the powered sheath is collapsed, and $\Phi_{\text{wall}}(t)$ on the ungrounded sections of the discharge chamber wall become positive due to the positive $\Phi_p(t)$ of the plasma bulk. The positive peak of Φ^+_{wall} is also much flatter than the negative peak Φ^-_{wall} or the cycle average Φ_{wall}, which results in less ambiguity in the definition of V'_{bias} (5.10).

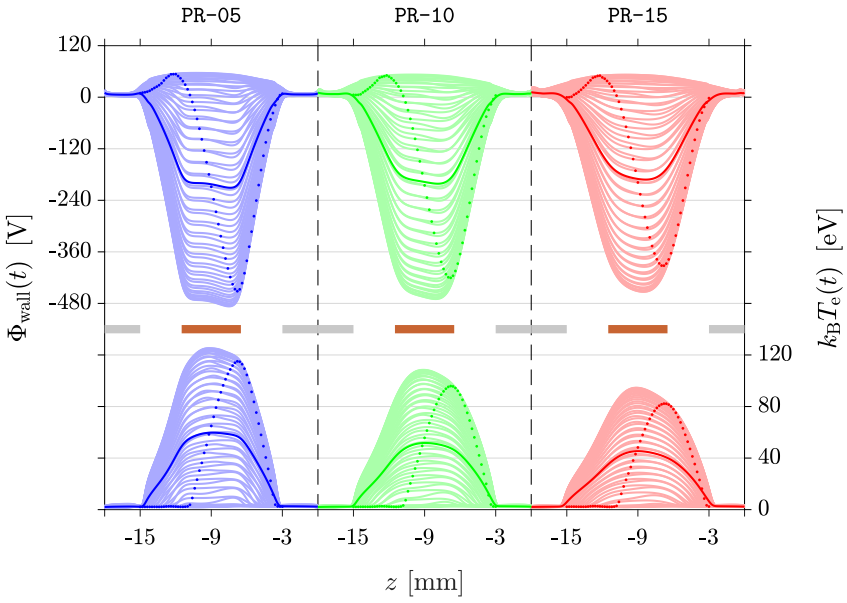

Figure 5.12: Spatially and temporally resolved electric potential $\Phi_{\text{wall}}(t)$ (top) and electron energy $k_{\text{B}}T_{\text{e}}(t)$ (bottom) profiles along the surface of the discharge chamber wall in `PR-05` (light blue — lines), `PR-10` (light green — lines), and `PR-15` (light red — lines). Coloured — lines denote the cycle average, while the ····· curves illustrate the oscillation of the respective profiles over one RF cycle.

The emission region for secondary electrons is not limited to the section of the discharge chamber wall underneath powered electrode, but extends to cover the insulated section as well. The $k_{\text{B}}T_{\text{e}}(t)$ axial profiles are low and flat in the emission region during τ_+, and likewise along the grounded section of the discharge cavity wall but for the whole RF cycle instead, indicating the absence of high energy secondary electrons in the respective regions during these periods. The $k_{\text{B}}T_{\text{e}}(t)$ axial profile only rises during τ_+, as illustrated by the ····· curve in each profile.

Figure 5.13 shows a 2D axisymmetric colour map of the secondary electron energy $k_{\text{B}}T_{\text{e}}$ in the discharge chamber at the negative peak of the RF cycle for `PR-05` (top), `PR-10` (middle), and `PR-15` (bottom). The colour scale ranges from 0 eV (blue) to 127 eV (magenta), with isocurves (black — lines) denoting every 20 eV. $k_{\text{B}}T_{\text{e}}$ peaks at 127 eV, 111 eV, and 99 eV for `PR-05`, `PR-10`, and `PR-15` respectively. The high energy secondary electrons indicate the full extent of the powered sheath during the negative peak of $\Phi_{\text{wall}}(t)$. CFD-ACE+ is capable of producing plots like these for any tracked parameter with high spatial and temporal resolution (determined by the set mesh density and time-step size), which may be viewed as an animation to demonstrate the temporal evolution of fluid, electrical, and plasma properties in the simulation domain.

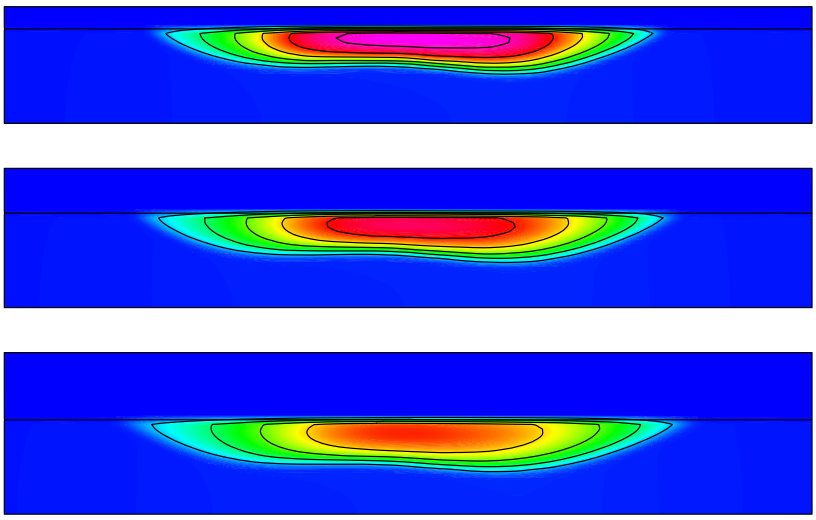

Figure 5.13: 2D colour map of the secondary electron energy $k_B T_e$ in the discharge chamber at the negative peak of the RF cycle for `PR-05` (top), `PR-10` (middle), and `PR-15` (bottom). The colour scale ranges from 0 eV (blue) to 127 eV (magenta), with isocurves (black — lines) denoting every 20 eV.

5.5 Chapter summary

This chapter investigates the self-bias in the `PR` discharge arising from the geometrical area asymmetry of the grounded and powered electrodes. CFD-plasma simulations are performed for three geometries, `PR-05`, `PR-10`, and `PR-15`, with varying discharge chamber wall thickness. A RF circuit model of the `PR` discharge is derived using the electric potential across the discharge chamber wall, and the powered and grounded plasma sheaths. The computed voltage division between these components of the RF circuit model is compared to a theoretical estimate of their respective impedances. The results are in very good agreement, apart from a small discrepancy at the grounded sheath caused by not accounting for the preference of the plasma to return to ground at surfaces nearer to the discharge chamber. Additionally, the plasma current quantified as the sum of the electron, ion, and secondary electron currents gives a reasonably accurate electrical model of the `PR` discharge.

The CFD-plasma simulations and the derived RF circuit model provides a comprehensive picture of the `PR` discharge. Due to the capacitive impedance of the dielectric discharge chamber wall, the electric potential at the plasma-facing surface is different to the applied RF waveform on the powered electrode, and varies along the length of the discharge chamber since the self-bias is spatially nonuniform. The CFD-plasma simulation results show an asymmetric response in the plasma potential at the surface of the discharge chamber wall,

where the negative peaks are displaced due to the extraneous impedance introduced by the dielectric discharge chamber wall, while the positive peaks remain constant across `PR-05`, `PR-10`, and `PR-15`. This is in good agreement with experimental observations of the bimodal ion energy distribution in the powered sheath, and the electric potential profiles also show the diminished trailing edge at each positive peak in accordance with experimental observations of self-biased voltage waveforms.

Consequently, the traditional high frequency regime quasi-steady-state sheath circuit model definition of the self-bias voltage using the mean electric potential at the plasma-facing surface of the discharge chamber wall is no longer valid; firstly because the ion transit time across the powered sheath is on the order of a RF period, and secondly because the mean electric potential is different in each geometry despite there being no change in the area ratio of the grounded and powered electrodes. The definition of the self-bias voltage used in the thin sheath regime is also inaccurate as it does not account for the asymmetric response of the plasma potential, nor the spatially nonuniform self-bias. Under these circumstances, the maxima envelope of the computed electric potential alternatively provides a more stable baseline for a more rigorous definition of the self-bias voltage, since it is characteristic of the plasma parameters and the geometry of the plasma system. Another advantage of this definition is that it is applicable to non-sinusoidal waveforms, and directly correlates with the measurable low energy peak of the ion energy distribution in the powered sheath.

Finally, the CFD-plasma simulations are used to study the spatiotemporal electron dynamics within the RF cycle. Secondary electrons are only emitted when the electric potential at the plasma-facing surface of the discharge chamber wall is negative, and have much higher energies than the bulk electrons.

Chapter 6

Vacuum expansion

The CFD and CFD-plasma simulations and experiments discussed in the preceding chapters have been performed with a background pressure of $p_0 = 0.349\,\text{Torr}$ set at the outlet boundary. However, for application as a space microthruster, a better model with $p_0 = 0\,\text{Torr}$ is desired for a more accurate depiction of the propellant expanding into vacuum.

This chapter presents CFD simulations of the cold gas operation of the *Pocket Rocket* (`PR`) and *Mini Pocket Rocket* (`MiniPR`) radiofrequency electrothermal microthrusters, replicating experiments performed in both sub-Torr and vacuum environments. For the present purposes, hybrid or DSMC modelling techniques are not necessary since the primary interest is in modelling the relatively low Kn internal regions of the microthrusters. The present CFD modelling technique takes advantage of the flow velocity choking phenomenon to unconventionally circumvent the problem of including vacuum regions within a CFD simulation, while still preserving the accuracy of the desired results in the upstream fluid regions. A third variation of the microthruster with a constricted nozzle throat, designated as `PR-C`, is designed and used to validate the reliability of the vacuum expansion CFD simulations.

The theory of flow velocity choking is discussed, followed by an analysis of the CFD simulation results, and the computed thrust force is compared with experimental pendulum thrust balance measurements performed with `MiniPR`. For low thrust conditions where experimental instruments are not sufficiently sensitive, the CFD simulations provide additional data points against which experimental results can be verified and extrapolated. Most importantly, the CFD simulations reveal details of rarefied boundary layer flow dynamics in the slip regime, which warrant a treatment distinct to conventional fluid flow in the continuum regime.

6.1 CFD simulation setup

MiniPR, previously described in [15, 46, 53], is a variation of the PR microthruster with a narrower discharge chamber. The internal diameter of the MiniPR discharge chamber is $r = 0.8\,\text{mm}$ instead of 2.1 mm, and the discharge chamber wall is 0.7 mm thick instead of 1.0 mm. All the other dimensions of MiniPR are identical to that of PR, and the MiniPR simulation mesh is therefore very similar to that of PR (Figure 2.8), but with fewer cells across the radius of the discharge chamber at the same $0.1\,\text{mm} \times 0.1\,\text{mm}$ mesh density.

PR-C is a new geometry (Figure 6.1), identical to PR in all dimensions except for a constriction in the discharge chamber that resembles a converging-diverging nozzle. The convergent section is between $-6.5\,\text{mm} \leq z \leq -3.0\,\text{mm}$, while the divergent section is between $-3.0\,\text{mm} \leq z \leq 0\,\text{mm}$. The constricted nozzle throat at $z = -3.0\,\text{mm}$ has a radius of $r = 1.05\,\text{mm}$, half that of the internal discharge chamber radius. As such, the exit to throat area ratio is $A_{\text{ex}}/A_{\text{tt}} = 4$.

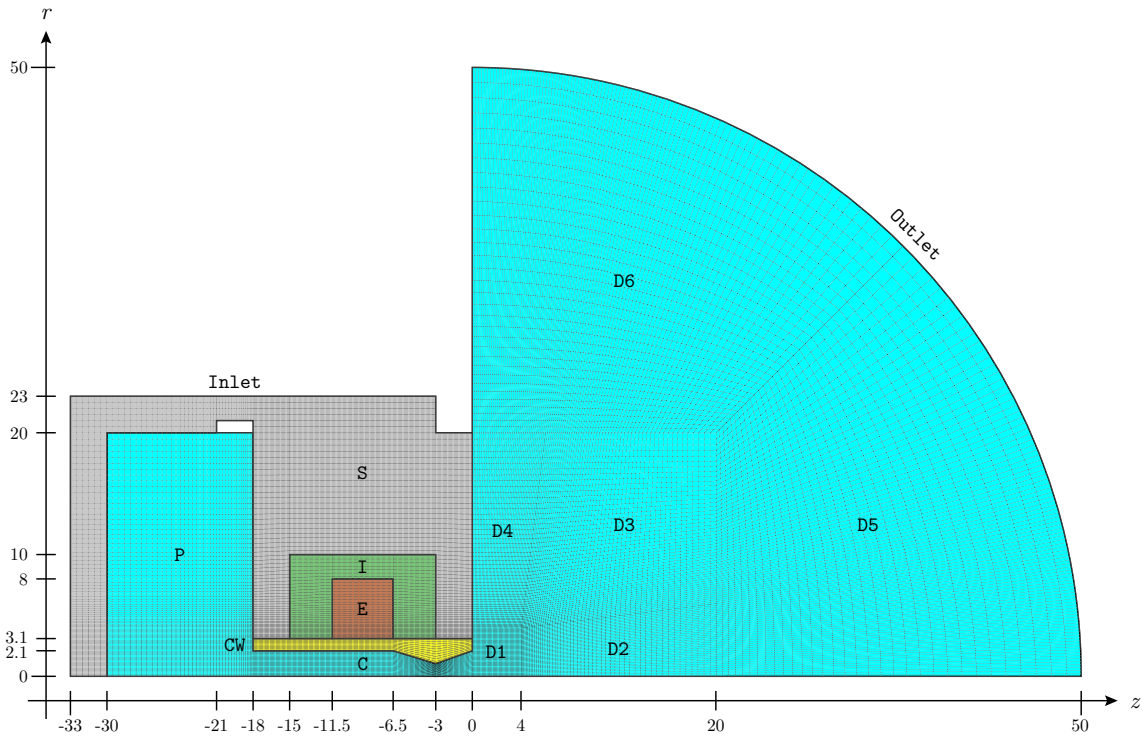

Figure 6.1: PR-C simulation mesh (36,288 cells). Fluid regions (aqua): plenum (P), discharge chamber (C), and downstream (D). Solid regions: Al structure (S, grey), Macor insulation (I, dark green), Cu powered electrode (E, brown), and Al_2O_3 discharge chamber wall (CW, yellow).

As mentioned earlier in Section 2.2.2, a hemispherical outlet boundary is chosen as it is equidistant from the discharge chamber exit and isotropic, thus eliminating any directional bias and circulation effects that arise from boundaries at unequal distances, as well as computational anomalies caused by corners. This becomes especially important when running CFD simulations using an outlet boundary static pressure of $p_0 = 0\,\text{Torr}$, since it is technically beyond the capabilities of the fluid numerical method because the flow in the downstream region enters the transitional ($0.1 \lesssim \text{Kn} \lesssim 10$) and free molecular regimes ($\text{Kn} \gtrsim 10$). To mitigate unphysical behaviour, the vacuum outlet boundary has to be place at a sufficient distance away from the important regions of the simulation, namely the discharge chamber (`C`) and the immediately neighbouring downstream region `D1`. This is the main reason for having the 50 mm radius hemispherical downstream region. If modelling $p_0 = 0\,\text{Torr}$ is not necessary, then the unimportant downstream region can be made much smaller to decrease the number of cells in the `PR` simulation mesh, and greatly reduce computation time.

The CFD simulations are set up using the same procedure detailed in Section 3.3. The `PR` and `PR-C` CFD simulations are run using $\dot{m} = 25$, 50, 75, 100, and 144 SCCM of cold Ar gas, while the `MiniPR` CFD simulation is run using $\dot{m} = 15$, 30, 45, 60 SCCM of cold Xe gas. The volume conditions are the same across the CFD simulations, except for the parameters specific to the respective gas species. The slip boundary condition is applied to all solid-plasma interfaces, with the recommended $\alpha_u = 0.9$ and $\alpha_T = 0.9$ tangential momentum and thermal accommodation coefficients for Ar, and $\alpha_u = 1.0$ and $\alpha_T = 0.8$ for Xe. The `PR` and `PR-C` CFD simulations are performed using outlet boundary static pressures set to the experimentally measured p_0 in the vacuum chamber at each $\dot{m}$ (Table 3.4) and a backflow temperature of $T_0 = 300\,\text{K}$, as well as $p_0 = 0\,\text{Torr}$ and $T_0 = 0\,\text{K}$ for vacuum expansion, while the `MiniPR` CFD simulations are performed using $p_0 = 0\,\text{Torr}$ and $T_0 = 0\,\text{K}$ only. The initial conditions in each case are modified slightly from Table 3.5 to accommodate the different stagnation pressures p_{st} resulting from using different gas species and geometries.

From this point on, '`PR-O`' is used to designate the original `PR` geometry, while '`PR`' refers to the *Pocket Rocket* microthruster in general.

6.2 Flow velocity choking

Flow velocity choking is a compressible flow effect. Consider isentropic flow of a compressible fluid through a stream tube. Assume that the cross sectional area A_r of the stream tube varies sufficiently slowly along the z-axis, so that the flow depends only on the distance along the stream tube and is approximately 1D. Through Bernoulli's equation, the conservation

of mass, and the isentropic flow relations [166], the variation in the axial velocity of the flow $\delta u_z/u_z$ can be related to the variation of the cross sectional area $\delta A_r/A_r$ by:

$$\frac{\delta u_z}{u_z} = \frac{1}{\mathrm{Ma}^2 - 1} \cdot \frac{\delta A_r}{A_r} \tag{6.1}$$

where $\mathrm{Ma} = u_z/c_\mathrm{s}$ is the Mach number, defined as the ratio of the axial velocity u_z to the local sound speed c_s (1.3).

(6.1) reveals that when the flow is subsonic ($\mathrm{Ma} < 1$), a decrease in A_r results in an increase in u_z ($\delta u_z \propto -\delta A_r$). Conversely, when then flow is supersonic ($\mathrm{Ma} > 1$), increasing A_r also increases u_z ($\delta u_z \propto \delta A_r$). At the critical state of $\mathrm{Ma} = 1$, $\delta A_r/A_r$ must necessarily be zero. This means that the flow must either be expanding into an infinite area, or that A_r must be at a minimum, i.e. at the *vena contracta* of the stream tube. This fact is of great significance in high speed flows as it dictates that a subsonic flow cannot be accelerated to supersonic speed without first having satisfied either of the aforementioned conditions. Hence, for a converging nozzle, the maximum flow velocity attainable is c_s, occurring at the exit. To achieve supersonic flow, a converging-diverging nozzle is required. The convergent section of the nozzle accelerates the subsonic flow, which then attains c_s when A_r narrows to the minimum at the throat. Thereafter, the divergent section of the nozzle further accelerates the sonic flow to supersonic speed.

6.2.1 Pressure gradient

The acceleration of the flow is directly related to the pressure gradient. If the pressure gradient is insufficiently steep, the flow does not become sonic. Thus, there is a minimum pressure difference across the *vena contracta* required for achieving sonic flow. For a polytropic gas with the adiabatic index γ, the ratio of the stagnation pressure p_st upstream of the *vena contracta* to the critical downstream pressure p_0^* required for achieving sonic flow is:

$$\frac{p_\mathrm{st}}{p_0^*} = \left(\frac{\gamma + 1}{2}\right)^{\frac{\gamma}{\gamma - 1}} \tag{6.2}$$

(6.2) is exact only if the pressure difference occurs in the immediate vicinity of the *vena contracta*. In such case, the critical pressure ratio is $p_\mathrm{st}/p_0^* = 2.053$ for a monatomic ideal gas with $\gamma = 5/3$, and $p_\mathrm{st}/p_0^* = 1.893$ for a diatomic ideal gas with $\gamma = 7/5$. The critical pressure ratio varies almost linearly with γ, and is of the same order of magnitude for all gases ($p_\mathrm{st}/p_0^* \sim 2$). When (6.2) is satisfied, the flow velocity attains c_s at the *vena contracta*. Further decreasing the downstream pressure does not cause the flow velocity at the *vena contracta* to exceed c_s, since $\mathrm{Ma} = 1$, if it occurs, must be at the *vena contracta*. This

phenomenon is known as flow velocity choking. When the flow is choked, the flow conditions upstream of the *vena contracta* become insensitive to the flow conditions downstream.

In reality, the pressure drop is not immediate but instead manifests over a nonzero distance. Figure 6.2 plots the static pressure p along the z-axis in `PR-O` for the CFD simulations performed with $\dot{m} = 100\,\text{SCCM}$ of Ar, using $p_0 = 0.349\,\text{Torr}$ (blue — line) and $p_0 = 0\,\text{Torr}$ (blue −·− line). Since p falls continuously along the entire length of the discharge chamber, p_{st}/p_0^* (6.2) cannot be used to determine if the flow velocity choking condition is met. Nonetheless, the close proximity of the p profiles (blue — and −·− lines) suggests that the flow conditions upstream are very similar despite the difference in p_0 downstream, and therefore is indicative of some degree of of flow velocity choking in `PR-O`.

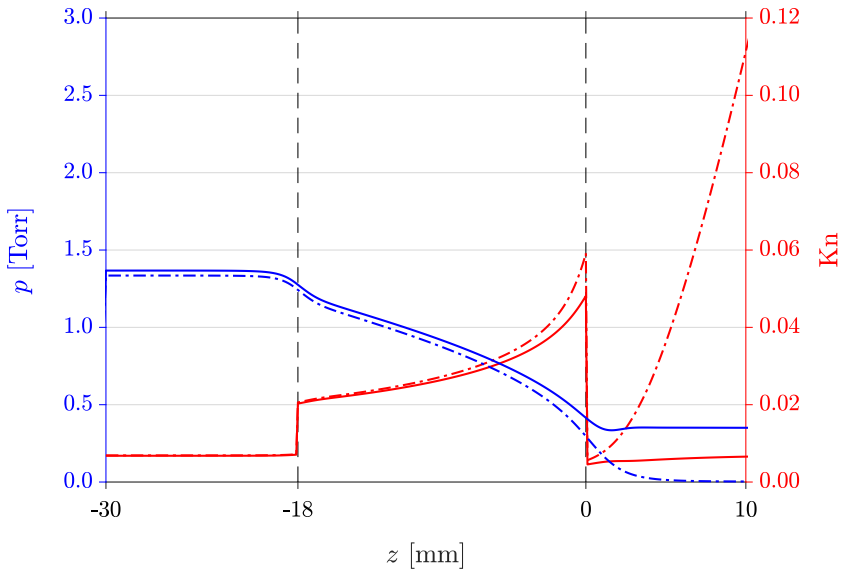

Figure 6.2: Static pressure p (blue) and Knudsen number Kn (red) along z-axis in `PR-O` for CFD simulations performed with $p_0 = 0.349\,\text{Torr}$ (— lines) and $p_0 = 0\,\text{Torr}$ (−·− lines). p falls continuously along the entire length of the discharge chamber, and exhibits deviation between the $p_0 = 0.349\,\text{Torr}$ and $p_0 = 0\,\text{Torr}$ cases.

`PR-C` on the other hand demonstrates a well defined choked flow behaviour. The p profiles for both the $p_0 = 0.349\,\text{Torr}$ (blue — line) and $p_0 = 0\,\text{Torr}$ (blue −·− line) cases shown in Figure 6.3 drop sharply in the vicinity of the constricted nozzle throat at $z = -3.0\,\text{mm}$. Furthermore, the p profiles in both cases coincide along the length of `PR-C` up to very near the discharge chamber exit, exhibiting the characteristic behaviour of choked flow, whereby flow conditions upstream of the constricted nozzle throat are identical despite the significant difference in the downstream pressure p_0. This is in contrast to the p profiles in `PR-O` (Figure 6.2), which show a small deviation.

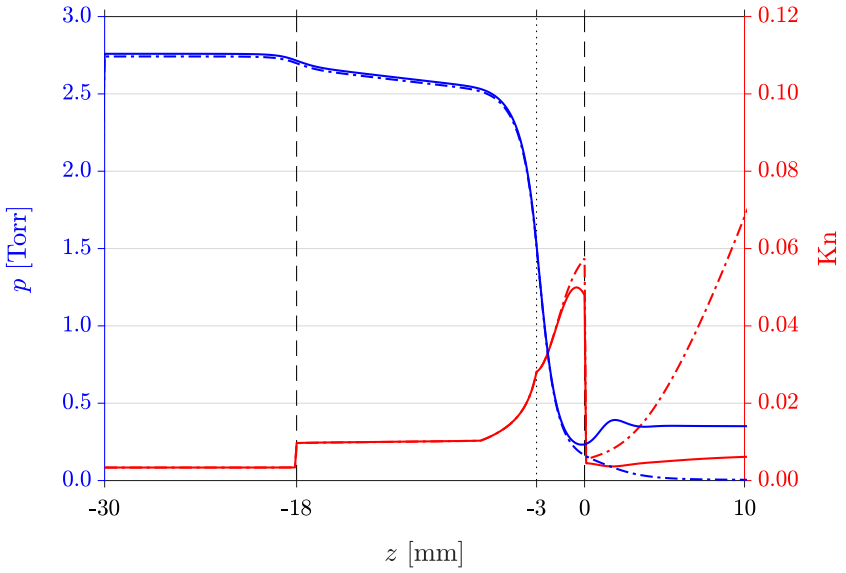

Figure 6.3: Static pressure p (blue) and Knudsen number Kn (red) along z-axis in `PR-C` for CFD simulations performed with $p_0 = 0.349$ Torr (— lines) and $p_0 = 0$ Torr (-·- lines). The pressure gradient is slight in the plenum and discharge chamber, and p is mostly dropped at the constricted nozzle throat. The p profiles in both cases coincide, exhibiting characteristic choked flow behaviour.

The stagnation pressure in the `PR-C` plenum for the $p_0 = 0$ Torr case is $p_{st} = 2.745$ Torr, which is about twice that of the `PR-O`, $p_0 = 0$ Torr case where $p_{st} = 1.336$ Torr. Due to the constricted nozzle throat, the discharge chamber upstream of the convergent section ($z \leq -6.5$ mm) is held at a high static pressure with only a slight gradient along the z-axis, in contrast with the continuously falling p in `PR-O`. Since most of the pressure difference is dropped over a short distance in the constricted nozzle, (6.2) is somewhat applicable for `PR-C`. Using the value of p_{st} quoted above, the critical downstream pressure is $p_0^* \lesssim 1.337$ Torr. This is another confirmation that the flow in `PR-C` is choked for both the $p_0 = 0.349$ Torr and $p_0 = 0$ Torr cases.

Also plotted in Figures 6.2 and 6.3 is the Knudsen number Kn (3.2) in the plenum, discharge chamber, and downstream regions (red — and -·- lines lines). Since Kn $\propto 1/p$, a decrease in p results in an increase in Kn. In the discharge chamber, Kn is highest at the exit ($z = 0$ mm), but remains in the slip regime (Kn $\lesssim 0.1$) within which the fluid numerical method is completely valid. However, for the $p_0 = 0$ Torr cases, the low pressure in the downstream region causes Kn (red -·- line) to rise very quickly, and the fluid numerical method ceases to be valid at a certain distance beyond the discharge chamber exit. While the Kn $\lesssim 0.1$ limit may be used as a guide, it is by no means a definitive indicator of when the

fluid numerical method breaks down. Hence, the CFD simulation results in the downstream region beyond $z > 0\,\text{mm}$ are not used for analysis. Regardless, the CFD simulation results for $z \leq 0\,\text{mm}$ up to the discharge chamber exit are unaffected by virtue of flow velocity choking.

6.2.2 Axial velocity

Figure 6.4 plots the axial velocity u_z (blue) and the local sound speed $c_\text{s} = \sqrt{\gamma k_\text{B} T/m}$ (red) in `PR-O` for the $p_0 = 0.349\,\text{Torr}$ (— lines) and $p_0 = 0\,\text{Torr}$ (-·- lines) cases. At the entrance of the discharge chamber, there is an increase in u_z accompanying the drop in p due to the Venturi effect, as the radius of the flow system shrinks from $r = 20\,\text{mm}$ in the plenum to $r = 2.1\,\text{mm}$ in the discharge chamber. In the discharge chamber, the propellant is gradually accelerated by the negative pressure gradient (Figure 6.2) up to c_s near the exit. For the $p_0 = 0.349\,\text{Torr}$ case, $c_\text{s} = 284.8\,\text{m}\,\text{s}^{-1}$ is attained at $z = -0.58\,\text{mm}$. u_z peaks slightly beyond the discharge chamber exit and then starts to decrease as the propellant encounters the static background gas in the downstream region. For the $p_0 = 0\,\text{Torr}$ case, $c_\text{s} = 283.5\,\text{m}\,\text{s}^{-1}$ is attained slightly further upstream at $z = -1.58\,\text{mm}$, and u_z continues to rise beyond the discharge chamber exit. The CFD simulation results in the downstream region for the $p_0 = 0\,\text{Torr}$ case are not guaranteed to be accurate due to Kn being higher than what the fluid numerical method is suitable for, but are nonetheless indispensable for creating the conditions required for vacuum expansion.

Figure 6.5 plots the same parameters u_z (blue) and c_s (red) in `PR-C` for the $p_0 = 0.349\,\text{Torr}$ (— lines) and $p_0 = 0\,\text{Torr}$ (-·- lines) cases. The increase in u_z due to the Venturi effect at the entrance of the discharge chamber is smaller since the pressure difference between the plenum and the discharge chamber is small. Unlike in `PR-O`, the negative pressure gradient only develops in the constricted nozzle ($-6.5\,\text{mm} \leq z \leq 0.0\,\text{mm}$). Hence, u_z holds a constant value in the straight section of the discharge chamber, and the propellant only begins to accelerate as it enters the constricted nozzle. u_z becomes sonic slightly downstream of the constricted nozzle throat at $z = -2.79\,\text{mm}$ for both cases, though at slightly different velocities with $c_\text{s} = 280.3\,\text{m}\,\text{s}^{-1}$ for the $p_0 = 0.349\,\text{Torr}$ case and $c_\text{s} = 279.3\,\text{m}\,\text{s}^{-1}$ for the $p_0 = 0\,\text{Torr}$ case. u_z only begins to deviate near the discharge chamber exit. u_z peaks at $z = -0.4\,\text{mm}$ within the divergent section of the constricted nozzle due to overexpansion in the $p_0 = 0.349\,\text{Torr}$ environment, which also causes the instability in u_z that is visible slightly beyond the discharge chamber exit. Overall, the congruence of the u_z profiles within `PR-C` again demonstrates a well defined choked flow behaviour.

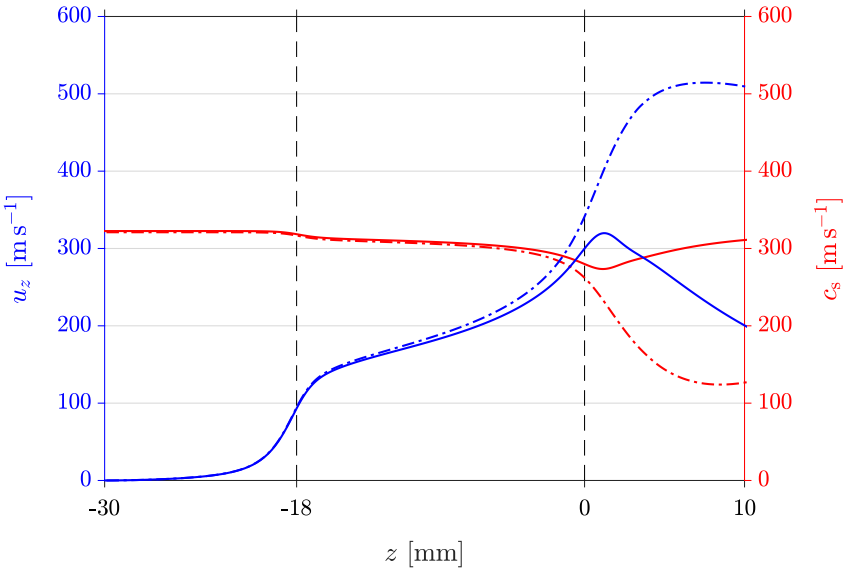

Figure 6.4: Axial velocity u_z (blue) and local sound speed c_s (red) along z-axis in PR-O for CFD simulations performed with $p_0 = 0.349\,\text{Torr}$ (— lines) and $p_0 = 0\,\text{Torr}$ (-·- lines). u_z rises gradually along the discharge chamber and becomes sonic near the exit.

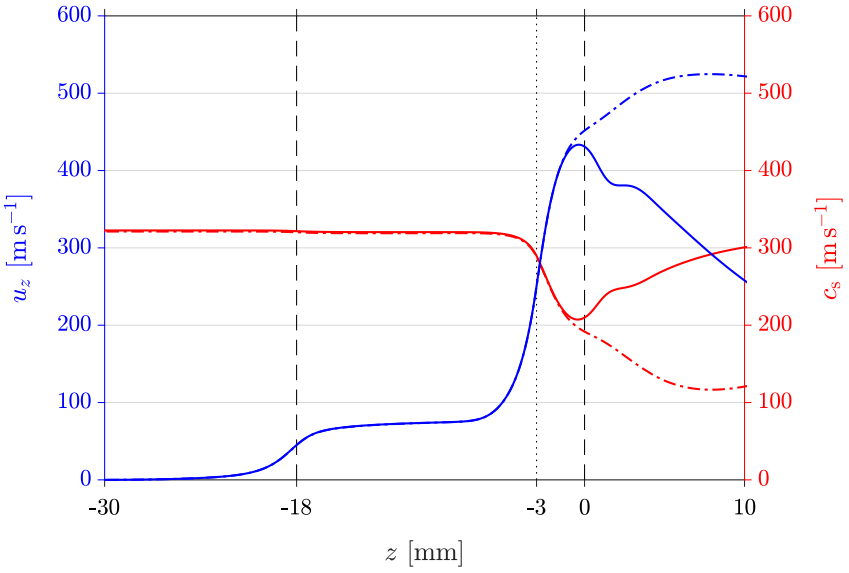

Figure 6.5: Axial velocity u_z (blue) and local sound speed c_s (red) along z-axis in PR-C for CFD simulations performed with $p_0 = 0.349\,\text{Torr}$ (— lines) and $p_0 = 0\,\text{Torr}$ (-·- lines). u_z rises rapidly and becomes sonic in the constricted nozzle throat.

6.2.3 Sonic surface

The u_z profiles plotted in Figures 6.4 and 6.5 only show the 1D flow behaviour on the z-axis. However, in the narrow discharge chamber of PR, the overall flow behaviour is strongly dictated by the boundary layer adjacent to the discharge chamber wall. A complete de-

scription of the flow velocity choking effects therefore requires a 2D characterisation. Figure 6.6 is a 2D cross section colour map of the velocity magnitude $u = \sqrt{u_z^2 + u_r^2}$ in: (a) PR-O with $p_0 = 0.349\,\text{Torr}$, (b) PR-O with $p_0 = 0\,\text{Torr}$, (c) PR-C with $p_0 = 0.349\,\text{Torr}$, (d) PR-C with $p_0 = 0\,\text{Torr}$, all using $\dot{m} = 100\,\text{SCCM}$ of Ar, and (e) MiniPR with $p_0 = 0\,\text{Torr}$ using $\dot{m} = 60\,\text{SCCM}$ of Xe. The colour scale ranges from $0\,\text{m}\,\text{s}^{-1}$ (blue) to $500\,\text{m}\,\text{s}^{-1}$ (magenta), and isocurves black — lines are drawn representing Mach numbers Ma = 0.25, 0.5, 0.75, and 1.0. The plenum (left) and downstream (right) regions have been cropped to focus mainly on the flow behaviour in the discharge chamber.

In all cases, the propellant enters the discharge chamber uniformly across the greater portion of the cross section, except in the slow boundary layer near the discharge chamber wall. In PR-O (Figures 6.6a and 6.6b) and MiniPR (Figure 6.6e) The parabolic shape of the u profile (2D colour map) and the Ma = 0.5 and 0.75 isocurves reveal that the middle of the flow accelerates faster than the boundary layer flow which remains at a relatively low velocity until near the discharge chamber exit. In PR-C (Figures 6.6c and 6.6d) on the other hand, the u profile is radially uniform in the straight section of the discharge chamber, and Ma = 0.25, 0.5, and 0.75 are only attained after the propellant enters the convergent section of the constricted nozzle.

In the PR-O (Figure 6.6b) and MiniPR (Figure 6.6e) $p_0 = 0\,\text{Torr}$ vacuum expansion cases, the Ma = 1.0 sonic surface is parabolic in shape and curves slightly inwards near the wall, which is in line with theoretical predictions [167]. The shape of the sonic surface is determined primarily by the geometry of the stream tube, while the local sound speed c_s is dependent on the gas species. In MiniPR for example, Ma = 1.0 is attained on the z-axis at $z = -2.31\,\text{mm}$ with $c_s = 156.5\,\text{m}\,\text{s}^{-1}$ in Xe. In both of these cases, the propellant leaving the discharge chamber is supersonic across most of the exit area, although PR-O (Figure 6.6b) has a thicker boundary layer due to a larger mean free path λ (3.2) at the local fluid conditions. The flow in these two cases are considered to be fully choked given the formation of a full sonic surface across the diameter of the discharge chamber.

In the PR-O (Figure 6.6a) $p_0 = 0.349\,\text{Torr}$ case however, the slightly lower axial velocity u_z is insufficient for developing a full sonic surface, and the propellant leaving the discharge chamber is supersonic only in the middle of the exit area. Hence, the flow in this case is considered to be only partially choked. At lower mass flow rates of $\dot{m} \lesssim 75\,\text{SCCM}$ of Ar, the flow is subsonic even though the ratio of the stagnation pressure p_{st} in the plenum to the downstream static pressure p_0 is greater than the critical pressure ratio (6.2) required for choked flow to occur. This further reinforces that (6.2) cannot be used in cases where the pressure drop is not immediate.

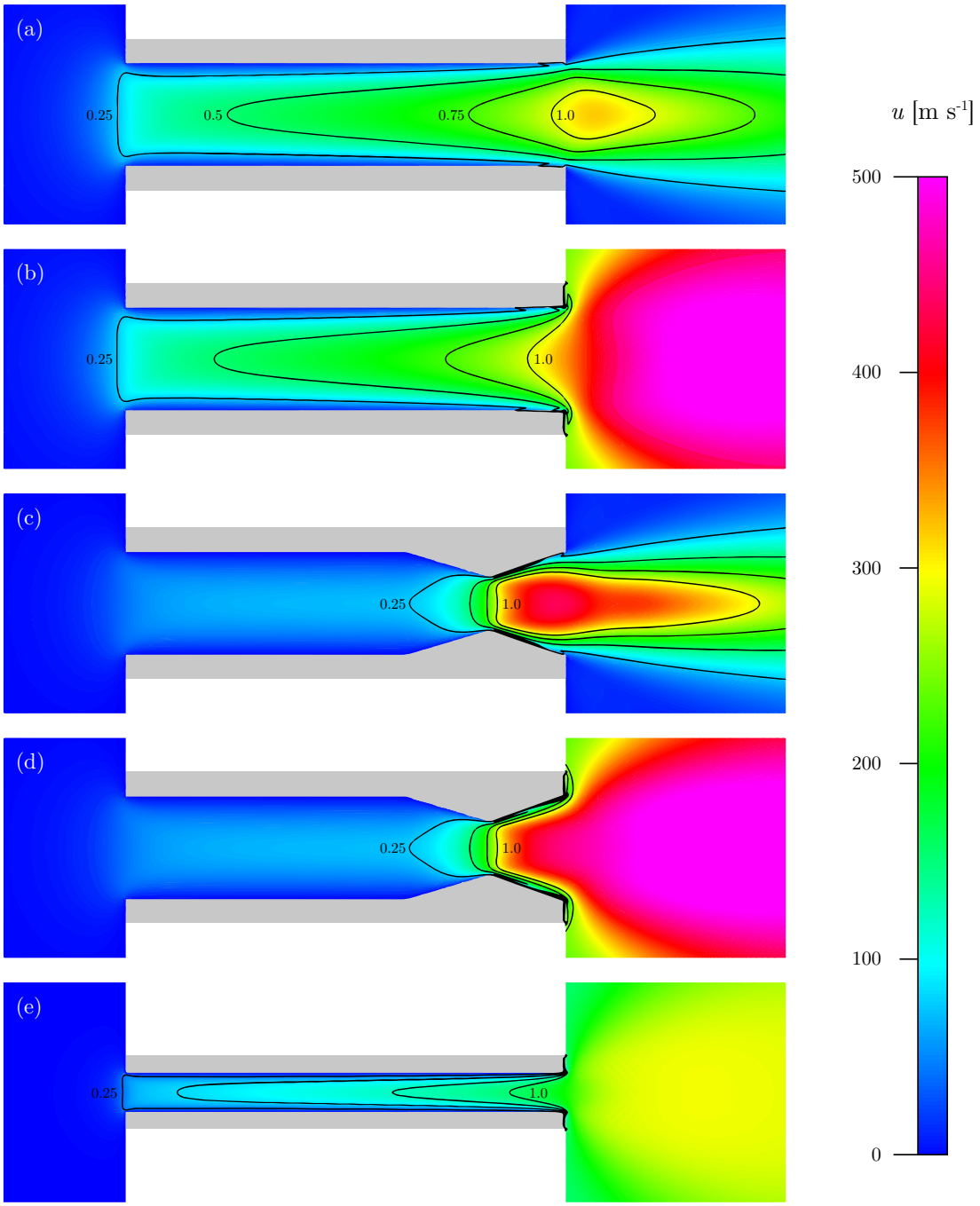

Figure 6.6: 2D colour map of the velocity magnitude u in: (a) `PR-O` with $p_0 = 0.349\,\text{Torr}$, (b) `PR-O` with $p_0 = 0\,\text{Torr}$, (c) `PR-C` with $p_0 = 0.349\,\text{Torr}$, (d) `PR-C` with $p_0 = 0\,\text{Torr}$, and (e) `MiniPR` with $p_0 = 0\,\text{Torr}$, The black — lines show the Mach isocurves for Ma = 0.25, 0.5, 0.75, and 1.0. `PR-O` and `PR-C` are operating with $\dot{m} = 100\,\text{SCCM}$ of Ar, while `MiniPR` is operating with $\dot{m} = 60\,\text{SCCM}$ of Xe.

As for PR-C, the $p_0 = 0.349\,\text{Torr}$ (Figure 6.6c) and $p_0 = 0\,\text{Torr}$ (Figure 6.6d) cases show very similar choked flow behaviour. The Ma = 1.0 sonic surface develops slightly beyond the constricted nozzle throat, instead of exactly at the *vena contracta* due to the existence of the boundary layer. The propellant is further accelerated to supersonic velocities in the divergent section of the constricted nozzle. In the $p_0 = 0.349\,\text{Torr}$ case however, the flow is almost immediately decelerated upon leaving the discharge chamber as the overexpanded propellant encounters the static background gas in the downstream region. Most importantly, Figures 6.6c and 6.6d demonstrate that when the flow velocity is choked at the constricted nozzle throat, the flow conditions upstream of the sonic surface are identical in the two cases despite the difference in the downstream pressure p_0. This behaviour is consistent for all the mass flow rates tested with PR-C, with small differences in the exact position and shape of the sonic surface due to the different widths of the boundary layer for different $\dot{m}$.

6.3 Thrust force

The thrust from cold gas and electrothermal thrusters is generated as a reactionary force to the linear momentum of the ejected neutral gas propellant, as distinct from electrostatic and electromagnetic thrusters where the thrust is generated as a reactionary force to the acceleration of ions through an electric field [168, 169]. PR belongs to the former class of neutral gas thrusters; it operates as an electrothermal microthruster when RF power is supplied to ionise and heat the neutral gas propellant, and as a cold gas microthruster when no RF power is supplied.

6.3.1 General thrust equation

The general thrust equation is used to calculate the thrust force generated by neutral gas thrusters, including conventional rockets:

$$F_\text{t} = \dot{m}\left(u_{z,\text{ex}} - u_{z,0}\right) + \left(p_\text{ex} - p_0\right) A_\text{ex} \tag{6.3}$$

where $\dot{m}$ is the mass flow rate of the propellant, A is the area, and the subscripts 'ex' and '0' denote exit and the ambient free stream respectively. For the present purpose, the free stream velocity $u_{z,0}$ is zero, and the free stream pressure is defined to be equal to the outlet pressure. The first term in (6.3) represents the component of the thrust force arising from the momentum of the ejected propellant, while the second term represents the pressure force difference between the exit area and the equivalent external area on the front of the thruster.

The general thrust equation (6.3) is visually represented in Figure 6.7a, showing the external pressure forces p_{ex} (red $\rightarrow$ and black $\leftarrow/\rightarrow$ arrows) and p_0 (blue $\leftarrow$ arrow) acting on the thruster and the force $\dot{m}u_{z,\text{ex}}$ imparted to the ejected propellant (green $\rightarrow$ arrows).

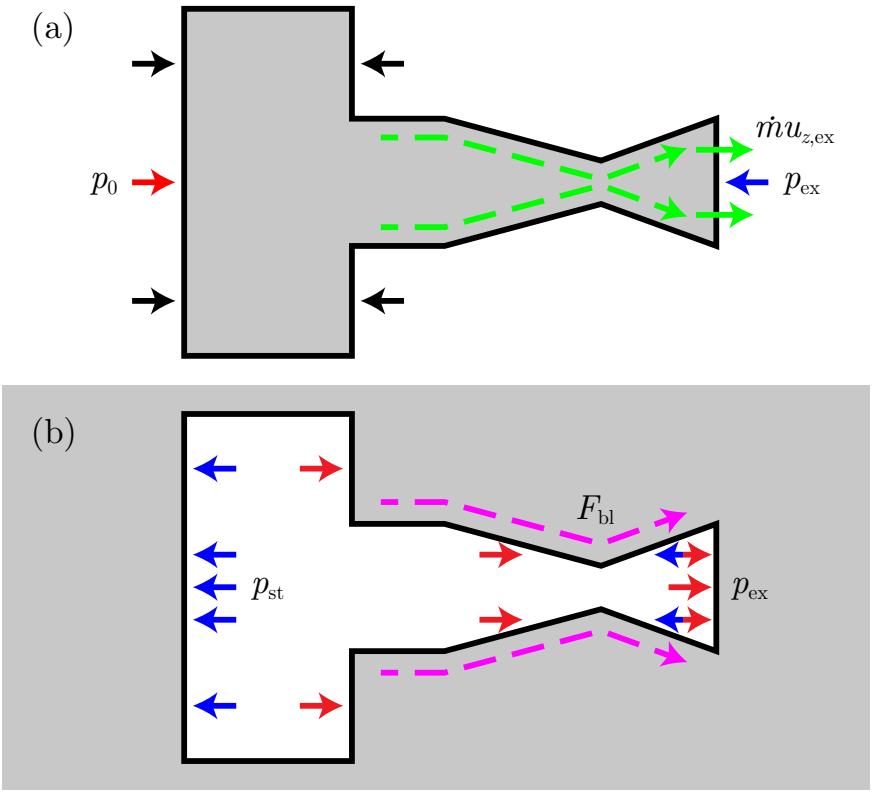

Figure 6.7: (a) Force diagram for the general thrust equation. The thrust force is the sum of the external pressure forces p_{ex} (red $\rightarrow$ and black $\leftarrow/\rightarrow$ arrows) and p_0 (blue $\leftarrow$ arrow) acting on the thruster and the reaction to the force $\dot{m}u_{z,\text{ex}} = \rho_{\text{ex}}u_{z,\text{ex}}^2$ imparted to the exiting propellant (green $\rightarrow$ arrows). (b) Force diagram for the internal forces method (Section 6.3.3). The thrust force is the sum of all the pressure forces within the propellant volume acting on the walls of the thruster (blue $\leftarrow$ and red $\rightarrow$ arrows) and on the background environment at the exit. This also includes the boundary layer friction force (magenta $\rightarrow$), which must be accounted for to avoid overestimating the thrust force.

In cases where $p_{\text{ex}} \approx p_0$ and $u_{z,\text{ex}} \approx c_{\text{s}}$ across the exit, the equation $F_{\text{t}}' = \dot{m}c_{\text{s}}$ may be used to give a rough estimation of the thrust force. For high pressure and large geometries as in conventional rocket nozzles, this approximation is valid since the static pressure p_{ex}, axial velocity $u_{z,\text{ex}}$, and mass flow rate density $\dot{m}/A_{\text{ex}}$ are typically uniform in the main flow across most of the exit area. However, for the low operating pressures and small geometries of microthrusters, boundary layer effects near the wall are nontrivial and often significant

compared to the main flow, resulting in nonuniform profiles for all the three parameters p_{ex}, $u_{z,\text{ex}}$, and $\dot{m}$. As seen in Figure 6.6, the sonic surfaces are typically not planar. Furthermore, the position of the sonic surface does not coincide with the exit surface, and can vary significantly depending on the gas species and the specific choked flow conditions. Additionally, the local sound speed c_{s} at the thruster exit is dependent on the local temperature which, in most cases, is different from the initial temperature or stagnation temperature of the propellant upstream, and difficult to measure. In cases where $p_{\text{ex}} \neq p_0$, and especially for real case applications in space where $p_{\text{ex}} > p_0$, the pressure thrust force (second term in (6.3)) can be significant and its contribution must be taken into account with the addition of a term in the form of $p_{\text{ex}} A_{\text{ex}}$, though in practice p_{ex} cannot be measured easily.

Figure 6.8 uses `PR-C` as an example, plotting the axial velocity $u_{z,\text{ex}}$ (blue), static pressure p_{ex} (red), and mass density ρ_{ex} (black) across the radius of the discharge chamber exit for the $p_0 = 0.349\,\text{Torr}$ (left, — lines) and $p_0 = 0\,\text{Torr}$ (right, -·- lines) cases. While the u_z profile has a parabolic shape that is to some extent theoretically predictable, the p_{ex} and ρ_{ex} profiles are nontrivial. In the $p_0 = 0.349\,\text{Torr}$ case in particular, overexpansion of the propellant to $p_{\text{ex}} < p_0$ causes a dip in the p_{ex} profile (left, red — line) in the middle of the discharge chamber exit. Additionally, the supersonic $u_{z,\text{ex}}$ cannot be calculated simply from first principles, as the boundary layer effectively reduces the exit area A_{ex} by an indefinite amount depending on the local flow conditions.

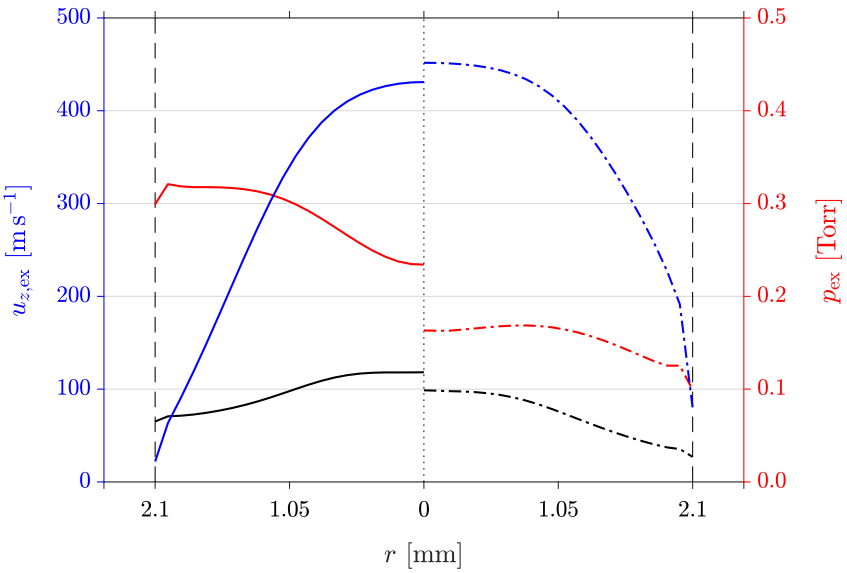

Figure 6.8: Axial velocity $u_{z,\text{ex}}$ (blue), static pressure p_{ex} (red), and mass density ρ_{ex} (black, in units of $[\times 10^{-2}\,\text{kg m}^3]$ on the right vertical axis) for the `PR-C` $p_0 = 0.349\,\text{Torr}$ case (left, — lines) and $p_0 = 0\,\text{Torr}$ case (right, -·- lines). The profiles are generally nontrivial.

In these circumstances, calculation of the thrust force requires the integral form of the general thrust equation:

$$F_\mathrm{t} = 2\pi \int_0^R r \left(\rho_\mathrm{ex} u_{z,\mathrm{ex}}^2 + p_\mathrm{ex} - p_0 \right) \mathrm{d}r \tag{6.4}$$

with the fluid density ρ_ex, axial velocity $u_{z,\mathrm{ex}}$, and pressure p_ex profiles across the exit. The integration is performed beginning at the central axis at $r = 0\,\mathrm{mm}$ and ending at the discharge chamber wall at $r = 2.1\,\mathrm{mm}$ for `PR-O` and `PR-C`, and at $r = 0.8\,\mathrm{mm}$ for `MiniPR` respectively. To ascertain the accuracy of the thrust force calculations, a similar integration of the mass flow rate of the gas $\dot{m}_\mathrm{ex} = \rho_\mathrm{ex} u_{z,\mathrm{ex}}$ is performed across the exit area and compared to the supplied mass flow rate $\dot{m}$ at the inlet. The error is found to be in the range $-4.9\,\% \leq \Delta\dot{m}_\mathrm{ex} \leq -0.4\,\%$ for the `PR-O` and `PR-C` CFD simulations, indicating that the results are reasonably precise. The error is significantly greater at $-10.3\,\%$ on average for the `MiniPR` CFD simulations, which is most likely caused by having an insufficient number of cells across the radius of the discharge chamber (8 cells over $r = 0.8\,\mathrm{mm}$) to accurately resolve the boundary layer and a smooth profile for the various fluid parameters. $\Delta\dot{m}_\mathrm{ex}$ is taken into account by modifying ρ_ex in (6.4) to bring $\dot{m}_\mathrm{ex}$ in line with the supplied $\dot{m}$.

The computed cold gas thrust force for `MiniPR` is presented in the following section. Results from `PR-O` and `PR-C` are discussed later in Chapter 7 together with the computed thrust force during plasma operation.

6.3.2 Pendulum thrust balance

For thrust experiments [53], `MiniPR` is mounted on a pendulum thrust balance inside a 1700 L cylindrical space simulation chamber of dimensions 1.0 m in diameter and 2.2 m in length, that is evacuated to a base pressure of $\lesssim 1\,\mu\mathrm{Torr}$ by a series of scroll, turbomolecular, and cryogenic pumps. Performing cold gas and plasma thrust measurement experiments of this nature is challenging due to the present prototype design of `MiniPR` (and `PR`) since the propellant and the RF power must be routed to the microthruster from external sources. The gas line and the RF cable used for this purpose introduce mechanical resistance which can only be slightly alleviated by anchoring them to the thrust balance. Similar challenges were observed in [8], which resorted to using indirect measurement methods that employed a baffle plate and a Pitot probe. A solution that is currently under development is to use integrated autonomous propellant and RF power subsystems on the microthruster. However, as such a system is not yet available, CFD simulations have the ability to produce more precise thrust results than experiments at the present time.

The computed stagnation pressure p_{st} in the plenum across the range of mass flow rates closely match the experimentally measured values, with a small systematic discrepancy of about $\Delta p_{st} = +0.28\,\text{Torr}$. This error can be attributed to a slight miscalibration of $\Delta\dot{m} = -2.3\,\text{SCCM}$ in the mass flow controller (MFC) if the pressure measurements are taken to be the baseline. Figure 6.9 plots the computed thrust force (blue ▽ markers) in `MiniPR` at $\dot{m} = 15$, 30, 45, and 60 SCCM of Xe, in comparison with the experimentally measured thrust force (red □ markers) with error bars denoting the uncertainty in each measurement [53].

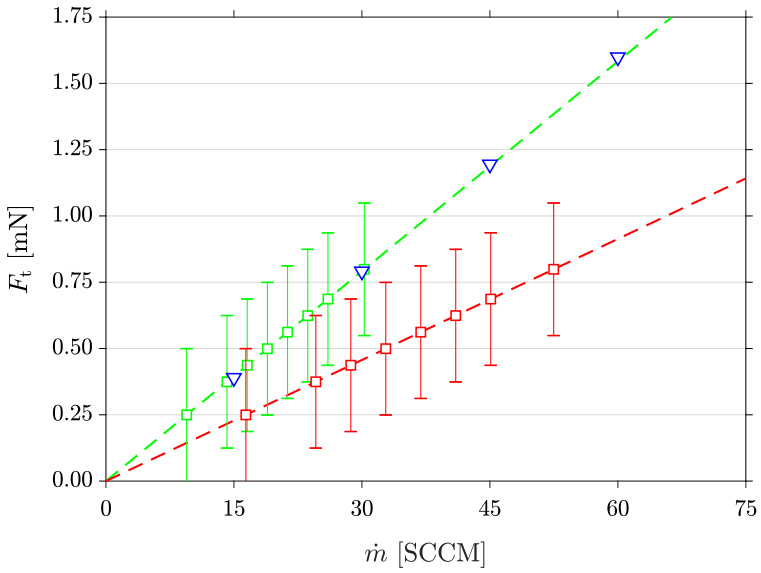

Figure 6.9: Comparison of the computed (blue △ markers) and experimentally measured (red □ markers) thrust force F_t in `MiniPR`. Correcting the mass flow rate $\dot{m}'$ to 57.7 % of the reported value gives a trend line (green -- line) that fits the computed F_t.

Due to technical constraints in the experimental setup, the thrust force measurements were taken after the gas supply had been terminated at the MFC. This means that the gas entering `MiniPR` was from the residual volume of gas trapped in the gas line (1 mm in diameter and 4 m in length) between the MFC and `MiniPR`. As the trapped gas require many hours to be fully depleted, it is reasonable to approximate a constant but slightly diminished mass flow rate $\dot{m}'$ in the short duration when each measurement was taken. Assuming that $\dot{m}'$ is 57.7 % of the initial $\dot{m}$ and applying this multiplicative factor to the experimental results (green □ markers) gives a trend line (green -- line) that fits the computed thrust force values.

To confirm that the computed thrust force values are indeed accurate, the specific impulse $I_{sp} = F_t/g_0\dot{m}$ (1.4) is calculated for each data point from the `MiniPR` CFD simulations and

experiment, and compared against the theoretical maximum specific impulse (1.5) of $\hat{I}_{sp} = 31.4\,s$ for Xe. The computed specific impulse from the CFD simulations is $I_{sp} = 27.6\,s$ (green -- line), while the original experimental measurements (red □ markers) give $I_{sp} = 15.9\,s$ (red -- line), which is significantly below the theoretically expected $\hat{I}_{sp}$ value. The corrected experimental data points give the same I_{sp} as the CFD simulations by definition, since they are fitted to the $F_t/\dot{m}$ gradient of the CFD simulation data points. Hence, the calculated I_{sp} values corroborate the claim that the measured thrust forces were underestimated in the original experiment.

6.3.3 Boundary layer friction force

Figure 6.7b shows the more commonly used method for calculating the thrust force in conventional nozzles. Instead of summing all the forces from the exterior acting upon the volume of propellant contained within the thruster, the 'internal forces method' involves summing all the forces acting upon the surroundings from the volume of propellant within the interior of the thruster. Using this method, the net thrust force is given by:

$$F_t = (p_{st} - p_{ex})\,A_{ex} - F_{bl} \tag{6.5}$$

where F_{bl} (magenta → arrows) is the friction force between the boundary layer and the wall. However, F_{bl} is almost always omitted when applying (6.5) to continuum regime flow ($\mathrm{Kn} \lesssim 0.01$) in conventional nozzles. While this is a valid decision in those circumstances, F_{bl} is crucially important in slip regime flow ($0.01 \lesssim \mathrm{Kn} \lesssim 0.1$) in microthruster nozzles, where the boundary layer plays a significant role in dictating the overall flow behaviour. In PR in particular, the magnitude of F_{bl} is on par with that of the net thrust force F_t (Table 7.1). Neglecting F_{bl} can thus lead to a gross overestimation of F_t to be twice or more of the actual value. Conversely, in the general thrust equation (6.4), the effects of F_{bl} are already imprinted in the axial velocity u_z profile, and do not require separate treatment.

To explain the origin of F_{bl}, suppose an inviscid fluid is flowing through the discharge chamber with a frictionless, adiabatic wall. Then the axial velocity of the flow is high and uniform across the diameter and length of the discharge chamber, and p_{st} in the plenum is low since the gas is able to leave the discharge chamber without any resistance. In this hypothetical case, where $F_{bl} = 0\,N$, the total thrust is merely the pressure force difference between the internal front and rear faces of the plenum, given by $(p_{st} - p_{ex})\,A_{ex}$.

Suppose that the flowing fluid was then imbued with the viscosity and friction (represented by the tangential momentum accommodation coefficient α_u) of a real gas, then the gas molecules incident on the wall must slow down due to the friction force, and the axial

velocity of the surrounding flow also decreases due to the viscosity of the fluid. This produces a velocity profile that is peaked in the middle of the discharge chamber, as expected with laminar pipe flow in the continuum and slip regimes. The deceleration of the boundary layer flow compared to the main flow is evidence that momentum is being transferred from the flow to the wall through friction and viscosity effects, resulting in a force F_{bl} acting in the direction of flow. Since this direction is opposite to the direction of intended motion, F_{bl} detracts from the total thrust.

As a direct consequence of F_{bl}, p_{st} in the plenum increases as the flow through the discharge volume becomes restricted by the boundary layer effects. Additionally, if the wall was nonadiabatic, the wall material then acts as a thermal source (or sink), further increasing (or decreasing) p_{st} accordingly. For flows on larger scales or where $\mathrm{Kn} \to 0$, p_{st} remains mostly unaffected and the magnitude of F_{bl} is negligible when compared with the net pressure force term in Equation (6.5). However, on miniature scales such as in `PR`, p_{st} is greatly inflated and F_{bl} manifests as an unavoidable and significant fraction of the inflated net pressure force. Hence, using the inflated p_{st} without accounting for F_{bl} inevitably results in a overestimation of the net thrust.

In practice, quantifying F_{bl} by itself is greatly nontrivial. Nevertheless, F_{bl} can be calculated by equating (6.4) and (6.5) when all the other variables are known. Since F_{bl} is dependent on the location and extensiveness of the boundary layer, it is ultimately dependent on the geometry of the microthruster. However, despite its inconvenience, information on the magnitude of F_{bl} can be used to optimise the surface properties or geometry of the microthruster, and thereby maximise performance and efficiency.

6.4 Chapter summary

This chapter explores modelling vacuum expansion in CFD simulations, without the use of hybrid or DSMC methods, by taking advantage of the flow velocity choking phenomenon. Flow velocity choking is a compressible flow effect, and occurs only when there is a sufficiently steep pressure gradient in the flow system. The velocity of the flow is accelerated by the pressure gradient up to the local sound speed. The location of the sonic surface depends on the geometry of the stream tube. In the cylindrical geometry of `PR` and `MiniPR`, the sonic surface is parabolic in shape. In the constricted nozzle geometry of `PR-C`, the sonic surface forms at the throat where the area of the stream tube is a minimum. CFD simulations performed with a vacuum downstream region are compared with those performed with a nonzero background pressure valid for fluid numerical methods, and the results are consistent.

Thrust force is calculated using the integral form of the general thrust equation, as the fluid parameter profiles are not uniform across the exit surface due to significant boundary layer effects in the slip regime. This is in contrast to conventional nozzles in the continuum regime, in which the boundary layer friction force is often ignored. The computed thrust force for `MiniPR` is compared against experimental measurements obtained using a pendulum thrust balance in a space simulation chamber. Discrepancies between the CFD simulation and experimental results are ascribed to experimental error, and the CFD simulation results are shown to be reasonable as the computed specific impulse is in line with theoretical predictions once a justifiable correction is applied to experimental results. The CFD simulation results may be compared against future experimental results upon the integration of the `PR` propellant and RF power subsystems.

Chapter 7

Discharge geometry

As discussed in Chapter 6, the geometry of the discharge chamber has a significant influence on the cold gas flow behaviour in *Pocket Rocket*. Extra factors come into play during plasma operation: in addition to flow velocity choking and boundary layer effects, the plasma is also influenced by electric potentials, plasma sheath dynamics, chemical reactions, neutral gas temperature, and neutral pumping. A comprehensive CFD-plasma model is necessary for understanding these processes, and how each of these can be controlled by shaping the physical and electrical geometry of the discharge.

This chapter presents CFD-plasma simulations of three geometrical variations of *Pocket Rocket*: the original `PR-O` (Figure 2.8) with a cylindrical discharge chamber, `PR-C` (Figure 6.1) with a constricted nozzle introduced in Chapter 6, and a new design prototype `PR-N` (Figure 7.1) featuring a sculpted converging-diverging nozzle that achieves desirable plasma confinement while providing higher performance. Slight modifications to the CFD-plasma modelling technique allows the outlet boundary static pressure to be set to a lower value of $p_0 = 0.1\,\text{Torr}$, thereby producing a CFD-plasma model that gives the closest approximation of real vacuum scenarios. While numerical limitations prevent plasma modelling in a true vacuum environment, results may be obtained by extrapolating from plasma simulations performed in a pressurised environment, using the performance delta from cold gas simulations performed in both environments.

7.1 Plasma microthruster design

PR-N is the culmination of an iterative design process targeting plasma confinement within the discharge chamber. This is advantageous as it eliminates the return ion current onto the exterior surfaces of the spacecraft, thus preventing the contamination of externally mounted solar panels and interference with sensitive instruments. While the overall configuration of PR-N is the same as in the original PR-O, the geometry and dimensions of the components have been altered to reduce volume and mass, thus enabling better compatibility with nanosatellite and CubeSat form factors while also improving its performance characteristics.

Figure 7.1 showcases the PR-N simulation mesh in more detail. The thickness of the Al structure (S) has been reduced from 3 mm to 1.6 mm, for compatibility with standard 0.063 in mounts for printed circuit boards. The length of the discharge chamber (C) has been reduced from 18 mm to 12.6 mm ($-12.6\,\text{mm} \leq z \leq 0\,\text{mm}$), and the length of the plenum (P) has been reduced from 12 mm to 5.8 mm ($-18.4\,\text{mm} \leq z \leq -12.6\,\text{mm}$), thus reducing the overall length of PR-N to just 20 mm. The radius of the plenum has also been reduced to 18.4 mm, making the overall radius 20 mm including the thickness of the structure. A short but wide cylindrical plenum maximises the area of the upstream grounded electrode S-P. This is critically essential for maintaining the geometrical asymmetry self-bias, since the confinement of the plasma upstream of the nozzle throat, while having its own advantages, eliminates electrical contact with the downstream grounded electrode S-D.

The design of the PR-N nozzle follows a couple of recommendations from [85]. Firstly, the angles of the converging-diverging nozzle are set to 15° converging and 20° diverging, optimised for thrust forces on the order of $\sim 1\,\text{mN}$. The divergent angle is greater than those of conventional nozzles to account for the formation of the boundary layer in rarefied flow conditions. Secondly, a sharp angle at the nozzle throat is used instead of a smooth curvature as it requires a shorter divergent length for a fixed exit radius, thereby minimising boundary layer friction losses. Through several design iterations, the length of the divergent section of the nozzle is optimised to 3.98 mm, and the radius of the nozzle throat in PR-N is reduced to 0.75 mm from 1.05 mm in PR-C. This gives an exit radius of 2.2 mm, and the entrance of the discharge chamber is set to the same radius for simplicity.

The Al_2O_3 discharge chamber (CW) wall must therefore be sculpted to the quoted dimensions. The minimum thickness of the discharge chamber wall is kept at 1 mm to preserve structural integrity. Presently, an experimental prototype uses machinable Macor instead of Al_2O_3 for preliminary testing. Macor is also used for the thermal and electrical insulation layer (I) between the powered electrode and the structure.

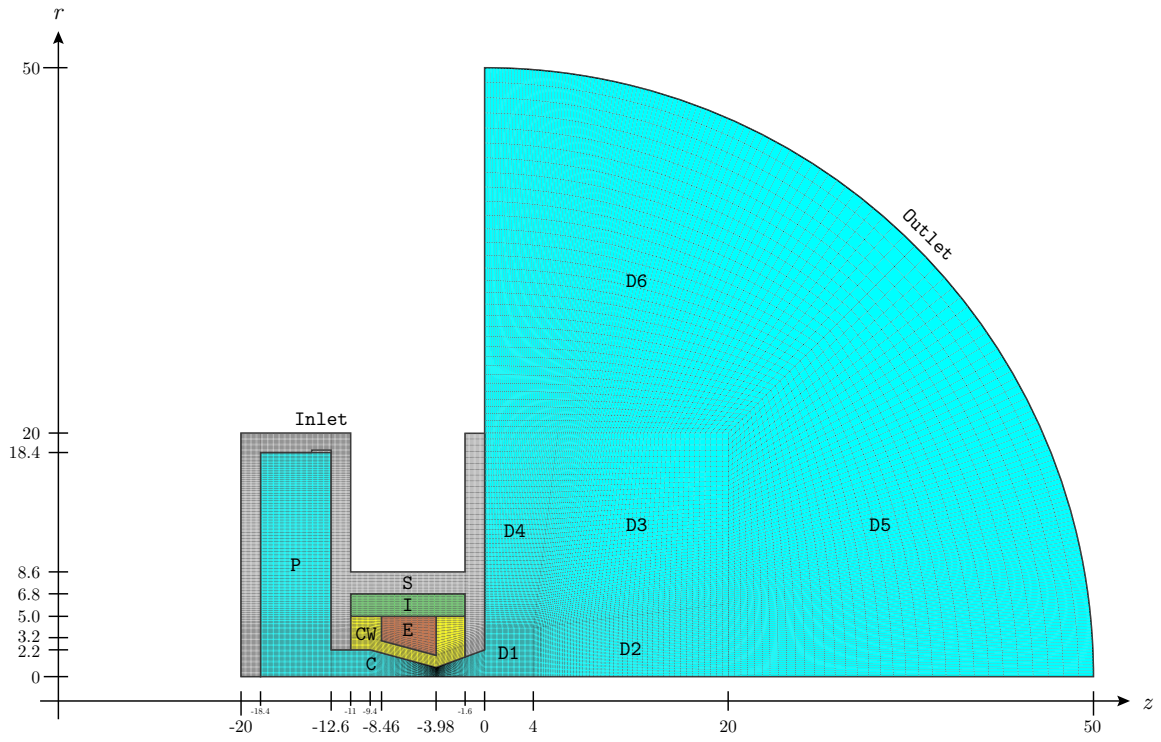

Figure 7.1: PR-N simulation mesh (33,667 cells). Fluid regions (aqua): plenum (P), discharge chamber (C), and downstream (D). Solid regions: Al structure (S, grey), Macor insulation (I, dark green), Cu powered electrode (E, brown), and Al_2O_3 discharge chamber wall (CW, yellow).

The Cu powered electrode (E) is an annulus with an external radius of 5 mm and a length of 4.48 mm. It has a trapezoidal cross section, and the internal edge conforms to the angle of the convergent section of the nozzle. The placement of the upstream and downstream structure walls (S-C) around the entrance and the exit of the discharge chamber electrically confines the self-bias to the section of the discharge chamber wall underneath the powered electrode, primarily in the convergent section of the nozzle. The rear corner of the powered electrode is positioned directly over the nozzle throat in order to concentrate the self-bias, thereby creating a virtual cathode at the nozzle throat that facilitates the formation of a plasma sheath.

Exploring design variations via CFD and CFD-plasma simulation models are more time and cost effective than producing and experimentally testing multiple physical design iterations. When a simulation model delivers a promising design, it is then manufactured as a prototype, and procedures more suited for experimentation (e.g. scaling and variation of various input parameters) can proceed. Thus, work on PR progresses in a leapfrogging manner between modelling and experimentation.

7.2 CFD-plasma simulation setup

The CFD-plasma modelling technique is slightly altered for `PR-N`, using 120 time-steps per RF cycle (plasma time-step $\Delta\tau_p = 0.615\,\text{ns}$) instead of the original 60 time-steps per RF cycle ($\Delta\tau_p = 1.229\,\text{ns}$), in order to implement a lower p_0, and also to manage the stronger coupling between the fluid and plasma parameters (i.e. plasma-induced heating and neutral pumping) in the discharge chamber due to the narrower nozzle throat. Additionally, the higher static pressures in `PR-N` allows local thermal equilibrium to be attained quicker than in `PR-O`, and simulation convergence is also achieved earlier. Hence, final solution is taken after 500 RF cycles of the convergence run (Section 2.2.4) instead of 1000 RF cycles. The final solution in the `PR-N` CFD-plasma simulations is constituted of the final 5 RF cycles at 120 time-steps per RF cycle, instead of 10 RF cycles at 60 time-steps per RF cycle.

The volume, boundary, and initial conditions for all the `PR-O`, `PR-C`, and `PR-N` CFD-plasma simulations are set using the same guidelines detailed in Section 4.3. All the simulations are run using a propellant mass flow rate of $\dot{m} = 100\,\text{SCCM}$ of Ar at the inlet. The CFD-plasma simulations are run using a $V_{pwr} = 300\,\text{V}$ amplitude sinusoidal RF waveform at 13.56 MHz on the powered electrode. The plasma operation mode targets a power budget of $\lesssim 10\,\text{W}$, adhering to values suitable for single or multiple-unit CubeSats. The secondary electron emission coefficient is set to a constant $\gamma_{e'} = 0.1$ for all the internal plasma-facing solid surfaces, in all but two of the CFD-plasma simulations meant for investigating the effects of a lower $\gamma_{e'} = 0.05$.

The low background pressure case `PR-N` CFD and CFD-plasma simulations use an outlet boundary static pressure of $p_0 = 0.1\,\text{Torr}$, and the backflow temperature is set to $T_0 = 100\,\text{K}$ instead of 300 K to ensure that the downstream region is an absolute thermal energy sink so as to realistically replicate vacuum expansion. These are the lowest values of p_0 and T_0 that produce a convergent solution for the CFD-plasma simulations. While flow velocity choking is able to stabilise fluid behaviour upstream despite undesirable conditions downstream, there is no equivalent phenomenon that can mask downstream conditions from upstream electric fields. Consequently, CFD-plasma simulations using a vacuum background pressure of $p_0 = 0\,\text{Torr}$ and $T_0 = 0\,\text{K}$ invariably result in divergent solutions since these conditions are beyond the capabilities of the fluid and plasma numerical methods. Nonetheless, the $p_0 = 0.1\,\text{Torr}$ and $T_0 = 100\,\text{K}$ cold gas CFD simulations have been verified against CFD simulations performed with $p_0 = 0\,\text{Torr}$ and $T_0 = 0\,\text{K}$, and they produce identical results by virtue of the flow velocity choking phenomenon discussed earlier in Section 6.2. Since $p_0 = 0.1\,\text{Torr}$ and $T_0 = 100\,\text{K}$ are well within the specifications of the fluid and plasma

numerical methods, the CFD-plasma simulations performed using these outlet boundary conditions are expected to be a valid and reliable approximation of real vacuum expansion scenarios.

Table 7.1 lists all the CFD-plasma simulations that have been performed for the present thrust modelling study, categorised into different sets according to the geometry and the background pressure boundary condition p_0. Simulations that are the subject of the preceding chapters and previous publications (`S01`, `S02`, `S03`, `S05`, and `S07`) are referenced accordingly, while the rest are new simulations making their first appearance in the present chapter. The metrics for plasma operation represent the performance at $\sim 1\,\mathrm{s}$ after plasma ignition. The rows marked with an asterisk * are not actual CFD-plasma simulations that have been run with $p_0 = 0\,\mathrm{Torr}$, but rather results that have been extrapolated from the referenced CFD and CFD-plasma simulations. The method by which the extrapolation is done is discussed in more detail in Section 7.5.1, along with commentary addressing the accuracy of the method.

7.3 Performance overview

`PR` is similar to arcjets, where propellant is heated volumetrically and directly by a plasma. Also, like in resistojets, the discharge chamber wall in `PR` heats up after a period of operation and acts as a source of thermal energy even after the RF power is terminated. On the other hand, unlike resistojets and hollow cathodes which require time to warm up, plasma breakdown in `PR` occurs on a $\sim \mu\mathrm{s}$ time scale; the propellant reaches target temperatures on a time scale of $\sim 100\,\mathrm{ms}$, and thermal equilibrium is attained with the discharge chamber wall on the order of $\sim 10\,\mathrm{s}$ (Section 4.4.1) [51].

Figure 7.2 shows a 2D colour map of the ion density during plasma operation in the various `PR` geometries: (a) `PR-O:S02`, (b) `PR-C:S06`, and (c) `PR-N:S10` all operating in a background pressure of $p_0 = 0.349\,\mathrm{Torr}$, and (d) `PR-N:S14` operating in $p_0 = 0.1\,\mathrm{Torr}$. The colour scale is logarithmic with the yellow region of the spectrum representing 1/10 of the full scale. n_i peaks in the middle of the discharge chamber, and the plasma extends upstream into the plenum. The exhaust plume in the downstream region of `PR-O:S02` is visually similar to that which was observed in `PR` experiments [170]. However, when the p_0 is sufficiently low, plasma confinement can be achieved by manipulating the physical and electrical geometry of the discharge, as seen in `PR-N:S14`.

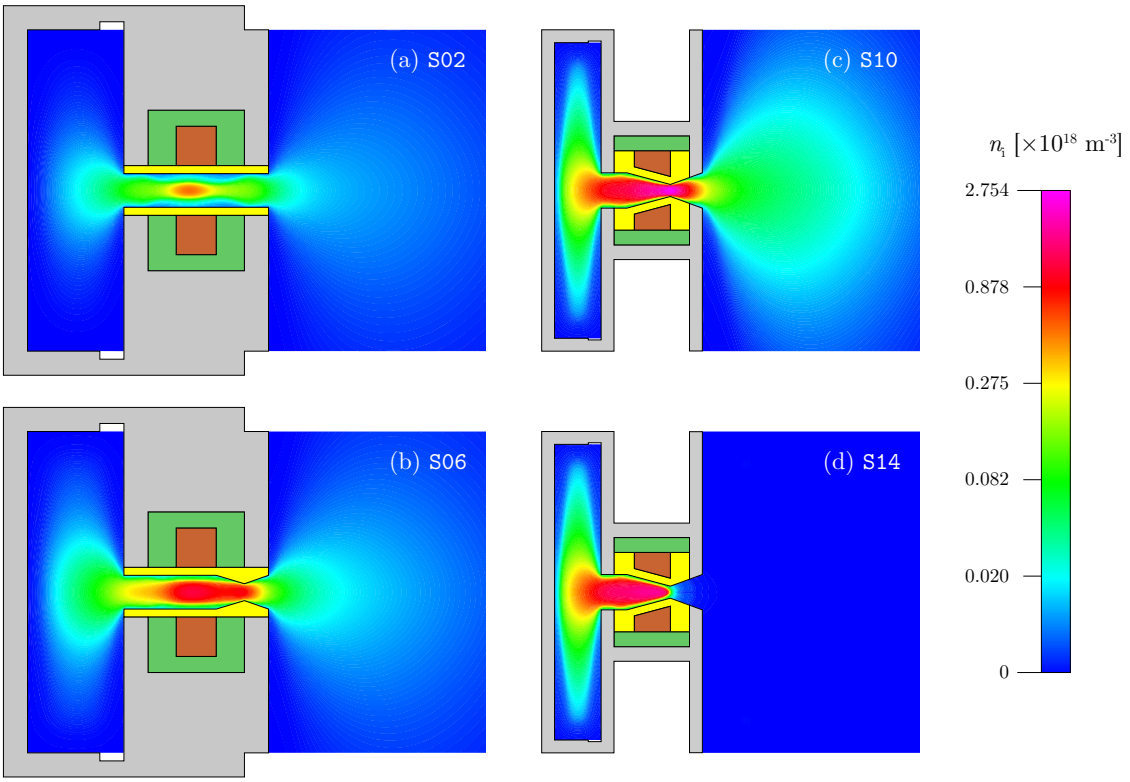

Figure 7.2: 2D colour map of the cycle average ion density n_i in the cross section of the different geometrical variations of PR. The colour scale is logarithmic with the yellow region of the spectrum representing 1/10 of the full scale. The propellant inlet is the notch in the corner of the plenum, and the flow direction is from left to right. From top to bottom: (a) PR-O:S02, (b) PR-C:S06, and (c) PR-N:S10 operating in a background pressure of $p_0 = 0.349$ Torr, and (d) PR-N:S14 demonstrating plasma confinement when operating in $p_0 = 0.1$ Torr. The solid regions are: the discharge chamber wall (yellow, Al_2O_3), powered RF electrode (brown, Cu), insulation (dark green, Macor), and structure (grey, Al).

In addition to the simulation number and input parameters: geometry, operation mode, and background pressure p_0, Table 7.1 also summarises the computed performance metrics: stagnation pressure p_{st} in the plenum, the RF power draw P of the PR discharge (for the performed CFD-plasma simulations only), the thrust force F_t, the boundary layer friction force F_{bl} (Section 6.3.3), and the specific impulse I_{sp}. The quoted values are averaged over all the RF cycles in the final solution. F_t values for simulations run with nonzero p_0 are printed in grey; the primary interest is the performance of PR in a vacuum environment.

The CFD-plasma simulation results presented in this chapter represent the transient conditions in each PR geometry on the order of ~ 1 s after plasma ignition, which is enough time for propellant to be heated by the plasma and attain local thermal equilibrium, but

Table 7.1: Summary of main performance metrics

Geometry	Sim.	Mode	p_0 [Torr]	p_{st} [Torr]	P [W]	F_t [mN]	F_{bl} [−mN]	I_{sp} [s]	References
PR-O	S01	Cold gas	0.349	1.367	–	0.794	1.095	27.3	Chapters 3 and 6; [171]
	S02	Plasma	0.349	1.532	5.010	0.897	1.307	30.8	Chapters 4 and 5; [48, 50, 66]
	S03	Cold gas	0	1.335	–	1.363	0.764	46.8	Chapter 6; [171]
	* S04	Plasma	0	1.496	–	1.493	0.943	51.2	Extrapolated: S01, S02, S03
PR-C	S05	Cold gas	0.349	2.759	–	0.851	1.208	29.2	Chapter 6; [171]
	S06	Plasma	0.349	3.408	13.28	1.116	1.553	38.3	Present chapter
	S07	Cold gas	0	2.742	–	1.425	0.826	48.9	Chapter 6; [171]
	* S08	Plasma	0	3.386	–	1.818	1.014	62.4	Extrapolated: S05, S06, S07
PR-N	S09	Cold gas	0.349	4.992	–	0.855	1.383	29.3	Present chapter
	S10	Plasma	0.349	6.802	12.39	1.201	2.008	41.2	Present chapter
	S11	Cold gas	0	4.890	–	1.432	1.010	49.1	Present chapter
	* S12	Plasma	0	6.664	–	2.033	1.318	69.8	Extrapolated: S09, S10, S11
PR-N	S13	Cold gas	0.1	4.963	–	1.248	1.194	42.8	Present chapter
	S14	Plasma	0.1	6.380	12.01	1.607	1.591	55.2	Present chapter
	S15	Cold gas	0	4.890	–	1.432	1.010	49.1	Same as S11
	* S16	Plasma	0	6.286	–	1.821	1.357	62.5	Extrapolated: S13, S14, S15
PR-N	S17	Plasma	0.349	6.560	10.62	1.143	1.920	39.2	S10, $\gamma_{e'} = 0.05$
	* S18	Plasma	0	6.427	–	1.942	1.268	66.7	Extrapolated: S09, S10, S17
PR-N	S19	Plasma	0.1	6.165	8.746	1.525	1.548	52.3	S14, $\gamma_{e'} = 0.05$
	* S20	Plasma	0	6.074	–	1.735	1.320	59.6	Extrapolated: S13, S14, S19

before any significant heating of the discharge chamber wall or structure. For this reason, the performance demonstrated here represents the 'instantaneous' or transient lower limit performance of PR from a cold start. Performance is expected to further increase as the temperature of the discharge chamber wall rises and attains thermal equilibrium with the heated propellant, in a scenario similar to that of the self-heating mode of a hollow cathode thruster. The simulation results are discussed in the following sections, detailing the plasma, temperature, velocity, and thrust characteristics of each PR geometry. Comparisons are made to the cold gas operation mode to envisage the transient or pulsed plasma operation performance of PR.

7.4 Plasma behaviour

7.4.1 Ion density

The ion density $n_i(t)$ along the central (axisymmetric) z-axis at each time-step during the RF cycle is plotted in linear scale for the CFD-plasma simulations: PR-O:S02 (Figure 7.3, light blue — lines), PR-C:S06 (Figure 7.3, light red — lines), PR-N:S10 (Figure 7.4, light blue — lines), and PR-N:S14 (Figure 7.4, light red — lines). The coloured — line in the middle of each $n_i(t)$ profile denotes the cycle average ion density n_i (shown earlier in Figure 7.2). Vertical -- lines divide the plots into three sections from left to right: plenum, discharge chamber, and the downstream region. A vertical ····· line marks the location of the nozzle throat for PR-C in Figure 7.3 and PR-N in Figure 7.4.

The $n_i(t)$ profiles track the n_i profiles closely, without any anomalous deviation from the cycle average. For PR-O and PR-C, n_i peaks underneath the powered electrode with $n_i = 5.373 \times 10^{17}\,\mathrm{m}^{-3}$ at $z = -9.9\,\mathrm{mm}$, and $n_i = 1.159 \times 10^{18}\,\mathrm{m}^{-3}$ at $z = -9.4\,\mathrm{mm}$ respectively. The position of the central peak is slightly upstream of the midpoint of the powered electrode mainly because of the negative pressure and density gradient along the discharge chamber. The shape of the n_i profile is due to two separate ionisation modes that are dominant during the negative and positive periods of the RF cycle.

In PR, a negative self-bias manifests in the section of the discharge chamber wall shielding the powered electrode (Figure 5.12). During the negative period of the RF cycle, ions are accelerated from the positive plasma potential towards the negative discharge chamber wall. Ion bombardment onto the surface of the discharge chamber wall results in the emission of high energy secondary electrons. These secondary electrons induce a gamma mode ionisation as they are accelerated through the plasma sheath into the plasma bulk, giving rise to the

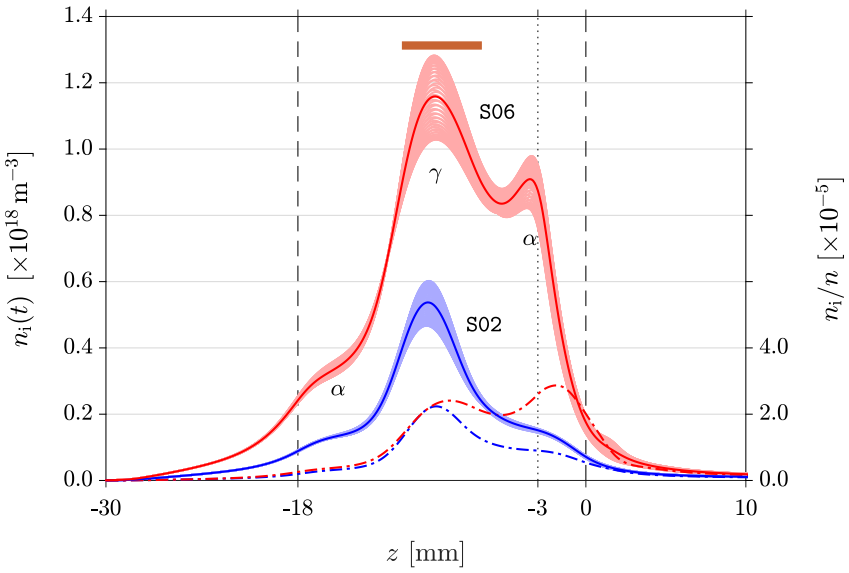

Figure 7.3: Temporally varying ion density $n_i(t)$ along the z-axis for PR-O:S02 (light blue — lines) and PR-C:S06 (light red — lines). Cycle average ionisation fraction n_i/n along the z-axis for PR-O:S02 (blue -·- lines) and PR-C:S06 (red -·- lines). $-30\,\text{mm} \leq z \leq 18\,\text{mm}$ is the plenum, while $-18\,\text{mm} \leq z \leq 0\,\text{mm}$ is the discharge chamber. The nozzle throat in PR-C is located at $z = -3\,\text{mm}$. The brown bar at the top shows the location of the powered electrode at $-11.5\,\text{mm} \leq z \leq -6.5\,\text{mm}$.

strong central gamma mode peak seen in the n_i profile of PR-O:S02 in Figure 7.3. During the positive period of the RF cycle, the self-biased section of the discharge chamber wall maintains a positive electric potential, and hence there are no secondary electrons emitted during this time. Instead, bulk electrons from upstream and downstream of the powered electrode are attracted towards the positive electric potential. Their motion in the discharge chamber induces two regions of alpha mode ionisation, giving rise to the two shoulder alpha mode plateaus seen on either side of the central gamma mode peak.

A similar n_i profile is observed in PR-C:S06 (Figure 7.3, red — line). There is still a strong central gamma mode peak, but the downstream shoulder alpha mode plateau becomes a second peak just upstream of the nozzle throat, with $n_i = 0.909 \times 10^{18}\,\text{m}^{-3}$ at $z = -3.5\,\text{mm}$. This is due to the high concentration of the electric field lines at the nozzle throat. During the positive period of the RF cycle, bulk electrons from the divergent section of the nozzle travel upstream towards the powered electrode along these electric field lines, inducing a high ionisation rate at the nozzle throat. To confirm that this is the case rather than a second gamma mode peak, it is necessary to examine the alpha mode ionisation rate.

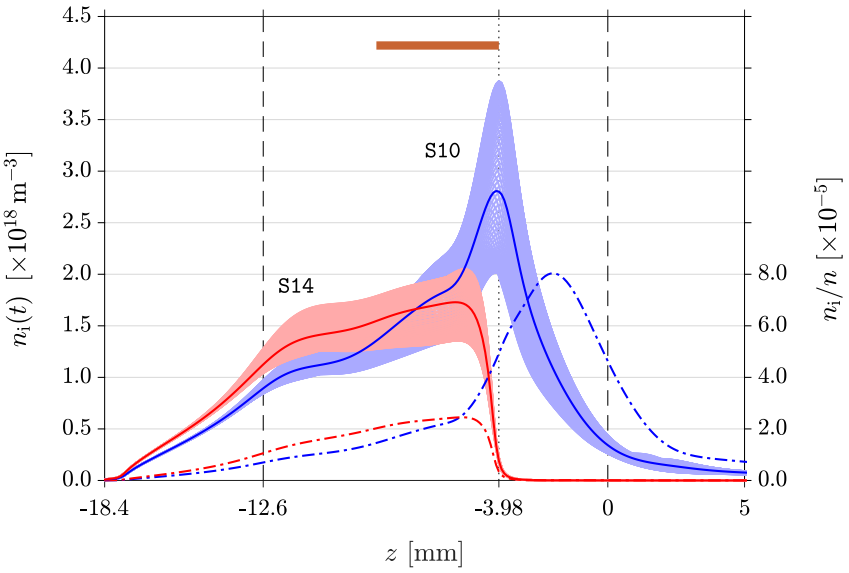

Figure 7.4: Temporally varying ion density $n_i(t)$ along the z-axis for `PR-N:S10` (light blue — lines) and `PR-N:S14` (light red — lines). Cycle average ionisation fraction n_i/n along the z-axis for `PR-O:S10` (blue -·- lines) and `PR-C:S14` (red -·- lines). $-18.4\,\text{mm} \leq z \leq 12.6\,\text{mm}$ is the plenum, while $-12.6\,\text{mm} \leq z \leq 0\,\text{mm}$ is the discharge chamber. The nozzle throat in `PR-N` is located at $z = -3.98\,\text{mm}$. The brown bar at the top shows the location of the powered electrode at $-8.46\,\text{mm} \leq z \leq -3.98\,\text{mm}$.

7.4.2 Alpha mode ionisation

Figure 7.5 shows a 2D colour plot of the alpha mode direct ionisation rate R_α during the positive peak of the RF cycle. The colour scale is logarithmic with the green region of the spectrum representing 1/10 of the full scale. Bulk electrons are responsible for ionisation events during the positive period of the RF cycle since secondary electrons are only present during the negative period of the RF cycle. Figure 7.5a reflects the two shoulder alpha mode plateaus visible in the n_i profile of `PR-O:S02`. Correspondingly, Figure 7.5b confirms that the second n_i peak at the nozzle throat of `PR-C:S06` is due to alpha mode ionisation by bulk electrons travelling upstream, and not gamma mode ionisation by secondary electrons.

While there are significant differences between the geometries of `PR-N` and `PR-C`, the n_i profile of `PR-N:S10` (Figure 7.4, blue — line) still bears some resemblance to that of `PR-C:S06` (Figure 7.3, red — line). The upstream shoulder alpha mode plateau is present, as well as the downstream alpha mode peak with $n_i = 2.807 \times 10^{18}\,\text{m}^{-3}$ at $z = -4.1\,\text{mm}$ near the nozzle throat, but the central gamma mode peak is now a diminished hump in the n_i profile. However, the ionisation fraction in `PR-N:S10` (Figure 7.4, blue -·- line) is roughly

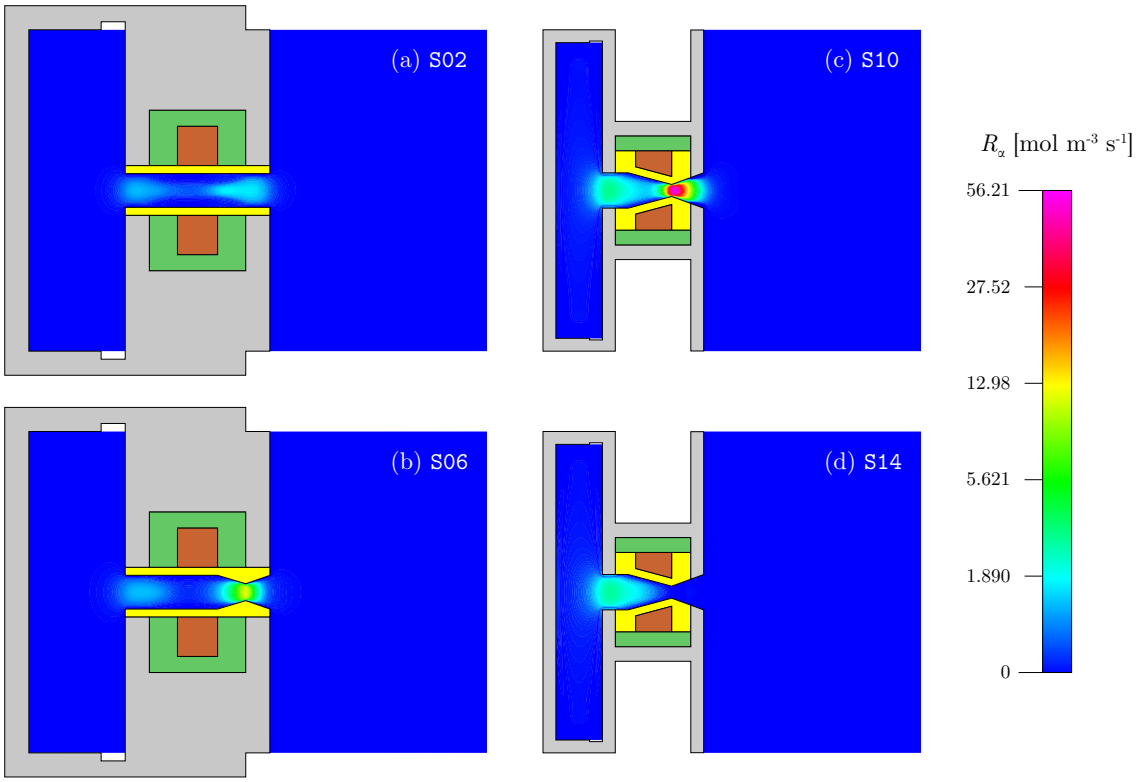

Figure 7.5: 2D colour map of the alpha mode direct ionisation rate R_α in (a) `PR-O:S02`, (b) `PR-C:S06`, (c) `PR-N:S10`, and (d) `PR-N:S14` during the positive peak of the RF cycle. The colour scale is logarithmic with the green region of the spectrum representing 1/10 of the full scale.

the same as `PR-O:S02` and `PR-C:S06` (Figure 7.3, -·- lines) at $n_i/n \approx 2 \times 10^{-5}$. Instead of a strong central peak, the gamma mode discharge is present along the length of the convergent section of the nozzle under the powered electrode. Like in `PR-C:S06`, `PR-N:S10` has a high ionisation fraction in the divergent section of the nozzle, mainly due to the lower pressure and neutral density in the expanding plume. This is corroborated by the region of high alpha mode ionisation at the nozzle throat in Figure 7.5c, which shows the bulk electrons from the divergent section of the nozzle travelling upstream during the positive period of the RF cycle.

7.4.3 Gamma mode ionisation

For comparison, Figure 7.6 shows a 2D colour plot of the secondary electron gamma mode ionisation rate R_γ during the negative peak of the RF cycle. The colour scale is linear, with 14.19 mol m^{-3} s^{-1} full scale for `PR-O:S02` and `PR-C:S06` (left), and 70.96 mol m^{-3} s^{-1} full scale for `PR-N:S10` and `PR-N:S14` (right). Secondary electrons generated at the plasma-

facing surface of the discharge chamber wall from ion bombardment are repelled from the negative powered electrode and the self-biased section of the discharge chamber wall, and accelerated through the plasma sheath into the positive plasma potential of the plasma bulk.

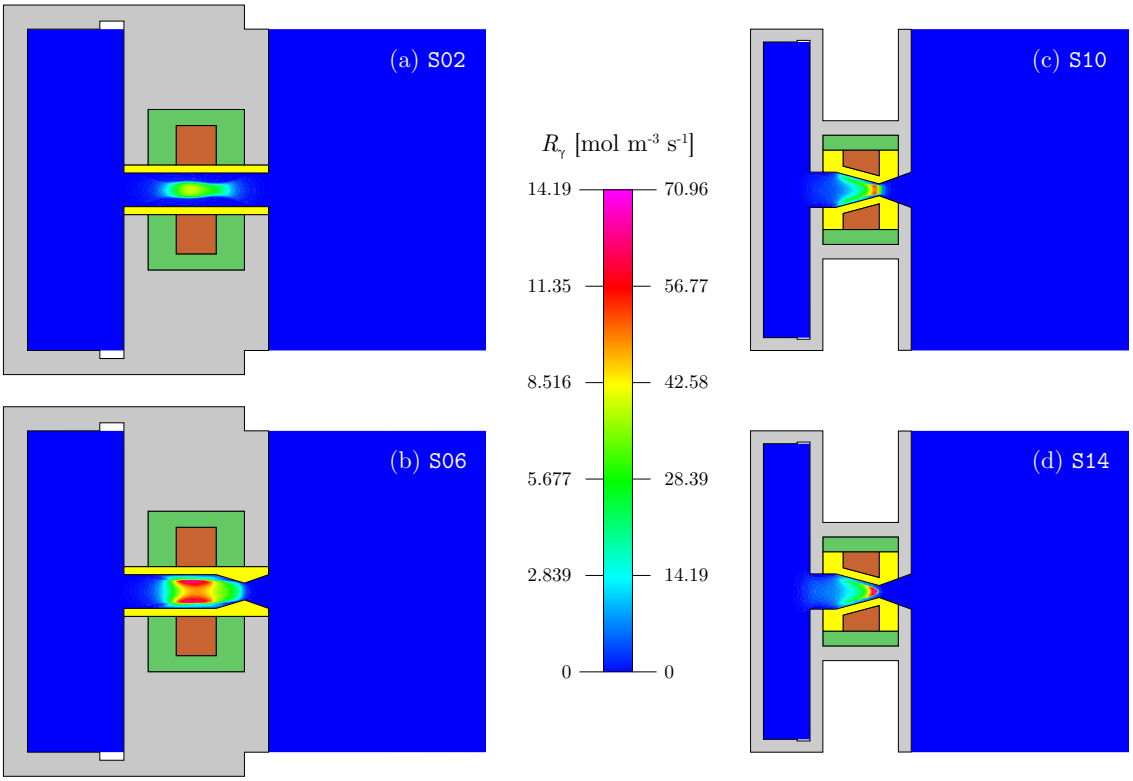

Figure 7.6: 2D colour map of the secondary electron gamma mode ionisation rate R_γ in (a) `PR-O:S02`, (b) `PR-C:S06`, (c) `PR-N:S10`, and (d) `PR-N:S14` during the negative peak of the RF cycle. The linear colour scale for `PR-O:S02` and `PR-C:S06` (left) is magnified 5 times that of `PR-N:S10` and `PR-N:S14` (right).

Alpha mode ionisation by bulk electrons are ongoing, but the ionisation rate during negative period of the RF cycle is predominantly the gamma mode driven by secondary electrons. While the alpha mode bulk electrons move through the discharge chamber in the axial direction, the gamma mode secondary electrons are only present underneath the powered electrode and move radially away from the discharge chamber wall. This gives rise to the opposite alpha and gamma mode ionisation regions shown in Figures 7.5 and 7.6. In `PR-N` (Figures 7.6c and 7.6d) in particular, the gamma mode ionisation regions are also parallel to the wall of the convergent section of the nozzle where the self-bias manifests. R_γ is highest at the nozzle throat where self-bias in the discharge chamber wall is the most concentrated.

7.4.4 Plasma confinement

The trapezoidal annulus shape of the powered electrode in PR-N is designed to bring the self-biased region of the discharge chamber wall closer to the nozzle throat. This results in the creation of a virtual cathode at the nozzle throat and the formation of a conical plasma sheath that confines the plasma upstream. The consequences of this can be seen more clearly in PR-N:S14, which gives starkly different results when the background pressure is lowered to $p_0 = 0.1\,\text{Torr}$. In PR-N:S14 (Figure 7.4, light red — lines) the downstream alpha mode peak at the nozzle throat disappears completely, in exchange for a slightly higher ionisation fraction (Figure 7.4, red -·- line) throughout the discharge chamber. The gamma mode plateau merges with the upstream alpha mode plateau, forming a more uniform discharge (Figure 7.2d), with peak $n_\text{i} = 1.729 \times 10^{18}\,\text{m}^{-3}$ at $z = -5.6\,\text{mm}$. Although p_0 is not zero, PR-N:S14 is demonstrative of how PR-N operates in the vacuum environment of space. The accuracy of these results is substantiated later in this chapter.

The most important effect observed in PR-N:S14 is the plasma confinement upstream of the nozzle throat. This occurs because the static pressure p is much lower in the divergent section of the nozzle, and the width of the plasma sheath, which varies approximately with $1/\sqrt{p}$ [172, 173], becomes larger than the radius of the nozzle throat. Consequently, the cylindrical plasma sheath along the discharge chamber wall merges to form a cone that terminates at the nozzle throat (Figure 7.2d). Thus, the plasma is restricted to the region upstream of the nozzle throat. Since there are no bulk electrons downstream of the nozzle throat, alpha mode ionisation is evidently absent in this region (Figure 7.5d). Similar ionisation loss behaviour has also been observed experimentally in the supersonic expanding plume of a cascade arc discharge [174, 175], in which ion-neutral charge exchange collisions are responsible for enhancing recombination in the first few centimetres of the expansion. The plasma confinement is also beneficial for the convergence of the CFD-plasma simulation in the low p_0 environment of the downstream region.

Another interesting feature is the steep drop in electric potential across the plasma sheath at the nozzle throat. Figure 7.7 plots the temporally varying plasma potential $\Phi_\text{p}(t)$ (light blue — lines) along the z-axis in PR-N:S14, showing the steep potential drop occurring just after $z = -3.98\,\text{mm}$. Ions falling through the plasma sheath are accelerated to very high velocities in the axial direction into the virtual cathode. Ion-neutral charge exchange collisions in the divergent section of the nozzle not only aid fast recombination and ensures a neutral plume, but may also impart axial momentum to a small population of neutrals and be beneficial for thrust performance [176]. However, due to the low ionisation fraction, this

contribution and the thrust force from the remaining ions in the exhaust plume are expected to be very small relative to the main flow.

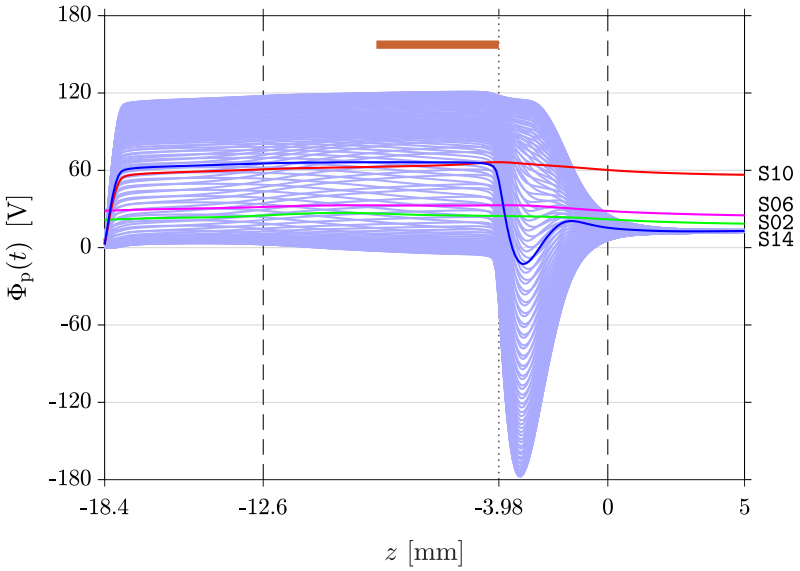

Figure 7.7: Temporally varying plasma potential $\Phi_p(t)$ (light blue — lines) and the cycle average Φ_p (blue — line) along the z-axis in `PR-N:S14`. Superimposed are Φ_p in `PR-O:S02` (green — line), `PR-C:S06` (magenta — line), and `PR-N:S10` (red — line). The brown bar at the top shows the location of the powered electrode in `PR-N` at $-8.46\,\text{mm} \leq z \leq -3.98\,\text{mm}$. The discharge chamber ($-18\,\text{mm} \leq z \leq 0\,\text{mm}$) and the powered electrode ($-11.5\,\text{mm} \leq z \leq -6.5\,\text{mm}$) in `PR-O` and `PR-C` are unmarked.

7.5 Propellant behaviour

7.5.1 Neutral gas temperature

The primary purpose of the plasma is to impart energy to the gas propellant in the form of heat. Many experimental techniques [114] have been used to characterise neutral gas temperatures in plasmas. These include using atomic line profiles from Doppler, Stark, and van der Waals broadening, as well as rotational spectroscopy [49, 55, 115] and laser-induced fluorescence [116]. However, rotational spectroscopy becomes unreliable at low pressures [115, 116], and the temperature profile in `PR` is highly nonuniform. Hence, validated computational modelling techniques are required.

The cycle average temperature T of the background neutral Ar gas is plotted along the z-axis for the first four sets of simulations (`S01` to `S16`) in Figures 7.8 to 7.11, comparing

cold gas operation (blue) to plasma operation (red). CFD and CFD-plasma simulations run with a nonzero background pressure p_0 are represent by — lines, while CFD simulations run with $p_0 = 0$ Torr and CFD-plasma 'simulations' extrapolated to $p_0 = 0$ Torr (`S04`, `S08`, `S12`, and `S16`) are represented by –·– lines. The brown bar at the top of each figure shows the location of the powered electrode in the respective `PR` geometry.

The variation of $T(t)$ at each time-step during the RF cycle is also shown (light red — lines) for the performed CFD-plasma simulations (`S02`, `S06`, `S10`, and `S14`). However, it is only for visual reference because the variation of the fluid parameters at each time-step is to a large extent a consequence of the large fluid time-step $\Delta\tau_\mathrm{f}$ rather than an actual response to the variation of the plasma parameters over the plasma time-step $\Delta\tau_\mathrm{p}$. Hence, the fluid parameters must be averaged over the RF cycle for valid interpretation. Nonetheless, the $T(t)$ profiles provide some insight into where, along the z-axis, that heating of the neutral gas by the plasma is taking place.

The radial T profile of the background neutral Ar gas in the discharge chamber peaks on the z-axis ($r = 0$ mm) in all of the CFD-plasma simulations. They are very similar to that of `S02` (original `PR` geometry, Figure 4.7) and are not discussed in this chapter.

Extrapolation to vacuum

The extrapolated profiles are obtained using a pointwise function that transforms cold gas operation in nonzero background pressure cases ($p_0 = 0.349$ Torr and $p_0 = 0.1$ Torr) to cold gas operation in $p_0 = 0$ Torr cases. Using the `PR-0` CFD simulations as an example, a function f_T specifically for temperature is found such that $f_T(T_{\texttt{S01}}) = T_{\texttt{S03}}$, fitting all of the T data points in both `S01` (blue — line) and `S03` (blue –·– line). Note that these CFD simulations are steady state, so the T profiles in `S01` and `S03` do not vary with time. The same function is then applied to each of the temporally varying $T(t)$ profiles (light red — lines) of the transient CFD-plasma simulation `S02` in order to calculate the temporally varying $T(t)$ profiles of `S04` (not shown in Figure 7.8).

$f_T(T_{\texttt{S02}}(t)) = T_{\texttt{S04}}(t)$ thereby gives a prediction of the $T(t)$ profiles in `PR-0:S04` during plasma operation in $p_0 = 0$ Torr, using data from the three performed simulations in $p_0 = 0.349$ Torr (`S01`, `S02`, and `S03`). Finally, the calculated $T(t)$ profiles of `PR-0:S04` are averaged over the RF cycle, resulting in the T profile of `PR-0:S04` plotted in Figure 7.8 (red –·– line). The same procedure is performed for each of the other sets of simulations, with unique f_T for each respective set. The procedure also works for other fluid parameters such as density, pressure, and velocities, with functions specific to each parameter, e.g. $f_{u_z}\big(u_{z,\texttt{S01}}(t)\big) =$

$u_{z,\texttt{S03}}(t) \Rightarrow f_{u_z}\big(u_{z,\texttt{S02}}(t)\big) = u_{z,\texttt{S04}}(t)$. Plasma parameters cannot be extrapolated since the cold gas simulations do not contain such information.

PR-0

Figure 7.8 plots the T profiles of the cold gas operation cases S01 (blue — line) and S03 (blue –·– line). The initial temperature of the neutral gas propellant is $T = 300\,\mathrm{K}$ at the front plenum wall ($z = -30\,\mathrm{mm}$). There is a slight drop in T as the propellant enters the discharge chamber ($z = -18\,\mathrm{mm}$). This is due to a slight acceleration of the flow called the Venturi effect, caused by the sudden constriction of the flow diameter from 40 mm in the plenum to 4.2 mm in the discharge chamber. Along the plenum and discharge chamber, T falls monotonically as the propellant is accelerated by the pressure gradient bridging the stagnation pressure p_{st} in the plenum (see Table 7.1) to p_0 downstream. There is another drop in T as the propellant exits the discharge chamber and expands into the lower pressure environment downstream.

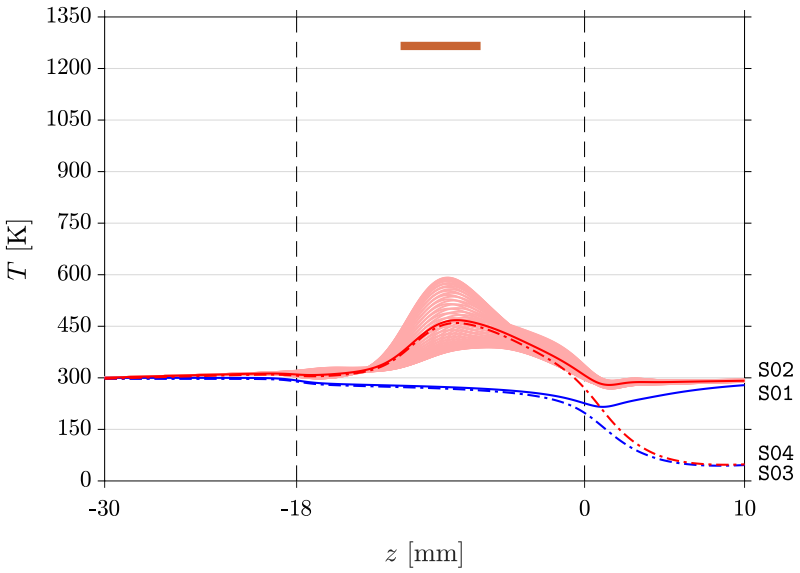

Figure 7.8: Cycle average neutral gas temperature T along the z-axis for PR-0. Cold gas operation: S01 (blue — line, $p_0 = 0.349\,\mathrm{Torr}$) and S03 (blue –·– line, $p_0 = 0\,\mathrm{Torr}$). Plasma operation: S02 (red — line, $p_0 = 0.349\,\mathrm{Torr}$) and S04 (red –·– line, $p_0 = 0\,\mathrm{Torr}$, extrapolated results).

In S01 (blue — line), T returns to thermal equilibrium with the ambient gas at $p_0 = 0.349\,\mathrm{Torr}$ and $T = 300\,\mathrm{K}$. In S03 (blue –·– line) on the other hand, T continues to fall as the propellant expands into vacuum. The accuracy of the fluid parameters at a certain

distance beyond the discharge chamber exit cannot be guaranteed for the CFD simulations run with $p_0 = 0\,\text{Torr}$. This is discussed in more detail with respect to the Knudsen number Kn (Section 7.5.2).

During plasma operation, the T profile of `S02` (red — line) rises slightly in the plenum due to the presence of a weak plasma in the region. The slight drop at $z = -18\,\text{mm}$ is still present, but T rises rapidly in the discharge chamber due to the plasma-induced heating. A peak temperature of $T = 467.7\,\text{K}$ is attained at $z = -8\,\text{mm}$ slightly downstream of the n_i peak. This is expected as thermalisation happens while the propellant is flowing downstream at significant velocities. The difference in temperature between plasma operation (`S02`) and cold gas operation (`S01`) is $\Delta T = +195.9\,\text{K}$ at this location.

The extrapolated T profile of `S04` (red –·– line) mostly follows that of `S02` (red — line) in the plenum and discharge chamber. This is the expected result since the flow conditions upstream of the sonic surface [167] are insensitive to the flow conditions downstream due to flow velocity choking (Section 6.2). Beyond the discharge chamber exit, the T profile of `S04` transitions to follow that of `S03` (blue –·– line). Consequently, it deviates from the verifiable T profile of `S02`, and there is indeterminate uncertainty regarding the accuracy of the data in the downstream region. Nonetheless, only the results up to $z \leq 0\,\text{mm}$ are necessary for characterising the performance of `PR`, and the deviation is small within the discharge chamber.

`PR-C`

Figure 7.9 plots the T profiles of `PR-C`, and the main features are quite similar to those of `PR-O` (Figure 7.8). In `PR-C`, the pressure gradient is mostly dropped at the nozzle throat, and so the temperature drop associated with the acceleration of the propellant occurs at the nozzle throat ($z = -3\,\text{mm}$).

The temporally varying $T(t)$ profiles of `S06` (light red — lines) reveal a peak that corresponds to the position of the central gamma mode peak, as well as a second peak that corresponds to the downstream alpha mode peak at the nozzle throat. The combined heating from these two locations result in a T profile (red — line) that peaks in between the powered electrode and the nozzle throat. The maximum temperature of $T = 704.9\,\text{K}$ ($\Delta T = +409.5\,\text{K}$) is attained at $z = -6.6\,\text{mm}$. The larger increase in temperature is primarily due to higher n_i, and also constitutes a higher RF power draw. At the discharge chamber exit, the T profile shows a large dip, which indicates significant overexpansion of the exhaust plume. This behaviour is expected, as the nozzle geometry is more suited for operating in a near-vacuum

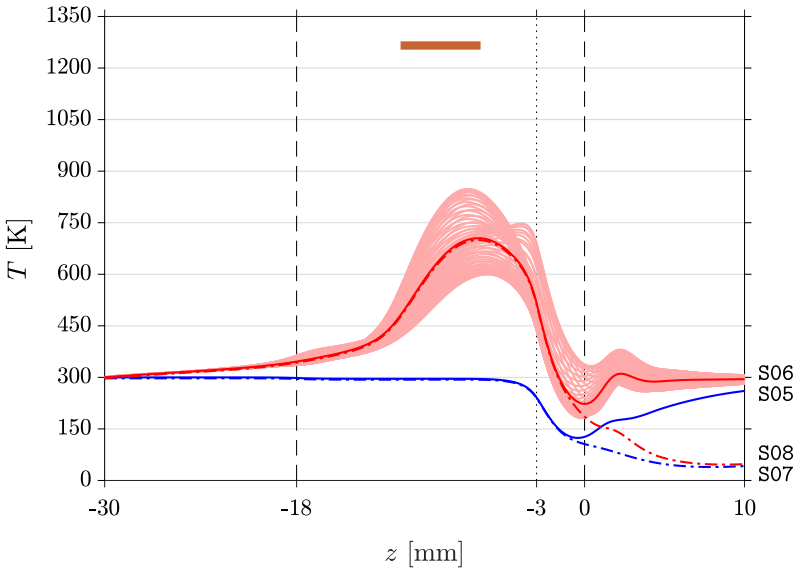

Figure 7.9: Cycle average neutral gas temperature T along the z-axis for PR-C. Cold gas operation: S05 (blue — line, $p_0 = 0.349$ Torr) and S07 (blue –·– line, $p_0 = 0$ Torr). Plasma operation: S06 (red — line, $p_0 = 0.349$ Torr) and S08 (red –·– line, $p_0 = 0$ Torr, extrapolated results).

environment rather than at $p_0 = 0.349$ Torr. There is a small bump following the dip as the fast expanding exhaust plume encounters the static background gas before reaching thermal equilibrium.

As for S08 (red –·– line), the T profile follows that of S06 almost exactly in the discharge chamber. There is less deviation in the results upstream of the nozzle throat since the nozzle throat provides a more well defined *vena contracta*. This is advantageous as there is less error or uncertainty in the f_T (as well as the functions for other fluid parameters), and all the extrapolated fluid parameters are accurate up to the nozzle throat. However, there is still a similar amount of deviation near the discharge chamber exit in PR-C as in PR-O.

PR-N

Figure 7.10 plots the T profiles of PR-N (S09 to S12). While the cold gas operation S09 (blue — line) and S11 (blue –·– line) look very similar to those of PR-C (Figure 7.9), there is a striking difference in the T profile of S10 during plasma operation (red — line). The temperature in the plenum is increased significantly, and rises almost linearly along the z-axis. This creates a T profile in the shape of a wedge instead of a peaked profile like those seen earlier in PR-O and PR-C.

Closer inspection of the temporally varying $T(t)$ profiles (light red — lines) reveal features very similar to the shape of the n_i profile (Figure 7.2c; Figure 7.4, blue — line). In the discharge chamber, there is a plateau in the $T(t)$ profiles, followed by a peak, and then a second peak. The plateau in the $T(t)$ profiles is more evident in `PR-N` as the upstream alpha mode ionisation is significantly higher than in `PR-O` and `PR-C` (see Figure 7.5). While the top of the T profile is almost flat, the maximum temperature $T = 764.0\,\mathrm{K}$ is attained at $z = -5.4\,\mathrm{mm}$, slightly upstream of the nozzle throat. This gives a temperature difference of $\Delta T = +474.9\,\mathrm{K}$.

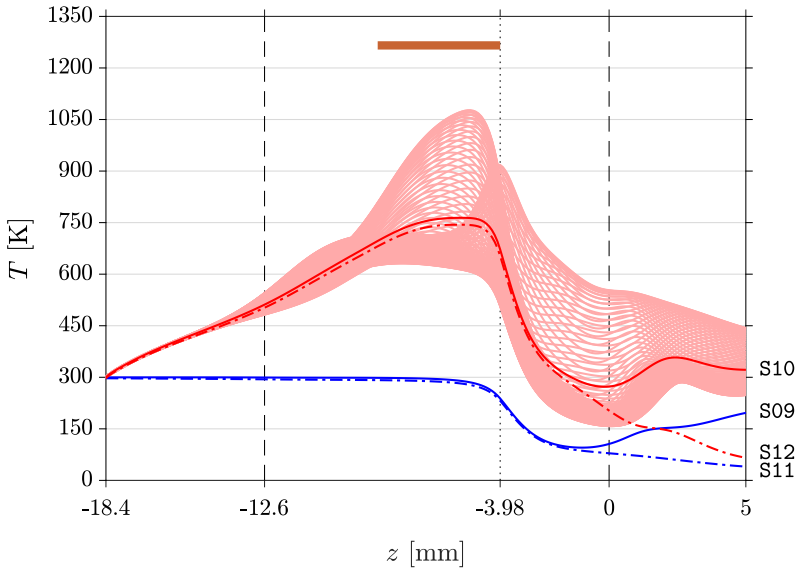

Figure 7.10: Cycle average neutral gas temperature T along the z-axis for `PR-N`. Cold gas operation: `S09` (blue — line, $p_0 = 0.349\,\mathrm{Torr}$) and `S11` (blue –·– line, $p_0 = 0\,\mathrm{Torr}$). Plasma operation: `S10` (red — line, $p_0 = 0.349\,\mathrm{Torr}$) and `S12` (red –·– line, $p_0 = 0\,\mathrm{Torr}$, extrapolated results).

An interesting result is the large variation in the $T(t)$ profiles in the divergent section of the nozzle in `S10`. This is mainly due to the cyclic heating by the alpha mode discharge at the nozzle throat. The variation is much larger than in `PR-C` (Figure 7.9, light red — lines) as it directly corresponds to $n_\mathrm{i}(t)$ (Figure 7.4, light blue — lines) and the alpha mode ionisation (Figure 7.5c) at the nozzle throat. The large variation in the $T(t)$ profiles persists in the downstream region, but as a whole produces the same overexpansion feature in T seen earlier in `PR-C`. The temporal variation in $T(t)$ together with the overexpansion results in a larger deviation of the T profile of `S12` (red –·– line) from that of `S10` at the discharge chamber exit.

The fourth set of simulations performed with PR-N (Figure 7.11, S13 to S16) eliminates all of the issues mentioned earlier: the deviation of the extrapolated results from the results of the performed CFD-plasma simulation, the overexpansion of the exhaust plume exiting into a high p_0 environment, and the inability to accurately model the plasma operation of PR in a vacuum environment. For the cold gas operation cases S13 (blue — line) and S15 (blue –·– line), the T profiles are very similar to that of S09 (Figure 7.10, blue — line) and S11 (Figure 7.10, blue –·– line), except that they deviate after $z = 0\,\text{mm}$ rather than before. This is evidence that $p_0 = 0.1\,\text{Torr}$, which is sufficiently high for fluid numerical techniques to be valid, is at the same time sufficiently low for emulating the fluid parameters of PR-N operating in vacuum, with adequate accuracy at least up to $z \leq 0\,\text{mm}$.

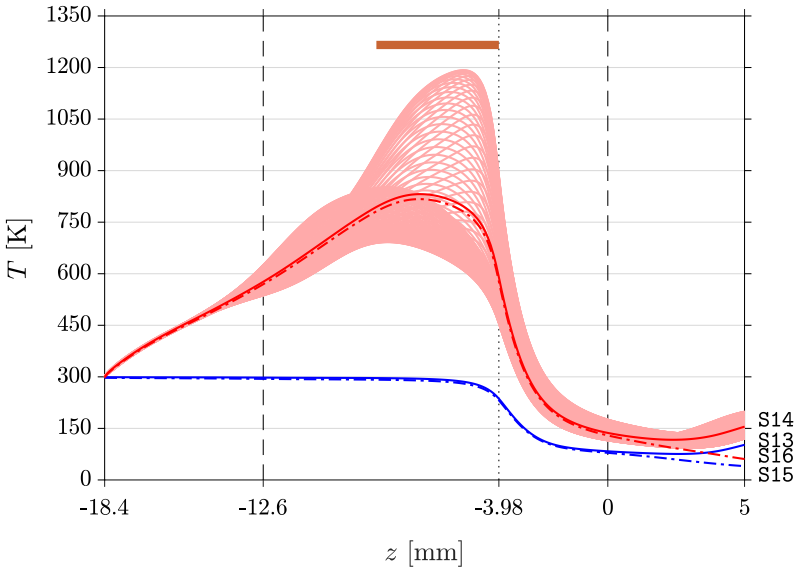

Figure 7.11: Cycle average neutral gas temperature T along the z-axis for PR-N. Cold gas operation: S13 (blue — line, $p_0 = 0.1\,\text{Torr}$) and S15 (blue –·– line, $p_0 = 0\,\text{Torr}$). Plasma operation: S14 (red — line, $p_0 = 0.1\,\text{Torr}$) and S16 (red –·– line, $p_0 = 0\,\text{Torr}$, extrapolated results).

The $T(t)$ profiles of S14 (light red — lines) differ from that of S10 (Figure 7.10, light red — lines) even though the same geometry is used. This is because of the distinctly different discharge characteristics in PR-N when operating in a background pressure of $p_0 = 0.1\,\text{Torr}$. The upstream plateau and downstream peak features in the $T(t)$ profiles are replaced by a single lower but wider peak corresponding to the location of the alpha mode ionisation (Figure 7.5d). The overlap of the alpha mode and gamma mode ionisation regions results in a much higher peak in $T(t)$ under the powered electrode. The absence of plasma in the

divergent section of the nozzle (Figure 7.2d; Figure 7.4, light red — lines) has also resulted in a stable temperature in neutral exhaust plume.

Overall, the cycle average T profile of `S14` (red — line) still has the shape of a wedge, but with steeper gradients and a rounded top. The maximum temperature is $T = 831.6\,\mathrm{K}$, attained at $z = -6.9\,\mathrm{mm}$. The difference in temperature when compared with cold gas operation is $\Delta T = +537.2\,\mathrm{K}$, which is the greatest increase recorded so far. The T profile also does not show overexpansion at the discharge chamber exit, indicating that $p_0 = 0.1\,\mathrm{Torr}$ is low enough to mimic vacuum expansion of the propellant in `PR-N`.

Because the T profiles of `S13` (blue — line) and `S15` (blue –·– line) are almost identical throughout `PR-N`, the extrapolation function f_T makes very little adjustments to the T profile of `S16` (red –·– line) up to $z \leq 0\,\mathrm{mm}$. Essentially, this means that `S14` performed with $p_0 = 0.1\,\mathrm{Torr}$ can be considered as a proxy for obtaining an equivalent CFD-plasma model of `PR-N` operating in $p_0 = 0\,\mathrm{Torr}$, thereby overcoming the limitations of the fluid and plasma numerical techniques in a vacuum environment. Nonetheless, extrapolation of `S16` is performed for consistency and comparison to other extrapolated results (`S04`, `S08`, and `S12`).

7.5.2 Knudsen number

Another reason for addressing the problem via CFD-plasma modelling is that the alternative via theoretical means brings about particular difficulties as the flow is in the slip regime, where the Navier-Stokes equations are only valid in the main flow and not in the boundary layer. In this regime, it is necessary to use the slip boundary condition, which requires a full CFD treatment.

The slip regime is characterised by a Knudsen number in the range of $0.01 \lesssim \mathrm{Kn} \lesssim 0.1$. Kn is a dimensionless parameter given by the ratio of the mean free path of a molecule λ to the characteristic length of the flow system L. In the plenum L is half the length; in the discharge chamber L is the radius which varies along the z-axis in the nozzle `PR` geometries; in the downstream region $L = 22.5\,\mathrm{mm}$ (radius of the glass expansion tube in the experimental setup [14]) is used as a worst case scenario. Figure 7.12 plots Kn along the z-axis for the fourth set of simulations using `PR-N` as an example, demonstrating that most of the flow is in the slip regime, and hence simple theoretical calculations using continuum fluid dynamics are inadequate for providing an accurate understanding of the flow characteristics in `PR-N`.

CFD and CFD-plasma modelling techniques on the other hand are well suited to treating flows in the slip regime. In particular, the low Kn in the downstream region of `S13` (blue — line) and `S14` (red — line) confirms that the fluid and plasma results are valid at $p_0 =$

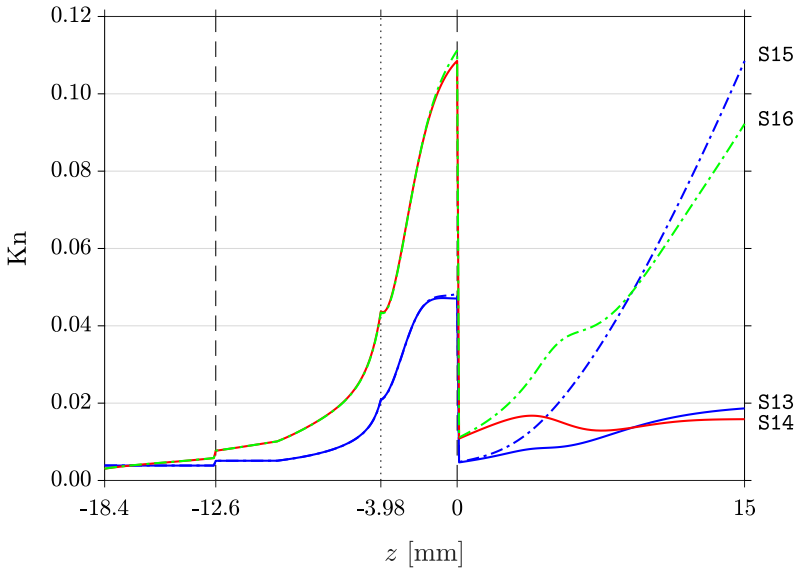

Figure 7.12: Knudsen number Kn along the z-axis for `S13` (blue — line), `S14` (red — line), `S15` (blue –·– line), and `S16` (green –·– line). Flow in `PR-N` is in the slip regime ($0.01 \lesssim \text{Kn} \lesssim 0.1$).

0.1 Torr. Although Kn is at the upper limit of the slip regime in `S15` (blue –·– line), the results from this CFD simulation are almost identical to that of `S13` (Figure 7.11), indicating that they are also valid and accurate to a high degree. Similarly, the extrapolated `S16` results are very close the the original `S14` results (Figure 7.11), and `S16` is therefore equally valid and accurate as the original CFD-plasma simulation up to $z \leq 0\,\text{mm}$. However, because Kn rises rapidly in the downstream region for `S15` (blue –·– line) and `S16` (green –·– line), there is a limited distance beyond the discharge chamber exit whereby the CFD and CFD-plasma results remain accurate. In practice, all results beyond $z > 0\,\text{mm}$ are discarded to preserve the integrity of the data and the rigour of the method.

7.5.3 Axial velocity

The primary purpose of heating in `PR` is to increase the exit velocity of the propellant. There is no easy method to experimentally measure the velocity profile of the propellant inside the discharge chamber due to its geometry and small physical dimensions. Again, the only way is by computational means, with a full treatment of boundary layer effects which are dominant in the slip regime.

Figures 7.13 to 7.16 plot the cycle average axial velocity u_z profiles for the first four sets of simulations (`S01` to `S16`), comparing cold gas operation (blue) to plasma operation

(red) as well as operation in a nonzero p_0 environment (— lines) to operation in a vacuum environment with $p_0 = 0\,\text{Torr}$ (-·- lines). The brown bar at the top of each figure shows the location of the powered electrode in the respective PR geometry.

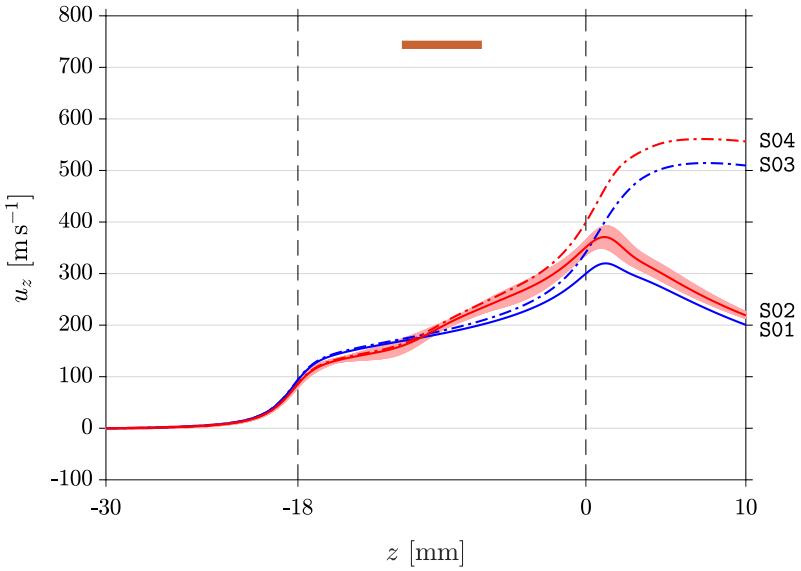

Figure 7.13: Cycle average axial velocity u_z along the z-axis for PR-O. Cold gas operation: S01 (blue — line, $p_0 = 0.349\,\text{Torr}$) and S03 (blue -·- line, $p_0 = 0\,\text{Torr}$). Plasma operation: S02 (red — line, $p_0 = 0.349\,\text{Torr}$) and S04 (red -·- line, $p_0 = 0\,\text{Torr}$, extrapolated results).

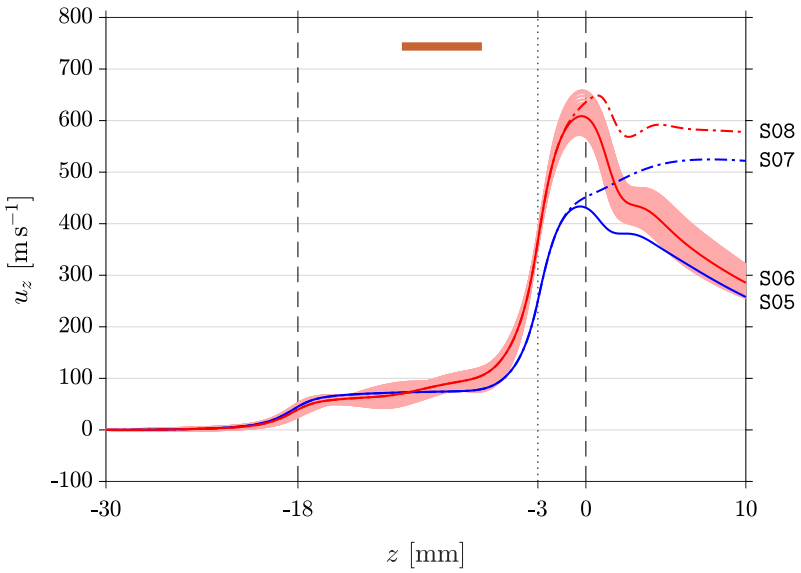

Figure 7.14: Cycle average axial velocity u_z along the z-axis for PR-C. Cold gas operation: S05 (blue — line, $p_0 = 0.349\,\text{Torr}$) and S07 (blue -·- line, $p_0 = 0\,\text{Torr}$). Plasma operation: S06 (red — line, $p_0 = 0.349\,\text{Torr}$) and S08 (red -·- line, $p_0 = 0\,\text{Torr}$, extrapolated results).

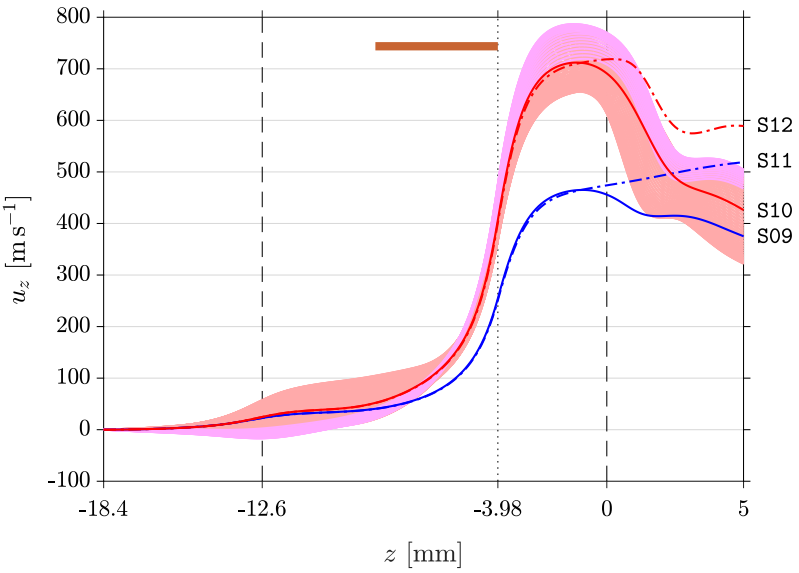

Figure 7.15: Cycle average axial velocity u_z along the z-axis for PR-N. Cold gas operation: S09 (blue — line, $p_0 = 0.349$ Torr) and S11 (blue -·- line, $p_0 = 0$ Torr). Plasma operation: S10 (red — line, $p_0 = 0.349$ Torr) and S12 (red -·- line, $p_0 = 0$ Torr, extrapolated results). The light magenta — lines highlight the portion of the $u_z(t)$ profile (time-steps 91 to 113 out of 120) that is suggestive of neutral pumping.

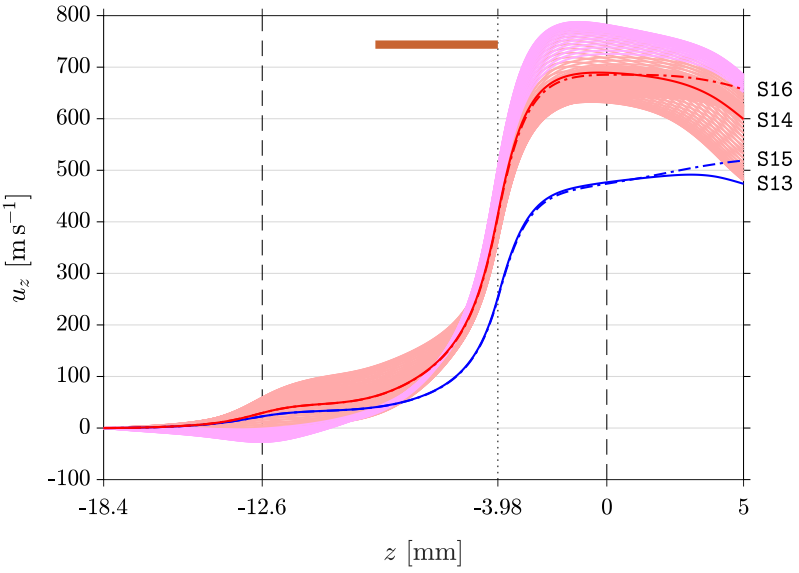

Figure 7.16: Cycle average axial velocity u_z along the z-axis for PR-N. Cold gas operation: S13 (blue — line, $p_0 = 0.1$ Torr) and S15 (blue -·- line, $p_0 = 0$ Torr). Plasma operation: S14 (red — line, $p_0 = 0.1$ Torr) and S16 (red -·- line, $p_0 = 0$ Torr, extrapolated results). The light magenta — lines highlight the portion of the $u_z(t)$ profile (time-steps 90 to 112 out of 120) that is suggestive of neutral pumping.

During plasma operation, the u_z profiles (red — lines) clearly show a marked increase in the acceleration of the propellant at the nozzle throat of PR-C (Figure 7.14) and PR-N (Figures 7.15 and 7.16). Although plasma operation raises the temperature of the propellant in PR-O (Figure 7.13), the thermal energy of the hot propellant is not effectively transformed into linear kinetic energy for acceleration. Another advantage of the nozzle geometries of PR-C and PR-N is the low u_z in the discharge chamber. The propellant takes a longer time to transit through the discharge chamber, thereby allowing more time for effective thermalisation with the hot ions through ion-neutral charge exchange collisions (Section 4.5.2), which are also more numerous at the higher pressures within PR-C and PR-N.

For a short time (approximately 22 out of 120 time-steps or 13.52 ns) just after the negative peak of the RF cycle, the temporally varying $u_z(t)$ profiles of S10 (Figure 7.15) and S14 (Figure 7.16) are negative (light magenta — lines) in the region of the discharge chamber just upstream of the powered electrode while simultaneously being the highest downstream of the powered electrode. This behaviour is a strong suggestion of neutral pumping, i.e. the acceleration of neutrals by ion-neutral charge exchange collisions with fast ions [177, 178], for two reasons. Firstly, it occurs symmetrically upstream and downstream of the gamma mode discharge along the z-axis (Figure 7.4). Secondly, the time of its occurrence is just after the peak of the gamma mode ionisation, during which a new population of hot ions have been created. The neutral pumping is unlikely to be due to heating by electron-neutral elastic collisions, firstly because the ion-neutral charge exchange collisions are far more dominant in terms of the amount of power transferred to the neutrals (Section 4.5) and secondly the time and position of the peak electron-neutral elastic collision rate does not synchronise with the neutral pumping feature in the $u_z(t)$ profiles.

While the $u_z(t)$ profiles demonstrate neutral pumping both upstream against the main flow and downstream accelerating past the main flow, the same behaviour is not perceptible in the radial direction towards the discharge chamber wall, as the radial velocity u_r is convergent towards the central axis of the nozzle throat. In any case, the neutral pumping features (light magenta — lines) do not constitute absolute evidence of the phenomenon, as the temporal variation of the $u_z(t)$ profiles is to a certain degree a result of the large fluid time-step $\Delta\tau_\mathrm{f}$ rather than an actual response to the variation of the plasma parameters over the plasma time-step $\Delta\tau_\mathrm{p}$.

In all the simulations performed with $p_0 = 0.349$ Torr (Figures 7.13, 7.14, and 7.15; — lines), the u_z profiles decline rapidly as the exhaust plume encounters the static gas in the downstream region. For PR-C (Figure 7.14) and PR-N (Figure 7.15), the u_z profiles already start to decrease in the divergent section of the nozzle due to overexpansion into the high

background pressure. This creates an indeterminate uncertainty when extrapolating those results to $p_0 = 0\,\text{Torr}$, as seen by the deviation between the — and -·- lines. This problem is solved by using $p_0 = 0.1\,\text{Torr}$ instead (Figure 7.16, — lines), which produces almost identical results for `S13` (blue — line) and `S15` (blue -·- line). Extrapolation of the u_z profile from `S14` (red — line) to `S16` (red -·- line) is therefore minimal. Moreover, the u_z profile has an almost constant and flat gradient at the discharge chamber exit, indicating no overexpansion in the nozzle, and thus ensures a high degree of accuracy in the extrapolated results.

7.5.4 Transient thrust performance

Terrestrial experimental instruments are often not sufficiently accurate for measuring thrust forces on the order of $\sim 1\,\text{mN}$ or thrust force variations in smaller fractions of this value, and transient or pulsed operation brings with it even more challenges [179].

Alternatively, thrust forces are often estimated using theoretical methods that are only valid for conventional nozzles, neglecting the important slip regime boundary layer effects that are dominant at the operating conditions of the microthruster. For example, calculating the thrust force using only the pressure force imbalance in the microthruster does not take into account the friction forces between the boundary layer and the wall (Section 6.3.3). Another commonly used method is to assume that the exit velocity of the propellant is the local sound speed c_s (1.3). If there is a nozzle, then acceleration of the propellant is assumed to be relative to the ratio of the exit area to the throat area. In reality, the sonic surface is not flat, and the exit velocity has a profile that is highly modulated by the boundary layer near the wall, and cannot be simplified to a single number. Again, a full CFD treatment with the appropriate slip boundary condition is required to accurately model the flow characteristics in this $0.01 \lesssim \text{Kn} \lesssim 0.1$ regime.

Propellant exit velocity

Figures 7.17 to 7.20 plot the exit cycle average axial velocity $u_{z,\text{ex}}$ profiles for the first four sets of simulations. In `PR-O` (Figure 7.17), the $u_{z,\text{ex}}$ profiles of the $p_0 = 0\,\text{Torr}$ cases (-·- lines) are displaced positively relative to the $u_{z,\text{ex}}$ profiles of the $p_0 = 0.349\,\text{Torr}$ cases (— lines), while preserving the rounded shape. This indicates that the propellant flow is simply accelerated by a certain amount, and the width of the boundary layer at the exit is roughly the same in the four `PR-O` simulations.

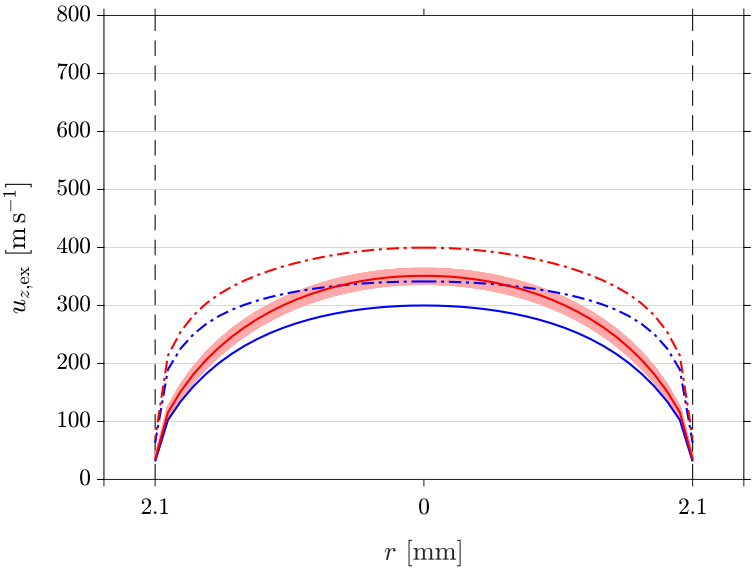

Figure 7.17: Cycle average axial velocity $u_{z,\mathrm{ex}}$ across the discharge chamber exit for `PR-O`. Cold gas operation: `S01` (blue — line, $p_0 = 0.349\,\mathrm{Torr}$) and `S03` (blue –·– line, $p_0 = 0\,\mathrm{Torr}$). Plasma operation: `S02` (red — line, $p_0 = 0.349\,\mathrm{Torr}$) and `S04` (red –·– line, $p_0 = 0\,\mathrm{Torr}$, extrapolated results).

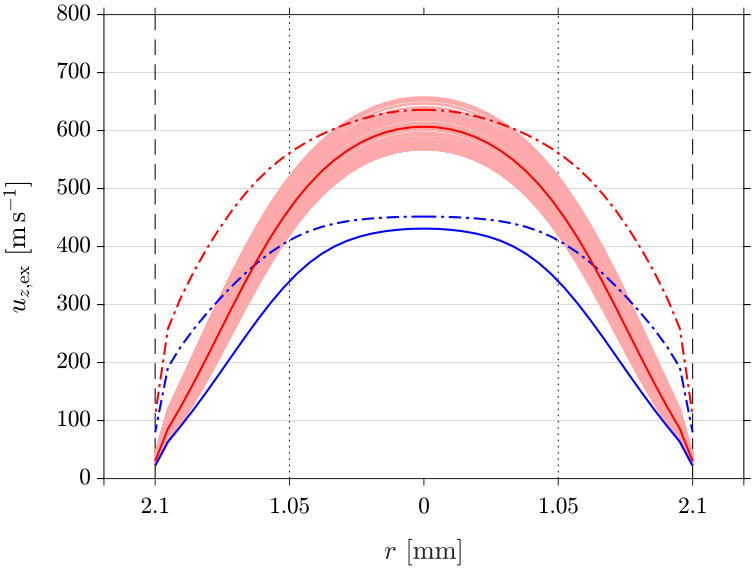

Figure 7.18: Cycle average axial velocity $u_{z,\mathrm{ex}}$ across the discharge chamber exit for `PR-C`. Cold gas operation: `S05` (blue — line, $p_0 = 0.349\,\mathrm{Torr}$) and `S07` (blue –·– line, $p_0 = 0\,\mathrm{Torr}$). Plasma operation: `S06` (red — line, $p_0 = 0.349\,\mathrm{Torr}$) and `S08` (red –·– line, $p_0 = 0\,\mathrm{Torr}$, extrapolated results). Vertical ····· lines mark the diameter of the nozzle throat.

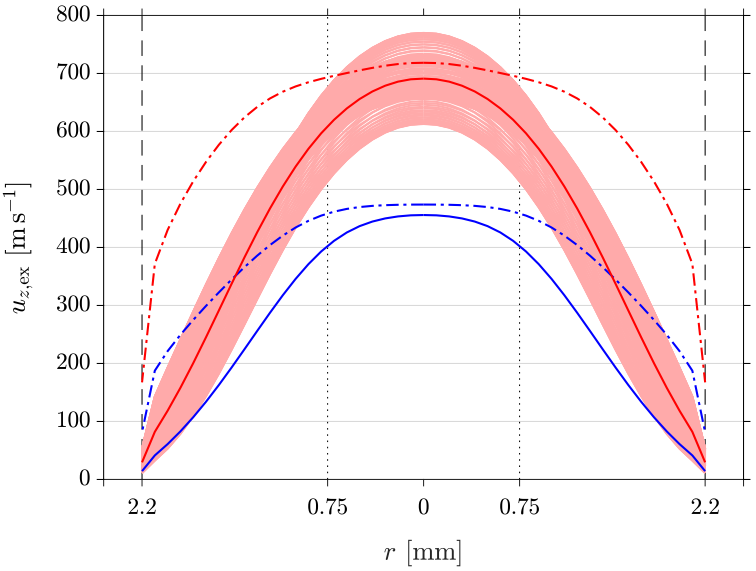

Figure 7.19: Cycle average axial velocity $u_{z,\mathrm{ex}}$ across the discharge chamber exit for `PR-N`. Cold gas operation: `S09` (blue — line, $p_0 = 0.349\,\mathrm{Torr}$) and `S11` (blue -·- line, $p_0 = 0\,\mathrm{Torr}$). Plasma operation: `S10` (red — line, $p_0 = 0.349\,\mathrm{Torr}$) and `S12` (red -·- line, $p_0 = 0\,\mathrm{Torr}$, extrapolated results). Vertical ····· lines mark the diameter of the nozzle throat.

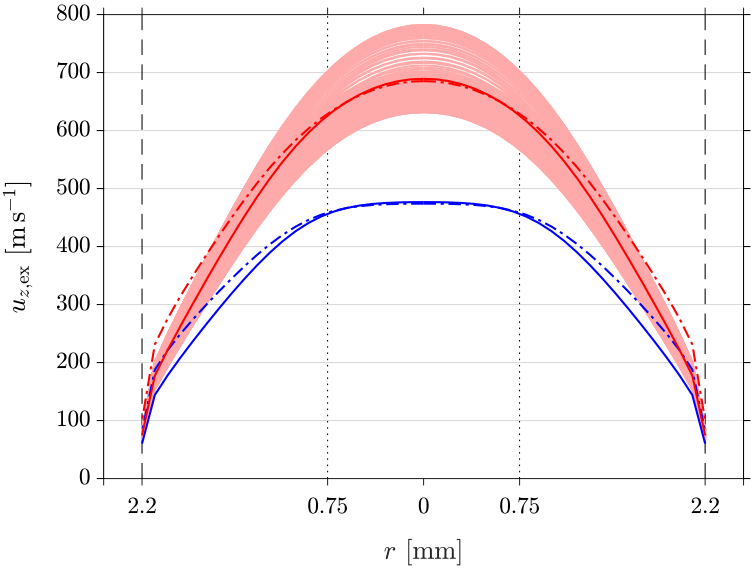

Figure 7.20: Cycle average axial velocity $u_{z,\mathrm{ex}}$ across the discharge chamber exit for `PR-N`. Cold gas operation: `S13` (blue — line, $p_0 = 0.1\,\mathrm{Torr}$) and `S15` (blue -·- line, $p_0 = 0\,\mathrm{Torr}$). Plasma operation: `S14` (red — line, $p_0 = 0.1\,\mathrm{Torr}$) and `S16` (red -·- line, $p_0 = 0\,\mathrm{Torr}$, extrapolated results). Vertical ····· lines mark the diameter of the nozzle throat.

On the other hand, there is a pronounced difference between the $u_{z,\mathrm{ex}}$ profiles for the $p_0 = 0\,\mathrm{Torr}$ (-·- lines) and $p_0 = 0.349\,\mathrm{Torr}$ (— lines) cases in PR-C (Figure 7.18) and the third set of simulations performed with PR-N (Figure 7.19). This is a sign of overexpansion in the $p_0 = 0.349\,\mathrm{Torr}$ cases (— lines). The concern here is with the accuracy of the extrapolated $u_{z,\mathrm{ex}}$ profiles (red -·- lines) in the first three sets of simulations, which have a large deviation from $u_{z,\mathrm{ex}}$ in the original CFD-plasma simulation results (red — lines). In the fourth set of simulations performed with PR-N (Figure 7.20), the propellant is ideally expanded in both the $p_0 = 0.1\,\mathrm{Torr}$ and $p_0 = 0\,\mathrm{Torr}$ cases.

The $u_{z,\mathrm{ex}}$ profiles of the nozzle geometries PR-C and PR-N (Figures 7.18, 7.19, and 7.20) are strongly peaked in the centre of the discharge chamber exit at $r = 0\,\mathrm{mm}$, as the flow on the central axis is least affected by viscosity and friction from the boundary layer. The rising portion of the $u_{z,\mathrm{ex}}$ profiles near the wall shows that the boundary layer is dominant over a significant area of the flow cross section. Neglecting to account for boundary layer effects, as it often happens, inevitably results in gross overestimations of the propellant exit velocity as well as the thrust force and other performance metrics. Trying to find the shape of the $u_{z,\mathrm{ex}}$ profile via theoretical means is nontrivial; the fictitious slip velocity and temperature jump [107] parameters at the wall must be determined using a full CFD treatment with appropriate tangential momentum and thermal accommodation coefficients (Section 3.2.2).

In the extrapolated plasma operation results, the cycle average peak exit velocities attained are: $u_{z,\mathrm{ex}} = 399.7\,\mathrm{m\,s^{-1}}$ (Mach 1.3, $c_{s,\mathrm{ex}} = 305.7\,\mathrm{m\,s^{-1}}$) in PR-O, $u_{z,\mathrm{ex}} = 635.9\,\mathrm{m\,s^{-1}}$ (Mach 2.5, $c_{s,\mathrm{ex}} = 252.5\,\mathrm{m\,s^{-1}}$) in PR-C, $u_{z,\mathrm{ex}} = 718.4\,\mathrm{m\,s^{-1}}$ (Mach 2.8, $c_{s,\mathrm{ex}} = 259.3\,\mathrm{m\,s^{-1}}$) in PR-N:S12, and $u_{z,\mathrm{ex}} = 685.3\,\mathrm{m\,s^{-1}}$ (Mach 3.2, $c_{s,\mathrm{ex}} = 211.4\,\mathrm{m\,s^{-1}}$) in PR-N:S16. Note that the Mach number is calculated relative to the cycle average local sound speed $c_{s,\mathrm{ex}}$ at $r = 0\,\mathrm{mm}$, which is dependent on the local temperature of the propellant. Since the exit velocity is limited by c_s at the sonic surface, it is beneficial to increase c_s as much as possible by increasing the local temperature of the propellant in the vicinity of the sonic surface. The PR-N geometry is the most effective in heating and accelerating the propellant. The peak $u_{z,\mathrm{ex}}$ in S14 is higher than in S16 primarily due to plasma-induced heating at the nozzle throat, which produces a hotter exhaust plume as well as a higher stagnation pressure p_st in the plenum (see Table 7.1).

Thrust force

The integral form of the general thrust equation (6.4) is used to calculate the thrust force F_t for each of the simulations listed in Table 7.1. The integration is performed beginning at

the central axis at $r = 0\,\text{mm}$ and ending at the discharge chamber wall at $r = 2.1\,\text{mm}$ for PR-O and PR-C, and $r = 2.2\,\text{mm}$ for PR-N. The integration of the mass flow rate of the gas $\dot{m}_{\text{ex}} = \rho_{\text{ex}} u_{z,\text{ex}}$ across the exit area compared to the supplied mass flow rate at the inlet of $\dot{m} = 100\,\text{SCCM}$ gives an error range of $-5.6\,\% \leq \Delta\dot{m}_{\text{ex}} \leq +0.1\,\%$, indicating that the results of CFD and CFD-plasma simulations are reasonably precise. Table 7.1 lists the computed thrust force F_t at $\dot{m} = 100\,\text{SCCM}$, with $\Delta\dot{m}_{\text{ex}}$ already taken into account. F_t values for simulations run with nonzero p_0 are printed in grey; the primary interest is the performance of PR in a vacuum environment.

The increase in the thrust force ΔF_{t} during plasma operation are: $+9.5\,\%$ in PR-O:S04, $+27.6\,\%$ in PR-C:S08, $+42.0\,\%$ in PR-N:S12, and $+27.2\,\%$ in PR-N:S16. The largest increase is seen in PR-N:S12, due to the heating of the propellant at the nozzle throat. However, it has been established that plasma operation in a vacuum environment drastically changes the discharge characteristics, and the ion density no longer peaks at the nozzle throat, and therefore PR-N:S12 is not an accurate representation of the performance in vacuum. Nonetheless, PR-N:S12 provides very useful information on how to further optimise the geometry of PR-N in order to reach a compromise between the desirable features of both plasma confinement and also plasma-induced heating at the nozzle throat. The optimised geometry may possibly achieve a $\Delta F_{\text{t}} \approx +35\,\%$ thrust force increase during plasma operation. Again, it must be stressed that these performance metrics and the F_{t} values represent the transient or pulsed plasma operation performance of PR at the present RF power draw, and higher performance is expected when the discharge chamber wall attains thermal equilibrium with the heated propellant or with higher RF power.

Specific impulse

The cycle average specific impulse I_{sp} calculated using F_t are also listed in Table 7.1. The values may be compared with the theoretical maximum specific impulse $\hat{I}_{\text{sp}}$ (1.5). For $T_{\text{st}} = 300\,\text{K}$, the theoretical maximum specific impulse for Ar gas is $\hat{I}_{\text{sp}} = 57.0\,\text{s}$. In the PR-N:S15 cold gas operation case, the steady state $I_{\text{sp}} = 49.1\,\text{s}$ is somewhat lower than $\hat{I}_{\text{sp}}$ due to frictional and viscous losses in the boundary layer, which are unavoidable in practice. In the PR-N:S16 plasma operation case on the other hand, the transient $I_{\text{sp}} = 62.5\,\text{s}$ represents the minimum value achieved at $\sim 1\,\text{s}$ after plasma ignition, and the eventual steady state I_{sp} is expected to be considerably higher after thermal equilibrium is attained (or with higher RF power).

Internal pressure force

The net internal pressure force F_p on PR can be measured by integrating the total fluid pressure force along all the internal-facing walls and the open exit area (illustrated by the blue ← and red → arrows in Figure 6.7b). Since the static pressure decreases along the z-axis, the pressure forces acting along the convergent and divergent sections of the nozzle vary along its length. The integration is performed radially, and excludes the radial component of the pressure force which cancels out on opposite sides of PR anyway. F_p obtained by this method is roughly 1.6 to 2.7 times of F_t. F_p must not be misinterpreted as the actual thrust force. It is not so, because this method fails to account for the friction force F_bl between the boundary layer and the wall (Section 6.3.3), and therefore results in a gross overestimation of the actual thrust force. F_bl can be thought of as a force exerted on the propellant by the wall which results in a loss against the momentum that the propellant has gained from the net pressure force imbalance. Alternatively, from the reference frame of the propellant, F_bl acts on the wall in the direction of flow, which is opposite to the intended direction of motion.

While there is no method for experimentally or theoretically measuring F_bl, the CFD and CFD-plasma simulations offer a means of obtaining its value by simply calculating the difference $F_\mathrm{t} - F_p = F_\mathrm{bl}$. Since the flow in PR is in the slip regime, boundary layer effects are significant, as made evident through the comparison of the respective values of F_bl and F_t listed in Table 7.1.

7.6 Power and thrust

7.6.1 Power deposition

Different amounts of RF power are required to drive the 300 V amplitude sinusoidal RF waveform on the powered electrode in each PR geometry and test case. The cycle average RF power draw P may be extracted by integrating the volumetric and surface energy at each time-step of the RF cycle. Volumetric power deposition (P_V) in the plasma is dominated by ion-neutral charge exchange collisions, but also includes processes such as electron-neutral elastic collisions and other volumetric reactions. Surface power deposition (P_S) is primarily due to ion bombardment onto the self-biased section of the discharge chamber wall shielding the powered electrode, with negligible contribution from other processes such as surface recombination and deexcitation reactions (Section 4.5). These values are listed in Table 7.2.

Table 7.2: Power deposition and thrust to power ratio

Sim.	P [W]	P_V [W]	P_V/P	P_S [W]	P_S/P	$\Delta F_t/P$ [μN W^{-1}]
PR-O:S02	5.010	0.34	6.87 %	4.67	93.1 %	+25.8 (S04)
PR-C:S06	13.28	1.16	8.74 %	12.1	91.3 %	+29.6 (S08)
PR-N:S10	12.39	2.14	17.3 %	10.2	82.7 %	+48.6 (S12)
PR-N:S14	12.01	1.97	16.4 %	10.0	83.6 %	+32.4 (S16)
PR-N:S17	10.62	1.47	13.8 %	9.15	86.2 %	+75.2 (S18)
PR-N:S19	8.746	1.20	13.7 %	7.55	86.3 %	+24.1 (S20)

In PR-O:S02, $P = 5.010$ W is in great agreement with the value of 4.725 W measured with a digital inline voltage/current (V/I) probe on the PR experimental setup. While the CFD and CFD-plasma modelling techniques have been fine tuned for PR-O against experimental and theoretical parameters such as pressure, velocity, thrust force, spatiotemporal heating trends, and the self-bias formation, the same techniques applied to PR-C and PR-N and different operating conditions produce results that are reasonable but not guaranteed to be absolutely accurate until they have been tested experimentally. For example, a CFD-plasma simulation of PR-O using a $V_{pwr} = 400$ V amplitude instead of 300 V show a RF power draw of $P = 16.26$ W which is significantly higher than the experimentally measured value of 10.0 W. This suggests that P is likely to be overestimated at higher RF voltages or at RF powers $\gtrsim 10$ W.

One possible solution is to empirically find the appropriate secondary electron emission coefficient $\gamma_{e'}$ that scales with RF voltages or RF powers. To explore this issue, CFD-plasma simulations PR-N:S17 and PR-N:S19 are run exactly in the same manner as PR-N:S10 and PR-N:S14 respectively, but with $\gamma_{e'} = 0.05$ instead of $\gamma_{e'} = 0.1$. The ensuing results have the same general characteristics as the respective prior cases, but with a slight scaling down of the ion density n_i and P, along with the other corresponding fluid and plasma parameters (see Tables 7.1 and 7.2). However, n_i and P are also dependent on a number of other factors such as the plasma impedance and the self-bias voltage at the discharge chamber wall (Section 5.3.5). Each of these factors must be treated rigorously in the CFD-plasma simulations and tested against experiments.

It is evident from Table 7.2 that the amount of power P_V deposited volumetrically into the propellant that effects heating is only a small proportion of the total RF power draw P. The remainder P_S, which is a significant proportion of P, is deposited onto the plasma-facing surface of the discharge chamber wall via ion bombardment. This energy is not wasted *per se*

since ion bombardment is a critical and necessary process for the creation of the secondary electrons that are ultimately responsible for sustaining the gamma mode discharge in PR. Additionally, P_S heats up the discharge chamber wall over time. As P_S is considerably higher than P_V, the thrust performance may increase quite significantly when the propellant is in thermal equilibrium with the discharge chamber wall. Unfortunately, this behaviour is not captured on the time scale of the present CFD-plasma simulations.

There is an improvement in P_V/P moving from `PR-O` to the nozzle geometries, with the highest proportion seen in `PR-N`. Interestingly for `PR-N`, the P_V/P in `S10` and `S14` are very similar, as are those of `S17` and `S19`. This is due to the dominant P_S which is directly related to ion dynamics in the plasma sheath along the self-biased section of the discharge chamber wall. Evidence of this is found in the cycle average electric potential on the plasma-facing surface of the discharge chamber wall Φ_{wall}, which is the main determining factor of ion dynamics in the plasma sheath apart from the value of $\gamma_{e'}$. In Figure 7.21, the Φ_{wall} profiles of `S10` (blue — line) and `S14` (red — line) track each other closely along the first half of the discharge chamber wall. The same behaviour is seen with the Φ_{wall} profiles of `S17` (cyan — line) and `S19` (magenta — line).

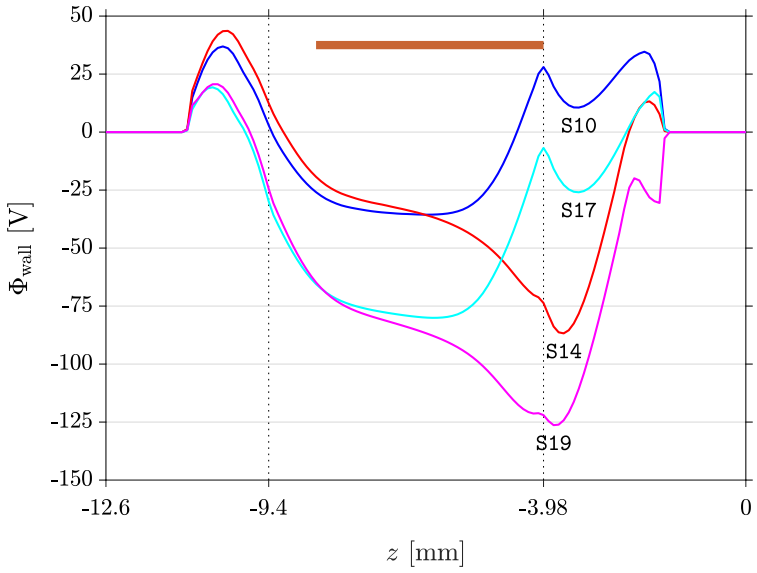

Figure 7.21: Cycle average electric potential on the plasma-facing surface of the discharge chamber wall Φ_{wall} in `S10` (blue — line), `S14` (red — line), `S17` (cyan — line), and `S19` (magenta — line). The convergent section of the nozzle ($-9.4\,\text{mm} \leq z \leq -3.98\,\text{mm}$) is demarcated by the vertical ····· lines. Note that Φ_{wall} is not necessarily the self-bias voltage (Section 5.3.4).

The partitioning of P_V versus P_S is directly related to the discharge impedance. Experimentally, this means that different PR designs require different impedance matching conditions. The CFD-plasma simulations are not affected since the RF voltage amplitude on the powered electrode is a fixed variable, with the assumption of perfect impedance matching in the RF electrical circuit between the powered electrode and the RF power generator. Overall, P tends to scale with n_i, but the problem is nonlinear and nontrivial. A greater number of ions increases the electrical conductivity of the discharge, and thus allows for more power to be coupled into the plasma while driving the powered electrode at the same RF voltage. This is analogous to the relation $P = V^2/R$.

7.6.2 Thrust to power ratio

The thrust to power ratio is quantified by calculating the increase in thrust force during plasma operation from cold gas operation per unit of supplied RF power. Most values of $\Delta F_t/P$ are in the range of $+24.1\,\mu N\,W^{-1}$ to $+32.4\,\mu N\,W^{-1}$. Table 7.2 shows PR-N:S12 and PR-N:S18 both giving a surprisingly high thrust to power ratio. This indicates that plasma-induced heating at the nozzle throat is very desirable, if it is indeed achievable in $p_0 = 0$ Torr conditions. Further optimisation of the nozzle geometry and discharge impedance can potentially allow PR to attain higher $\Delta F_t/P$ values, and become a highly attractive propulsion option on nanosatellite missions.

PR performs well in comparison with other electrothermal thrusters. A 4 GHz microwave electrothermal microthruster [180], which has dimensions similar to PR, operating with $P = 6\,W$ and $\dot{m} = 70\,SCCM = 0.20\,mg\,s^{-1}$ of He sees an increase of $\Delta F_t \approx 0.51\,mN - 0.33\,mN = +0.18\,mN$, thus giving $\Delta F_t/P \sim +30\,\mu N\,W^{-1}$. The TIHTUS hybrid electric thruster [8] operating in arcjet mode with $P = 50\,kW$ and $\dot{m} = 200\,SLPM = 300\,mg\,s^{-1}$ of H_2 increases the thrust force produced by $\Delta F_t = 2.04\,N - 0.98\,N = +1.06\,N$, thus giving $\Delta F_t/P = +21.1\,\mu N\,W^{-1}$. Finally, the hollow cathode thruster under development by the Surrey Space Centre [9] achieves a maximum $F_t = 1.6\,mN$ when operating with $P = 53\,W$ and $\dot{m} = 20\,SCCM = 1.95\,mg\,s^{-1}$ of Xe. The quoted specific impulse of $I_{sp} = 85\,s$ suggests a propellant temperature of $T = 2200\,K$. Estimating the cold gas thrust force to be $F_t' = \dot{m}c_s \approx 0.35\,mN$ at $T = 300\,K$ gives $\Delta F_t/P \approx +23.6\,\mu N\,W^{-1}$. However, the 30 W of power drawn by the heating element that is required for igniting the discharge is not accounted for in this value.

For perspective, the current record holder for the greatest thrust force generated by an electric thruster is the X3 three-channel nested Hall effect thruster [30, 31]. It has a mass of 230 kg, and uses Xe propellant flowing at up to $\dot{m} = 2000\,SCCM = 195\,mg\,s^{-1}$. X3

produces $F_t = 5.42\,\text{N}$ while drawing $P = 98.4\,\text{kW}$, giving it a gross thrust to power ratio of $F_t/P = 55.1\,\mu\text{N}\,\text{W}^{-1}$. The BHT-200 [25] has one of the highest gross thrust to power ratios among Hall effect thrusters at $F_t/P = 64\,\mu\text{N}\,\text{W}^{-1}$, producing $F_t = 12.8\,\text{mN}$ when operating with $P = 200\,\text{W}$ and $\dot{m} = 9.62\,\text{SCCM} = 0.94\,\text{mg}\,\text{s}^{-1}$ of Xe. Most other Hall effect thrusters typically fall in the range of $40\,\mu\text{N}\,\text{W}^{-1} \lesssim F_t/P \lesssim 60\,\mu\text{N}\,\text{W}^{-1}$ [28].

`PR-N:S16` operating with $\dot{m} = 100\,\text{SCCM} = 2.97\,\text{mg}\,\text{s}^{-1}$ of Ar produces $F_t = 1.821\,\text{mN}$ while drawing $P = 12.01\,\text{W}$ (see `S14` and `S16` in Table 7.1). This gives a gross thrust to power ratio of $F_t/P = 151.6\,\mu\text{N}\,\text{W}^{-1}$. A lower secondary electron emission coefficient of $\gamma_{e'} = 0.05$ instead of $\gamma_{e'} = 0.1$ results in `PR-N:S20` which produces a slightly lower $F_t = 1.735\,\text{mN}$ but at an even lower $P = 8.746\,\text{W}$ (see `S19` and `S20` in Table 7.1). This gives a further improved $F_t/P = 198.4\,\mu\text{N}\,\text{W}^{-1}$. As such, the gross thrust to power ratio of `PR-N` exceeds that of the aforementioned microwave electrothermal microthruster, arcjet, and hollow cathode thruster examples, which have $F_t/P = 85\,\mu\text{N}\,\text{W}^{-1}$ [180], $40.8\,\mu\text{N}\,\text{W}^{-1}$, [8] and $30.2\,\mu\text{N}\,\text{W}^{-1}$ [9] respectively. Most importantly, this level of performance is achievable within the volume, mass, and power budgets of a microspacecraft.

7.7 Chapter summary

This chapter investigates the performance of three different geometries of the `PR`: the original `PR-O` with a cylindrical discharge chamber, `PR-C` with a constricted nozzle, and a new design prototype `PR-N` featuring a sculpted converging-diverging nozzle. The reduced volume and mass of `PR-N` enables better compatibility with nanosatellite and CubeSat form factors, and the nozzle geometry is also optimised for the slip regime by accounting for the formation of the boundary layer in rarefied flow conditions.

The plasma, temperature, velocity, thrust force, and power parameters of `PR` are discussed in detail, with comparisons between the geometries, as well as between cold gas and plasma operation modes. The alpha and gamma mode ionisation profiles during the positive and negative periods of the RF cycle are examined, and are used to explain the shape of the ion density profile in the different geometries. Another interesting feature is the steep drop in the plasma potential at the nozzle throat in `PR-N`, where a plasma sheath forms at a virtual cathode. Ions accelerated to very high velocities across this potential gradient may impart axial momentum to a small population of neutrals in the exiting propellant and be beneficial for thrust performance. The CFD-plasma simulation results are also suggestive of neutral pumping caused by ion-neutral charge exchange collisions in the `PR-N` discharge.

The fluid parameters from the CFD-plasma simulations are extrapolated to vacuum conditions via pointwise transformation functions using the vacuum expansion cold gas CFD simulation results. The extrapolated results are most consistent in the $p_0 = 0.1\,\mathrm{Torr}$ `PR-N` simulations due to effective flow velocity choking and plasma confinement.

During plasma operation, the thrust force is increased by $\sim +30\,\%$ with a reasonable thrust to power ratio of $\sim +30\,\mu\mathrm{N\,W^{-1}}$ at a total RF power draw of $\sim 10\,\mathrm{W}$, in line with the power budget on a microspacecraft. At the standard operating conditions, `PR-N` achieves a gross thrust to power ratio between $\sim 150\,\mu\mathrm{N\,W^{-1}}$ and $\sim 200\,\mu\mathrm{N\,W^{-1}}$, exceeding that of many other electrothermal and Hall effect thrusters. These performance metrics represent the transient performance of `PR` at $\sim 1\,\mathrm{s}$ after plasma ignition, and higher performance is expected when the discharge chamber wall attains thermal equilibrium with the heated propellant or with higher RF power.

The most desirable discharge characteristics are found in the sculpted `PR-N` geometry. A higher ion density is achieved, and more RF power can be coupled into the plasma at a fixed RF voltage. The nozzle geometry not only increases the transit time of the propellant through the discharge chamber, which allows for more effective heating through more numerous ion-neutral charge exchange collisions, but is also able to confine the plasma within the discharge chamber due to the formation of a conical plasma sheath at the nozzle throat. The supersonic expanding plume is essentially neutral, likely due to enhanced recombination aided by ion-neutral charge exchange collisions, thereby avoiding contamination of externally mounted solar panels and interference with sensitive instruments. Future optimisations of `PR` are recommended to seek a compromise between plasma-induced heating at the nozzle throat and plasma confinement.

Chapter 8

Conclusion

8.1 Summary of results

In this thesis, progressive models of the *Pocket Rocket* RF CCP electrothermal microthruster have been developed via CFD and CFD-plasma simulations:

- Cold gas benchmark model ..... Chapter 3
- Plasma benchmark model ..... Chapter 4
- RF circuit model ..... Chapter 5
- Cold gas vacuum expansion model ..... Chapter 6
- Plasma vacuum expansion model ..... Chapter 7

The models are tailored for the standard operating conditions of `PR` with $\dot{m} = 100\,\text{SCCM}$ of Ar cold gas propellant and a $V_{\text{pwr}} = 300\,\text{V}$ amplitude sinusoidal waveform at $13.56\,\text{MHz}$ on the powered electrode. The `PR` discharge operates in the $p \gtrsim 1\,\text{Torr}$ regime, with propellant temperatures approaching $T \sim 1000\,\text{K}$ using $P \lesssim 10\,\text{W}$ of radiofrequency power, and produces a thrust force on the order of $F_{\text{t}} \sim 1\,\text{mN}$.

8.1.1 Cold gas benchmark model

The cold gas benchmark model gives an exact reproduction of the flow dynamics in the `PR` device. In the slip regime where the Knudsen number is in the range of $0.01 \lesssim \text{Kn} \lesssim 0.1$, the slip boundary condition must be applied with the correct tangential momentum and thermal accommodation coefficients. The referenced experiments recommend using $\alpha_u = 0.9$ and $\alpha_T = 0.9$ for Ar, $\alpha_u = 0.9$ and $\alpha_T = 0.8$ for N_2, and $\alpha_u = 1.0$ and $\alpha_T = 0.8$ for Xe. Due to the way α_T is implemented in CFD-ACE+, it is necessary to use a modified thermal

accommodation α'_T to preserve accuracy. The accommodation coefficients introduce fictitious slip velocity and temperature jump conditions at the flow boundary, such that when fulfilled, give a solution of the Navier-Stokes equation in the main flow that resembles the flow kinetics in reality.

Different boundary conditions are tested in the CFD simulations. The computed stagnation pressure p_{st} in the plenum confirms that only the slip boundary condition with the appropriate α values produces results that precisely match experimental measurements. p_{st} is overestimated with the commonly used no slip boundary condition, and underestimated with the inviscid boundary condition.

8.1.2 Plasma benchmark model

The plasma benchmark model enables a microscopic view into the plasma-induced heating of the neutral gas propellant in PR. To validate the accuracy of the CFD-plasma simulation results, the computed stagnation pressure, power draw, ion density, and neutral gas temperature are compared against experimental measurements.

The converged final solution represents conditions at $\sim 1\,\mathrm{s}$ after plasma ignition, when the neutral gas attains local thermal equilibrium but before any significant heating of the discharge chamber wall. The computed $p_{\mathrm{st}} = 1.532\,\mathrm{Torr}$ is 3.4 % higher than the measured $p_{\mathrm{st}} = 1.482\,\mathrm{Torr}$ target, and is therefore in good agreement. The computed $P = 5.010\,\mathrm{W}$ is also in good agreement with the measured $P_{\mathrm{PR}} = 4.725\,\mathrm{W}$. The computed n_{i} profile along the z-axis shows a strong central gamma mode peak, with $n_{\mathrm{i}} = 5.373 \times 10^{17}\,\mathrm{m}^{-3}$ at $z = -9.9\,\mathrm{mm}$, and two shoulder alpha mode plateaus. The upstream half of the n_{i} profile is in good agreement with the ion saturation current profile taken with a Langmuir probe, but the probe measurements taken in the downstream half of the discharge chamber are prone to greater errors due to constriction of the flow and perturbation of the plasma. Finally, a peak of $T = 467.7\,\mathrm{K}$ is attained at $z = -8.0\,\mathrm{mm}$, in agreement with the reported $T \sim 400\,\mathrm{K}$ measured in a N_2 plasma by rotational spectroscopy. The n_{i} and T profiles obtained from the CFD-plasma simulation are arguably more accurate than those that have been obtained experimentally due to limitations of the experimental instruments or techniques.

Three heat transfer mechanisms are examined in detail: electron-neutral elastic collisions, ion-neutral charge exchange collisions, and surface heating via ion bombardment. The amount of power deposited in the neutral gas via the former two volumetric processes is $P_{\mathrm{V}} = 0.344\,\mathrm{W}$, of which the majority is deposited in the discharge chamber. Ion-neutral charge exchange collisions are responsible for $\gtrsim 95.1\,\%$ of P_{V}, with values estimated at

$0.332\,\mathrm{W} \lesssim \sum_{\mathtt{P,C,D}} \epsilon_\mathrm{i} < 0.344\,\mathrm{W}$ across all the plasma regions in the PR simulation domain, while electron-neutral elastic collisions account for the remainder with $\sum_{\mathtt{C}} \epsilon_\mathrm{e} \lesssim 0.013\,\mathrm{W}$. A theoretical analysis of the energy transfer process during ion-neutral charge exchange collisions reveal that the radial T profile of the neutral gas follows two local models, being proportional to n_i in the plasma bulk, and $n_\mathrm{i}E_r^2$ in the plasma sheath.

The total surface power deposition is $P_\mathrm{S} = 4.666\,\mathrm{W}$, 99.5 % of which or $\sum_{\mathtt{CW}} \epsilon_\mathrm{S} = 4.641\,\mathrm{W}$ is deposited on the plasma-facing surface of the discharge chamber wall. Of the latter, $\sum_{\mathtt{CW}} \epsilon_\mathrm{c} = 0.098\,\mathrm{W}$ of chemical energy is released via surface recombination, and $\sum_{\mathtt{CW}} \epsilon_\mathrm{k} = 4.543\,\mathrm{W}$ of kinetic energy is released via ion bombardment which accounts for 90.7 % of the total power draw of $P = 5.010\,\mathrm{W}$.

Ion transport in the plasma sheath is therefore a very important process in PR. The radial ion velocity in the powered sheath attains a high of $u_{r,\mathrm{i}} = 30.35\,\mathrm{km\,s^{-1}}$ at the coordinates $(z, r) = (-9.9, 2.0)$. This value is taken one cell away from the discharge chamber wall, as CFD-ACE+ renders certain parameters over the width of two whole cells at the solid-plasma interface. Using a fourth order Runge-Kutta analysis on $u_{r,\mathrm{i}}$, the cycle average radial drift position of an ion $r_\mathrm{i}(t)$ is obtained as a function of time. Following the path of an ion across the radius of the discharge chamber finds that the average transit time through the plasma bulk is $\tau_\mathrm{i,bulk} = 19.25 \cdot \tau_\mathrm{RF} = 1.419\,\mathrm{\mu s}$, and the average transit time through the plasma sheath is $\tau_\mathrm{i,sheath} = 1.4 \cdot \tau_\mathrm{RF} = 103\,\mathrm{ns}$. An ion starting at $r = 0\,\mathrm{mm}$ spends 93.3 % of the total transit time in the plasma bulk, and only 6.7 % in the plasma sheath, which alternatively confirms that heat transfer via ion-neutral charge exchange collisions and thermalisation happens much more effectively in the plasma bulk than in the plasma sheath.

8.1.3 RF circuit model

The RF circuit model of the PR discharge is derived from electrical and plasma parameters obtained from the plasma benchmark model. The plasma potential in the plasma bulk oscillates between $\Phi_\mathrm{p}^- = 12.0\,\mathrm{V}$ and $\Phi_\mathrm{p}^+ = 60.9\,\mathrm{V}$, with a cycle average of $\Phi_\mathrm{p} = 27.0\,\mathrm{V}$. The electric potential at the plasma-facing surface of the discharge chamber wall is displaced negatively due to the self-bias that originates from the geometrical area asymmetry of the grounded and powered electrodes, and oscillates between $\Phi_\mathrm{wall}^- = -458.1\,\mathrm{V}$ and $\Phi_\mathrm{wall}^+ = 52.7\,\mathrm{V}$, with a cycle average of $\Phi_\mathrm{wall} = -193.0\,\mathrm{V}$. The peak-to-peak voltage falls from the applied 600 V on the powered electrode to 510.8 V due to the capacitive impedance of the dielectric discharge chamber wall, estimated at $C_\mathrm{wall} = 6.9\,\mathrm{pF}$ and $Z_\mathrm{wall} = 1.7\,\mathrm{k\Omega}$.

The $\Phi_{\text{wall}}(t)$ profile exhibits a diminished trailing edge at each positive peak, in accordance with the referenced experimental observations of self-biased voltage waveforms. The CFD-plasma simulation also captures the asymmetric response of $\Phi_{\text{wall}}(t)$ in the thin sheath $\tau_{\text{i}} \sim \tau_{\text{RF}}$ regime, in which the negative peaks are displaced due to the extraneous impedance introduced by the dielectric discharge chamber wall while the positive peaks remain constant, which is in good agreement with experimental observations of the bimodal ion energy distribution in the powered sheath. Consequently, the definition of the self-bias voltage used by traditional sheath circuit models are no longer valid. The maxima envelope Φ^{+}_{wall} alternatively provides a more stable baseline for a more rigorous definition of V_{bias}, since it is characteristic of the plasma parameters and the geometry of the plasma system. Additional advantages of this definition is that it is directly correlated with the measurable low energy peak of the ion energy distribution in the powered sheath, and also applicable to non-sinusoidal waveforms. Using this definition gives a consistent $V_{\text{bias}} = -246.5\,\text{V}$ across the different configurations of `PR` with the same electrode area ratio $A_{\text{gnd}}/A_{\text{pwr}}$, but different Z_{wall}.

The voltage division between the components of the RF circuit model enables the powered and grounded sheath impedances to be quantified, at $\left|Z_{\text{s,pwr}}\right| = 9.0\,\text{k}\Omega$ and $\left|Z_{\text{s,gnd}}\right| = 0.42\,\text{k}\Omega$ respectively. Using Ohm's law then gives a RMS RF plasma current of $\bar{I}_{\text{RF}} = 19\,\text{mA}$, which corresponds to a power of $P_{\text{RF}} = 4.0\,\text{W}$. P_{RF} only accounts for the power involved in the movement of the electrically charged species Ar^{+} and e^{-} at the grounded and powered electrodes, and excludes the power sunk into non-electrical processes such as plasma heating of the neutral gas and chemical reactions, and is in good agreement with the integrated steady state power $P = 5.010\,\text{W}$. A simple electrical model using sinusoidal current waveforms comprising of the ion, electron, and secondary electron fluxes is compared to the RF circuit model, and are in agreement to within 6 %.

Finally, the secondary electron emission profile is examined. The electron energy is approximately constant in the plasma bulk at $k_{\text{B}}T_{\text{e}} = 2.9\,\text{eV}$, and peaks at $k_{\text{B}}T_{\text{e}} = 111\,\text{eV}$ in the plasma sheath due to the population of high energy secondary electrons emitted from the surface of the discharge chamber wall by ion bombardment. $k_{\text{B}}T_{\text{e}}(t)$ of the secondary electrons varies temporally with $\Phi_{\text{wall}}(t)$, and the emission region is not limited to the section of the discharge chamber wall underneath powered electrode, but extends to cover the insulated section as well.

8.1.4 Cold gas vacuum expansion model

The cold gas vacuum expansion model takes advantage of the flow velocity choking phenomenon to unconventionally circumvent the problem of including vacuum regions within a CFD simulation. For a monatomic ideal gas, the minimum upstream to downstream pressure ratio of $p_{\mathrm{st}}/p_0^* = 2.053$ is required for the flow velocity to be choked. However, this criterion is only valid when the pressure difference occurs in the immediate vicinity of the *vena contracta* in a stream tube, as is the case in the constricted nozzle geometry of `PR-C`, and cannot be applied to the straight cylindrical geometry of the `PR-O` discharge chamber where the static pressure falls gradually along its length.

Although the propellant leaving the discharge chamber in `PR-O` is supersonic only in the middle of the exit area in the $p_0 = 0.349\,\mathrm{Torr}$ case, the flow is sufficiently choked that the flow conditions upstream of the sonic surface are insensitive to the flow conditions downstream. This is verified by the similarly shaped axial profiles of the static pressure and axial velocity as well as the Mach isocurves for the CFD simulations performed with the default $p_0 = 0.349\,\mathrm{Torr}$ and $p_0 = 0\,\mathrm{Torr}$. In the former case, u_z attains the local sound speed of $c_{\mathrm{s}} = 284.8\,\mathrm{m\,s^{-1}}$ at $z = -0.58\,\mathrm{mm}$, while in the latter case $c_{\mathrm{s}} = 283.5\,\mathrm{m\,s^{-1}}$ is attained at $z = -1.58\,\mathrm{mm}$. For `PR-C`, these profiles are essentially identical upstream of the constricted nozzle throat, demonstrating well defined choked flow behaviour. u_z becomes sonic at slightly different velocities with $c_{\mathrm{s}} = 280.3\,\mathrm{m\,s^{-1}}$ for the $p_0 = 0.349\,\mathrm{Torr}$ case and $c_{\mathrm{s}} = 279.3\,\mathrm{m\,s^{-1}}$ for the $p_0 = 0\,\mathrm{Torr}$ case, slightly downstream of the constricted nozzle throat at $z = -2.79\,\mathrm{mm}$.

Thrust force is calculated using the integral form of the general thrust equation since the fluid parameter profiles are not uniform across the exit surface due to significant boundary layer effects in the slip regime. This is in contrast to conventional nozzles in the continuum regime, in which the boundary layer friction force is often ignored. The computed F_{t} for `MiniPR` over a range of mass flow rates of Xe propellant is compared against experimental measurements obtained using a pendulum thrust balance in a space simulation chamber to validate the accuracy of the CFD simulations. The gradient of the computed F_{t} against $\dot{m}$ gives a specific impulse of $I_{\mathrm{sp}} = 27.6\,\mathrm{s}$, which is in good agreement with the theoretical maximum specific impulse of $\hat{I}_{\mathrm{sp}} = 31.4\,\mathrm{s}$. The experimental results on the other hand significantly underestimates $I_{\mathrm{sp}} = 15.9\,\mathrm{s}$, due to a systematic error arising from a diminished $\dot{m}'$ at 57.7 % of the expected value.

8.1.5 Plasma vacuum expansion model

The plasma vacuum expansion model is developed by incorporating the cold gas benchmark and vacuum expansion models with the plasma benchmark model. A pointwise transformation function is derived for each fluid parameter that transforms cold gas operation in nonzero background pressure cases ($p_0 = 0.349\,\text{Torr}$ and $p_0 = 0.1\,\text{Torr}$) to cold gas operation in $p_0 = 0\,\text{Torr}$ cases. The pointwise transformation functions are applied to the fluid parameters from the CFD-plasma simulations to extrapolate the CFD-plasma simulation results to vacuum conditions. Plasma parameters cannot be extrapolated as the cold gas simulations do not contain such information.

A sculpted converging-diverging nozzle is designed for `PR-N`. The convergent and divergent angles are set to 15° and 20° respectively. The divergent angle is greater than those of conventional nozzles to account for the formation of the boundary layer in rarefied flow conditions. The nozzle throat has a sharp angle to allow for a shorter 3.98 mm divergent section in order to minimise boundary layer friction losses. The nozzle throat has a radius of 0.75 mm, which is narrower than the width of the plasma sheath. Consequently, the plasma sheath along the discharge chamber wall merges into a conical shape in the nozzle throat and forms a virtual cathode, confining the plasma upstream. The supersonic expanding plume is essentially neutral, likely due to enhanced recombination aided by ion-neutral charge exchange collisions. The plasma confinement in `PR-N` is a desirable performance characteristic since it eliminates the return ion current on the exterior surfaces of the spacecraft, thereby avoiding contamination of externally mounted solar panels and interference with sensitive instruments. Additionally, plasma confinement is also beneficial for the convergence of the CFD-plasma simulation in the low $p_0 = 0.1\,\text{Torr}$ background pressure, as well as the veracity of the extrapolation of the fluid parameters to vacuum conditions.

Many other discharge characteristics are altered by the physical and electrical geometry of `PR-N`. The alpha and gamma mode ionisation profiles are more unified, creating a more uniform discharge and more concentrated heating. During plasma operation, a maximum temperature of $T = 831.6\,\text{K}$ is attained at $z = -6.9\,\text{mm}$, and $\Delta T = +537.2\,\text{K}$ over cold gas operation is the greatest increase recorded in all the CFD-plasma simulations. The nozzle geometry also optimises the expansion of the propellant as it leaves the discharge chamber, resulting in fluid parameter profiles that are congruent throughout `PR-N`. This means that the CFD-plasma simulation of `PR-N` performed with $p_0 = 0.1\,\text{Torr}$ can be considered as a proxy for obtaining an equivalent CFD-plasma model of `PR-N` operating in $p_0 = 0\,\text{Torr}$,

thereby overcoming the limitations of the fluid and plasma numerical techniques in a vacuum environment.

The computed F_t during cold gas operation and $\sim 1\,s$ after plasma ignition for each geometry are as follows. In PR-O, F_t increases from 1.363 mN to 1.493 mN (+9.5 %), with $P = 5.010\,W$ ($\Delta F_t/P = +25.8\,\mu N\,W^{-1}$, $F_t/P = 297.9\,\mu N\,W^{-1}$). In PR-C, F_t increases from 1.425 mN to 1.818 mN (+27.6 %), with $P = 13.28\,W$ ($\Delta F_t/P = +29.6\,\mu N\,W^{-1}$, $F_t/P = 136.9\,\mu N\,W^{-1}$). Finally in PR-N, F_t increases from 1.432 mN to 1.821 mN (+27.2 %), with $P = 12.01\,W$ ($\Delta F_t/P = +32.4\,\mu N\,W^{-1}$, $F_t/P = 151.6\,\mu N\,W^{-1}$). However, the CFD-plasma simulations tend to overestimate P at higher RF voltages or at RF powers $\gtrsim 10\,W$. A solution is to empirically find the appropriate secondary electron emission coefficient that scales with V_{pwr}. A CFD-plasma simulation of PR-N run with $\gamma_{e'} = 0.05$ instead of the default $\gamma_{e'} = 0.1$ gives the same general characteristics, but with a slight scaling down of n_i and P, along with the other corresponding fluid and plasma parameters. This results in a slightly lower $F_t = 1.735\,\mu N$ (+21.2 %), with $P = 8.746\,W$ ($\Delta F_t/P = +24.1\,\mu N\,W^{-1}$, $F_t/P = 198.4\,\mu N\,W^{-1}$).

The plasma operation performance metrics represent the 'instantaneous' or transient lower limit performance of PR at the stated RF power draw from a cold start. Performance is expected to further increase as the temperature of the discharge chamber wall rises and attains thermal equilibrium with the heated propellant on a time scale of $\sim 10\,s$, in a scenario similar to that of the self-heating mode of a hollow cathode thruster. The geometry of PR-N may possibly be further optimised to reach a compromise between plasma confinement and increased thrust force from plasma heating in the nozzle throat.

8.2 Future work

8.2.1 *Pocket Rocket*

Integration of PR on the CubeSat platform is ongoing alongside the development of the propellant and RF power subsystems. This is aided by design recommendations made with a better understanding of the PR discharge gained from the cold gas, plasma, and RF circuit models presented in this thesis. The CFD-plasma modelling technique may be expanded to encompass longer time scales in order to investigate the performance of PR as the temperature of the discharge chamber wall rises towards thermal equilibrium with the heated propellant.

Following the high performance and ideal discharge characteristics displayed by PR-N in the plasma vacuum expansion model, a physical prototype has been fabricated for experi-

mental testing. Despite the small dimensions of some components (Figure 7.1), conventional manufacturing processes are sufficient and no 3D printing is required. A plasma has been successfully ignited in the PR-N prototype, and experimental methods are being refined to investigate the criteria required to achieve the plasma confinement behaviour exhibited in the CFD-plasma simulations S14 and S19 (Table 7.1 and Figure 7.2d).

The abrupt drop in the plasma potential of $\Delta\Phi_p \approx 80\,\text{V}$ over a short distance of $\Delta z \approx 2\,\text{mm}$ at the nozzle throat of PR-N that occurs with plasma confinement displays the signature of a stationary current-free electric double layer. The CFD-plasma simulations in Chapter 7 suggest that the formation of the double layer is spontaneous in PR-N at standard operating conditions, and only requires a reduction in the background pressure from $p_0 = 0.349\,\text{Torr}$ to $p_0 = 0.1\,\text{Torr}$. Detailed investigations are commencing to study the new fundamental physics of the unmagnetised current-free electric double layer in the collisional regime.

8.2.2 Atmospheric pressure plasma jet

The CFD-plasma modelling technique and analysis presented in this thesis are not restricted to the PR discharge, and may be adapted for other discharges at different pressure regimes and physical scales. An example is the atmospheric pressure plasma jet (APPJ) used in applications ranging from surface modification [181] and thin film deposition [182] to biomedical treatments [183].

A preliminary CFD-plasma model has been developed for a nonthermal helium (He) APPJ source to complement experimental investigations of the biological tissue target [183, 184]. Typical operating conditions are with $\dot{m} = 4\,\text{SLPM}$ (standard litres per minute) of He gas, and a 50 kHz sinusoidal waveform with 10 kV peak-to-peak voltage. The CFD-plasma model consists of seven plasma species: He, He($2\,^3$S), He($2\,^1$S), He($2\,^3$P), He($2\,^1$P), He^+, and e^-, and a total of 38 volumetric chemical reactions. Atmospheric species and chemical reactions occurring outside of the APPJ source are not considered, as the primary focus is on the electrical and plasma characteristics of the discharge.

In the APPJ study, several modifications have been made to the PR CFD-plasma modelling technique to accommodate the low frequency waveform and high static pressure. As a $\sim 1\,\text{ns}$ time-step resolution is required for resolving plasma dynamics, 18,000 time-steps per cycle are used for the 20 µs period, which is significantly more than the 60 time-steps per RF cycle used for PR. Fortunately, convergence occurs more easily at atmospheric pressure, and therefore the number of fluid and plasma iterations can be reduced to $i_f = 3$ and $i_p = 1$, from $i_f = 10$ and $i_p = 5$ used for PR. Convergence is also quicker at atmospheric pressure,

requiring on the order of ~ 100 cycles instead of ~ 1000 RF cycles. However, the total computation time is still considerably longer for the He APPJ CFD-plasma simulation, taking around ~ 10 weeks compared to a fortnight for `PR`.

An experimental investigation is currently under way to verify the time resolved behaviour seen in the CFD-plasma model of the APPJ by fast optical imaging. Future work involves tailoring the APPJ simulation mesh to replicate different experimental configurations, and further refining the CFD-plasma modelling technique to improve accuracy and reduce computation time. The completed CFD-plasma model can then contribute data that are otherwise difficult, expensive, or impossible to obtain by experimental techniques.

Bibliography

[1] E. Gill et al. 'Formation flying within a constellation of nano-satellites: The QB50 mission'. *Acta Astronautica* 82.1 (May 2012), pp. 110–117. DOI: 10.1016/j.actaastro.2012.04.029.

[2] J. Virgili and P. C. E. Roberts. 'ΔDsat, a QB50 CubeSat mission to study rarefied-gas drag modelling'. *Acta Astronautica* 89 (Apr. 2013), pp. 130–138. DOI: 10.1016/j.actaastro.2013.04.006.

[3] D. L. Hitt, C. M. Zakrzwski and M. A. Thomas. 'MEMS-based satellitemicropropulsion via catalyzed hydrogen peroxide decomposition'. *Smart Materials and Structures* 10.6 (Nov. 2001), pp. 1163–1175. DOI: 10.1088/0964-1726/10/6/305.

[4] A. M. Baker et al. '"You can get there from here": Advanced low cost propulsion concepts for small satellites beyond LEO'. *Acta Astronautica* 57.2-8 (July 2005), pp. 288–301. DOI: 10.1016/j.actaastro.2005.03.046.

[5] A. D. Ketsdever, R. H. Lee and T. C. Lilly. 'Performance testing of a microfabricated propulsion system for nanosatellite applications'. *Journal of Micromechanics and Microengineering* 15.12 (Oct. 2005), pp. 2254–2263. DOI: 10.1088/0960-1317/15/12/007.

[6] H. Horisawa and I. Kimura. 'Very low-power arcjet testing'. *Vacuum* 59.1 (Oct. 2000), pp. 106–117. DOI: 10.1016/S0042-207X(00)00260-8.

[7] H. Horisawa, H. Ashiya and I. Kimura. 'Discharge characteristics of a very low-power arcjet'. *International Electric Propulsion Conference*. Toulouse, Mar. 2003.

[8] H. Böhrk and M. Auweter-Kurtz. 'Thrust measurement of the hybrid electric thruster TIHTUS by a baffle plate'. *Journal of Propulsion and Power* 25.3 (May 2009), pp. 729–736. DOI: 10.2514/1.34324.

[9] D. A. Lamprou et al. 'Hollow cathode thruster design and development for small satellites'. *International Electric Propulsion Conference*. Wiesbaden, Sept. 2011.

[10] A. N. Grubisic and S. B. Gabriel. 'Assessment of the T5 and T6 hollow cathodes as reaction control thrusters'. *Journal of Propulsion and Power* 32.4 (May 2016), pp. 810–820. DOI: 10.2514/1.B35556.

[11] V. Vekselman et al. 'Characterization of a heaterless hollow cathode'. *Journal of Propulsion and Power* 29.2 (Feb. 2012), pp. 475–486. DOI: 10.2514/1.B34628.

[12] D. Lev et al. 'Low current heaterless hollow cathode development overview'. *International Electric Propulsion Conference*. Atlanta, Oct. 2017.

[13] R. W. Boswell. 'Plasma micro-thruster'. World Intellectual Property Organization, Nov. 2012, WO2012–151639–A1. URL: https://patentscope.wipo.int/search/en/detail.jsf?docId=WO2012151639.

[14] C. Charles and R. W. Boswell. 'Measurement and modelling of a radiofrequency micro-thruster'. *Plasma Sources Science and Technology* 21.2 (Mar. 2012), p. 022002. DOI: 10.1088/0963-0252/21/2/022002.

[15] C. Charles et al. 'A short review of experimental and computational diagnostics for radiofrequency plasma micro-thrusters'. *Plasma Chemistry and Plasma Processing* 36.1 (Sept. 2015), pp. 29–44. DOI: 10.1007/s11090-015-9654-5.

[16] C. Charles et al. 'The Pocket Rocket electro-thermal plasma thruster for 'CubeSat' nano-satellites'. *International Astronautical Congress*. Adelaide, Sept. 2017.

[17] M. J. Patterson et al. 'Annular engine development status'. *Joint Propulsion Conference*. San Jose, July 2013. DOI: 10.2514/6.2013-3892.

[18] M. J. Patterson et al. 'High thrust-to-power annular engine technology'. *Joint Propulsion Conference*. Orlando, July 2015. DOI: 10.2514/6.2015-3719.

[19] M. J. Patterson and S. Benson. 'NEXT ion propulsion system development status and performance'. *Joint Propulsion Conference*. Cincinnati, July 2007. DOI: 10.2514/6.2007-5199.

[20] J. E. Polk et al. 'An overview of NASA's electric propulsion programs, 2010-11'. *International Electric Propulsion Conference*. Wiesbaden, Sept. 2011.

[21] J. Gonzalez, G. Saccoccia and H. von Rohoden. 'Field emission electric propulsion: Experimental investigations on microthrust FEEP thrusters'. *International Electric Propulsion Conference*. Seattle, Sept. 1993.

[22] D. M. Goebel and I. Katz. *Fundamentals of Electric Propulsion. Ion and Hall Thrusters*. Wiley: Hoboken, Oct. 2008. ISBN: 9780470429273.

[23] V. Khayms. 'Advanced propulsion for microsatellites'. PhD thesis. Massachusetts Institute of Technology, Cambridge, Sept. 2000.

[24] A. Smirnov, Y. Raitses and N. J. Fisch. 'Parametric investigation of miniaturized cylindrical and annular Hall thrusters'. *Journal of Applied Physics* 92.10 (Nov. 2002), pp. 5673–5679. DOI: 10.1063/1.1515106.

[25] M. A. Cappelli, N. Gascon and W. A. Hargus Jr. 'Millimetre wave plasma interferometry in the near field of a Hall plasma accelerator'. *Journal of Physics D: Applied Physics* 39.21 (Oct. 2006), pp. 4582–4588. DOI: 10.1088/0022-3727/39/21/013.

[26] W. A. Hargus and C. S. Charles. 'Near exit plane velocity field of a 200-Watt Hall thruster'. *Journal of Propulsion and Power* 24.1 (Jan. 2008), pp. 127–133. DOI: 10.2514/1.29949.

[27] R. R. Hofer. 'High-specific impulse operation of the BPT-4000 Hall thruster for NASA science missions'. *Joint Propulsion Conference*. Nashville, July 2010. DOI: 10.2514/6.2010-6623.

[28] M. Dudeck et al. 'Plasma propulsion for geostationary satellites and interplanetary spacecraft'. *Romanian Journal of Physics* 56 (2011), pp. 3–14. URL: http://www.nipne.ro/rjp/2011_56_Suppl/0003_0014.pdf.

[29] I. S. Director. 'Reverse Proxy - - ANU' (Oct. 2013). URL: http://pepl.engin.umich.edu/pdf/IEPC-2013-394.pdf.

[30] S. J. Hall et al. 'Implementation and initial validation of a 100-kW class nested-channel Hall thruster'. *Joint Propulsion Conference*. Cleveland, July 2014. DOI: 10.2514/6.2014-3815.

[31] S. J. Hall, S. E. Cusson and A. D. Gallimore. '30-kW performance of a 100-kW class nested-channel Hall thruster'. *International Electric Propulsion Conference*. Kobe, July 2015.

[32] C. Charles and R. W. Boswell. 'Current-free double-layer formation in a high-density helicon discharge'. *Applied Physics Letters* 82.9 (Mar. 2003), pp. 1356–1358. DOI: 10.1063/1.1557319.

[33] M. R. LaPointe and P. G. Mikellides. 'High power MPD thruster development at the NASA Glenn Research Center'. *Joint Propulsion Conference*. Joint Propulsion Conference: Salt Lake City, July 2001. DOI: 10.2514/6.2001-3499.

[34] A. D. Kodys and E. Y. Choueiri. 'A critical review of the state-of-the-art in the performance of applied-field magnetoplasmadynamic thrusters'. *Joint Propulsion Conference*. Joint Propulsion Conference: Tucson, July 2005. DOI: 10.2514/6.2005-4247.

[35] M. Keidar et al. 'Electric propulsion for small satellites'. *Plasma Physics and Controlled Fusion* 57.1 (Nov. 2015), p. 014005. DOI: 10.1088/0741-3335/57/1/014005.

[36] C. Charles. 'Plasmas for spacecraft propulsion'. *Journal of Physics D: Applied Physics* 42.16 (July 2009), p. 163001. DOI: 10.1088/0022-3727/42/16/163001.

[37] S. Mazouffre. 'Electric propulsion for satellites and spacecraft: Established technologies and novel approaches'. *Plasma Sources Science and Technology* 25.3 (Apr. 2016), p. 033002. DOI: 10.1088/0963-0252/25/3/033002.

[38] M. M. Micci and A. D. Ketsdever. *Micropropulsion for Small Spacecraft*. AIAA: Reston, Jan. 2000. ISBN: 9781563474484. DOI: 10.2514/4.866586.

[39] D. Scharfe and A. D. Ketsdever. 'A review of high thrust, high delta-v options for microsatellite missions'. *Joint Propulsion Conference*. Denver, Aug. 2009. DOI: 10.2514/6.2009-4824.

[40] G. P. Sutton and O. Biblarz. *Rocket Propulsion Elements*. 9th ed. Wiley: Hoboken, Nov. 2016. ISBN: 9781118753910.

[41] R. W. Boswell et al. 'Plasma expansion from a radio frequency microdischarge'. *IEEE Transactions on Plasma Science* 39.11 (May 2011), pp. 2512–2513. DOI: 10.1109/TPS.2011.2143434.

[42] C. Charles, R. W. Boswell and K. Takahashi. 'Investigation of radiofrequency plasma sources for space travel'. *Plasma Physics and Controlled Fusion* 54.12 (Nov. 2012), p. 124021. DOI: 10.1088/0741-3335/54/12/124021.

[43] T. Charoy. 'Design of a gas injection system for a micro electro thermal thruster'. Undergraduate thesis. The Australian National University, Canberra, Mar. 2016.

[44] A. Pascale. 'Design and construction of a propellant sub-system for SP3's CubeSat plasma thruster'. Honours thesis. The Australian National University, Canberra, Oct. 2016.

[45] A. Stuchbery. 'Development, integration, and testing of the 'Pocket Rocket' plasma thruster'. Honours thesis. The Australian National University, Canberra, Oct. 2017.

[46] C. Charles, R. W. Boswell and A. Bish. 'Low-weight fixed ceramic capacitor impedance matching system for an electrothermal plasma microthruster'. *Journal of Propulsion and Power* 30.4 (Apr. 2014), pp. 1117–1121. DOI: 10.2514/1.B35119.

[47] C. Charles et al. 'Vacuum testing of a miniaturized switch mode amplifier powering an electrothermal plasma micro-thruster'. *Frontiers in Physics* 5 (Aug. 2017), p. 36. DOI: 10.3389/fphy.2017.00036.

[48] T. S. Ho, C. Charles and R. W. Boswell. 'Performance modelling of plasma microthruster nozzles in vacuum'. *Journal of Applied Physics* 123.17 (May 2018), p. 173301. DOI: 10.1063/1.5012765.

[49] A. Greig et al. 'Direct measurement of neutral gas heating in a radio-frequency electrothermal plasma micro-thruster'. *Applied Physics Letters* 103.7 (Aug. 2013), p. 074101. DOI: 10.1063/1.4818657.

[50] T. S. Ho, C. Charles and R. W. Boswell. 'Neutral gas heating and ion transport in a constricted plasma flow'. *Physics of Plasmas* 24.8 (July 2017), p. 084501. DOI: 10.1063/1.4996014.

[51] A. Greig, C. Charles and R. W. Boswell. 'Spatiotemporal study of gas heating mechanisms in a radio-frequency electrothermal plasma micro-thruster'. *Frontiers in Physics* 3 (Oct. 2015), p. 84. DOI: 10.3389/fphy.2015.00084.

[52] S. J. Doyle et al. 'Spatio-temporal plasma heating mechanisms in a radio frequency electrothermal microthruster'. *Plasma Sources Science and Technology* 27.8 (Aug. 2018), p. 085011. DOI: 10.1088/1361-6595/aad79a.

[53] C. Charles et al. 'Direct measurement of axial momentum imparted by an electrothermal radiofrequency plasma micro-thruster'. *Frontiers in Physics* 4 (May 2016), p. 19. DOI: 10.3389/fphy.2016.00019.

[54] N. S. J. Braithwaite. 'Introduction to gas discharges'. *Plasma Sources Science and Technology* 9.4 (Oct. 2000), pp. 517–527. DOI: 10.1088/0963-0252/9/4/307.

[55] A. Greig et al. 'Volume and surface propellant heating in an electrothermal radio-frequency plasma micro-thruster'. *Applied Physics Letters* 105 (Aug. 2014), p. 054102. DOI: 10.1063/1.4892656.

[56] T. S. Ho, C. Charles and R. W. Boswell. 'Redefinition of the self-bias voltage in a dielectrically shielded thin sheath RF discharge'. *Journal of Applied Physics* 123.19 (May 2018), p. 193301. DOI: 10.1063/1.5023076.

[57] P. Belenguer and J.-P. Boeuf. 'Transition between different regimes of rf glow discharges'. *Physical Review A* 41.8 (Apr. 1990), pp. 4447–4459. DOI: 10.1103/PhysRevA.41.4447.

[58] S. Dixon. 'Experimental study of expanding hollow cathode discharges'. PhD thesis. The Australian National University, Canberra, July 2014.

[59] *MKS Type 1179A and 2179A Mass-Flo Controller and Type 179A Mass-Flo Meter*. Manual. MKS Instruments: Andover, Mar. 1999.

[60] A. Greig. 'Pocket Rocket: An electrothermal plasma micro-thruster'. PhD thesis. The Australian National University, Canberra, July 2015.

[61] V. I. Kolobov et al. 'Comparison of computational tools for simulations of glow and corona discharges'. *International Conference on Phenomena in Ionized Gases*. Granada, July 2013.

[62] *CFD-ACE+*. Manual. ESI Group: Huntsville, July 2014.

[63] M. J. Kushner. 'Hybrid modelling of low temperature plasmas for fundamental investigations and equipment design'. *Journal of Physics D: Applied Physics* 42.19 (Sept. 2009), p. 194013. DOI: 10.1088/0022-3727/42/19/194013.

[64] M. J. Kushner. 'Introduction to the Hybrid Plasma Equipment Model'. University of Illinois: Urbana, Jan. 1999. URL: http://uigelz.eecs.umich.edu/pub/odp_files/hpem_intro.pdf.

[65] M. J. Kushner and J. Lu. 'Plasma equipment modeling from process design'. University of Illinois: Urbana, 2000. URL: http://uigelz.eecs.umich.edu/pub/articles/vmic_proc_0600.pdf.

[66] A. Greig, C. Charles and R. W. Boswell. 'Simulation of main plasma parameters of a cylindrical asymmetric capacitively coupled plasma micro-thruster using computational fluid dynamics'. *Frontiers in Physics* 2 (Jan. 2015), p. 80. DOI: 10.3389/fphy.2014.00080.

[67] E. W. Lemmon, M. O. McLinden and D. G. Friend. 'Thermophysical Properties of Fluid Systems'. *NIST Chemistry WebBook. NIST Standard Reference Database 69*. Ed. by P. J. Linstrom and W. G. Mallard. National Institute of Standards and Technology: Gaithersburg, 2017. URL: https://webbook.nist.gov/chemistry/fluid.

[68] Munro, R G. *Structural Ceramics Database. NIST Standard Reference Database Number 30*. Ed. by R. G. Munro. National Institute of Standards and Technology: Gaithersburg, June 2015. DOI: 10.18434/T4F30D.

[69] W. M. Haynes. *CRC Handbook of Chemistry and Physics*. 96th ed. CRC Press: Boca Raton, June 2015. ISBN: 9781482260960.

[70] *MatWeb*. URL: http://www.matweb.com/.

[71] I. Amdur and E. A. Mason. 'Properties of gases at very high temperatures'. *Physics of Fluids* 1.5 (Sept. 1958), pp. 370–383. DOI: 10.1063/1.1724353.

[72] J. H. Dymond. 'High temperature transport coefficients for the rare gases neon to xenon'. *Journal of Physics B: Atomic and Molecular Physics* 4.4 (Mar. 2001), pp. 621–627. DOI: 10.1088/0022-3700/4/4/025.

[73] F. Hutchinson. 'Self-diffusion in argon'. *Journal of Chemical Physics* 17.11 (Nov. 1949), pp. 1081–1086. DOI: 10.1063/1.1747116.

[74] E. B. Winn. 'The temperature dependence of the self-diffusion coefficients of argon, neon, nitrogen, oxygen, carbon dioxide, and methane'. *Physical Review* 80.6 (Dec. 1950), pp. 1024–1027. DOI: 10.1103/PhysRev.80.1024.

[75] E. R. S. Winter. 'Diffusion properties of gases'. *Transactions of the Faraday Society* 47 (Jan. 1951), pp. 342–347. DOI: 10.1039/TF9514700342.

[76] A. A. Westenberg and R. E. Walker. 'New method of measuring diffusion coefficients of gases'. *Journal of Chemical Physics* 26.6 (June 1957), pp. 1753–1754. DOI: 10.1063/1.1743618.

[77] I. Amdur and T. F. Schatzki. 'Diffusion coefficients of the systems Xe-Xe and Ar-Xe'. *Journal of Chemical Physics* 27.5 (Nov. 1957), pp. 1049–1054. DOI: 10.1063/1.1743930.

[78] H. F. Vugts, A. J. Boerboom and J. Los. 'Diffusion coefficients of isotopic mixtures of CO and N_2'. *Physica* 50.4 (Dec. 1970), pp. 593–605. DOI: 10.1016/0031-8914(70)90216-8.

[79] S. Chapman and T. G. Cowling. *The Mathematical Theory of Non-uniform Gases. An Account of the Kinetic Theory of Viscosity, Thermal Conduction and Diffusion in Gases*. 3rd ed. Cambridge University Press: Cambridge, Jan. 1991. ISBN: 9780521408448.

[80] E. L. Cussler. *Diffusion. Mass Transfer in Fluid Systems*. 3rd ed. Cambridge University Press: Cambridge, Feb. 2009. ISBN: 9780521871211.

[81] P. J. Linstrom and W. G. Mallard, eds. *NIST Chemistry WebBook. NIST Standard Reference Database 69*. Gaithersburg. DOI: 10.18434/T4D303.

[82] B. E. Poling, J. M. Prausnitz and J. P. OConnell. *The Properties of Gases and Liquids*. 5th ed. McGraw-Hill: New York, Nov. 2000. ISBN: 9780070116825. DOI: 10.1036/0070116822.

[83] R. D. Johnson III. *Computational Chemistry Comparison and Benchmark Database. NIST Standard Reference Database Number 101*. Ed. by P. J. Linstrom and W. G. Mallard. 18th ed. National Institute of Standards and Technology: Gaithersburg, Oct. 2016. DOI: 10.18434/T47C7Z.

[84] G. E. Karniadakis, A. Beskok and N. Aluru. *Microflows and Nanoflows. Fundamentals and Simulation*. Springer: New York, July 2005. ISBN: 9780387221977. DOI: 10.1007/0-387-28676-4.

[85] F. La Torre. 'Gas flow in miniaturized nozzles for micro-thrusters'. PhD thesis. Delft University of Technology, Delft, June 2011.

[86] J. C. Maxwell. 'On stresses in rarified gases arising from inequalities of temperature'. *Philosophical Transactions of the Royal Society of London* 170 (Jan. 1879), pp. 231–256. DOI: 10.1098/rstl.1879.0067.

[87] B. V. Deryagin and N. N. Fedyakin. 'Complete specular reflection of molecules at low angles of incidence and its effect on the molecular flow of gases through very narrow capillaries'. *Progress in Surface Science* 43.1 (Aug. 1993), pp. 290–301. DOI: 10.1016/0079-6816(93)90040-3.

[88] A. V. Bogdanov et al. *Interaction of Gases with Surfaces. Detailed Description of Elementary Processes and Kinetics*. Springer: Berlin, Apr. 1995. ISBN: 9783540588023. DOI: 10.1007/978-3-540-49107-1.

[89] K. S. Dadzie and G. J. Méolans. 'Anisotropic scattering kernel: Generalized and modified Maxwell boundary conditions'. *Journal of Mathematical Physics* 45.5 (Apr. 2004), pp. 1804–1819. DOI: 10.1063/1.1690491.

[90] C. Cercignani and M. Lampis. 'Kinetic models for gas-surface interactions'. *Transport Theory and Statistical Physics* 1.2 (1971), pp. 101–114. DOI: 10.1080/00411457108231440.

[91] B. T. Porodnov et al. 'Experimental investigation of rarefied gas flow in different channels'. *Journal of Fluid Mechanics* 64.03 (July 1974), pp. 417–438. DOI: 10.1017/S0022112074002485.

[92] J. Maurer et al. 'Second-order slip laws in microchannels for helium and nitrogen'. *Physics of Fluids* 15.9 (Aug. 2003), pp. 2613–2621. DOI: 10.1063/1.1599355.

[93] S. Colin, P. Lalonde and R. Caen. 'Validation of a second-order slip flow model in rectangular microchannels'. *Heat Transfer Engineering* 25.3 (Apr. 2004), pp. 23–30. DOI: 10.1080/01457630490280047.

[94] T. Ewart et al. 'Tangential momemtum accommodation in microtube'. *Microfluidics and Nanofluidics* 3.6 (Feb. 2007), pp. 689–695. DOI: 10.1007/s10404-007-0158-3.

[95] I. A. Graur et al. 'Measurements of tangential momentum accommodation coefficient for various gases in plane microchannel'. *Physics of Fluids* 21.10 (Oct. 2009), p. 102004. DOI: 10.1063/1.3253696.

[96] P. Perrier et al. 'Mass flow rate measurements in microtubes: From hydrodynamic to near free molecular regime'. *Physics of Fluids* 23.4 (Apr. 2011), p. 042004. DOI: 10.1063/1.3562948.

[97] H. Yamaguchi et al. 'Experimental measurement on tangential momentum accommodation coefficient in a single microtube'. *Microfluidics and Nanofluidics* 11.1 (Feb. 2011), pp. 57–64. DOI: 10.1007/s10404-011-0773-x.

[98] M. Hadj Nacer et al. 'Gas flow through microtubes with different internal surface coatings'. *Journal of Vacuum Science & Technology A: Vacuum, Surfaces, and Films* 32.2 (Nov. 2013), p. 021601. DOI: 10.1116/1.4828955.

[99] S. Song and M. M. Yovanovich. 'Contact interface gas heat transfer: A method of measuring thermal accommodation coefficient'. *International Conference on Electronics Packaging*. San Diego, Sept. 1989, pp. 925–936.

[100] B. T. Porodnov, A. N. Kulev and F. T. Tuchvetov. 'Thermal transpiration in a circular capillary with a small temperature difference'. *Journal of Fluid Mechanics* 88.4 (Oct. 1978), pp. 609–622. DOI: 10.1017/S002211207800230X.

[101] D. J. Rader et al. 'Measurements of thermal accommodation coefficients'. Sandia National Laboratories: Albuquerque, Oct. 2005. DOI: 10.2172/876357.

[102] W. M. Trott et al. 'An experimental assembly for precise measurement of thermal accommodation coefficients'. *Review of Scientific Instruments* 82.3 (Mar. 2011), p. 035120. DOI: 10.1063/1.3571269.

[103] D. Ganta et al. 'Optical method for measuring thermal accommodation coefficients using a whispering-gallery microresonator'. *Journal of Chemical Physics* 135.8 (Aug. 2011), p. 084313. DOI: 10.1063/1.3631342.

[104] H. Yamaguchi et al. 'Investigation on heat transfer between two coaxial cylinders for measurement of thermal accommodation coefficient'. *Physics of Fluids* 24.6 (June 2012), p. 062002. DOI: 10.1063/1.4726059.

[105] N. B. Vargaftik, A. A. Voshchinin and V. V. Kerzhentsev. 'Experimental determination of the accommodation coefficients of argon and xenon on nickel at high temperatures'. *Journal of Engineering Physics* 25.5 (Nov. 1973), pp. 1391–1393. DOI: 10.1007/BF00838115.

[106] L. B. Thomas and F. Olmer. 'The accommodation coefficients of He, Ne, Ar, H_2, D_2, O_2, CO_2, and Hg on platinum as a function of temperature'. *Journal of the American Chemical Society* 65.6 (June 1943), pp. 1036–1043. DOI: 10.1021/ja01246a011.

[107] M. N. Kogan. *Rarefied Gas Dynamics*. Springer: New York, Jan. 1969. ISBN: 9781489961891. DOI: 10.1007/978-1-4899-6381-9.

[108] D. A. Lockerby et al. 'Velocity boundary condition at solid walls in rarefied gas calculations'. *Physical Review E* 70.1 (July 2004), p. 017303. DOI: 10.1103/PhysRevE.70.017303.

[109] M. Smoluchowski von Smolan. 'Ueber Wärmeleitung in verdünnten Gasen'. *Annalen der Physik* 300.1 (1898), pp. 101–130. DOI: 10.1002/andp.18983000110.

[110] P. L. Kapizta. 'Viscosity of liquid helium below the λ-point'. *Nature* 141.3558 (Jan. 1938), p. 74. DOI: 10.1038/141074a0.

[111] A. Agarwal, S. Rauf and K. Collins. 'Gas heating mechanisms in capacitively coupled plasmas'. *Plasma Sources Science and Technology* 21.5 (Aug. 2012), p. 055012. DOI: 10.1088/0963-0252/21/5/055012.

[112] S. Nunomura, M. Kondo and H. Akatsuka. 'Gas temperature and surface heating in plasma-enhanced chemical vapour deposition'. *Plasma Sources Science and Technology* 15.4 (Aug. 2006), pp. 783–789. DOI: 10.1088/0963-0252/15/4/023.

[113] M. Laroussi and X. Lu. 'Room-temperature atmospheric pressure plasma plume for biomedical applications'. *Applied Physics Letters* 87.11 (Sept. 2005), p. 113902. DOI: 10.1063/1.2045549.

[114] P. J. Bruggeman et al. 'Gas temperature determination from rotational lines in non-equilibrium plasmas: a review'. *Plasma Sources Science and Technology* 23.2 (Apr. 2014), p. 023001. DOI: 10.1088/0963-0252/23/2/023001.

[115] A. Greig, C. Charles and R. W. Boswell. 'Neutral gas temperature estimates and metastable resonance energy transfer for argon-nitrogen discharges'. *Physics of Plasmas* 23.1 (Jan. 2016), p. 013508. DOI: 10.1063/1.4939028.

[116] J.-P. Booth et al. 'Gas temperature measurements in oxygen plasmas by high-resolution Two-Photon Absorption Laser-induced Fluorescence'. *Journal of Instrumentation* 10.11 (Nov. 2015), p. C11003. DOI: 10.1088/1748-0221/10/11/C11003.

[117] C. D. Pintassilgo and V. Guerra. 'On the different regimes of gas heating in air plasmas'. *Plasma Sources Science and Technology* 24.5 (Aug. 2015), p. 055009. DOI: 10.1088/0963-0252/24/5/055009.

[118] G. Shivkumar et al. 'Analysis of hydrogen plasma in a microwave plasma chemical vapor deposition reactor'. *Journal of Applied Physics* 119.11 (Mar. 2016), p. 113301. DOI: 10.1063/1.4943025.

[119] C. E. Moore. *Atomic Energy Levels. As Derived from the Analyses of Optical Spectra*. Vol. 1. U.S. Government Printing Office: Washington, Dec. 1971. URL: https://nvlpubs.nist.gov/nistpubs/Legacy/NSRDS/nbsnsrds35v1.pdf.

[120] A. Kramida, Y. Ralchenko and J. Reader. *Atomic Spectra Database*. v5.5.2. National Institute of Standards and Technology: Gaithersburg, Jan. 2018. URL: https://physics.nist.gov/asd.

[121] C. E. Moore. *Ionization Potentials and Ionization Limits Derived from the Analyses of Optical Spectra*. U.S. Government Printing Office: Washington, Sept. 1970. URL: https://nvlpubs.nist.gov/nistpubs/Legacy/NSRDS/nbsnsrds34.pdf.

[122] M. W. Chase Jr. *NIST-JANAF Thermochemical Tables. Journal of Physical and Chemical Reference Data*. 4th ed. American Institute of Physics: New York, Aug. 1998. ISBN: 9781563968310.

[123] M. A. Khakoo et al. 'Electron impact excitation of the argon $3p^5 4s$ configuration: Differential cross-sections and cross-section ratios'. *Journal of Physics B: Atomic, Molecular and Optical Physics* 37.1 (Jan. 2004), pp. 247–281. DOI: 10.1088/0953-4075/37/1/016.

[124] J. E. Chilton et al. 'Measurement of electron-impact excitation into the $3p^5 4p$ levels of argon using Fourier-transform spectroscopy'. *Physical Review A* 57.1 (Jan. 1998), pp. 267–277. DOI: 10.1103/PhysRevA.57.267.

[125] L. L. Alves. 'The IST-LISBON database on LXCat'. *Journal of Physics: Conference Series* 565.1 (Dec. 2014), p. 012007. DOI: 10.1088/1742-6596/565/1/012007.

[126] C. Yamabe, S. J. Buckman and A. V. Phelps. 'Measurement of free-free emission from low-energy-electron collisions with Ar'. *Physical Review A* 27.3 (Mar. 1983), pp. 1345–1352. DOI: 10.1103/PhysRevA.27.1345.

[127] D. Rapp and P. Englander-Golden. 'Total cross sections for ionization and attachment in gases by electron impact. I. Positive ionization'. *Journal of Chemical Physics* 43.5 (Sept. 1965), pp. 1464–1479. DOI: 10.1063/1.1696957.

[128] J. T. Guðmundsson and E. G. Thorsteinsson. 'Oxygen discharges diluted with argon: Dissociation processes'. *Plasma Sources Science and Technology* 16.2 (Apr. 2007), pp. 399–412. DOI: 10.1088/0963-0252/16/2/025.

[129] S. Ashida, C. Lee and M. A. Lieberman. 'Spatially averaged (global) model of time modulated high density argon plasmas'. *Journal of Vacuum Science & Technology A: Vacuum, Surfaces, and Films* 13.5 (Sept. 1995), pp. 2498–2507. DOI: 10.1116/1.579494.

[130] C. M. Ferreira, J. Loureiro and A. Ricard. 'Populations in the metastable and the resonance levels of argon and stepwise ionization effects in a low-pressure argon positive column'. *Journal of Applied Physics* 57.1 (Jan. 1985), pp. 82–90. DOI: 10.1063/1.335400.

[131] F. Kannari, M. Obara and T. Fujioka. 'An advanced kinetic model of electron-beam-excited KrF lasers including the vibrational relaxation in $KrF^{\bullet}(B)$ and collisional mixing of $KrF^{\bullet}(B, C)$'. *Journal of Applied Physics* 57.9 (May 1985), pp. 4309–4322. DOI: 10.1063/1.334590.

[132] N. L. Bassett and D. J. Economou. 'Effect of Cl_2 additions to an argon glow discharge'. *Journal of Applied Physics* 75.4 (Feb. 1994), pp. 1931–1939. DOI: 10.1063/1.356340.

[133] G. S. Hurst, E. B. Wagner and M. G. Payne. 'Energy transfer from the resonance states Ar ($^1P_1$) and Ar ($^3P_1$) to ethylene'. *Journal of Chemical Physics* 61.9 (Nov. 1974), pp. 3680–3685. DOI: 10.1063/1.1682553.

[134] M.-H. Lee, S.-H. Jang and C.-W. Chung. 'On the multistep ionizations in an argon inductively coupled plasma'. *Physics of Plasmas* 13.5 (May 2006), p. 053502. DOI: 10.1063/1.2193535.

[135] M. A. Lieberman and A. J. Lichtenberg. *Principles of Plasma Discharges and Materials Processing*. 2nd ed. Wiley: Hoboken, Apr. 2005. ISBN: 9780471720010.

[136] *MKS Baratron Type 626B Absolute Pressure Transducers*. Manual. MKS Instruments: Andover, Mar. 2013.

[137] B. J. Nichols and F. C. Witteborn. 'Measurements of resonant charge exchange cross sections in nitrogen and argon between 0.5 and 17 eV'. *NASA Technical Note* (Feb. 1966), pp. 1–30. URL: https://ntrs.nasa.gov/search.jsp?R=19660006802.

[138] E. A. Edelberg and E. S. Aydil. 'Modeling of the sheath and the energy distribution of ions bombarding rf-biased substrates in high density plasma reactors and comparison to experimental measurements'. *Journal of Applied Physics* 86.9 (Nov. 1999), pp. 4799–4812. DOI: 10.1063/1.371446.

[139] C. Steinbrüchel. 'Universal energy dependence of physical and ion-enhanced chemical etch yields at low ion energy'. *Applied Physics Letters* 55.19 (Nov. 1989), pp. 1960–1962. DOI: 10.1063/1.102336.

[140] H. Jansen et al. 'A survey on the reactive ion etching of silicon in microtechnology'. *Journal of Micromechanics and Microengineering* 6.1 (Mar. 1996), pp. 14–28. DOI: 10.1088/0960-1317/6/1/002.

[141] T. A. Lafleur, P. Chabert and J.-P. Booth. 'Secondary electron induced asymmetry in capacitively coupled plasmas'. *Journal of Physics D: Applied Physics* 46.13 (Feb. 2013), p. 135201. DOI: 10.1088/0022-3727/46/13/135201.

[142] B. G. Heil et al. 'On the possibility of making a geometrically symmetric RF-CCP discharge electrically asymmetric'. *Journal of Physics D: Applied Physics* 41.16 (July 2008), p. 165202. DOI: 10.1088/0022-3727/41/16/165202.

[143] T. A. Lafleur. 'Tailored-waveform excitation of capacitively coupled plasmas and the electrical asymmetry effect'. *Plasma Sources Science and Technology* 25.1 (Nov. 2015), p. 013001. DOI: 10.1088/0963-0252/25/1/013001.

[144] M. Wiebold, Y.-T. Sung and J. E. Scharer. 'Ion acceleration in a helicon source due to the self-bias effect'. *Physics of Plasmas* 19.5 (May 2012), p. 053503. DOI: 10.1063/1.4714605.

[145] H. S. Butler and G. S. Kino. 'Plasma sheath formation by radio-frequency fields'. *The Physics of Fluids* 6.9 (Sept. 1963), pp. 1346–1355. DOI: 10.1063/1.1706905.

[146] K. Köhler et al. 'Plasma potentials of 13.56-MHz RF argon glow discharges in a planar system'. *Journal of Applied Physics* 57.1 (Jan. 1985), pp. 59–66. DOI: 10.1063/1.335396.

[147] M. M. Salem and J. F. Loiseau. 'Experiments to sort out theoretical models concerning the area ratio law for plasma reactors'. *Journal of Physics D: Applied Physics* 29.5 (May 1996), pp. 1181–1187. DOI: 10.1088/0022-3727/29/5/011.

[148] J.-P. Booth et al. 'The transition from symmetric to asymmetric discharges in pulsed 13.56 MHz capacitively coupled plasmas'. *Journal of Applied Physics* 82.2 (July 1997), pp. 552–560. DOI: 10.1063/1.365614.

[149] C. Charles, R. W. Boswell and M. A. Lieberman. 'Energy balance in a low pressure capacitive discharge driven by a double-saddle antenna'. *Physics of Plasmas* 10.3 (Mar. 2003), pp. 891–899. DOI: 10.1063/1.1555058.

[150] H. B. Smith. 'Computational studies of an asymmetric RF plasma using particle-in-cell techniques'. PhD thesis. The Australian National University, Canberra, Oct. 1994.

[151] H. B. Smith et al. 'Bias formation in a pulsed radiofrequency argon discharge'. *Journal of Applied Physics* 82.2 (June 1998), pp. 561–565. DOI: 10.1063/1.365615.

[152] T. A. Lafleur and R. W. Boswell. 'Particle-in-cell simulations of hollow cathode enhanced capacitively coupled radio frequency discharges'. *Physics of Plasmas* 19.2 (Feb. 2012), p. 023508. DOI: 10.1063/1.3685709.

[153] M. A. Lieberman. 'Analytical solution for capacitive RF sheath'. *IEEE Transactions on Plasma Science* 16.6 (Dec. 1988), pp. 638–644. DOI: 10.1109/27.16552.

[154] M. A. Lieberman. 'Dynamics of a collisional, capacitive RF sheath'. *IEEE Transactions on Plasma Science* 17.2 (Apr. 1989), pp. 338–341. DOI: 10.1109/27.24645.

[155] P. M. Vallinga, P. M. Meijer and F. J. de Hoog. 'Sheath properties of RF plasmas in a parallel plate etch reactor; the high-frequency regime ($\omega > \omega_i$)'. *Journal of Physics D: Applied Physics* 22.11 (Nov. 1989), pp. 1650–1657. DOI: 10.1088/0022-3727/22/11/014.

[156] V. A. Godyak and N. Sternberg. 'Dynamic model of the electrode sheaths in symmetrically driven rf discharges'. *Physical Review A* 42.4 (Aug. 1990), pp. 2299–2312. DOI: 10.1103/PhysRevA.42.2299.

[157] E. Kawamura et al. 'Ion energy distributions in rf sheaths; review, analysis and simulation'. *Plasma Sources Science and Technology* 8.3 (Aug. 1999), R45–R64. DOI: 10.1088/0963-0252/8/3/202.

[158] A. Metze, D. W. Ernie and H. J. Oskam. 'Application of the physics of plasma sheaths to the modeling of rf plasma reactors'. *Journal of Applied Physics* 60.9 (Nov. 1986), pp. 3081–3087. DOI: 10.1063/1.337764.

[159] P. M. Vallinga and F. J. de Hoog. 'Sheath properties of RF plasmas in a parallel-plate etch reactor; the low-frequency regime ($\omega < \omega_i$)'. *Journal of Physics D: Applied Physics* 22.7 (July 1989), pp. 925–932. DOI: 10.1088/0022-3727/22/7/007.

[160] P. A. Miller and M. E. Riley. 'Dynamics of collisionless rf plasma sheaths'. *Journal of Applied Physics* 82.8 (Oct. 1997), pp. 3689–3709. DOI: 10.1063/1.365732.

[161] M. A. Sobolewski. 'Monitoring sheath voltages and ion energies in high-density plasmas using noninvasive radio-frequency current and voltage measurements'. *Journal of Applied Physics* 95.9 (May 2004), pp. 4593–4604. DOI: 10.1063/1.1687975.

[162] C. Charles et al. 'Absolute measurements and modeling of radio frequency electric fields using a retarding field energy analyzer'. *Physics of Plasmas* 7.12 (Dec. 2000), pp. 5232–5241. DOI: 10.1063/1.1322557.

[163] M. A. Sobolewski. 'Sheath model for radio-frequency-biased, high-density plasmas valid for all ω/ω_i'. *Physical Review E* 62.6 (Dec. 2000), pp. 8540–8553. DOI: 10.1103/PhysRevE.62.8540.

[164] M. A. Sobolewski. 'Measuring the ion current in high-density plasmas using radio-frequency current and voltage measurements'. *Journal of Applied Physics* 90.6 (Aug. 2001), pp. 2660–2671. DOI: 10.1063/1.1390491.

[165] M. A. Sobolewski. 'Effects of wafer impedance on the monitoring and control of ion energy in plasma reactors'. *Journal of Applied Physics* 100.6 (Sept. 2006), p. 063310. DOI: 10.1063/1.2353203.

[166] C. J. Chapman. *High Speed Flow*. Cambridge University Press: Cambridge, Mar. 2000. ISBN: 9780521666473.

[167] H. R. Murphy and D. R. Miller. 'Effects of nozzle geometry on kinetics in free-jet expansions'. *Journal of Physical Chemistry* 88.20 (Sept. 1984), pp. 4474–4478. DOI: 10.1021/j150664a005.

[168] L. Garrigues et al. 'Model study of the influence of the magnetic field configuration on the performance and lifetime of a Hall thruster'. *Physics of Plasmas* 10.12 (Dec. 2003), pp. 4886–4892. DOI: 10.1063/1.1622670.

[169] L. Garrigues et al. 'Performance modeling of a thrust vectoring device for Hall effect thrusters'. *Journal of Propulsion and Power* 25.5 (Sept. 2009), pp. 1003–1012. DOI: 10.2514/1.39680.

[170] A. Greig, C. Charles and R. W. Boswell. 'Plume characteristics of an electrothermal plasma microthruster'. *IEEE Transactions on Plasma Science* 42.10 (May 2014), pp. 2728–2729. DOI: 10.1109/TPS.2014.2321176.

[171] T. S. Ho, C. Charles and R. W. Boswell. 'A comprehensive cold gas performance study of the Pocket Rocket radiofrequency electrothermal microthruster'. *Frontiers in Physics* 4 (Jan. 2017), p. 55. DOI: 10.3389/fphy.2016.00055.

[172] N. Mutsukura, K. Kobayashi and Y. Machi. 'Plasma sheath thickness in radio-frequency discharges'. *Journal of Applied Physics* 68.6 (Sept. 1990), pp. 2657–2660. DOI: 10.1063/1.346491.

[173] M. Surendra and D. B. Graves. 'Capacitively coupled glow discharges at frequencies above 13.56 MHz'. *Applied Physics Letters* 59.17 (June 1998), pp. 2091–2093. DOI: 10.1063/1.106112.

[174] M. J. de Graaf et al. 'Thermal plasma source of hydrogen atoms and ions'. *Journal de Physique Colloques* 51 (Sept. 1990), pp. 387–392. DOI: 10.1051/jphyscol:1990546.

[175] R. F. G. Meulenbroeks et al. 'Depolarization Rayleigh scattering as a means of molecular concentration determination in plasmas'. *Physical Review Letters* 69.9 (Aug. 1992), pp. 1379–1382. DOI: 10.1103/PhysRevLett.69.1379.

[176] A. Fruchtman. 'The thrust of a collisional-plasma source'. *IEEE Transactions on Plasma Science* 39.1 (Dec. 2010), pp. 530–539. DOI: 10.1109/TPS.2010.2089067.

[177] A. Fruchtman. 'Energizing and depletion of neutrals by a collisional plasma'. *Plasma Sources Science and Technology* 17.2 (May 2008), p. 024016. DOI: 10.1088/0963-0252/17/2/024016.

[178] A. Fruchtman. 'Neutral gas depletion in low temperature plasma'. *Journal of Physics D: Applied Physics* 50.47 (Oct. 2017), p. 473002. DOI: 10.1088/1361-6463/aa87a9.

[179] M. A. Kemp and S. D. Kovaleski. 'Thrust measurements of the ferroelectric plasma thruster'. *IEEE Transactions on Plasma Science* 36.2 (Apr. 2008), pp. 356–362. URL: http://ieeexplore.ieee.org/document/4456912/?reload=true.

[180] T. Takahashi et al. 'Microwave-excited microplasma thruster with helium and hydrogen propellants'. *Physics of Plasmas* 18.6 (June 2011), p. 063505. DOI: 10.1063/1.3596539.

[181] O. V. Penkov et al. 'A review of recent applications of atmospheric pressure plasma jets for materials processing'. *Journal of Coatings Technology and Research* 12.2 (Mar. 2015), pp. 225–235. DOI: 10.1007/s11998-014-9638-z.

[182] Y. Ito et al. 'High speed deposition of SiO_2 films with plasma jet based on capillary dielectric barrier discharge at atmospheric pressure'. *Applied Physics Express* 1.6 (June 2008), p. 067009. DOI: 10.1143/APEX.1.067009.

[183] E. J. Szili et al. 'Modelling the helium plasma jet delivery of reactive species into a 3D cancer tumour'. *Plasma Sources Science and Technology* 27.1 (Dec. 2017), p. 014001. DOI: 10.1088/1361-6595/aa9b3b.

[184] J.-S. Oh et al. 'Mass spectrometry analysis of the real-time transport of plasma-generated ionic species through an agarose tissue model target'. *Journal of Photopolymer Science and Technology* 30.3 (June 2017), pp. 317–323. DOI: 10.2494/photopolymer.30.317.